

ZR

ISSN 2095-8137 CN 53-1229/Q

Volume 40 Issue 5
18 September 2019

Zoological Research



CODEN: DOYADI

www.zoores.ac.cn

ZOOLOGICAL RESEARCH

Volume 40, Issue 5 18 September 2019

CONTENTS

Commentary

- Progress in *in vitro* culture and gene editing of porcine spermatogonial stem cells
.....Yi-Zhuo Sun, Si-Tong Liu, Xiao-Meng Li, Kang Zou (343)

Review

- Stem cell therapy for Parkinson's disease using non-human primate models
.....Zhen-Zhen Chen, Yu-Yu Niu (349)

Articles

- Counting stripes: revision of the *Lipinia vittigera* complex (Reptilia, Squamata, Scincidae) with description of two new species from Indochina
.....Nikolay A. Poyarkov Jr., Peter Geissler, Vladislav A. Gorin, Evgeniy A. Dunayev, Timo Hartmann, Chatmongkon Suwannapoom (358)
- Synchronization between frontal eye field and area V4 during free-gaze visual search
.....Ting Yan, Hui-Hui Zhou (394)
- A soluble FcγR homolog inhibits IgM antibody production in ayu spleen cells
.....Kai Chen, Yu-Hong Shi, Jiong Chen, Ming-Yun Li (404)

Reports

- Immunodetection of ephrin receptors in the regenerating tail of the lizard *Podarcis muralis* suggests stimulation of differentiation and muscle segmentation.....
.....Lorenzo Alibardi (416)
- Genetic diversity and temporal changes of an endemic cyprinid fish species, *Ancherythroculter nigrocauda*, from the upper reaches of Yangtze River
.....Dong-Dong Zhai, Wen-Jing Li, Huan-Zhang Liu, Wen-Xuan Cao, Xin Gao (427)
- Non-invasive genetic analysis indicates low population connectivity in vulnerable Chinese gorals: concerns for segregated population management
.....Jing Yang, Guo-Fen Zhu, Jian Jiang, Chang-Lin Xiang, Fu-Li Gao, Wei-Dong Bao (439)
- Postural effect on manual laterality during grooming in northern white-cheeked gibbons (*Nomascus leucogenys*)
.....Da-Peng Zhao, Bo-Song Li, Bao-Guo Li (449)

Letters to the editor

- A new species of Mountain Dragon (Reptilia: Agamidae: *Diploderma*) from the *D. dymondi* complex in southern Sichuan Province, China
.....Kai Wang, Jia-Wei Wu, Ke Jiang, Jin-Min Chen, Ben-Fu Miao, Cameron D. Siler, Jing Che (456)
- Nest sanitation facilitates egg recognition in the common tailorbird, a plaintive cuckoo host
.....Chang-Zhang Feng, Can-Chao Yang, Wei Liang (466)

Cover design: Li-Bin Wu

Progress in *in vitro* culture and gene editing of porcine spermatogonial stem cells

Research on *in vitro* culture and gene editing of domestic spermatogonial stem cells (SSCs) is of considerable interest but remains a challenging issue in animal science. In recent years, some progress on the isolation, purification, and genetic manipulation of porcine SSCs has been reported. Here, we summarize the characteristics of porcine SSCs as well current advances in their *in vitro* culture, potential usage, and genetic manipulation. Furthermore, we discuss the current application of gene editing in pig cloning technology. Collectively, this commentary aims to summarize the progress made and obstacles encountered in porcine SSC research to better serve animal husbandry, improve livestock fecundity, and enhance potential clinical use.

Gene editing technology can not only improve livestock and poultry reproduction and meat quality (Gonen et al., 2017), but can also promote the study of gene function and therapy for human disease models via precise fixed-point editing (Gori et al., 2015; Zhao et al., 2019). Existing research suggests that SSCs maintain stability through self-renewal and can differentiate into sperm in order to produce offspring (Dym, 1994). However, the number of SSCs in mammalian testis is limited, and enrichment of SSCs is usually required using *in vitro* culture. In this context, constructing a suitable *in vitro* culture system that facilitates stable passage and maintenance of undifferentiated SSCs will help to reveal the biological characteristics of SSCs. Furthermore, it will allow for exploration of their potential usage and mechanisms of self-renewal and differentiation, as well as their application in transgenic manipulation and male infertility (Kubota & Brinster, 2006). For instance, a recent study established long-term propagation of tree shrew SSCs, paving the way for genetic modification of this animal for biomedical research (Li et al., 2017).

Gene editing is a genomic manipulation process involving base deletion, insertion, or mutation of a target gene sequence by means of the cell's own DNA damage repair

mechanism (Hwang et al., 2013; Ma et al., 2018). To date, the protocols for the isolation, purification, *in vitro* culture, and transplantation of murine SSCs have been established successfully (Brinster & Avarbock, 1994; Kubota et al., 2003, 2011; Nagano et al., 1998; Shinohara et al., 1999, 2000a, 2000b), and are widely accepted and used within the field. In contrast, the lack of a reliable protocol for the establishment of porcine SSC (pSSC) lines remains challenging and a major obstacle in genetic manipulation. However, many scientists are attempting to overcome these difficulties, with particular progress reported in recent years (Park et al., 2017b). Here, we summarize the characteristics of pSSCs, difficulties in establishment of pSSC lines, and recent advances in the field, which we hope will provide a useful reference for researchers.

SSCs are a population of germline stem cells residing in the testes of male animals. They are a type of unipotent stem cell with capacities of self-renewal and differentiation, which is the basis of spermatogenesis and male reproduction (de Rooij, 1998). Due to these abilities, SSCs can be permanently maintained to continuously produce sperm over the lifetime of a male, and thus allow the transmission of genetic information to the next generation. Therefore, SSCs are a core factor of male animal fertility.

Primordial germ cells (PGCs), the precursors of germ line cells, undergo a series of changes to eventually develop into SSCs. In the embryonic stages, the pre-spermatogonia are arrested, and it is generally believed that they regain proliferative activity within one week after birth in mice (Huckins & Clermont, 1968; Sapsford, 1962). Postnatally, SSCs are located on the basement membrane of the seminiferous tubule of male testes and function as initiating cells for spermatogenesis regulated by their microenvironment. The signals in the niche microenvironment affect the fate of SSCs, which can maintain their own population through self-renewal or can be directed to differentiate and eventually produce sperm (Chiarini-Garcia et al., 2003). Glial cell line-derived neurotrophic factor (GDNF) is essential for SSCs to maintain their reserves via constant self-

Open Access

This is an open-access article distributed under the terms of the Creative Commons Attribution Non-Commercial License (<http://creativecommons.org/licenses/by-nc/4.0/>), which permits unrestricted non-commercial use, distribution, and reproduction in any medium, provided the original work is properly cited.

Copyright ©2019 Editorial Office of Zoological Research, Kunming Institute of Zoology, Chinese Academy of Sciences

Received: 09 May 2019; Accepted: 31 July 2019; Online: 06 August 2019

Foundation items: This work was supported by the Fundamental Research Funds for the Central Universities in China (KYDS201807) and Ministry of Science and Technology, China (2016YFE0128500)

DOI: 10.24272/j.issn.2095-8137.2019.051

renewal (Bugeaw et al., 2005; Meng et al., 2000), with the stable pool of SSCs forming the basis of continuous spermatogenesis throughout life (Meachem et al., 2001). The production of type A spermatogonia marks the beginning of spermatogenesis (Takagi et al., 2001). According to the hierarchy of differentiation, type A cells can be subdivided into single (A_s), paired (A_{pr}), and aligned (A_{al}) spermatogonia, which are also called undifferentiated spermatogonia (de Rooij, 1998; de Rooij & Russell, 2000). Normally, about half of the A_s spermatogonial cell population divide into A_{pr} spermatogonial cells, whereas the other half undergo self-renewal and division to maintain the pool of stem cells. The A_{pr} spermatogonia then divide further to form 4, 8, or 16 A_{al} spermatogonial cell chains (Meachem et al., 2001). All of these processes are under precise control.

Spermatogenesis is a complex process of sperm cell development, including mitosis and meiosis, starting from SSCs to derived differentiated germ cells. Although markers for developing germ cells have been well studied in mice (Encinas et al., 2012), developmental stage-specific markers of germ cells in livestock have not yet been identified (Park et al., 2017a). Existing studies suggest that PLZF, ID4, and E-cadherin are markers of undifferentiated spermatogonia (Abbasi et al., 2013; Borjigin et al., 2010; Costa et al., 2012; Reding et al., 2010; Sun et al., 2015). In addition, c-kit is thought to be a marker for differentiated spermatozoa in porcine testis after puberty (Ran et al., 2018). These findings may contribute to future research on pig spermatogenesis (Ran et al., 2018). Moreover, the GDNF signaling pathway is essential for maintaining SSC self-renewal and replication in SSC culture systems. Excessive GDNF can lead to testicular germ cell tumors, whereas insufficient GDNF expression causes premature depletion of SSCs in testes (Ferranti et al., 2012; Hofmann, 2008). Zheng et al. (2014) identified the expression of thymus cell antigen 1 (THY1) in pig testicular tissue and subsequently used THY1 to isolate and enrich SSCs from testes of newborn piglets, showing that THY1 is a surface marker of SSCs in pre-pubertal testes and can be used for SSC identification and isolation in pigs. Moreover, THY1 has been used for the purification of SSCs in bulls (Reding et al., 2010) and goats (Abbasi et al., 2013). Notably, previous study has also reported that SSCs from tree shrews, a species closely related to primates, can be successfully enriched using THY1, with the Wnt/ β -catenin signaling pathway also identified as pivotal for their maintenance (Li et al., 2017). These observations indicate similarity in the characteristics of SSCs from different species, and that the experience gained from species with established SSC lines may be valuable for pSSC study.

An effective culture system of primary pSSCs is a very powerful tool for both research and animal husbandry and provides a good platform for exploring spermatogenesis *in vitro*. In addition, further establishment of a highly efficient *in vitro* culture system for pSSCs would be conducive for studies on biological characteristics, and also lay a foundation for the application of SSCs in transgenic animals or in the treatment of human infertility. However, pig spermatogonial stem cell

establishment is a universal problem, with many large obstacles that need to be overcome to realize the long-term culture (Lin et al., 2016). The survival of SSCs requires a specific microenvironment, called the SSC niche. Thus, SSCs can only survive transiently or spontaneously differentiate when they are detached from the microenvironment on which they depend (Brinster & Zimmermann, 1994). Therefore, a suitable culture system combining feeder cells and growth factors is required to effectively expand SSCs and maintain their undifferentiated state *in vitro* (Brinster & Zimmermann, 1994). Although rodent SSC lines have been successfully established *in vitro* (de Rooij & van Beek, 2013), there are few reports on the establishment of pSSCs. In addition to the rareness of SSCs in the testis and the lack of reliable surface markers, which hinder the isolation and purification of SSCs from livestock, the lack of stable culture systems *in vitro* is another challenging obstacle in this field. For rodent SSC culture, finite growth factors and suitable cell feeders have been identified (de Rooij & van Beek, 2013). GDNF is a well-known factor for maintenance of SSCs both *in vivo* and *in vitro*, and mammalian single-minded (SIM) mouse embryo-derived thioguanine and ouabain resistant cells (STO) or mouse embryonic fibroblasts (MEF) are feeder cells that secrete essential factors for the proliferation of rodent SSCs (Bellvé et al., 1977). However, the pSSC culture system is imperfect, and the existing culture system for rodent SSCs cannot be applied to fully realize the long-term culture of pSSCs *in vitro* (Kuijk et al., 2009). In the established system for rodent SSCs, neither the serum-containing nor serum-free system appear to work well for pSSCs, and the feeders are unsuitable for pSSC maintenance. Therefore, optimizing the *in vitro* culture system of pSSCs is necessary to lay the foundation for exploring their biological characteristics (Schlatt, 2002). Typically, SSCs should be stably passaged under an undifferentiated state.

Based on the efforts of many scientific teams, we have learned that *in vitro* culture of pSSCs requires efficient enrichment of SSCs, identification of key growth factors, component finite medium, and appropriate feeder cells. Zhang et al. (2017b) optimized *in vitro* culture conditions for undifferentiated pig spermatogonia, in which germ cells were isolated and enriched from 7-d-old pig testes by optimized differential plating. They tested the effects of several different growth factors and feeder layers to maintain spermatogonia for at least two months *in vitro* without losing stem cell characteristics (Zhang et al., 2017b). Moreover, they found PLD6 to be a surface marker of undifferentiated spermatogonia in pre-adolescent boar testes, which could be used to enrich undifferentiated spermatogonia in an unprecedented way (Zhang et al., 2017a). Liu et al. (2017) identified SETDB1 as a novel epigenetic regulator of male porcine germ cells, which helps maintaining germ cell survival under regulation of H3K27me3. These findings provide a sufficient theoretical basis for the future epigenetic regulation of spermatogenesis (Liu et al., 2017). Zhao et al. (2018) attempted to establish a culture system for spermatogenesis of Bama mini-pig SSCs. They co-cultured dissociated

testicular cells from 30-d-old pigs to simulate spermatogenesis, confirming that SSCs can differentiate in α -MEM-supplemented knockout serum replacement medium and develop to the post-meiosis stage (Zhao et al., 2018). Park et al. (2017b) developed a 3D culture microenvironment to promote the self-renewal of pig SSCs. In brief, pSSCs were cultured in agarose-based 3D hydrogels and 2D culture plates, followed by analysis of cell colony formation, morphology, alkaline phosphatase activity, transcription and translational regulation of self-renewal related genes, cell viability, etc. Proliferation was determined by the effect of 3D culture on the maintenance of undifferentiated SSCs, with the final results indicating that self-renewal of pSSCs was more

effectively maintained in the 3D than in the 2D culture microenvironment (Park et al., 2017b). These findings will play an important role in the future development of new SSC culture systems for different species, and thus help in advancing SSC research (Park et al., 2017b). The aforementioned studies indicate a step forward for the maintenance of pSSCs *in vitro*. Accordingly, we constructed a summary schematic to briefly delineate the establishment of porcine SSCs in Figure 1. Although the current system for pSSC isolation and *in vitro* culture remains imperfect, we believe that continued progress will play an important role in the future development of new culture systems for SSCs from different species.

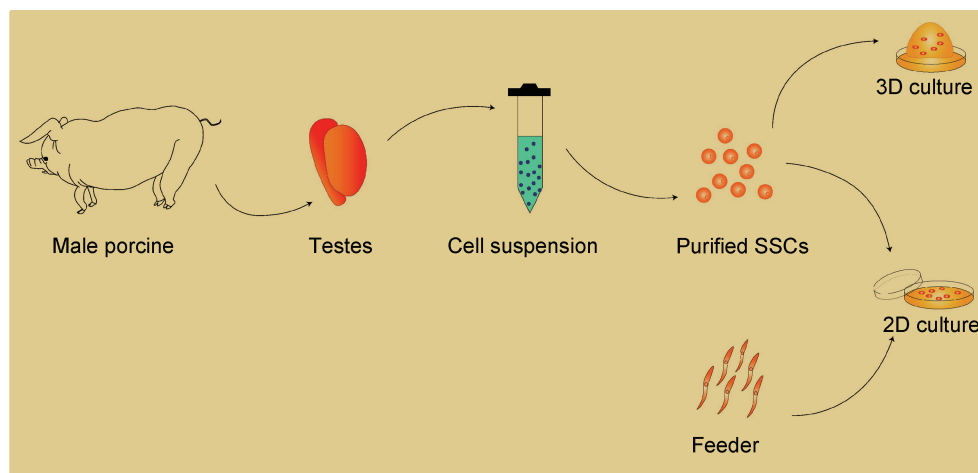


Figure 1 Schematic of pSSC isolation and culture

Testes harvested from male porcine were enzymatically digested and sorted, and the purified pSSCs were plated on feeders or maintained with 3D matrix gel for *in vitro* culture.

Traditional selective breeding methods in animals are limited by the low efficiency of species source and cell screening. The birth and development of gene editing technologies have broken this technical barrier, and allowed for improvements in livestock and poultry production, including growth and development, meat quality, and disease resistance (Hampton, 2017). Typically, gene editing technology can greatly shorten the time required to construct modern pig breeding and disease models, which should increase the relevance of porcine models in agricultural science and biomedical research (Whitworth & Prather, 2017). Recently developed DNA targeting endonuclease technologies, including ZFN (Zinc-finger nucleases), TALEN (transcription activator-like effector nucleases), and CRISPR (clustered regularly interspaced short palindromic repeats)-Cas9, have enabled researchers to specifically edit any chromosomal sequence for genetic operation. For the above three gene editing approaches, the cell initiates an endogenous mechanism to repair the site cleaved by nucleases or Cas9, with a mutation, deletion, or insertion introduced during the repair process; furthermore, a homologous recombination mechanism can be induced in the presence of a homologous sequence in the cell to obtain a specific fixed point for

mutation, deletion, or insertion (Polejaeva et al., 2000). In recent years, these technologies have been widely used in gene function research and genetically modified breeding (Li et al., 2016; Luo et al., 2014; Proudfoot et al., 2015), disease resistance breeding (Wu et al., 2015), biological disease model establishment (Whitworth et al., 2014), and other biological research. For example, Zhao et al. (2016) applied TALEN and CRISPR-Cas9 technology to humanize pig insulin by replacing the nucleotides that encode the one amino acid that differs between porcine and human insulin. As such, they successfully obtained gene-edited cloned pigs that expressed human insulin using somatic cell nuclear transfer (SCNT), thus providing the basis for the mass production of human insulin and treatment of diabetes. In addition, Park et al. (2017c) used CRISPR/Cas9 technology combined with SCNT technology to prepare Nanos2 mutant large white pigs, which may serve as a potential model for pSSC transplantation. Thus, genetically modified breeding has opened up a whole new field. With the development of gene editing technology, its application in livestock breeding such as that of pigs, cattle, and sheep is increasing, especially to improve the traits of species with no stem cell lines currently available (Park et al., 2017c). A recent study reported that knockout of the MSTN

(myostatin) gene in pigs using ZFN technology can significantly increase skeletal muscle fibers and lean meat mass (Zou et al., 2015). Polyunsaturated fatty acids (such as n-3 PUFAs), which are important nutritionally, can also exhibit anti-inflammatory and anti-coagulation activity as well as alleviate cardio-cerebral vascular diseases and influence immune regulation to improve atherosclerosis status (Belluzzi, 2004; Weber et al., 2006). However, under natural conditions, PUFAs are only found in a few plants and seafood, with very low yield. The cbr-fat-1 gene derived from *Caenorhabditis elegans* encodes n-3 PUFAs and catalyzes the formation of n-3 PUFAs from n-6 PUFAs. Based on this principle, Zhou et al. (2014a) constructed a transgenic pig that highly expressed cbr-fat-1, thus laying the foundation for the production of pork rich in n-3 PUFAs. In short, the application of gene editing technology has greatly shortened the breeding period and increased the potential of pigs and other livestock in agricultural production.

In addition to gene editing methods based on SCNT or embryonic operation, germline transmission is an alternative strategy. Production of genetically modified spermatozoa could enhance the efficiency of transgenic pig production, although technical obstacles continue to impede the application of pSSC transplantation in animal cloning. Recently, however, some remarkable achievements have been made. Increased efficiency of gene delivery in pSSCs may eliminate one of barricades to livestock transgenic operation, which has hampered the development of animal cloning for many years (Kim et al., 2019; Park et al., 2019). Success in cryopreservation of pSSCs has also facilitated the application of porcine cloning using pSSCs (Lee et al., 2014). Genetically edited pSSCs with a purity higher than 90% have been obtained recently using TALEN (Tang et al., 2018). Furthermore, the busulfan-induced SSC recipient model has been established in porcine (Lin et al., 2017). Such progress indicates that the essential conditions for pSSC editing and transplantation are ready, and we believe that gene-edited pigs derived from pSSCs will be generated soon.

Continued advances in pSSC research will be reported in the next decade as the considerable advantages of pSSCs are recognized by researchers. We look forward to the development of a rapid and stable protocol for the establishment of pSSCs and their application in transgenic operation. We believe this achievement will benefit many fields, including biomedical research, regenerative medicine, and agricultural research and production, in the near future.

COMPETING INTERESTS

The authors declare that they have no competing interests.

AUTHORS' CONTRIBUTIONS

Y. Z. S. and S. T. L. wrote the manuscript. X. M. L. and K. Z. reviewed and corrected the manuscript. All authors read and approved the final version of the manuscript.

Yi-Zhuo Sun¹, Si-Tong Liu^{2,3}, Xiao-Meng Li^{3,*}, Kang Zou^{1,*}

¹ *Germline Stem Cells and Microenvironment Lab, College of Animal Science and Technology, Nanjing Agricultural University, Nanjing Jiangsu 210095, China*

² *College of Life Sciences, Jilin University, Changchun Jilin 130012, China*

³ *Key Laboratory of Molecular Epigenetics of MOE, Institute of Genetics and Cytology, Northeast Normal University, Changchun Jilin 130024, China*

*Corresponding authors, E-mail: kangzou@njau.edu.cn; lixm441@nenu.edu.cn

REFERENCES

- Abbasi H, Tahmoorespur M, Hosseini SM, Nasiri Z, Bahadorani M, Hajian M, Nasiri MR, Nasr-Esfahani MH. 2013. THY1 as a reliable marker for enrichment of undifferentiated spermatogonia in the goat. *Theriogenology*, **80**(8): 923–932.
- Belluzzi A. 2004. Polyunsaturated fatty acids (n-3 PUFAs) and inflammatory bowel disease (IBD): pathogenesis and treatment. *European Review for Medical and Pharmacological Sciences*, **8**(5): 225–229.
- Bellvé AR, Cavicchia JC, Millette CF, O'Brien DA, Bhatnagar YM, Dym M. 1977. Spermatogenic cells of the prepubertal mouse: Isolation and morphological characterization. *Journal of Cell Biology*, **74**(1): 68–85.
- Borjigin U, Davey R, Hutton K, Herrid M. 2010. Expression of promyelocytic leukaemia zinc-finger in ovine testis and its application in evaluating the enrichment efficiency of differential plating. *Reproduction, Fertility and Development*, **22**(5): 733–742.
- Brinster RL, Avarbock MR. 1994. Germline transmission of donor haplotype following spermatogonial transplantation. *Proceedings of the National Academy of Sciences of the United States of America*, **91**(24): 11303–11307.
- Brinster RL, Zimmermann JW. 1994. Spermatogenesis following male germ-cell transplantation. *Proceedings of the National Academy of Sciences of the United States of America*, **91**(24): 11298–11302.
- Buageaw A, Sukhwani M, Ben-Yehudah A, Ehmcke J, Rawe VY, Pholpramool C, Orwig KE, Schlatt S. 2005. GDNF family receptor alpha1 phenotype of spermatogonial stem cells in immature mouse testes. *Biology of Reproduction*, **73**(5): 1011–1016.
- Chiarini-Garcia H, Raymer AM, Russell LD. 2003. Non-random distribution of spermatogonia in rats: evidence of niches in the seminiferous tubules. *Reproduction*, **126**(5): 669–680.
- Costa GMJ, Avelar GF, Rezende-Neto JV, Campos-Junior PHA, Lacerda SMSN, Andrade BSC, Thomé RG, Hofmann M-C, Franca LR. 2012. Spermatogonial stem cell markers and niche in equids. *PLoS One*, **7**(8): e44091.
- de Rooij DG. 1998. Stem cells in the testis. *International Journal of Experimental Pathology*, **79**(2): 67–80.
- de Rooij DG, Russell LD. 2000. All you wanted to know about spermatogonia but were afraid to ask. *Journal of Andrology*, **21**(6): 776–798.
- de Rooij DG, van Beek MEAB. 2013. Computer simulation of the rodent spermatogonial stem cell niche. *Biology of Reproduction*, **88**(5): 131.
- Dym M. 1994. Spermatogonial stem cells of the testis. *Proceedings of the National Academy of Sciences of the United States of America*, **91**(24): 11303–11307.

11287–11289.

- Encinas G, Zogbi C, Stumpp T. 2012. Detection of four germ cell markers in rats during testis morphogenesis: Differences and similarities with mice. *Cells Tissues Organs*, **195**(5): 443–455.
- Ferranti F, Muciaccia B, Ricci G, Dovere L, Canipari R, Magliocca F, Stefanini M, Catizone A, Vicini E. 2012. Glial cell line-derived neurotrophic factor promotes invasive behaviour in testicular seminoma cells. *International Journal of Andrology*, **35**(5): 758–768.
- Gonen S, Jenko J, Gorjanc G, Mileham AJ, Whitelaw CBA, Hickey JM. 2017. Potential of gene drives with genome editing to increase genetic gain in livestock breeding programs. *Genetics Selection Evolution*, **49**(1): 3.
- Gori JL, Hsu PD, Maeder ML, Shen S, Welstead GG, Bumcrot D. 2015. Delivery and specificity of CRISPR-Cas9 genome editing technologies for human gene therapy. *Human Gene Therapy*, **26**(7): 443.
- Hampton T. 2017. Gene editing could help pave the way for pig-to-human transplantations. *Circulation*, **136**(21): 2083–2084.
- Hofmann MC. 2008. Gdnf signaling pathways within the mammalian spermatogonial stem cell niche. *Molecular and Cellular Endocrinology*, **288**(1–2): 95–103.
- Huckins C, Clermont Y. 1968. Evolution of gonocytes in the rat testis during late embryonic and early post-natal life. *Archives D'anatomie, D'histologie et D'embryologie Normales et Experimentales*, **51**(1): 341–354.
- Hwang WY, Fu Y, Reyon D, Maeder ML, Tsai SQ, Sander JD, Peterson RT, Yeh JR, Joung JK. 2013. Efficient genome editing in zebrafish using a CRISPR-Cas system. *Nature Biotechnology*, **31**(3): 227–229.
- Kim MS, Park MH, Park JE, Yun JI, Choi JH, Lee E, Lee ST. 2019. Establishment of an electroporation-mediated gene delivery system in porcine spermatogonial stem cells. *In Vitro Cellular & Developmental Biology - Animal*, **55**(3): 177–188.
- Kubota H, Brinster RL. 2006. Technology Insight: in vitro culture of spermatogonial stem cells and their potential therapeutic uses. *Nature Clinical Practice Endocrinology & Metabolism*, **2**(2): 99–108.
- Kubota H, Avarbock MR, Brinster RL. 2003. Spermatogonial stem cells share some, but not all, phenotypic and functional characteristics with other stem cells. *Proceedings of the National Academy of Sciences of the United States of America*, **100**(11): 6487–6492.
- Kubota H, Wu X, Goodyear SM, Avarbock MR, Brinster RL. 2011. Glial cell line-derived neurotrophic factor and endothelial cells promote self-renewal of rabbit germ cells with spermatogonial stem cell properties. *The FASEB Journal*, **25**(8): 2604–2614.
- Kuijk EW, Colenbrander B, Roelen BAJ. 2009. The effects of growth factors on *in vitro*-cultured porcine testicular cells. *Reproduction*, **138**(4): 721–731.
- Lee YA, Kim YH, Ha SJ, Kim KJ, Kim BJ, Kim BG, Choi SH, Kim IC, Schmidt JA, Ryu BY. 2014. Cryopreservation of porcine spermatogonial stem cells by slow-freezing testis tissue in trehalose. *Journal of Animal Science*, **92**(3): 984–995.
- Li CH, Yan LZ, Ban WZ, Tu Q, Wu Y, Wang L, Bi R, Ji S, Ma YH, Nie WH, Lv LB, Yao YG, Zhao XD, Zheng P. 2017. Long-term propagation of tree shrew spermatogonial stem cells in culture and successful generation of transgenic offspring. *Cell Research*, **27**(2): 241.
- Li H, Wang G, Hao Z, Zhang G, Qing Y, Liu S, Qing L, Pan W, Chen L, Liu G, Zhao P, Jia B, Zeng L, Guo J, Zhao L, Zhao H, Lv C, Xu K, Cheng W, Li H, Zhao H, Wang W, Wei H. 2016. Generation of biallelic knock-out sheep via gene-editing and somatic cell nuclear transfer. *Scientific Reports*, **6**: 33675.
- Lin Z, Bao J, Kong Q, Bai Y, Luo F, Zhou S, Wu Y, Huang J. 2017. Effective production of recipient male pigs for spermatogonial stem cell transplantation by intratesticular injection with busulfan. *Theriogenology*, **89**: 365–373.e2.
- Liu TT, Zhang P, Li TJ, Chen XX, Zhu ZS, Lyu YH, Li XL, Tian X, Zeng WX. 2017. SETDB1 plays an essential role in maintenance of gonocyte survival in pigs. *Reproduction*, **154**(1): 23–34.
- Luo J, Song Z, Yu S, Cui D, Wang B, Ding F, Li S, Dai Y, Li N. 2014. Efficient generation of myostatin (MSTN) biallelic mutations in cattle using zinc finger nucleases. *PLoS One*, **9**(4): e95225.
- Ma X, Wong SY, Tam HY, Tsui YK, Chung LS, Feng B. 2018. *In vivo* genome editing thrives with diversified CRISPR technologies. *Zoological Research*, **39**(2): 58–71.
- Meachem S, Schönfeldt VV, Schlatt S. 2001. Spermatogonia: stem cells with a great perspective. *Reproduction*, **121**(6): 825–834.
- Meng X, Lindahl M, Hyvönen ME, Parvinen M, de Rooij DG, Hess MW, Raatikainen-Ahokas A, Sainio K, Rauvala H, Lakso M, Pichel JG, Westphal H, Saarma M, Sariola H. 2000. Regulation of cell fate decision of undifferentiated spermatogonia by GDNF. *Science*, **287**(5457): 1489 – 1493.
- Nagano M, Avarbock MR, Leonida EB, Brinster CJ, Brinster RL. 1998. Culture of mouse spermatogonial stem cells. *Tissue and Cell*, **30**(4): 389–397.
- Park HJ, Lee R, Lee WY, Kim JH, Do JT, Park C, Song H. 2017a. Stage-specific expression of Sal-like protein 4 in boar testicular germ cells. *Theriogenology*, **101**: 44–52.
- Park JE, Park MH, Kim MS, Park YR, Yun JI, Cheong HT, Kim M, Choi JH, Lee E, Lee ST. 2017b. Porcine spermatogonial stem cells self-renew effectively in a three dimensional culture microenvironment. *Cell Biology International*, **41**(12): 1316–1324.
- Park K, Kim MS, Kang M, Kang T, Kim B, Lee ST. 2019. Successful genetic modification of porcine spermatogonial stem cells via an electrically responsive Au nanowire injector. *Biomaterials*, **193**: 22–29.
- Park KE, Kaucher AV, Powell A, Waqas MS, Sandmaier SE, Oatley MJ, Park CH, Tibary A, Donovan DM, Blomberg LA, Lillico SG, Bruce C, Whitelaw A, Mileham A, Telugu BP, Oatley JM. 2017c. Generation of germline ablated male pigs by CRISPR/Cas9 editing of the *NANOS2* gene. *Scientific Reports*, **7**: 40176.
- Polejaeva IA, Chen SH, Vaught TD, Page RL, Mullins J, Ball S, Dai Y, Boone J, Walker S, Ayares DL, Colman A, Campbell KHS. 2000. Cloned pigs produced by nuclear transfer from adult somatic cells. *Nature*, **407**(6800): 86–90.
- Proudfoot C, Carlson DF, Huddart R, Long CR, Pryor JH, King TJ, Lillico SG, Mileham AJ, McLaren DG, Whitelaw CBA, Fahrenkrug SC. 2015. Genome edited sheep and cattle. *Transgenic Research*, **24**(1): 147–153.
- Ran L, Lee WY, Park HJ, Ha WT, Woo JS, Chung HJ, Lee JH, Hong K, Song H. 2018. Stage-specific expression of DDX4 and C-kit at different developmental stages of the porcine testis. *Animal Reproduction Science*, **190**: 18–26.
- Reding SC, Stepnoski AL, Cloninger EW, Oatley JM. 2010. THY1 is a conserved marker of undifferentiated spermatogonia in the pre-pubertal bull testis. *Reproduction*, **139**(5): 893–903.
- Sapsford CS. 1962. Changes in the cells of the Sex Cords and

- Seminiferous Tubules during the development of the Testis of the rat and mouse. *Australian Journal of Zoology*, **10**(2): 178–192.
- Schlatt S. 2002. Spermatogonial stem cell preservation and transplantation. *Molecular and Cellular Endocrinology*, **187**(1–2): 107–111.
- Shinohara T, Avarbock MR, Brinster RL. 1999. β 1- and α 6-integrin are surface markers on mouse spermatogonial stem cells. *Proceedings of the National Academy of Sciences of the United States of America*, **96**(10): 5504–5509.
- Shinohara T, Avarbock MR, Brinster RL. 2000a. Functional analysis of spermatogonial stem cells in steel and cryptorchid infertile mouse models. *Developmental Biology*, **220**(2): 401–411.
- Shinohara T, Orwig KE, Avarbock MR, Brinster RL. 2000b. Spermatogonial stem cell enrichment by multiparameter selection of mouse testis cells. *Proceedings of the National Academy of Sciences of the United States of America*, **97**(15): 8346–8351.
- Sun F, Xu Q, Zhao D, Chen CD. 2015. Id4 marks spermatogonial stem cells in the mouse testis. *Scientific Reports*, **5**: 17594.
- Takagi S, Itoh N, Kimura M, Sasao T, Tsukamoto T. 2001. Spermatogonial proliferation and apoptosis in hypospermatogenesis associated with nonobstructive azoospermia. *Fertility and Sterility*, **76**(5): 901–907.
- Tang L, Bondareva A, González R, Rodríguez-Sosa JR, Carlson DF, Webster D, Fahrenkrug S, Dobrinski I. 2018. TALEN-mediated gene targeting in porcine spermatogonia. *Molecular Reproduction and Development*, **85**(3): 250–261.
- Weber HS, Selimi D, Huber G. 2006. Prevention of cardiovascular diseases and highly concentrated n-3 polyunsaturated fatty acids (PUFAs). *Herz*, **31**(Suppl 3): 24–30.
- Whitworth KM, Prather RS. 2017. Gene editing as applied to prevention of reproductive porcine reproductive and respiratory syndrome. *Molecular Reproduction and Development*, **84**(9): 926–933.
- Whitworth KM, Lee K, Benne JA, Beaton BP, Spate LD, Murphy SL, Samuel MS, Mao J, O'gorman C, Walters EM, Murphy CN, Driver J, Mileham A, McLaren D, Wells KD, Prather RS. 2014. Use of the CRISPR/Cas9 system to produce genetically engineered pigs from in vitro-derived oocytes and embryos. *Biology of Reproduction*, **91**(3): 78–78.
- Wu H, Wang Y, Zhang Y, Yang M, Lv J, Liu J, Zhang Y. 2015. TALE nickase-mediated *SP110* knockin endows cattle with increased resistance to tuberculosis. *Proceedings of the National Academy of Sciences of the United States of America*, **112**(13): E1530–E1539.
- Yang Y, Wang K, Wu H, Qin J, Ruan D, Zhen O, Zhao B, Liu Z, Zhao Y, Zhang Q, Fan N, Liu Q, Guo S, Bu L, Fan Y, Sun X, Li X, Lai L. 2016. Genetically humanized pigs exclusively expressing human insulin are generated through custom endonuclease-mediated seamless engineering. *Journal of Molecular Cell Biology*, **8**(2): 174–177.
- Zhang P, Qin Y, Zheng Y, Zeng W. 2017a. Phospholipase D family member 6 (PLD6) is a surface marker for enrichment of undifferentiated spermatogonia in the pre-pubertal boars. *Stem Cells and Development*, **27**(1): 55–64.
- Zhang P, Chen X, Zheng Y, Zhu J, Qin Y, Lv Y, Zeng W. 2017b. Long-term propagation of porcine undifferentiated spermatogonia. *Stem Cells and Development*, **26**(15): 1121–1131.
- Zhao H, Nie J, Zhu X, Lu Y, Liang X, Xu H, Yang X, Zhang Y, Lu K, Lu S. 2018. *In vitro* differentiation of spermatogonial stem cells using testicular cells from Guangxi Bama mini-pig. *Journal of Veterinary Science*, **19**(5): 592–599.
- Zhao J, Lai L, Ji W, Zhou Q. 2019. Genome editing in large animals: Current status and future prospects. *National Science Review*, **6**(3): 402–420.
- Zheng Y, He Y, An J, Qin J, Wang Y, Zhang Y, Tian X, Zeng W. 2014. THY1 is a surface marker of porcine gonocytes. *Reproduction Fertility & Development*, **26**(4): 533–539.
- Zhou Y, Lin Y, Wu X, Feng C, Long C, Xiong F, Wang N, Pan D, Chen H. 2014. The high-level accumulation of n-3 polyunsaturated fatty acids in transgenic pigs harboring the n-3 fatty acid desaturase gene from *Caenorhabditis briggsae*. *Transgenic Research*, **23**(1): 89–97.
- Zou Q, Wang X, Liu Y, Ouyang Z, Long H, Wei S, Xin J, Zhao B, Lai S, Shen J, Ni Q, Yang H, Zhong H, Li L, Hu M, Zhang Q, Zhou Z, He J, Yan Q, Fan N, Zhao Y, Liu Z, Guo L, Huang J, Zhang G, Ying J, Lai L, Gao X. 2015. Generation of gene-target dogs using CRISPR/Cas9 system. *Journal of Molecular Cell Biology*, **7**(6): 580–583.

Stem cell therapy for Parkinson's disease using non-human primate models

Zhen-Zhen Chen^{1,2}, Yu-Yu Niu^{2,*}

¹ Faculty of Life Science and Technology, Kunming University of Science and Technology, Kunming Yunnan 650500, China

² Institute of Primate Translational Medicine, Kunming University of Science and Technology, Kunming Yunnan 650500, China

ABSTRACT

Stem cell therapy (SCT) for Parkinson's disease (PD) has received considerable attention in recent years. Non-human primate (NHP) models of PD have played an instrumental role in the safety and efficacy of emerging PD therapies and facilitated the translation of initiatives for human patients. NHP models of PD include primates with 1-methyl-4-phenyl-1, 2, 3, 6-tetrahydropyridine (MPTP)-induced parkinsonism, who are responsive to dopamine replacement therapies, similar to human PD patients. Extensive research in SCT has been conducted to better treat the progressive dopaminergic neurodegeneration that underlies PD. For effective application of SCT in PD, however, a number of basic parameters still need to be tested and optimized in NHP models, including preparation and storage of cells for engraftment, methods of transplantation, choice of target sites, and timelines for recovery. In this review, we discuss the current status of NHP models of PD in stem cell research. We also analyze the advances and remaining challenges for successful clinical translation of SCT for this persistent disease.

Keywords: Stem cell therapy; Non-human primates; Parkinson's disease

INTRODUCTION

Parkinson's disease (PD) is a common neurodegenerative disorder that results from progressive loss of dopaminergic (DA) neurons in the substantia nigra of the midbrain. This loss is associated with characteristic motor dysfunction, including bradykinesia, rigidity, and rest tremor. The molecular hallmark of PD is the presence of Lewy bodies (LBs) composed of the alpha-synuclein (α -syn) protein in the substantia nigra and cortical regions of the brain (Dauer & Przedborski, 2003). Treatment with the dopamine precursor levodopa can improve symptoms, but does not prevent DA neuron destruction (Kim et al., 2002). Although no cure is currently available, cell-based therapy (CBT) (in which cellular material, usually intact, living cells such as T cells capable of fighting cancer via cell-mediated immunity, is injected into the patient during immunotherapy) is considered one of the most promising methods for eradicating PD (Sonntag et al., 2018). Currently, stem cells are among the best cell sources for CBT.

Pioneering studies on the application of CBT in rodent models provided invaluable information on neuronal survival, migration, and post-grafting integration (Kim et al., 2013). Nevertheless, clinical translation of CBT for PD requires further investigation and evaluation in different species. Experiments in NHP models are ideally suited for such exceptional and invasive brain therapy (Didier et al., 2016).

Stem cells have the capacity to proliferate and differentiate into multiple cellular lineages, offering an enormous pool of resources for therapeutic applications such as autologous stem cell transplants (Drouin-Ouellet, 2014). Using stem cells to treat neurodegenerative diseases has become an area of intense interest. Current clinical applications of stem cells

Open Access

This is an open-access article distributed under the terms of the Creative Commons Attribution Non-Commercial License (<http://creativecommons.org/licenses/by-nc/4.0/>), which permits unrestricted non-commercial use, distribution, and reproduction in any medium, provided the original work is properly cited.

Copyright ©2019 Editorial Office of Zoological Research, Kunming Institute of Zoology, Chinese Academy of Sciences

Received: 19 March 2019; Accepted: 26 June 2019; Online: 23 July 2019

Foundation items: This study was supported by the National Key R&D Program of China (2016YFA0101401)

*Corresponding author, E-mail: niuyy@lpbr.cn

DOI: 10.24272/j.issn.2095-8137.2019.053

have targeted Alzheimer's disease (Kwak et al., 2018), PD (Parmar, 2018), amyotrophic lateral sclerosis (Robinson, 2018), and multiple sclerosis (Shirani & Stuve, 2018), and are predicted to increase in coming years. Furthermore, SCT has been proposed to counteract the characteristic massive loss in DA neurons observed in PD (Chiu & Hall, 2006).

Since the first clinical trials in the late 1980s using fetal midbrain tissue to replace lost DA neurons, hundreds of patients worldwide have been subjected to neural fetal tissue grafting, with many showing long-term graft survival, good clinical outcomes, and physiological release of dopamine over decades (Barker et al., 2017). Furthermore, the derivation of human embryonic stem cells (hESCs) (Thomson et al., 1998) provided a new scalable cell source for stem cell therapy (SCT), which may potentially replace fetal tissue. However, the road to clinical application of these cells has proven to be long, involving a number of key steps such as gaining control over cell subtype differentiation, producing safe and efficacious cells, adhering to good manufacturing regulations, scaling-up production processes, and obtaining regulatory approval of the final cell products.

Although CBT is the most promising treatment for a variety of neurodegenerative diseases, animal experiments remain limited. NHPs exhibit great similarity to humans in regard to genetics, brain/cognitive function and development, organs, metabolism, and drug susceptibility (Zhang et al., 2014). Therefore, experimental results from NHP-based studies are critical and convincing.

Since the early 1980s, scientists have relied on NHP models to assess the potential benefits of CBT for PD (Cowen, 1986). Compared to rodents, PD-relevant behavioral outcomes, such as fine motor skills, can be easily tested in NHPs (Camus et al., 2015). Clinically relevant behavioral parameters are critical for evaluating the efficacy of therapeutic strategies, such as the choice of intracerebral grafting targets (Bentlage et al., 1999; Kauhausen et al., 2015; Thompson et al., 2010). NHPs and humans show similar organization of the neo-striatum, with the caudate nucleus and putamen clearly delineated by white matter tracts of the internal capsule (Howson et al., 2019). In contrast, in rodents, the transecting white matter tracts of the internal capsule are broken into bundles (pencils of Willis) that perforate the entire striatum without presenting a distinct physical barrier for cell distribution (Coizet et al., 2017). Thus, NHP models have facilitated CBT progress toward clinical application.

Humans and NHPs possess similar behavioral elements, physiology, anatomy, biochemistry, organ mechanisms, and immune functions (Vierboom et al., 2012). Therefore, NHP models enable the translation of therapy-focused research from small animals to humans. In particular, NHP models of human disease provide exceptional opportunities to advance SCT by addressing pertinent translational concerns associated with this research, including the application of autologous/allogeneic-induced pluripotent stem cell (iPSC)-derived cellular products, immune responsiveness, clinical delivery techniques, and evaluation of candidate cell line profiles following transplantation (Wang et al., 2017; Wei et

al., 2016). Furthermore, NHP models offer unique possibilities to evaluate the complexity of the biochemical, physiological, behavioral, and imaging end points relevant to current human conditions (Koprach et al., 2017).

Given the ethical concerns, expense of specialized equipment, and necessity of highly trained staff, the value of using NHPs must be carefully assessed. Well-designed and less resource-demanding studies in small animal models, such as rodents, are essential for ultimately translating NHP model research into human patient therapy. Each disease-specific research community should focus on developing relevant NHP models that advance the translation of stem cell research and therapy.

In this review, we discuss the role of NHP models in developing SCT for PD, stem cell types that can be used for transplantation, and value of NHP studies in translating these therapies for clinical application.

NHP MODELS OF PD FOR SCT RESEARCH

Neurotoxin-induced models

The most commonly used neurotoxins for generating models of PD are 6-hydroxydopamine (6-OHDA) and 1-methyl-4-phenyl-1,2,3,6-tetrahydropyridine (MPTP).

6-OHDA models

As a neurotoxic compound, 6-OHDA induces cell death via oxidative stress after uptake by the catecholamine transport system (Zhou & Cheng, 2019). 6-OHDA is commonly used in rodents as they are much less sensitive to MPTP compared with humans and NHPs. Although many researchers have reported that 6-OHDA can cause cell death *in vivo* (Bernstein et al., 2011; Tobón-Velasco et al., 2013), several studies have found no markers of cell death upon treatment with this compound (Kostrzewa, 2000), suggesting possible phenotype loss. In the application of 6-OHDA for PD model development, the severity of the resulting disease depends on the number, size, and location (e.g., striatum, substantia nigra, or medial forebrain bundle) of 6-OHDA injections (Emborg, 2004). Eslamboli et al. (2003) applied nine striatal injections of 6-OHDA to model PD in common marmoset monkeys; however, due to the spontaneous recovery of symptoms 10 weeks after surgery, Eslamboli et al. (2005) developed a new model using 18 unilateral intrastratial injections.

One drawback of the above model is the numerous intracerebral needle passages necessary for appropriate 6-OHDA distribution to decrease the extent of spontaneous recovery (Santana et al., 2015). As with other stereotaxic procedures, this model requires surgical settings and trained personnel to perform brain surgery and provide recovery care.

MPTP models

Administration of MPTP is a classic method for generating PD due to the selective toxicity of this chemical toward DA neurons (Jiang & Dickson, 2018; Lei et al., 2016; Li et al., 2015a; Su et al., 2015). It is historically important in animal models of PD and provides utility to test certain CBT

parameters. After crossing the blood-brain barrier, MPTP is transformed by monoamine oxidase B into its active metabolite, 1-methyl-4-phenylpyridinium ion (MPP⁺), which is then carried by dopamine transporters into DA neurons of the substantia nigra pars compacta (SNpc), where the compound blocks mitochondrial complex I activity (Huang et al., 2018). Although it has limitations, MPTP treatment is the current standard in NHPs. The discovery of this mechanism of action in the 1990s paved the way for subsequent studies exploring mitochondrial function in PD and provided a prominent animal model of the disease (Emborg, 2017).

Pesticide/herbicide-induced models Paraquat models

Paraquat is an important member of the bipyridylum family of broad-spectrum herbicides and is commonly used to control pests in important crops such as soybeans, sorghum, sugar cane, cotton, and corn. It interferes with photosynthetic electron transport and reduces oxygen to superoxide free radicals, leading to membrane rupture and leaf desiccation (Sarwar et al., 2015). Many countries have already banned paraquat due to its acute pulmonary and cutaneous toxicity or established restricted-use measures, such as limited concentrations of the active ingredient in formulated products and manipulation by licensed mixers and ground applicators only (Kuo & Yu, 1991). In experimental models, paraquat has been linked to the production of reactive oxygen species (ROS), oxidative stress, and aggregation of α -syn proteins in DA neurons (Kuter et al., 2007, 2010). However, the mechanism used by paraquat to access DA neurons is not yet fully understood (Vaccari et al., 2017; Zhou et al., 2017).

Rotenone models

As a mitochondrial toxin, rotenone can produce dose-dependent systemic toxicity and mortality (Sanders & Greenamyre, 2013). Following delivery of this compound (via osmotic minipump), a proportion of animals becomes parkinsonian, with different degrees of nigrostriatal lesions (Perier et al., 2003). Furthermore, rotenone (2–3 mg/kg/day) is reported to elicit selective nigrostriatal degeneration, generally without nonspecific lesions (Trigo et al., 2018). For example, Cicchetti et al. (2010) found that rotenone caused severe digestive issues, with an enlarged stomach full of undigested food, following systemic application. Although it was not recognized as such, this may have been the first indication that rotenone can reproduce the lesser-known gastrointestinal symptoms of PD, such as gastroparesis (Johnson et al., 2018). Indeed, Bové & Perier (2012) reported that rotenone accurately recapitulates the pathological and functional features of parkinsonian gastrointestinal impairment.

Although the reasons for the discrepancies between research results are uncertain, recent refinements of the rotenone model have made it more reproducible and reduced the number of nonspecific toxicities. Smirnova et al. (2016) demonstrated that withdrawal of rotenone led to counter-regulation of mir-7 and the *ASS1*, *CTH*, and *SHTM2* genes, suggesting a possible role of these genes in direct cellular responses to this toxicant and the suitability of the model at

addressing the processes of resilience and recovery in neurotoxicology and PD. Furthermore, Cimdins et al. (2019) used rotenone, as a potent complex I-specific mitochondrial inhibitor, to determine the neuroprotective effects of APP and sAPP α *in vitro*, in neuronal cell lines over-expressing APP, and in a retinal neuronal rotenone toxicity mouse model *in vivo*. Overall, it is difficult to effectively model all aspects of a complex, age-related human disease such as PD in rats. Even genetically accurate models of PD have met limited success in replicating key behavioral and pathological features of the disease. Nevertheless, a great deal has been learned—and remains to be discovered—about the pathogenic mechanisms of PD using rotenone models of the disease.

Genetically engineered models

Genetic NHP PD models have been generated previously by intracerebral injection of viral vectors encoding mutant α -syn or administration of LB extracts (Marmion & Kordower, 2018). Nigral overexpression of human wild type or mutant A53T α -syn, induced by adeno-associated viral (AAV) vectors, has been shown to induce PD-like motor symptoms, significant nigral DA cell loss, and α -syn aggregates in common marmoset monkeys (Eslamboli et al., 2007; Kirik et al., 2003). AAV and lentiviral vectors encoding A53T α -syn have also been used in cynomolgus (Koprich et al., 2016) and rhesus monkeys (Yang et al., 2015). In both studies, expression of A53T α -syn led to nigral cell loss and α -syn accumulation and aggregation, though without behavioral changes. Furthermore, while AAV-induced overexpression of A53T α -syn and parkin, another PD-implicated protein, in cynomolgus monkeys led to a decrease in striatal DA markers and α -syn accumulation and phosphorylation, no PD motor symptoms were observed (Recasens et al., 2014). Notably, nigral injection of AAV expressing short hairpin RNA (shRNA) to knock down α -syn in vervet monkeys induced a region-specific decrease in tyrosine hydroxylase (TH)-positive nigral cell number and striatal innervation compared to animals that received scrambled shRNA, although no behavioral changes were reported (Collier et al., 2016). Intracerebral inoculation with α -syn fibrils has been extensively used in rodents, but not yet in monkeys (Luk et al., 2012; Paumier et al., 2015). On the other hand, cadaveric Lewy body extracts have been injected into the striatum and nigra of cynomolgus monkeys with and without previous treatment with MPTP (Recasens et al., 2014), which induced a variable decrease in striatal and nigral DA markers and an increase in α -syn expression, but no PD motor symptoms. It should be noted that, with the exception of AAV-mediated α -syn studies in marmosets, all investigations on genetically produced models have been performed using only a few subjects. Therefore, further characterization and validation of such models is necessary before they can be used as robust testing platforms for SCT.

Transgenic NHP models induced by injection of NHP oocytes with lentiviral vectors encoding PD-relevant proteins with mutations of interest have emerged in recent years. For example, transgenic rhesus monkeys overexpressing mutant A53T α -syn have been reported (Niu et al., 2015), with some

behavioral deficits observed at 1.5–2.5 years of age. New technologies such as CRISPR/Cas9-genomic editing also present an opportunity to generate NHP models with PD-associated mutations expressed at physiological levels, which may help clarify the mechanism of disease onset, including the development of motor and non-motor symptoms (Handscheil et al., 2011; Luol et al., 2016). These novel NHP models may provide clues to better understand α -syn-related disorders and enable the development of SCT to treat them.

STEM CELLS AS SOURCES FOR CBT

Embryonic stem cells

Embryonic stem cells (ESCs) have attracted considerable attention as an alternative source for the generation of DA neurons. Handscheil et al. (2011) described a technique for culturing ESCs in the absence of artificial scaffolds, which generated mineralized micromasses. This technique made it possible for ESCs to proliferate, which is a prerequisite for CBT. Due to their pluripotency and highly proliferative properties, ESCs can give rise to any type of cell in the body, including DA neurons (Thomson et al., 1998), which can be produced in sufficient numbers for transplantation therapy. ESCs are associated with the risk of tumorigenesis due to genomic instability in culture (Zhao et al., 2015), even if the cells appear to fully differentiate into DA neurons *in vitro* before transplantation (Luk et al., 2012). Myocyte enhancer factor 2 (MEF2C) directs the differentiation of mouse ESC-derived neural precursors into neurons (Skerjanc & Wilton, 2000). Furthermore, MEF2C confines hESCs to the neuronal lineage, which can be used to generate neurons and avoid tumor formation for use in SCT (Eslamboli et al., 2005). Human and rodent ESC-derived DA neurons have been shown to survive transplantation into the striatum of parkinsonian NHPs and generate a degree of functional recovery (Hayashi et al., 2013).

Nevertheless, studies have shown that the survival of ESC-derived DA neurons post transplantation is relatively low. Li et al. (2017) demonstrated that hESCs differentiated into DA neurons when co-cultured with PA6 cells, with almost 92% of hESC colonies containing cells positive for TH, a critical catecholaminergic enzyme, after three weeks of differentiation.

Two potential drawbacks may limit the therapeutic application of ESCs. First, the generation of hESCs requires fertilized eggs from donors and the destruction of early embryos, which raises a plethora of ethical and legal concerns. Second, hESC-derived grafts are allogeneic to recipient patients, thus making immuno-suppressive regimens necessary (Leng & Tian, 2016). Despite these limitations, hESCs are currently the "gold standard" of SCT for PD, and hESC-derived midbrain DA (mDA) neurons are currently being developed for clinical trials in the USA and Europe (Kern et al., 2018; Weick et al., 2011). Chinese scientists have also initiated clinical trials of ESC-based therapy for PD (Cyranoski, 2017).

Induced pluripotent stem cells (iPSCs)

iPSCs are adult somatic cells that are converted into pluripotent cells via the introduction of specific transcription factors found in normal PSCs. The cells can be differentiated into most somatic cell types and are self-renewable (Zhang et al., 2019). As recently as five years ago, direct therapeutic treatment of PD through transplantation of iPSCs was not feasible. Transplantation faced many problems such as low efficiency, virus requirements, and teratoma development (Li et al., 2015b). Attempts to use xenogeneic materials resulted in contamination by animal-source pathogens, which can cause an immune response after transplantation in humans (Bergstrom et al., 2011). However, researchers have since developed a xeno-free medium alongside a feeder-free culture system and cre-mediated excision of reprogramming factors to obtain transgene-free iPSCs with improved efficiency (0.15%–0.3%) (Lu et al., 2014). Although more testing is needed, especially in animal models, these results suggest that iPSCs are more viable than previously thought from an efficacy standpoint (Li et al., 2015b).

Recent progress in clinical treatment shows promise in animal models of PD. For example, Han et al. (2015) found that human iPSCs transplanted into 6-OHDA-induced parkinsonian rats improved functional "rotational asymmetry" defects several weeks after transplantation. In another study, iPSC-derived DA neurons were transplanted into parkinsonian cynomolgus monkeys and survived for two years over the length of the study; in addition, the transplanted DA neurons reinnervated the host brains, grew into the putamen, and showed long-term viability (Hallett et al., 2015). Although the results were only positive for one of the three tested monkeys, the study demonstrated that iPSC-derived DA neurons can be used for transplantation with long-term improvement in motor function without immunosuppression (Hallett et al., 2015).

Kikuchi et al. (2017) transplanted neurons derived from iPSCs into NHP brains and found that symptoms improved significantly after two years of tracking the monkeys. Morizane et al. (2017) also transplanted grafted DA neurons induced by cynomolgus iPSCs into allogeneic NHP PD models. Different from Kikuchi et al. (2017), who used FK506 (immune inhibitor) to reduce immune rejection, Morizane et al. (2017) used major histocompatibility complex (MHC)-matched allogeneic neural cell grafting in the brain, which is considered a less immune-responsive tissue, using iPSCs derived from MHC homozygous cynomolgus macaques. Furthermore, immunohistological analyses revealed that MHC-matching reduced the immune response by suppressing the accumulation of microglia (Iba-1+) and lymphocytes (CD45+) in the grafts (Morizane et al., 2017). These studies have made great contributions to cell transplantation.

Mesenchymal stem cells

Therapeutic stem cell studies have often utilized multipotent mesenchymal stem cells (MSCs) rather than ESCs, the use of which poses ethical concerns. Bone marrow, umbilical cord blood, and adult adipose-derived stromal tissue have been used as sources of MSCs for autologous grafts (Fallahi et al.,

2007; Park et al., 2015).

Using human umbilical MSCs, Wang et al. (2011) showed the potential of this approach for PD treatment. Specifically, human MSCs isolated from Wharton's jelly of the umbilical cord were induced to transform into DA neurons *in vitro* through stepwise culturing in neuron-conditioned medium, resulting in a 12.7% success rate, as characterized by positive staining for TH and dopamine released into the culture medium. When these cells were transplanted into the striatum of parkinsonian rats (induced by unilateral striatal lesioning with 6-OHDA), the transplantation partially corrected lesion-induced amphetamine-induced rotation, with the cells showing viability for at least four months. Furthermore, Wang (2011) also found MSCs showed protective effects on progressive DA neural loss *in vitro* and *in vivo*. Treatment decreased MG-132-induced DA neuronal loss with a significant reduction in caspase-3 activity. Subsequently, application of hMSCs in MG-132-treated rats dramatically reduced the decline in the number of TH-immunoreactive cells, with an almost 50% increase in the survival of these cells in the substantia nigra (Wang et al., 2011). Furthermore, hMSC treatment significantly decreased OX-6 immunoreactivity and caspase-3 activity (Park et al., 2015). While MSC transplantation may be effective in modulating the immune response in neurodegenerative diseases, it is highly unlikely that MSC-derived neurons will ever be used for cell replacement therapy (Xu et al., 2012). Treatment with MSCs suppresses autoimmunity and restores salivary gland secretory function in both mouse models and Sjogren syndrome patients (Xu et al., 2012). MSC treatment directs T cells toward Treg and Th2, while suppressing Th17 and Tfh responses, and can alleviate disease symptoms (Xu et al., 2012). Collectively, the immunological regulatory functions of MSCs play an important role in Sjogren syndrome pathogenesis, and allogeneic MSC treatment may provide a novel, effective, and safe therapy for patients with this syndrome.

Neural stem cells

Neural stem cells (NSCs) are multipotent cells capable of differentiating into both neurons and glial cells. By using a monkey model, a group reported that the engrafted newborn neurons could functionally integrate into the host neuronal network, and this had proved that transplantation of NSCs may be a valid way for curing brain injuries (Wang et al., 2017; Wei et al., 2017). There are two ways to obtain human NSCs (hNSCs), i.e., directly from the brain (Abe et al., 2016) and differentiated from other cells, including stem (Kim et al., 2004) and somatic cells (Ai et al., 2016). Bjugstad et al. (2005) transplanted hNSCs into the caudate and substantia nigra of MPTP-induced PD monkeys and concluded that hNSCs may be beneficial for maintaining a normal environment. Their research group also analyzed the differentiation and migration ratio of hNSCs transplanted into the body (Bjugstad et al., 2008; Kern et al., 2011). These studies provide an important basis for the clinical application of hNSCs.

Recent studies have indicated that certain NSCs persist in

the adult nervous system and are capable of regenerating new neurons (Bacigaluppi et al., 2016; L'episcopo et al., 2018). Compared with pluripotent stem cells, multipotent NSCs exhibit higher cellular survival rates and lower risk of teratoma formation (Pardal & Barneo, 2012). In addition to the fetal isolation of NSCs, these cells can be obtained from areas of the adult brain, including the subventricular zone, subgranular zone, and hippocampus (Wang et al., 2012). Acquisition of NSCs from non-fetal sources avoids the ethical issues associated with the use of ESCs. Because NSCs can self-renew and differentiate into many types of neurons, including those that are dysfunctional in neurodegenerative diseases, their potential use in the treatment of patients with PD is promising (Choi et al., 2017).

FUTURE DIRECTIONS OF NHP-ENABLED SCT RESEARCH

NHPs are similar to humans in size, behavior, physiology, biochemistry, and immune functions (Vierboom et al., 2012; Zhang et al., 2014). Due to their many advantages, NHP models of PD can compensate for the deficiencies in SCT clinical trials of PD and provide vital information unavailable from rodent models, such as cellular migration, survival, and differentiation after transplantation, choice of target sites, and timelines of recovery (Vermilyea & Emborg, 2018). To date, however, all NHP-based studies on CBT for PD have been performed in neurotoxin-induced PD models. Validating state-of-the-art, recently available genetic models are anticipated to facilitate the development of SCT for PD and its clinical translation.

Different types of stem cells, including ESCs, NSCs, MSCs, and iPSCs, can be used for specific cellular therapeutic approaches. Multiple factors can differentiate these cells into DA neurons, which can be used to replace damaged neurons in PD patients. Methods for inducing differentiation depend upon the type of stem cell. Furthermore, risks such as tumor formation remain after transferring DA cells into PD patients. ESCs and iPSCs have advantages over the other two stem cell types. For example, ESCs remain highly proliferative *in vivo* and can survive and generate DA neurons after transplantation. In turn, iPSCs can generate unlimited, PD patient-specific cells, and produce a degree of functional host recovery after transplantation (Morizane et al., 2017).

Graft distribution could also benefit from NHP-based studies and noninvasive imaging approaches. For example, Silvestrini et al. (2015) used real-time intraoperative magnetic resonance imaging (MRI) to monitor cell transplantation into a swine and cadaveric human head for possible application in the human brain. Furthermore, Malloy et al. (2017) used an MRI-compatible delivery system to monitor the distribution of cells pre-labeled with a contrast agent into the basal ganglia of a baboon. These new MRI-based imaging methods can increase the safety and accuracy of grafting procedures and facilitate the evaluation of different target sites.

In addition to the challenges mentioned above, many

questions remain to be answered in order to improve effective SCT for PD. For example, the influence of cell preparation and storage on engraftment, method of transplantation, choice of target sites, and timelines of recovery are basic parameters that still require evaluation in NHP models to improve SCT for PD and its translation into clinical treatment.

COMPETING INTERESTS

The authors declare that they have no competing interests.

AUTHORS' CONTRIBUTIONS

Y.Y.N. and Z.Z.C. wrote and revised the manuscript. All authors read and approved the final version of the manuscript.

REFERENCES

Abe S, Yamaguchi S, Sato Y, Harada K. 2016. Sphere-derived multipotent progenitor cells obtained from human oral mucosa are enriched in neural crest cells. *Stem Cells Translational Medicine*, **5**(1): 117–128.

Ai Z, Xiang Z, Li Y, Liu G, Wang H, Zheng Y, Qiu X, Zhao S, Zhu X, Li Y, Ji W, Li T. 2016. Conversion of monkey fibroblasts to transplantable telencephalic neuroepithelial stem cells. *Biomaterials*, **77**: 53–65.

Bacigaluppi M, Russo GL, Peruzzotti-Jametti L, Rossi S, Sandrone S, Butti E, De Ceglia R, Bergamaschi A, Motta C, Gallizioli M, Studer V, Colombo E, Farina C, Comi G, Politi LS, Muzio L, Villani C, Invernizzi RW, Hermann DM, Centonze D, Martino G. 2016. Neural stem cell transplantation induces stroke recovery by upregulating glutamate transporter GLT-1 in astrocytes. *The Journal of Neuroscience*, **36**(41): 10529–10544.

Barker RA, Parmar M, Studer L, Takahashi J. 2017. Human trials of stem cell-derived dopamine neurons for Parkinson's disease: dawn of a new era. *Cell Stem Cell*, **21**(5): 569–573.

Bentlage C, Nikkhah G, Cunningham MG, Bjorklund A. 1999. Reformation of the nigrostriatal pathway by fetal dopaminergic micrografts into the substantia nigra is critically dependent on the age of the host. *Experimental Neurology*, **159**(1): 177–190.

Bergstrom R, Strom S, Holm F, Feki A, Hovatta O. 2011. Xeno-free culture of human pluripotent stem cells. *Methods in Molecular Biology*, **767**: 125–136.

Bernstein AI, Garrison SP, Zambetti GP, O'malley KL. 2011. 6-OHDA generated ROS induces DNA damage and p53-and PUMA-dependent cell death. *Molecular Neurodegeneration*, **6**(1): 2–10.

Bjugstad KB, Redmond DE, Teng YD, Elsworth JD, Roth RH, Blanchard BC, Snyder EY, Sladek JR. 2005. Neural stem cells implanted into MPTP-treated monkeys increase the size of endogenous tyrosine hydroxylase-positive cells found in the striatum: A return to control measures. *Cell Transplantation*, **14**(4): 183–192.

Bjugstad KB, Teng YD, Redmond DE, Jr., Elsworth JD, Roth RH, Cornelius SK, Snyder EY, Sladek JR, Jr. 2008. Human neural stem cells migrate along the nigrostriatal pathway in a primate model of Parkinson's disease. *Experimental Neurology*, **211**(2): 362–369.

Bove J, Perier C. 2012. Neurotoxin-based models of Parkinson's disease. *Neuroscience*, **211**: 51–76.

Camus S, Ko WKD, Pioli E, Bezard E. 2015. Why bother using non-human

primate models of cognitive disorders in translational research?. *Neurobiology of Learning and Memory*, **124**: 123–129.

Chiu AY, Hall ZW. 2006. Stem cell research: the California experience. *The Journal of Neuroscience*, **26**(25): 6661–6663.

Choi DH, Kim JH, Kim SM, Kang K, Han DW, Lee J. 2017. Therapeutic potential of induced neural stem cells for Parkinson's disease. *International Journal of Molecular Sciences*, **18**(1): E224.

Cicchetti F, Drouin-Ouellet J, Gross RE. 2010. Viability of the rotenone model in question. *Trends in Pharmacological Sciences*, **31**(4): 142–143.

Cimdis K, Waugh HS, Chrysostomou V, Lopez Sanchez MIG, Johannsen VA, Cook MJ, Crowston JG, Hill AF, Duce JA, Bush AI, Trounce IA. 2019. Amyloid precursor protein mediates neuronal protection from rotenone toxicity. *Molecular Neurobiology*, **2**(3): 55–62.

Cowen D. 1986. The melanoneurons of the human cerebellum (nucleus pigmentosus cerebellaris) and homologues in the monkey. *Journal of Neuropathology and Experimental Neurology*, **45**(3): 205–221.

Coizet V, Heilbronner SR, Carcenac C, Mailly P, Lehman JF, Savasta M, David O, Deniau JM, Groenewegen HJ, Haber SN. 2017. Organization of the anterior limb of the internal capsule in the rat. *The Journal of Neuroscience*, **37**(10): 2539–2554.

Collier TJ, Redmond DE, Steece-Collier K, Lipton JW, Manfredsson FP. 2016. Is alpha-synuclein loss-of-function a contributor to Parkinsonian pathology? Evidence from Non-human Primates. *Frontiers in Neuroscience*, **10**(5): 12–20.

Cyranoski D. 2017. Trials of embryonic stem cells to launch in China. *Nature*, **546**(7656): 15–16.

Dauer W, Przedborski S. 2003. Parkinson's disease: Mechanisms and models. *Neuron*, **39**(6): 889–909.

Didier ES, Maclean AG, Mohan M, Didier PJ, Lackner AA, Kuroda MJ. 2016. Contributions of nonhuman primates to research on aging. *Veterinary Pathology*, **53**(2): 277–290.

Emborg ME. 2004. Evaluation of animal models of Parkinson's disease for neuroprotective strategies. *Journal of Neuroscience Methods*, **139**(2): 121–143.

Drouin-Ouellet J. 2014. The potential of alternate sources of cells for neural grafting in Parkinson's and Huntington's disease. *Neurodegenerative disease management*, **4**(4): 297–307.

Howson PA, Johnston TH, Ravenscroft P, Hill MP, Su J, Brochie JM, Koprich JB. 2019. Beneficial effects of trehalose on striatal dopaminergic deficits in rodent and primate models of synucleinopathy in Parkinson's disease. *Journal of Pharmacology and Experimental Therapeutics*, **369**(3): 364–374.

Emborg ME. 2017. Nonhuman primate models of neurodegenerative disorders. *Ilar Journal*, **58**(2): 190–201.

Eslamboli A, Baker HF, Ridley RM, Annett LE. 2003. Sensorimotor deficits in a unilateral intrastratial 6-OHDA partial lesion model of Parkinson's disease in marmoset monkeys. *Experimental Neurology*, **183**(2): 418–429.

Eslamboli A, Georgievska B, Ridley RM, Baker HF, Muzyczka N, Burger C, Mandel RJ, Annett L, Kirik D. 2005. Continuous low-level glial cell line-derived neurotrophic factor delivery using recombinant adeno-associated viral vectors provides neuroprotection and induces behavioral recovery in a primate model of Parkinson's disease. *The Journal of Neuroscience*, **25**(4): 769–777.

Eslamboli A, Romero-Ramos M, Burger C, Bjorklund T, Muzyczka N,

- Mandel RJ, Baker H, Ridley RM, Kirik D. 2007. Long-term consequences of human alpha-synuclein overexpression in the primate ventral midbrain. *Brain*, **130**: 799–815.
- Fallahi-Sichani M, Soleimani M, Najafi SMA, Kiani J, Arefian E, Atashi A. 2007. In vitro differentiation of cord blood unrestricted somatic stem cells expressing dopamine-associated genes into neuron-like cells. *Cell Biology International*, **31**(3): 299–303.
- Hallett PJ, Deleidi M, Astradsson A, Smith GA, Cooper O, Osborn TM, Sundberg M, Moore MA, Perez-Torres E, Brownell AL, Schumacher JM, Spealman RD, Isacson O. 2015. Successful function of autologous iPSC-derived dopamine neurons following transplantation in a non-human primate model of Parkinson's disease. *Cell Stem Cell*, **16**(3): 269–274.
- Han F, Wang W, Chen B, Chen C, Li S, Lu X, Duan J, Zhang Y, Zhang YA, Guo W, Li G. 2015. Human induced pluripotent stem cell-derived neurons improve motor asymmetry in a 6-hydroxydopamine-induced rat model of Parkinson's disease. *Cytotherapy*, **17**(5): 665–679.
- Handscheil J, Naujoks C, Depprich R, Lammers L, Kübler N, Meyer U, Wiesmann H. 2011. Embryonic stem cells in scaffold-free three-dimensional cell culture: osteogenic differentiation and bone generation. *Head & Face Medicine*, **7**(1): 12–12.
- Hayashi T, Wakao S, Kitada M, Ose T, Watabe H, Kuroda Y, Mitsunaga K, Matsuse D, Shigemoto T, Ito A, Ikeda H, Fukuyama H, Onoe H, Tabata Y, Dezawa M. 2013. Autologous mesenchymal stem cell-derived dopaminergic neurons function in parkinsonian macaques. *Journal of Clinical Investigation*, **123**(1): 272–284.
- Huang B, Wu S, Wang Z, Ge L, Rizak J, Wu J, Li J, Xu L, Lv L, Yin Y, Hu X, Li H. 2018. Phosphorylated α -synuclein accumulations and lewy body-like pathology distributed in Parkinson's disease-related brain areas of aged rhesus monkeys treated with MPTP. *Neuroscience*, **379**: 302–315.
- Johnson ME, Stringer A, Bobrovskaya L. 2018. Rotenone induces gastrointestinal pathology and microbiota alterations in a rat model of Parkinson's disease. *Neurotoxicology*, **65**: 174–185.
- Jiang PZ, Dickson DW. 2018. Parkinson's disease: experimental models and reality. *Acta Neuropathologica*, **135**(1): 13–32.
- Kauhausen JA, Thompson LH, Parish CL. 2015. Chondroitinase improves midbrain pathway reconstruction by transplanted dopamine progenitors in parkinsonian mice. *Molecular & Cellular Neuroscience*, **69**: 22–29.
- Kern DS, Maclean KN, Jiang H, Synder EY, Sladek JR, Jr., Bjugstad KB. 2011. Neural stem cells reduce hippocampal tau and reelin accumulation in aged Ts65Dn down syndrome mice. *Cell Transplantation*, **20**(3): 371–379.
- Kern R, Garitaonandia I, Gonzalez R, Sherman G, Noskov A, Cardiff D, Christiansen-Weber T, Semechkin A, Braine E, Shahru A, Nair G, Evans A. 2018. Interim clinical assessment of a neural stem cell Based therapy for Parkinson's disease. *Neurology*, **90**(1): 12–12.
- Kikuchi T, Morizane A, Doi D, Magotani H, Onoe H, Hayashi T, Mizuma H, Takara S, Takahashi R, Inoue H, Morita S, Yamamoto M, Okita K, Nakagawa M, Parmar M, Takahashi J. 2017. Human iPS cell-derived dopaminergic neurons function in a primate Parkinson's disease model. *Nature*, **548**(7669): 592–596.
- Kim SH, Hong JY, Joo SY, Kim JH, Moon SY, Yoon HS, Kim DH, Chung HM, Choi SJ. 2004. Derivation of neural precursor cells from human embryonic stem cells. *Reproductive & Developmental Biology*, **28**(4): 247–252.
- Kim SU, Lee HJ, Kim YB. 2013. Neural stem cell-based treatment for neurodegenerative diseases. *Neuropathology*, **33**(5): 491–504.
- Kim JH, Auerbach JM, Rodriguez-Gomez JA, Velasco I, Gavin D, Lumelsky N, Lee SH, Nguyen J, Sanchez-Pernaute R, Bankiewicz K, McKay R. 2002. Dopamine neurons derived from embryonic stem cells function in an animal model of Parkinson's disease. *Nature*, **418**(6893): 50–56.
- Kirik D, Annett L, Burger C, Muzyczka N, Mandel RJ, Björklund A. 2003. Nigrostriatal α -synucleinopathy induced by viral vector-mediated overexpression of human α -synuclein: a new primate model of Parkinson's disease. *Proceedings of the National Academy of Sciences of the United States of America*, **100**(5): 2884–2889.
- Koprach JB, Johnston TH, Reyes G, Omana V, Brotchie JM. 2016. Towards a non-human primate model of alpha-synucleinopathy for development of therapeutics for Parkinson's disease: optimization of AAV1/2 delivery parameters to drive sustained expression of alpha synuclein and dopaminergic degeneration in Macaque. *PLoS One*, **11**(11): e0167235.
- Koprach JB, Johnston TH, Su J, Fox SH, Ma YL, Zuo CT, Guan YH, Brotchie JM. 2017. A non-human primate model of Parkinson's disease based on viral vector mediated overexpression of alpha-synuclein. *Acta Pharmacologica Sinica*, **38**(7): 1090–1090.
- Kostrzewa RM. 2000. Review on apoptosis vs. necrosis of substantia nigra pars compacta in Parkinson's disease. *Neurotoxicity Research*, **2**(2–3): 239–250.
- Kuo TL & Yu HY. 1991. Effect of ethanol on the disposition of paraquat. *Toxicology Letters*, **58**(1): 107–115.
- Kuter K, Nowak P, Golembiowska K, Ossowska K. 2010. Increased reactive oxygen species production in the brain after repeated low-dose pesticide paraquat exposure in rats. A comparison with peripheral tissues. *Neurochemical Research*, **35**(8): 1121–1130.
- Kuter K, Smiałowska M, Wieronska J, Zieba B, Wardas J, Pietraszek M, Nowak P, Biedka I, Roczniak W, Konieczny J, Wolfarth S, Ossowska K. 2007. Toxic influence of subchronic paraquat administration on dopaminergic neurons in rats. *Brain Research*, **1155**: 196–207.
- Kwak KA, Lee SP, Yang JY, Park YS. 2018. Current perspectives regarding stem cell-based therapy for Alzheimer's disease. *Stem Cells International*, **2018**: 1–14.
- L'episcopo F, Tirolo C, Peruzzotti-Jametti L, Serapide MF, Testa N, Caniglia S, Balzarotti B, Pluchino S, Marchetti B. 2018. Neural stem cell grafts promote astroglia-driven neurorestoration in the aged Parkinsonian brain via wnt/beta-catenin signaling. *Stem Cells*, **36**(8): 1179–1197.
- Leng LG, Tian ZM. 2016. Transplantation of neural precursor cells in the treatment of Parkinson disease: an efficacy and safety analysis. *Turkish Neurosurgery*, **26**(3): 378–383.
- Perier C, Bove J, Vila M, Przedborski S. 2003. The rotenone model of Parkinson's disease. *Trends in Neurosciences*, **26**(7): 345–346.
- Lei X, Li H, Huang B, Rizak J, Li L, Xu L, Liu L, Wu J, Lü L, Wang Z, Hu YZ, Le WD, Deng XL, Li JL, Yao YG, Xu L, Hu XT, Zhang BR. 2016. 1-methyl-4-phenylpyridinium stereotactic infusion completely and specifically ablated the nigrostriatal dopaminergic pathway in rhesus macaque. *PLoS One*, **11**(1): e0147094.
- Li H, Ding C, Ding Z, Ling M, Wang T, Wang W, Huang B. 2017. 17 β -Oestradiol promotes differentiation of human embryonic stem cells into dopamine neurons via cross-talk between insulin-like growth factors-1 and oestrogen receptor β . *Journal of Cellular and Molecular Medicine*, **21**(8): 1605–1618.

- Li H, Lei XG, Huang BH, Rizak JD, Yang LC, Yang SC, Wu J, Lu LB, Wang JH, Yan T, Li HW, Wang ZB, Hu YZ, Le WD, Deng XL, Huang TZ, Li JL, Xu L, Zhang BR, Hu XT. 2015a. A quantitative approach to developing Parkinsonian monkeys (*Macaca fascicularis*) with intracerebroventricular 1-methyl-4-phenylpyridinium injections. *Journal of Neuroscience Methods*, **251**: 99–107.
- Li W, Chen SD, Li JY. 2015b. Human induced pluripotent stem cells in Parkinson's disease: A novel cell source of cell therapy and disease modeling. *Progress in Neurobiology*, **134**(5): 161–177.
- Lu HF, Chai C, Lim TC, Leong MF, Lim JK, Gao S, Lim KL, Wan ACA. 2014. A defined xeno-free and feeder-free culture system for the derivation, expansion and direct differentiation of transgene-free patient-specific induced pluripotent stem cells. *Biomaterials*, **35**(9): 2816–2826.
- Luk KC, Kehm V, Carroll J, Zhang B, O'Brien P, Trojanowski JQ, Lee VMY. 2012. Pathological α -synuclein transmission initiates parkinson-like neurodegeneration in nontransgenic mice. *Science*, **338**(6109): 949–953.
- Luo X, Li M, Su B. 2016. Application of the genome editing tool CRISPR/Cas9 in non-human primates. *Zoological Research*, **37**(4): 214–219.
- Malloy KE, Li J, Choudhury GR, Torres A, Gupta S, Kantorak C, Goble T, Fox PT, Clarke GD, Daadi MM. 2017. Magnetic resonance imaging-guided delivery of neural stem cells into the basal ganglia of nonhuman primates reveals a pulsatile mode of cell dispersion. *Stem Cells Translational Medicine*, **6**(3): 877–885.
- Marmion D, Kordower J. 2018. α -Synuclein nonhuman primate models of Parkinson's disease. *Journal of Neural Transmission*, **125**(3): 385–400.
- Morizane A, Kikuchi T, Hayashi T, Mizuma H, Takara S, Doi H, Mawatari A, Glasser MF, Shiina T, Ishigaki H, Itoh Y, Okita K, Yamasaki E, Doi D, Onoe H, Ogasawara K, Yamanaka S, Takahashi J. 2017. MHC matching improves engraftment of iPSC-derived neurons in non-human primates. *Nature Communications*, **8**(1): 385–385.
- Niu Y, Guo X, Chen Y, Wang C, Gao J, Yang W, Kang Y, Si W, Wang H, Yang S, Li S, Ji W, Li X. 2015. Early Parkinson's disease symptoms in α -synuclein transgenic monkeys. *Human Molecular Genetics*, **24**(8): 2308–2317.
- Pardal R, Barneo JL. 2012. Neural stem cells and transplantation studies in Parkinson's disease. *Advances in Experimental Medicine and Biology*, **741**(1): 206–216.
- Park JB, Lee JS, Cho BP, Rhee K-J, Baik SK, Kim J, Kang SJ, Park D-J, Oh J-E, Shin HC, Kim YM, Kim HS, Bae KS, Eom YW. 2015. Adipose tissue-derived mesenchymal stem cells cultured at high cell density express brain-derived neurotrophic factor and exert neuroprotective effects in a 6-hydroxydopamine rat model of Parkinson's disease. *Genes & Genomics*, **37**(2): 213–221.
- Parmar M. 2018. Towards stem cell based therapies for Parkinson's disease. *Development*, **145**(1): 201–204.
- Paumier K, Luk K, Manfredsson F, Kanaan N, Lipton J, Collier T, Collier KS, Kemp C, Celano S, Schulz E, Sandoval I, Fleming S, Dirr E, Polinski N, Trojanowski J, Lee V, Sortwell C. 2015. Intrastriatal injection of pre-formed mouse α -synuclein fibrils into rats triggers α -synuclein pathology and bilateral nigrostriatal degeneration. *Neurobiology of Disease*, **82**(3): 185–199.
- Recasens A, Dehay B, Bove J, Carballo-Carbajal I, Dovero S, Perez-Villalba A, Fernagut P-O, Blesa J, Parent A, Perier C, Farinas I, Obeso JA, Bezard E, Vila M. 2014. Lewy body extracts from Parkinson disease brains trigger α -synuclein pathology and neurodegeneration in mice and monkeys. *Annals of Neurology*, **75**(3): 351–362.
- Robinson R. 2018. At the bench-amyotrophic lateral sclerosis: in the lab, regulatory T cells slow ALS. *Neurology Today*, **18**(2): 225–231.
- Sanders LH, Greenamyre JT. 2013. Oxidative damage to macromolecules in human Parkinson disease and the rotenone model. *Free Radical Biology and Medicine*, **62**(3): 111–120.
- Santana M, Palmér T, Simplicio H, Fuentes R, Petersson P. 2015. Characterization of long-term motor deficits in the 6-OHDA model of Parkinson's disease in the common marmoset. *Behavioural Brain Research*, **290**(9): 90–101.
- Sarwar N, Ishaq W, Farid G, Shaheen MR, Imran M, Geng M, Hussain S. 2015. Zinc-cadmium interactions: Impact on wheat physiology and mineral acquisition. *Ecotoxicology and Environmental Safety*, **122**(1): 528–536.
- Shirani A, Stuve O. 2018. Natalizumab: Perspectives from the bench to bedside. *Cold Spring Harbor Perspectives in Medicine*, **8**(12): a029066.
- Silvestrini MT, Yin D, Martin AJ, Coppes VG, Mann P, Larson PS, Starr PA, Zeng X, Gupta N, Panter SS, Desai TA, Lim DA. 2015. Interventional magnetic resonance imaging-guided cell transplantation into the brain with radially branched deployment. *Molecular Therapy*, **23**(1): 119–129.
- Skerjanc IS & Wilton S. 2000. Myocyte enhancer factor 2C upregulates MASH-1 expression and induces neurogenesis in P19 cells. *FEBS Letters*, **472**(1): 53–56.
- Smirnova L, Harris G, Delp J, Valadares M, Pamies D, Hogberg HT, Waldmann T, Leist M, Hartung T. 2016. A LUHMES 3D dopaminergic neuronal model for neurotoxicity testing allowing long-term exposure and cellular resilience analysis. *Archives of Toxicology*, **90**(11): 2725–2743.
- Sonntag KC, Song B, Lee N, Jung JH, Cha Y, Leblanc P, Neff C, Kong SW, Carter BS, Schweitzer J, Kim K-S. 2018. Pluripotent stem cell-based therapy for Parkinson's disease: Current status and future prospects. *Progress in Neurobiology*, **168**(2): 1–20.
- Su LY, Li H, Lv L, Feng YM, Li GD, Luo RC, Zhou HJ, Lei XG, Ma L, Li JL, Xu L, Hu XT, Yao YG. 2015. Melatonin attenuates MPTP-induced neurotoxicity via preventing CDK5-mediated autophagy and SNCA/ α -synuclein aggregation. *Autophagy*, **11**(10): 1745–1759.
- Thomson JA, Itskovitz-Eldor J, Shapiro SS, Waknitz MA, Swiergiel JJ, Marshall VS, Jones JM. 1998. Embryonic stem cell lines derived from human blastocysts. *Science*, **282**(5391): 1145–1147.
- Thompson LH, Shane G, Deniz K, Anders BR. 2010. Reconstruction of the nigrostriatal dopamine pathway in the adult mouse brain. *European Journal of Neuroscience*, **30**(4): 625–638.
- Tobón-Velasco JC, Limón-Pacheco JH, Orozco-Ibarra M, Macías-Silva M, Vázquez-Victorio G, Cuevas E, Ali SF, Cuadrado A, Pedraza-Chaverrí J, Santamaría A. 2013. 6-OHDA-induced apoptosis and mitochondrial dysfunction are mediated by early modulation of intracellular signals and interaction of Nrf2 and NF- κ B factors. *Toxicology*, **304**(3): 109–119.
- Trigo DI, del Rey NL, Blesa J. 2018. Novel models for Parkinson's disease and their impact on future drug discovery. *Expert Opinion on Drug Discovery*, **13**(3): 229–239.
- Vaccari C, El Dib R, De Camargo JLV. 2017. Paraquat and Parkinson's disease: a systematic review protocol according to the OHAT approach for hazard identification. *Systematic Reviews*, **6**(1): 98–98.
- Vermilyea SC, Emborg ME. 2018. The role of nonhuman primate models in the development of cell-based therapies for Parkinson's disease. *Journal of*

- Neural Transmission*, **125**(3): 365–384.
- Vierboom M, Breedveld E, T Hart BA. 2012. New drug discovery strategies for rheumatoid arthritis: a niche for nonhuman primate models to address systemic complications in inflammatory arthritis. *Expert Opinion on Drug Discovery*, **7**(4): 315–325.
- Wang HW, Lin LM, He HY, You F, Li WZ, Huang TH, Ma GX, Ma L. 2011. Human umbilical cord mesenchymal stem cells derived from Wharton's jelly differentiate into insulin-producing cells in vitro. *Chinese Medical Journal*, **124**(10): 1534–1539.
- Wang S, Okun MS, Suslov O, Zheng T, Mcfarland NR, Vedam-Mai V, Foote KD, Roper SN, Yachnis AT, Siebzehnrbli FA, Steindlera DA. 2012. Neurogenic potential of progenitor cells isolated from postmortem human Parkinsonian brains. *Brain Research*, **1464**(1): 61–72.
- Wang ZB, Qin DD, Hu XT. 2017. Engrafted newborn neurons could functionally integrate into the host neuronal network. *Zoological Research*, **38**(1): 5–6.
- Wei JK, Wang WC, Zhai RW, Zhang YH, Yang SC, Rizak J, Li L, Xu LQ, Liu L, Pan MK, Hu YZ, Ghanemi A, Wu J, Yang LC, Li H, Lv LB, Li JL, Yao YG, Xu L, Feng XL, Yin Y, Qin DD, Xu XT, Wang ZB. 2016. Neurons differentiated from transplanted stem cells respond functionally to acoustic stimuli in the awake monkey brain. *Cell Reports*, **16**(4): 1016–1025.
- Weick JP, Liu Y, Zhang SC. 2011. Human embryonic stem cell-derived neurons adopt and regulate the activity of an established neural network. *Proceedings of the National Academy of Sciences of the United States of America*, **108**(50): 20189–20194.
- Xu J, Wang D, Liu D, Fan Z, Zhang H, Liu O, Ding G, Gao R, Zhang C, Ding Y, Bromberg JS, Chen W, Sun L, Wang S. 2012. Allogeneic mesenchymal stem cell treatment alleviates experimental and clinical Sjogren syndrome. *Blood*, **120**(15): 3142–3151.
- Yang WL, Wang GH, Wang CE, Guo XY, Yin P, Gao JQ, Tu ZC, Wang ZB, Wu J, Hu XT, Li SH, Li XJ. 2015. Mutant alpha-synuclein causes age-dependent neuropathology in monkey brain. *The Journal of Neuroscience*, **35**(21): 8345–8358.
- Zhang X, Hu D, Shang Y, Qi X. 2019. Using induced pluripotent stem cell neuronal models to study neurodegenerative diseases. *Biochimica et Biophysica Acta*, **5**(1): 67–75.
- Zhang XL, Pang W, Hu XT, Li JL, Yao YG, Zheng YT. 2014. Experimental primates and non-human primate (NHP) models of human diseases in China: current status and progress. *Zoological Research*, **35**(6): 447–464.
- Zhao B, Zhang WD, Duan YL, Lu YQ, Cun YX, Li CH, Guo K, Nie WH, Li L, Zhang R, Zheng P. 2015. Filia is an ESC-specific regulator of DNA damage response and safeguards genomic stability. *Cell Stem Cell*, **16**(6): 684–698.
- Zhou L, Cheng Y. 2019. Alpha-lipoic acid alleviated 6-OHDA-induced cell damage by inhibiting AMPK/mTOR mediated autophagy. *Neuropharmacology*, **155**: 98–103.
- Zhou Q, Zhang H, Wu Q, Shi J, Zhou S. 2017. Pharmacological manipulations of autophagy modulate paraquat-induced cytotoxicity in PC12 cells. *International Journal of Biochemistry and Molecular Biology*, **8**(2): 13–22.

Counting stripes: revision of the *Lipinia vittigera* complex (Reptilia, Squamata, Scincidae) with description of two new species from Indochina

Nikolay A. Poyarkov Jr.^{1,2,*}, Peter Geissler^{3,*}, Vladislav A. Gorin¹, Evgeniy A. Dunayev⁴, Timo Hartmann⁵, Chatmongkon Suwannapoom⁶

¹ Department of Vertebrate Zoology, Biological Faculty, Lomonosov Moscow State University, Moscow 119991, Russia

² Joint Russian-Vietnamese Tropical Research and Technological Center, Nghia Do, Cau Giay, Hanoi, Vietnam

³ Museum Natur und Mensch, Freiburg 79098, Germany

⁴ Zoological Museum, Moscow State University, Moscow 125009, Russia

⁵ Zoological Research Museum Alexander Koenig, Bonn 53113, Germany

⁶ School of Agriculture and Natural Resources, University of Phayao, Phayao 56000, Thailand

ABSTRACT

We provide an integrative taxonomic analysis of the *Lipinia vittigera* species complex from mainland Southeast Asia. Based on examination of external morphology, color pattern, and 681 base pairs of the cytochrome oxidase subunit I (*COI*) mitochondrial gene, we demonstrate the presence of four morphologically distinct lineages of *Lipinia* in Vietnam, Cambodia, Thailand, and Malaysia, showing a sequence divergence ranging 15.5%–20.4%. All discovered lineages are discretely diagnosable from one another by a combination of scalation traits and color patterns. A review of the published distribution data and a re-examination of available type material revealed the following results: (1) distribution of *L. vittigera* (Boulenger, 1894) *sensu stricto* is restricted to Sundaland and the Thai-Malay Peninsula south of the Isthmus of Kra; (2) *L. microcerus* (Boettger, 1901) **stat. nov.** is elevated to full species rank; the species has a wide distribution from central and southern Vietnam across Cambodia to eastern Thailand; we regard

Lygosoma vittigerum kronfanum Smith, 1922 and *Leiolopisma pranensis* Cochran, 1930 as its junior synonyms; (3) *Lipinia trivittata* **sp. nov.** occurs in hilly areas of southern Vietnam, Cambodia, and eastern Thailand; and (4) *Lipinia vassilievi* **sp. nov.** is currently known only from a narrow area along the Vietnamese-Cambodian border in the foothills of the central Annamite Mountain Range. We further provide an identification key for *Lipinia* occurring in mainland Southeast Asia.

Keywords: *Lipinia microcerus* **stat. nov.**; *Lipinia trivittata* **sp. nov.**; *Lipinia vassilievi* **sp. nov.**; Vietnam; Thailand; Cambodia; Biogeography; mtDNA; *COI*-barcoding

INTRODUCTION

The scincid genus *Lipinia* Gray, 1845 is an assemblage of arboreal and terrestrial lizards currently comprising at least 29

Open Access

This is an open-access article distributed under the terms of the Creative Commons Attribution Non-Commercial License (<http://creativecommons.org/licenses/by-nc/4.0/>), which permits unrestricted non-commercial use, distribution, and reproduction in any medium, provided the original work is properly cited.

Copyright ©2019 Editorial Office of Zoological Research, Kunming Institute of Zoology, Chinese Academy of Sciences

Received: 30 January 2019; Accepted: 10 July 2019; Online: 02 September 2019

Foundation items: The study was supported by the Russian Science Foundation (19-14-00050) to N.A.P. and partially supported by the Unit of Excellence 2019 on Biodiversity and Natural Resources Management, University of Phayao (UoE62005) to C.S.

*Authors contributed equally to this work

*Corresponding authors, E-mail: n. poyarkov@gmail. com; pgeissler84@yahoo.de

DOI: 10.24272/zj.issn.2095-8137.2019.052

valid species (Grismer et al., 2016; Uetz & Hošek, 2019). Many species of *Lipinia* were originally described as members of the genus *Lygosoma* Hardwicke and Gray, 1827. The genus was revived from its synonymy by Mittleman (1952). *Lipinia* skinks inhabit a large area from the Andaman and Nicobar Islands of India in the northwest, Mentawai and Sumatra Islands of Indonesia, eastward through Indochina and the Malay Peninsula to Borneo, the Philippines, numerous islands of the Indo-Australian Archipelago to New Guinea, and further eastwards throughout much of the South Pacific, including the archipelagos of Palau, Fiji, Samoa, and French Polynesia (Adler et al., 1995; Grismer et al., 2016; Günther, 2000; Linkem, 2013). *Lipinia* records east of Vanuatu have been suggested to be the result of anthropogenic introduction (Austin, 1999). Despite their significant diversity in Australasia, a biogeographic origin of the genus in Southeast Asia or the Philippines has been suggested (Austin, 1998).

Members of the genus *Lipinia* are characterized by the following combination of natural history traits and morphological characters: diurnal, arboreal, semi-arboreal, or secretive terrestrial lifestyle; small body size (snout vent length (SVL) to 58 mm); lower eyelid generally with transparent window (absent in some taxa); auricular lobules absent; body scales smooth; basal subdigital lamellae usually expanded; postorbital absent; vomers fused; pterygoid teeth absent; dorsal color pattern typically pale (rarely dark) middorsal stripe anteriorly (lacking in some taxa) (Das & Austin, 2007; Das & Greer, 2002; Grismer, 2011a, 2011b). Despite the overall morphological similarity, recent study has shown *Lipinia* to be a widely polyphyletic assemblage within the scincid tribe Sphenomorphini (Grismer et al., 2016; Linkem, 2013), and a stable phylogenetic hypothesis for *Lipinia* is still lacking.

In mainland Southeast Asia, *Lipinia* skinks occur widely in central to southern Indochina from easternmost Myanmar and northern Thailand southwards to southern Laos, central and southern Vietnam, Cambodia, and further southwards to the Thai-Malay Peninsula and Singapore (Figure 1). Boulenger (1894) described *Lygosoma vittigerum* from Mentawai (or Mentawai) Archipelago near the western coast of Sumatra, Indonesia. Shortly after, Boettger (1901) described *Lygosoma* (*Leiolopisma*) *microcerum* from Phuoc Son in Annam (now in Quang Nam Province, central Vietnam), noting that the new species appeared to be close to *L. vulcania* and *L. pulchella* from the Philippines. Annandale (1905) recorded a brightly colored tree-dwelling skink from Tavoy, Tenasserim (now Dawei, Tanintharyi Region, Myanmar) and identified it as *Lygosoma pulchellum*. Later, Smith (1922) described a new subspecies of Boulenger's *Lygosoma vittigerum* from Daban near Langbian in southern Vietnam as *Lygosoma vittigerum kronfanum*. Furthermore, Smith (1922) reported that this form also occurred in peninsular Siam (now Thailand) and differed from the nominate subspecies from the Mentawai Islands both in scalation and coloration pattern; among other characters, the main difference to the mainland form was the presence of five distinct light stripes on the dorsum and flank, instead of

one prominent vertebral light stripe in the nominate form. However, Smith (1922, p. 209) noted certain geographic variation in this character and reported a juvenile specimen from northern Siam (now Thailand) with three dorsal light stripes and predicted that "...further collections from this region may establish a race with 3 light stripes only". Soon after, Cochran (1930) analyzed the herpetological collections from Siam and described a new species of the genus *Leiolopisma* Duméril & Bibron from Pran (now Pran-Buri, Prachuap Khiri Khan, Thailand) and Doi Angka (Chiang Mai, Thailand) – *L. pranensis*, noting its affinity to *L. vittigerum*, to which it differed in midbody scale row count, number of subdigital lamellae, and distinct coloration.

Subsequently, in his review of lizards of British India and adjacent territories, Smith (1935) also assigned *L. vittigerum* to the genus *Leiolopisma*, and listed two subspecies: *L. v. vittigerum* in Tenasserim, northern, western, and southern Siam (Thailand), and the Malay Peninsula (including *L. pranensis* as a synonym without any justification for this decision), and *L. v. microcerum* in southern and central Annam (thus formally recognizing synonymy of his *kronfanum* with *microcerum* of Boettger, 1901). The two-subspecies taxonomy of Smith (1922, 1930, 1935) was well established for almost a century without any significant changes, with Indonesian, Malayan, and south-Thai populations traditionally assigned to the subspecies *L. v. vittigerum* (Boulenger, 1894), and Indochinese populations assigned to *L. v. microcerum* (Boettger, 1901) (note: after resurrection of the genus *Lipinia* by Mittleman, 1952, the gender of species names should be modified as *L. v. vittigera* and *L. v. microcerus*; for details see Etymology sections of respective species). However, the border between the ranges of the two forms and their evolutionary relationships remained unclear. Stuart (1999) mentioned the presence of distinct morphs of *Lipinia* in southern Laos. Recently, Grismer (2011b) reported on morphologically distinct types of *L. vittigera* in the Malay Peninsula and its offshore islands. More recently, Grismer et al. (2016) provided a preliminary phylogenetic tree for *Lipinia*, which included three specimens of *L. vittigera* from the Malay Peninsula and Indochina, each represented by a significantly divergent mtDNA lineage. However, the taxonomic value of these differences was not clear.

During our herpetological surveys in eastern Indochina over the last decade, we encountered a number of skink specimens tentatively identified as *L. v. cf. microcerus*. However, these specimens showed significant variation in scalation characters and body coloration, with three main color morphs recorded: i. e., (1) five-striped with narrow vertebral stripe; (2) three-striped with wide vertebral stripe; and (3) spotted with wide vertebral stripe. These forms were all found in close geographic proximity but not in sympatry (Figure 1), indicating that our knowledge of the taxonomy of *Lipinia* skinks in Indochina is far from complete. In the present paper, we provide descriptions of the available type material of the *L. vittigera* species complex and apply integrative approaches, including morphological and chromosomal analyses together with COI DNA-barcoding, to assess the

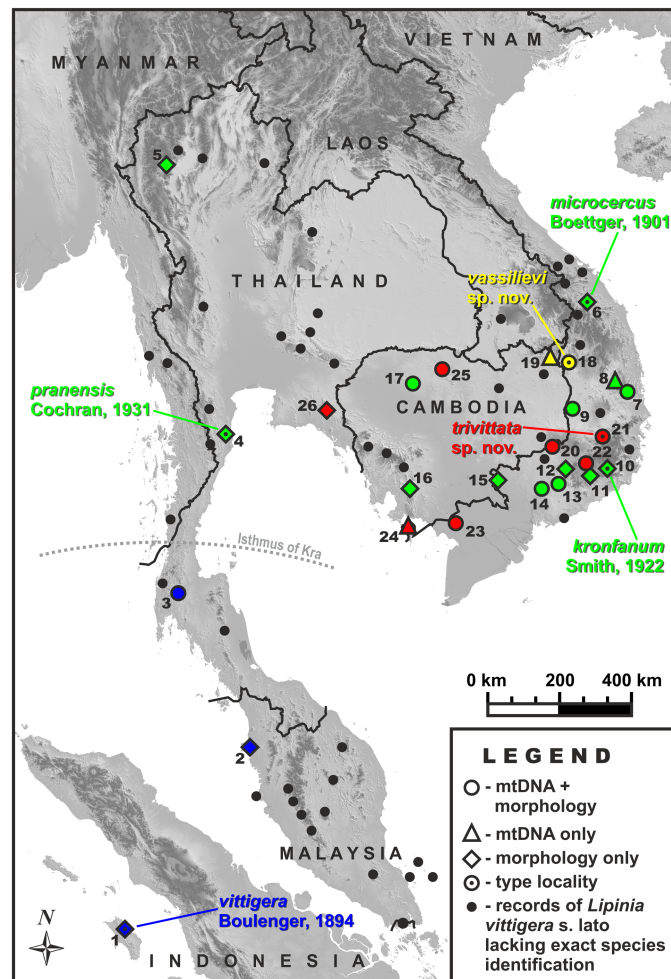


Figure 1 Map of Indochina, showing known distribution of the genus *Lipinia* and survey localities

Colors of localities correspond to those used in Figure 3. For voucher specimen information see Supplementary Table S1 and Appendix I. Dot in center of an icon corresponds to the type locality of a taxon. Black circles correspond to known localities of *Lipinia vittigera sensu lato* in Indochina without exact species identification; distribution records are taken from the following literature: Bobrov & Semenov, 2008; Grismer, 2011b; Mulcahy et al., 2018; Nguyen et al., 2009; Stuart et al., 2006, 2010; Taylor, 1963; Teynié et al., 2004. Localities: *Lipinia vittigera*: 1: Mentawai Isl., West Sumatra, Indonesia (type locality of *Lygosoma vittigerum* Boulenger, 1894); 2: Penang Isl., Penang, Malaysia; 3: Thailand, Surat Thani, Phnom Dist.; *Lipinia microcercus stat. nov.*: 4: Pran Buri, Prachuap Khiri Khan, Thailand (type locality of *Leiolopisma pranensis* Cochran, 1930); 5: Doi Angka, Chiang Mai, Thailand (origin of paratype of *Leiolopisma pranensis* Cochran, 1930); 6: Phuoc Son, Quang Nam, Vietnam (type locality of *Lygosoma microcercus* Boettger, 1901); 7: Buon Luoi, Gia Lai, Vietnam; 8: Kon Ka Kinh NP, Gia Lai, Vietnam; 9: Yok Don NP, Dak Lak, Vietnam; 10: Daban, Langbian, Lam Dong, Vietnam (type locality of *Lygosoma vittigerum kronfanum* Smith, 1922); 11: Bao Loc, Lam Dong, Vietnam; 12: Cat Loc NR, Lam Dong, Vietnam; 13: Cat Tien NP, Dong Nai, Vietnam; 14: Ma Da (Vinh Cuu), Dong Nai, Vietnam; 15: Lo Go-Xa Mat NP, Tay Ninh, Vietnam; 16: Kirirom NP, Kampong Speu, Cambodia; 17: Phnom Kulen NP, Siem Reap, Cambodia; *Lipinia vassilievi sp. nov.*: 18: Chu Mom Ray, Kon Tum, Vietnam (type locality); 19: Virachey NP, Ratanakiri, Cambodia; *Lipinia trivittata sp. nov.*: 20: Bu Gia Map NP, Binh Phuok, Vietnam; 21: Chu Yang Sin NP, Dak Lak, Vietnam (type locality); 22: Loc Bao, Lam Dong, Vietnam; 23: Nui Cam Mt., An Giang, Vietnam; 24: Phu Quoc NP, Kien Giang, Vietnam; 25: Kulen Prum Tep NP, Preah Vihear, Cambodia; 26: Khao Soi Dao NP, Chanthaburi, Vietnam.

taxonomy of this enigmatic group of skinks.

MATERIALS AND METHODS

Sample collection

Fieldwork was carried out in southern and central Vietnam (by

N.A.P. and P.G.) and Cambodia (by P.G., T.H., and E.A.D.) from 2009 to 2017. Specimens of *Lipinia* spp. were collected on tree trunks, on buildings, or on the ground (while foraging) by hand or using a rod with a loose loop. Specimens were euthanized by 20% benzocaine and muscle tissue samples were taken and stored in 96% ethanol for subsequent genetic

analysis. Specimens were subsequently preserved in 70% ethanol and deposited in the herpetological collections of the Zoological Museum of Moscow State University (ZMMU), Moscow, Russia, and the Zoologisches Forschungsmuseum Alexander Koenig (ZFMK), Bonn, Germany. Additionally, we isolated DNA from the ethanol-preserved specimens in ZMMU and ZFMK, resulting in 14 morphologically examined populations of *L. cf. vittigera* and 15 barcoded populations (25 specimens in total). The morphologically and genetically examined populations are presented in Figure 1.

All applicable international, national, and/or institutional guidelines for the care and use of animals were strictly followed; all animal collection protocols complied with the current laws of Vietnam, Cambodia, and Thailand. Specimen collection protocols and animal use were approved by the Institutional Ethical Committee of Animal Experimentation of the University of Phayao, Phayao, Thailand (certificate number UP-AE59-01-04-0022 issued to Chatmongkon Suwannapoom) and strictly complied with the ethical conditions of the Thailand Animal Welfare Act.

Morphological data and analyses

The following measurements were taken with digital vernier calipers (to the nearest 0.1 mm), following Bucklitsch et al. (2012), Das & Austin (2007), and Grismer et al. (2014): snout-vent length (SVL); tail (original or regenerated) length (TaL); trunk length (TrunkL), from posterior end of forelimb insertion to anterior part of hindlimb insertion, measured when stretched out; head length (HL), distance between posterior margin of parietal and snout-tip; head width (HW), measured across retroarticular process of mandibles; head height (HH), measured as greatest transverse depth of head, taken posterior of orbital region; snout length (SL), from anterior corner of eye to tip of snout; snout-tympanum length (STL), distance from snout tip to anterior border of tympanum; snout-forelimb length (SFIL), from tip of snout to anterior forelimb insertion, with limb held at right angles to body; eye-nostril distance (END), distance from anterior corner of eye to posterior border of nostril; horizontal eye length (EL), distance between anterior and posterior corners of eyelid; maximum diameter of tympanum (TYD); forelimb length (FLL), from anterior junction of forelimb and body wall to tip of fourth finger, with limb held at right angles to body; hind-limb length (HLL), from anterior junction of hind limb and body wall to tip of fourth toe, with limb held at right angles to body.

Nomenclature of head scales follow Taylor (1935); among other meristic features of pholidosis, we examined the following characters, which showed variation in representatives of the *L. vittigera* species complex: frontonasal width greater than its length (FNW); prefrontals in contact or not (PFC); frontal in contact with which supraoculars (FSO); number of supraoculars (SOC); frontoparietal in contact with which supraoculars (FPS); number of nuchals (Ncl); number of supraciliaries (Scil); number of postsupraoculars (pretemporals) (PSPO); number of postsuboculars (PSBO); number of supralabials (SLab); number of supralabials immediately below eye (SLO); number

of infralabials (ILab); number of midbody scale rows (MSR); number of middorsal (vertebral) scales (MdS); number of ventrals in transverse rows (Vent); number of enlarged precloacals (PrCl); number of subdigital lamellae on fourth finger (SDL4F); number of subdigital lamellae on fourth toe (SDL4T); and number of light stripes on dorsum and flanks (LStr). Nomenclature of body coloration included description of dark and light markings on body and head, as shown in Figure 2: middorsal light stripe (MDLS); paravertebral dark stripes (PVDS); dorsolateral light stripe (DLLS); lateral dark stripe (LDS); lateral light stripe (LLS); ventrolateral dark stripe (VLDS); and dark temporal markings (DTM). Comparative material examined is listed in Appendix I. Sources of additional comparative data on character states and distribution of other species of *Lipinia* are from Bourret (2009); Brongersma (1942); Bucklitsch et al. (2012); Cochran (1930); Das (1997, 2010); Das & Austin (2007); de Rooij (1915); Grismer (2011b); Grismer et al. (2014, 2016); Günther (2000); Koch (2012); Loveridge (1948); Smith (1935); Taylor (1917, 1922); Werner (1910); and Zweifel (1979).

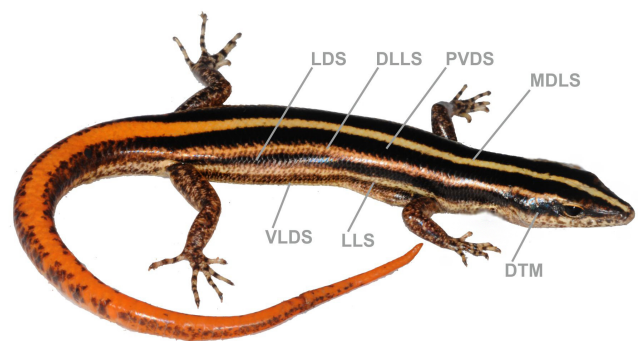


Figure 2 Terminology describing coloration of *Lipinia* used in present paper

Abbreviations: PVDS: Paravertebral dark stripe; DLLS: Dorsolateral light stripe; DTM: Dark temporal marking; LDS: Lateral dark stripe; LLS: Lateral light stripe; MDLS: Middorsal light stripe; PDS: Paravertebral dark stripes; VLDS: Ventrolateral dark stripe. Photo of *Lipinia microcercus* **stat. nov.** by Nikolay A. Poyarkov.

We examined all type specimens in the *L. vittigera* complex that were traceable in museum collections today. Museum abbreviations, where available, follow Leviton et al. (1985, 1988), including ZMMU, ZFMK, Field Museum of Natural History (FMNH), Chicago, USA; Senckenberg Museum Frankfurt (SMF), Germany; Museo Civico di Storia Naturale "Giacomo Doria" (MSNG), Genova, Italy; Institute of Ecology and Biological Resources (IEBR), Hanoi, Vietnam; University of Kansas, Museum of Natural History, Division of Herpetology (KU), USA; California Academy of Sciences, Department of Herpetology (CAS), USA; Museum of Vertebrate Zoology, University of California (MVZ), USA; and National Museum of Natural History, Division of Amphibians and Reptiles (USNM), USA. Other abbreviations include: Prov.: Province; Div.: Division; Dist.: District; Mt.: Mountain; NP: National park; WS: Wildlife sanctuary; NBCA: National Biodiversity and

Conservation Area.

One-way analysis of variance (ANOVA) was used for morphometric comparisons between species; a significance level of 95% was used for all statistical tests. Principal component analysis (PCA) was used to determine if the examined populations were separated from each other in morphospace and if this coincided with the mtDNA lineages recovered with molecular phylogenetic analysis. Sexes were analyzed together due to the small sample size for two out of the four analyzed lineages; juvenile specimens were excluded from analysis; a total of 30 specimens were included in the PCA. All meristic characters used in the PCA were log-transformed and scaled to their standard deviation prior to analysis to normalize their distribution and ensure characters with very large or very low values did not over-leverage the results due to intervariable nonlinearity and to ensure the data were analyzed based on correlation not covariance. Tail length (TaL) was excluded from the PCA as tails were broken or regenerated in many specimens. All other metric ($n=13$) and meristic ($n=16$) characters were subjected to PCA using Statistica v8.0 (StatSoft, Inc., 2007).

DNA isolation, polymerase chain reaction (PCR), and sequencing

Total genomic DNA was extracted from 95% ethanol-preserved muscle tissues using standard phenol-chloroform extraction protocols (Hillis et al., 1996). Total DNA concentration was estimated in 1 μ L using NanoDrop 2000 (Thermo Scientific, USA) and consequently adjusted to 100 ng DNA/ μ L.

We amplified 655 bp of cytochrome oxidase subunit I (*COI*), a mitochondrial barcoding marker widely used in vertebrates, including both reptiles and amphibians (Murphy et al., 2013; Nagy et al., 2012; Smith et al., 2008) and proven to be useful for species identification in various groups of lizards (Hartmann et al., 2013b; Nazarov et al., 2012, 2014; Neang et al., 2018; Solovyeva et al., 2011, 2018). Primers used for PCR and sequencing included ReptCOI-F (5'-TNTMTCAACNAAC CACAAAGA-3') and ReptCOI-R (5'-ACTTCTGGRTGKCCAA RAATCA-3') (Nagy et al., 2012). The PCR assays were performed in 25 μ L reactions using 50 ng of genomic DNA, 10 pmol of each primer, 15 nmol of each dNTP, 50 nmol additional $MgCl_2$, Taq PCR buffer (10 mmol/L Tris-HCl, pH 8.3, 50 mmol/L KCl, 1.1 mmol/L $MgCl_2$, and 0.01% gelatin), and 1 U of Taq DNA polymerase. The PCR conditions included an initial denaturation step of 5 min at 95 °C, 5 cycles of denaturation for 1 min at 94 °C, primer annealing for 40 s at 45 °C, and extension for 1 min at 72 °C, 30 cycles of denaturation for 1 min at 94 °C, primer annealing for 40 s at 53 °C, and extension for 1 min at 72 °C, and a final extension step for 5 min at 72 °C. The PCR products were visualized by agarose electrophoresis in the presence of ethidium bromide and purified using 2 μ L from a 1:4 dilution of ExoSapIt (Amersham, UK) per 5 μ L of PCR product prior to cycle sequencing. The obtained fragments were sequenced in both directions for each sample, and a consensus sequence was generated. Sequencing was performed in both directions

using the same primers as used in PCR on an ABI3730xl Automated Sequencer (Applied Biosystems, USA) in Evrogen Inc., Moscow. The newly obtained sequences were aligned and deposited in GenBank under the accession Nos. MK463827–MK463852, MK843792–MK843793, and GU657766–GU657767 (Supplementary Table S1). Sequences of three other *Lipinia* species used for comparisons were obtained from GenBank (Supplementary Table S1).

Phylogenetic analyses

The *COI* gene fragment was applied in the present study mainly as a barcoding marker for species identification rather than a tool for reconstructing phylogenetic relationships among species. Information on voucher specimens and GenBank accession Nos. used in phylogenetic analyses are summarized in Supplementary Table S1. In total, 58 *COI* fragment sequences of Scincidae, including 53 sequences of *Lipinia* spp. (including 25 sequences representing target *L. vittigera* species complex) and sequences of outgroup taxa, including representatives of scincid genera *Lygosoma*, *Eutropis*, *Tropidophorus*, *Sphenomorphus*, and *Eumeces* were included in the final alignment with a total length of 681 bp. Nucleotide sequences were initially aligned in the program MAFFT v6 (Kato et al., 2002) with default parameters, and then checked by eye in BioEdit 7.0.5.2 (Hall, 1999) and slightly adjusted. Mean uncorrected genetic distances (*P*-distances) between sequences were calculated with MEGA 7.0 (Kumar et al., 2016).

Matrilineal genealogy was inferred using Bayesian inference (BI) and maximum likelihood (ML) algorithms. We conducted BI analysis in MrBayes 3.1.2 (Huelsenbeck & Ronquist, 2001; Ronquist & Huelsenbeck, 2003). The dataset was divided into three codon-partitions of the *COI* gene; MODELTEST v.3.06 (Posada & Crandall, 1998) was used to estimate the optimal evolutionary models for each partition. The best-fitting model selected for the *COI* dataset was GTR+Gamma for the first and third codon positions and HKY+I for the second codon position. Metropolis-coupled Markov chain Monte Carlo (MCMCMC) analyses were run with one cold chain and three heated chains for twenty million generations, with sampling every 2 000 generations. Five independent MCMCMC runs were performed and 1 000 trees were discarded as burn-in. Stationarity from each run was checked using TRACER v1.6 (Rambaut & Drummond, 2007) to ensure an effective sample size (ESS) above 200 for all parameters.

The ML analysis was conducted using RAXML (<http://embnet.vital-it.ch/raxml-bb/>; Stamatakis et al., 2008), with the ML trees searched using default priors and the GTR+Gamma model of evolution for all codon positions. Confidence in node topology was tested by posterior probability (PP) for BI trees (Huelsenbeck & Ronquist, 2001) and by non-parametric bootstrapping with 1 000 replicates (ML BS, see Felsenstein, 1985) for ML trees. We *a-priori* regarded tree nodes with bootstrap (ML BS) values of $\leq 70\%$ and Bayesian posterior probabilities (BI PP) values >0.95 as sufficiently resolved; ML BS values between 70% and 50% (BI PP between 0.95 and 0.90) were treated as tendencies and nodes with ML BS

values below 50% (BI PP below 0.90) were regarded as unresolved (Felsenstein, 2004; Huelsenbeck & Hillis, 1993).

RESULTS

Genetic differentiation of Indochinese *Lipinia*

Sequence data: The final alignment of the *COI* gene contained 681 aligned characters, including 422 conserved sites and 257 variable sites, of which 252 were parsimony-informative. The transition-transversion bias (R) was

estimated as 1.577 (all data given for ingroup only). Nucleotide frequencies were 22.72% (A), 28.92% (T), 27.86% (C), and 20.50% (G).

Genetic diversity and geographic distribution of mtDNA

haplotypes: The phylogenetic analysis results of the examined *Lipinia* species are presented in Figure 3. We also calculated a tree with more outgroup taxa, representing different groups of lygosomine skinks (Supplementary Figure S1).

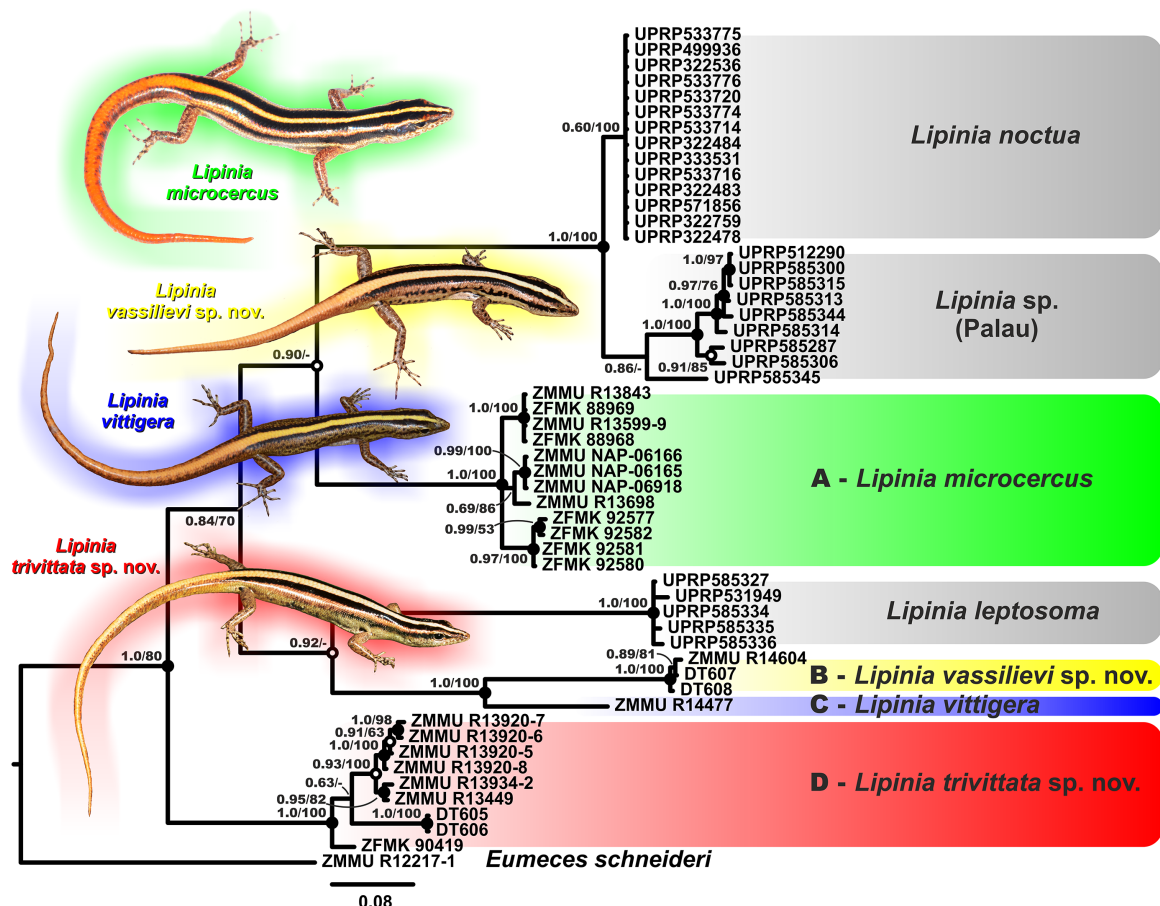


Figure 3 Bayesian inference tree of *Lipinia* derived from analysis of 681 bp of partial *COI* gene sequences

Voucher specimen information and GenBank accession Nos. are listed in Supplementary Table S1. Colors of boxes and thumbnails are consistent with those on map (see Figure 1). Numbers at tree nodes correspond to BI PP/ML BS support values, respectively. Photos by Nikolay A. Poyarkov, Evgeniy A. Dunayev, Eduard A. Galoyan, and Vitaly L. Trounov.

Both the BI and ML phylogenetic analyses resulted in essentially similar topologies. Phylogenetic relationships within the genus *Lipinia* remained fundamentally unresolved in our analyses, whereas monophyly of species-level groups was highly supported (1.0/100, hereafter node support values are given for BI PP/ML BS, respectively) (Figure 3). In the additional analysis involving more outgroup taxa, monophyly of the genus *Lipinia* was not supported, and all higher-level taxonomic relationships between this genus and other

lygosomine skink genera (i.e., *Lygosoma*, *Eutropis*, *Tropidophorus*, and *Sphenomorphus*) remained unresolved (Supplementary Figure S1). Monophyly of the *L. vittigera* species complex was not supported in either analysis (Figure 3; Supplementary Figure S1).

Our analyses revealed unexpectedly high genetic diversity within the Indochinese *Lipinia* skinks, contradicting current taxonomy of the group. In Indochina, four major mtDNA lineages were recovered (lineages A–D; see Figure 3 for

phylogenetic tree and Figure 1 for geographic distribution of revealed lineages):

(1) Lineage from southern peninsular Thailand (Surat Thani Province), corresponding to *L. vittigera sensu stricto* (see below) (lineage C, see Figure 3).

(2) Lineage from Kon Tum Province of Vietnam and adjacent part of Ratanakiri Province of Cambodia, corresponding to the spotted form of *L. cf. vittigera* (lineage B, see Figure 3). This lineage forms a well-supported clade with *L. vittigera sensu stricto* lineage C from southern Thailand (1.0/100).

(3) Lineage recorded from lowland and hilly areas of central and southern Vietnam, as well as from across Cambodia, five-striped form specimens, corresponding to the traditionally recognized subspecies *L. v. microcercus* (lineage A, see Figure 3).

(4) Lineage recorded from hilly areas in southern Vietnam and Cambodia, corresponding to the three-striped form of *L. cf. vittigera* (lineage D, see Figure 3).

The three mtDNA lineages of *L. cf. vittigera* recorded from Indochina, north of the Isthmus of Kra, correspond to distinct morphotypes and color forms and were never recorded in the same biotope. However, their ranges appear largely overlapping (see Figure 1) and the geographic distance between two localities where different mtDNA lineages/morphotypes occur is as little as 15 km (e. g., between localities 11 and 22 in Figure 1). While the five-striped form (lineage A, *L. v. microcercus*) widely occurs in southern Indochina from the central Annamites to southern Vietnam and Cambodia (possibly also penetrating into Thailand), the three-striped form (lineage D) is confined to hilly areas of southern Annam (Langbian Plateau), Cambodia, southernmost Vietnam (and possibly southeast Thailand), whereas the spotted form (lineage B) is restricted to a narrow area in the central Annamites on the border of Vietnam and Cambodia (Figure 1).

Genetic distances: The uncorrected *P*-distances among and within the studied mtDNA fragments for the examined *Lipinia* species are shown in Supplementary Table S2. Intraspecific genetic distances in all examined species were below the level $P=3.5\%$ (in the three-striped form, lineage D). The interspecific uncorrected genetic *P*-distances between *Lipinia* species varied from 7.1% (between *L. noctua* (Lesson) and *Lipinia* sp. from Palau) to 23.4% (between *Lipinia* sp. from Palau and spotted form, lineage B). Genetic differentiation among the four lineages of *L. vittigera sensu lato* from Indochina was surprisingly high and varied from 15.5% (between lineages B and C) to 20.4% (between lineages B and D). This degree of pairwise divergence is high, notably greater than the genetic divergence observed between many recognized species of Scincidae (e. g., Murphy et al., 2013; Nagy et al., 2012; Neang et al., 2018; Okamoto & Hikida, 2012).

Systematics

Recent study demonstrated that the genus *Lipinia* likely does

not represent a monophyletic group, but rather is an assemblage of distantly related sphenomorphine skinks (Grismer et al., 2016; Linkem, 2013). Reconstructing phylogenetic relationships among members of the *Lipinia* assemblage would require much broader taxon sampling and a multilocus approach combining data from several mtDNA and nuDNA markers. In the present paper, we applied COI DNA-barcoding, which is a useful tool for uncovering cryptic diversity in squamate reptiles, including members of the family Scincidae. We did not aim to discuss phylogenetic relationships of Indochinese *Lipinia* or use COI-barcoding solely for assessment of their genetic diversity and distribution of mtDNA lineages.

The four mtDNA lineages revealed within the *L. vittigera* species complex were highly divergent, with uncorrected genetic distances exceeding $P=15.5\%$. The PCA results corroborated these findings and indicated that each mtDNA lineage occupies a unique position in morphospace that did not overlap with any other species in the ordination of the first two principle components (PC) (Figure 4). PC1 accounted for 28.24% of the variation in the dataset, with loading for snout-tympanium length, snout-forelimb length, head width, head height, and snout-vent length, whereas PC2 accounted for an additional 16.05% of the variation, with loading for frontonasal width, snout length, number of light stripes on dorsum and flanks, and head length (Figure 4; Supplementary Table S3). These results suggest deep differentiation of the four Indochinese lineages of *Lipinia* skinks, not only in genetic, but also in morphological characters. Additional differences in morphological and color characters not amenable to statistical analyses are discussed in the comparison sections of each species and summarized in Table 1.

The data on genetic divergence, together with congruent

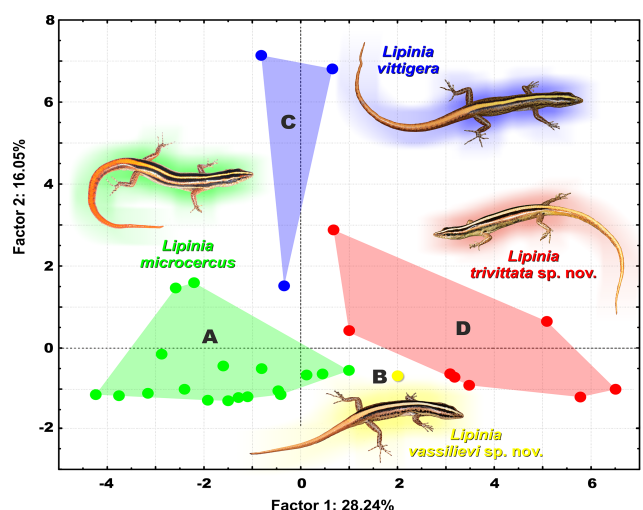


Figure 4 Two-dimensional plots of first two factors of principal component analysis (PCA) with convex hull polygons showing morphospacial relationships of species in the *Lipinia vittigera* species complex (Photos by Nikolay A. Poyarkov, Evgeniy A. Dunayev, Eduard A. Galoyan, and Vitaly L. Trounov)

Table 1 Morphological comparison between *Lipinia vittigera* species complex members found in Indochina and adjacent territories

Character	<i>Lipinia vittigera</i> s. str.	<i>Lipinia microcercus</i> stat. nov.	<i>Lipinia trivittata</i> sp. nov.	<i>Lipinia vassilievi</i> sp. nov.
SVL	35.5–37.8	30.1–41.9	31.0–44.4	39.4
TaL/SVL	–	0.98–1.65	0.81–1.55	1.04
TrunkL/SVL	0.41–0.47	0.44–0.54	0.44–0.51	0.47
SL/SVL	0.15–0.16	0.09–0.16	0.09–0.17	0.11
STL/SVL	0.25	0.21–0.26	0.21–0.26	0.25
SFIL/SVL	0.40–0.45	0.34–0.44	0.39–0.43	0.41
FLL/SVL	0.23–0.24	0.19–0.36	0.25–0.35	0.33
HLL/SVL	0.29–0.30	0.24–0.43	0.28–0.45	0.44
Frontonasal (W>L)	No	Yes	Yes	Yes
Prefrontals in contact	No or slightly	Yes	Yes or slightly	Yes
Frontal contacting supraoculars	1+2+3	1+2 or 1+2+3	1+2 or 1+2+3	1+2
Frontoparietals contacting supraoculars	3+4	3+4	3+4	3+4
Supraciliaries	7	6–9	7–9	10–11
MSR	30–32	28–32	28–32	28
MDSR	48–52	48–58	48–58	56
Ventrals	56	54–66	56–70	66
Subdigital lamellae on 4th finger	15–16	18–21	20–26	14–15
Subdigital lamellae on 4th toe	22–25	24–32	29–33	19–21
Dark temporal markings	Black mottling or irregular spots	Wide black stripe, at least two times wider than DLLS	Narrow black stripe ca. same width as DLLS	Narrow black stripe ca. same width as DLLS
Middorsal light stripe (MDLS)	Wide, 2-scales wide	Narrow, 1-scale wide	Wide, 2-scales wide	1–2-scales wide
Paravertebral dark stripes (PDS)	Subequal to MDLS, continuing on tail	Wider than MDLS, continuing on anterior 3/4 of tail	Subequal to MDLS, not continuing on tail	Subequal to MDLS, not continuing on tail
Dorsolateral light stripe (DLLS)	Indistinct	Distinct with regular borders, 1-scale wide	Distinct on head and anterior 1/3 of body	Distinct, with irregular borders; 2-scales wide
Lateral dark stripe (LDS)	Absent, irregular dark mottling	Always distinct, broad: 2–3-scales wide, running from temporal area to anterior 3/4 of tail, forming row of ocelli	Narrow: 1-scale wide, starting in temporal area and becoming indistinct in first 1/2 of body	Irregular row of dark ocelli running from temporal area to groin
Lateral light stripe (LLS)	Indistinct	Distinct with regular borders, 1-scale wide	Indistinct	Wide stripe (2–3-scales wide) with poorly defined borders
Ventrolateral dark stripe (VLDS)	Absent	Narrow (1-scale wide) stripe or row of dark ocelli between axilla and groin	Absent	Distinct row of dark ocelli from lower jaw to axilla continuing to groin

For character abbreviations see “Materials and Methods”. –: Not available.

differentiation of mtDNA lineages in morphospace revealed by PCA and other morphological differences compiled below, support our hypothesis that at least four distinct species, as described in the following taxonomic accounts, should be recognized within the Indochinese members of the *L. vittigera* species complex, two of which appear to be new to science.

Lipinia vittigera sensu stricto (= *Lygosoma vittigerum*) (Boulenger, 1894)
Figures 5A–B, 7A–B, 8–9; Tables 1, 2.

Chresonymy

Lygosoma vittigerum Boulenger, 1894, p. 615; Sworder, 1933, p. 102;

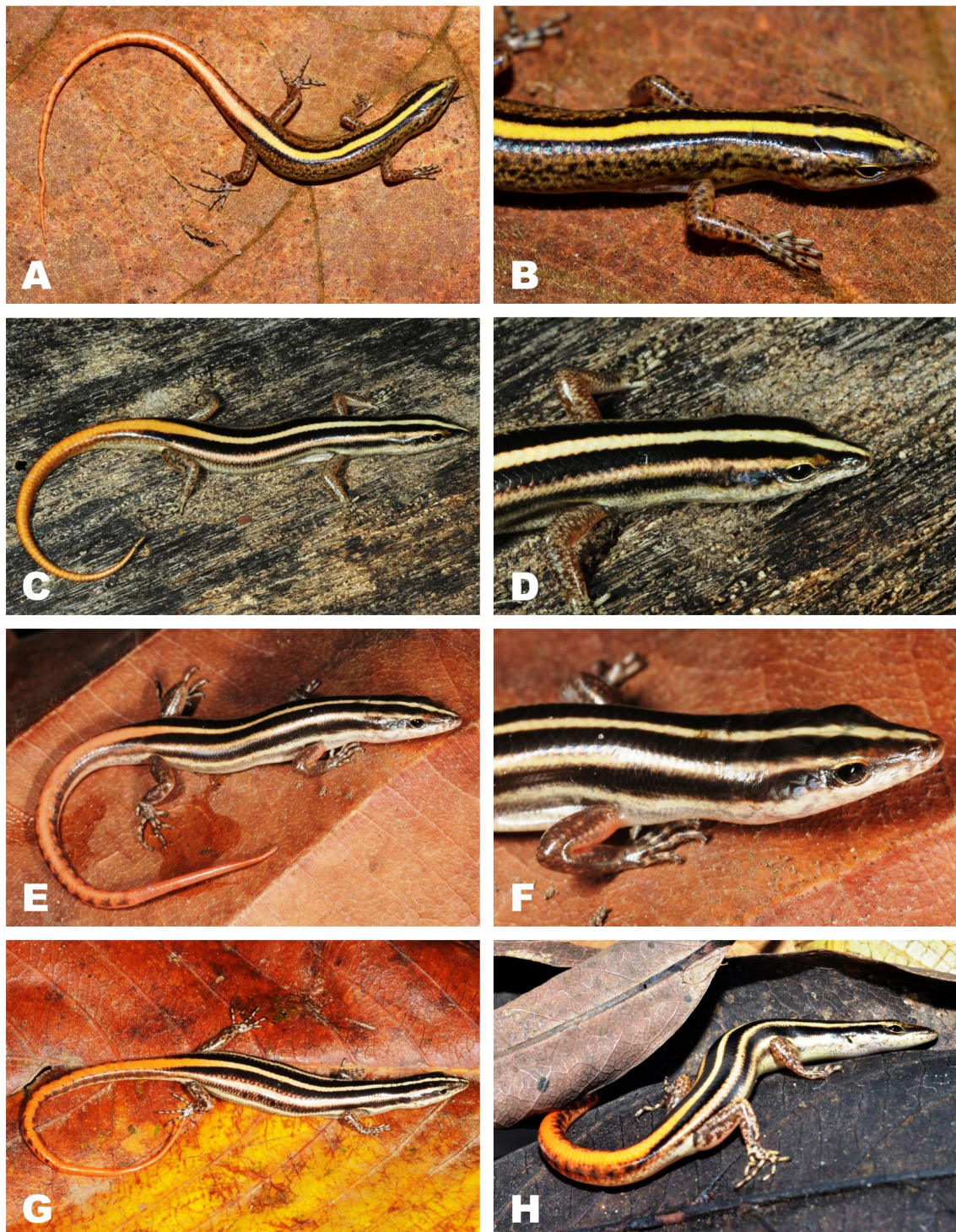


Figure 5 Photos of Indochinese *Lipinia* species in life (part I)

Lipinia cf. *vittigera*: General view (A) and head dorso-lateral view (B) of male (ZMMU R14477, Phanom Dist., Surat Thani, Thailand); *Lipinia microcercus* **stat. nov.**: General view (C) and head dorso-lateral view (D) of male (ZMMU NAP-06918, Buon Luoi, Gia Lai, Vietnam); General view (E) and head dorso-lateral view (F) of male (ZMMU R13698, Yok Don, Dak Lak, Vietnam); G: General view of male (ZMMU NAP-06165, Kon Ka Kinh, Gia Lai, Vietnam); H: General view of male from Kirirom NP, Kampong Speu, Cambodia. Photos A–B and H by Evgeniy A. Dunayev; C–G by Nikolay A. Poyarkov.

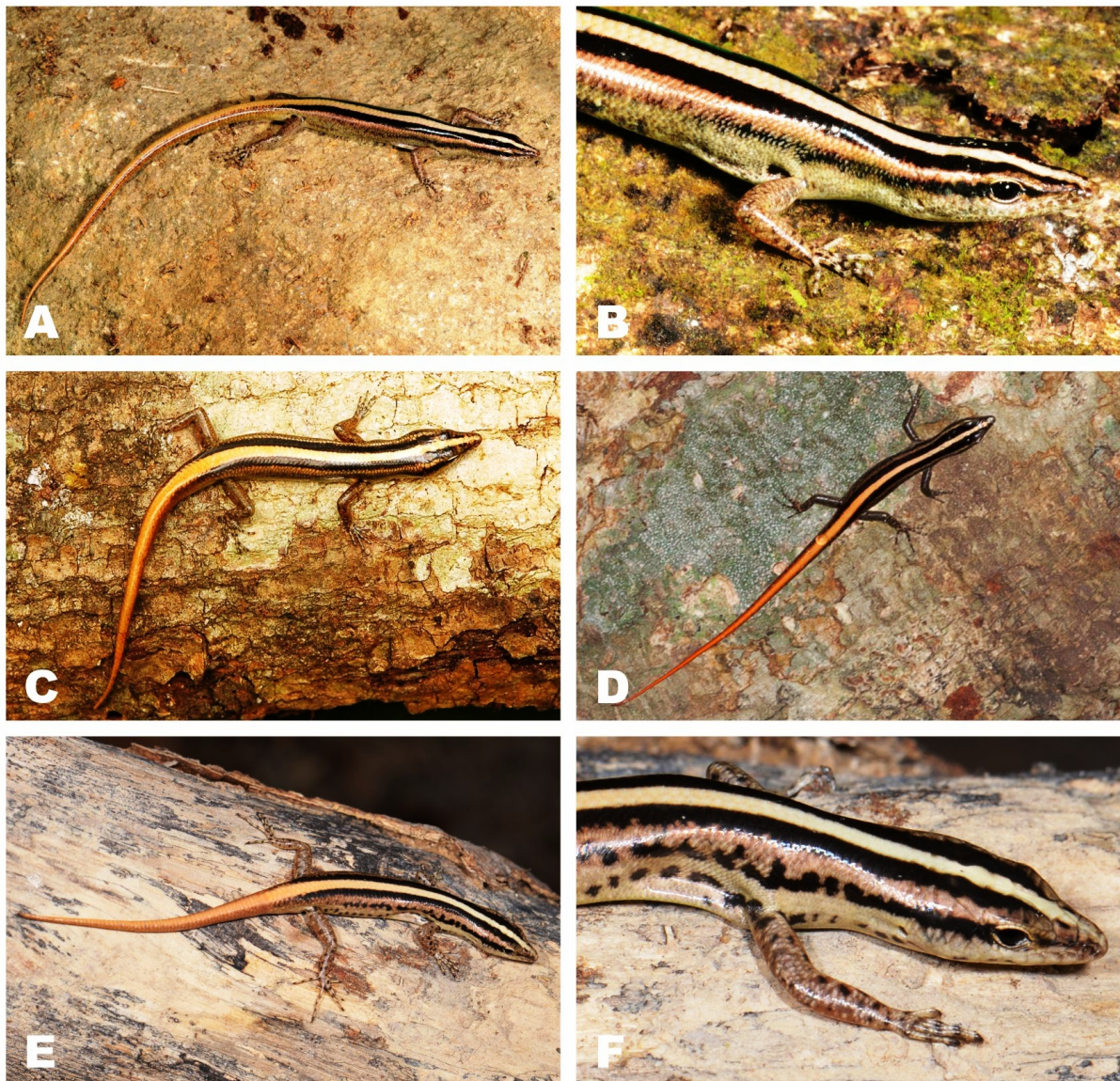


Figure 6 Photos of Indochinese *Lipinia* species in life (part II)

Lipinia trivittata sp. nov.: General view (A) and head dorso-lateral view (B) of female holotype (ZMMU R13920-58, Chu Yang Sin NP, Dak Lak, Vietnam); C: Dorsal view of male paratype (ZMMU R13449, Bu Gia Map NP, Binh Phuok, Vietnam); D: Adult specimen from Khao Soi Dao NP, Chanthaburi, Thailand (tentative identification); *Lipinia vassilievi* sp. nov.: General view (E) and head dorso-lateral view (F) of male holotype (ZMMU R14604, Chu Mom Ray NP, Kon Tum, Vietnam). Photos A–B by Eduard A. Galoyan; C by Nikolay A. Poyarkov; D by David Sargeant (North Thailand Birding); E–F by Vitaly L. Trounov.

Leiopisma vittigerum — Barbour, 1912, p. 187;

Leiopisma vittigerum vittigerum — Smith, 1935, p. 306; Taylor, 1963, p. 1029; Bourret, 2009, p. 274;

Lygosoma (Leiopisma) vittigerum — Smith, 1937, p. 224;

Lygosoma (Scincella) vittigerum vittigerum — Grandison, 1972, p. 82;

Lipinia vittigera — Greer, 1974, p. 11; Manthey & Grossmann, 1997, p. 266; Cox et al., 1998, p. 116; Grismer et al., 2002, p. 27; Pauwels et al., 2003, p. 28; Nguyen et al.,

2005, p. 59; Das & Austin, 2007, p. 66; Grismer, 2011a, p. 149; Grismer, 2011b, p. 606; Chan-ard et al., 2015, p. 111;

Lipinia cf. *vittigera* — Teo & Rajathurai, 1997, p. 415;

Lipinia vittigera (?) — Onn et al., 2010, p. 140;

Lipinia vittigera vittigera — Das, 2010, p. 237; Grossmann, 2010, p. 2; Bucklitsch et al., 2012, p. 325.

Lygosoma vittigerum — Grismer, 2011b, p. 606 (ex errore).

Holotype: MSNG 55855, adult male (Figure 8), collected by

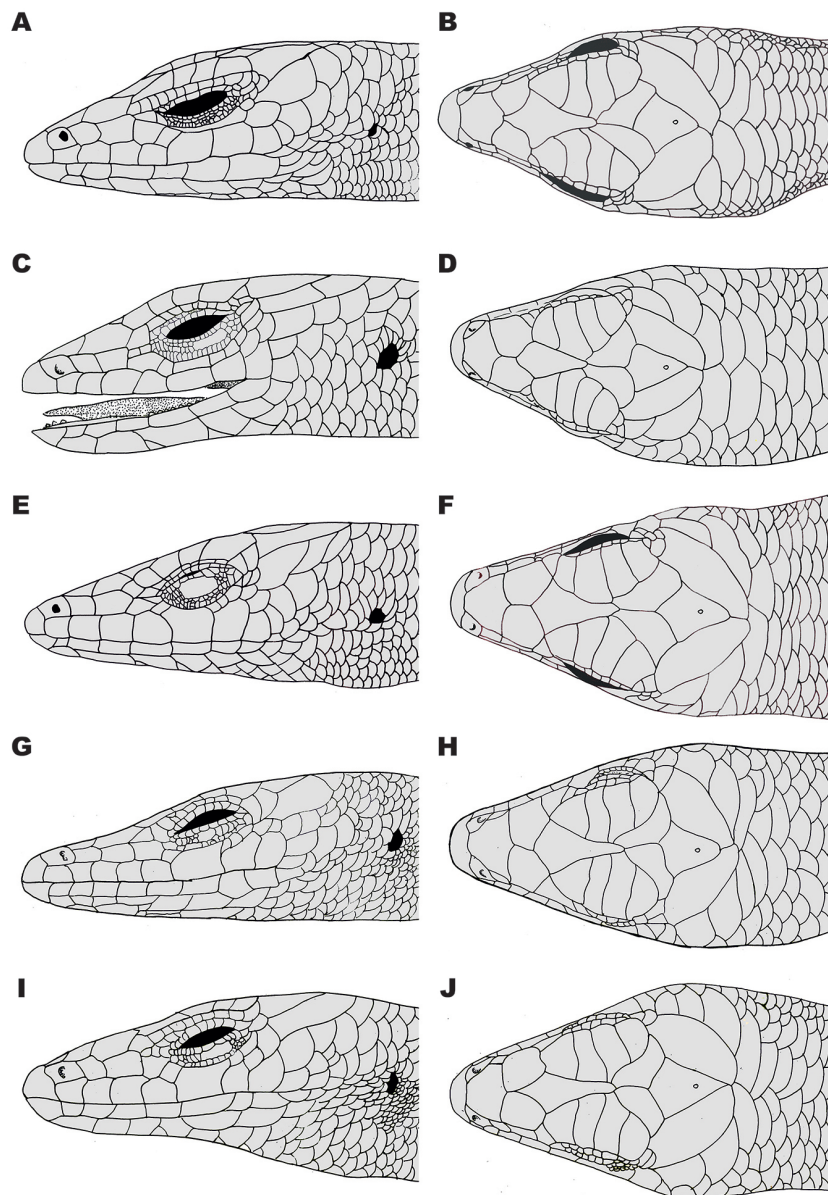


Figure 7 Head pholidosis of holotype specimens of Indochinese *Lipinia* in lateral (left) and dorsal (right) aspects

A, B: Holotype of *Lygosoma vittigerum* Boulenger, 1894 (MSNG 55855, male); C, D: Holotype of *Leiolopisma pranensis* Cochran, 1930 (USNM75591, male); E, F: Holotype of *Lygosoma microcerum* Boettger, 1901 (SMF 14593); G, H: Holotype of *Lipinia trivittata* **sp. nov.** (ZMMU R13920-58, female); I, J: Holotype of *Lipinia vassilievi* **sp. nov.** (ZMMU R14604, male). Drawings by Peter Geissler.

Elio Modigliani from Sereinu (=Sipora), Mentawai, Sumatra (Indonesia) (Figure 1, locality 1). A re-description of the holotype was published by Bucklitsch et al. (2012).

Paratypes: None.

Diagnosis: Based on the holotype, additional specimens examined from Penang (Malaysia) and peninsular Thailand (Appendix I) as well as literature data from peninsular Malaysia and Singapore (Grismer, 2011b): small (SVL to

44 mm) species of *Lipinia*, differentiated from congeners by the following combination of external traits: external ear opening present; lower eyelid bearing large transparent spectacle; 28–30 midbody scale rows; 48–56 middorsal scales between parietals and point above vent; 15–16 subdigital lamellae under finger IV; 20–26 lamellae under toe IV; prefrontals in punctiform or broad contact; seven supralabials, seven infralabials; broad middorsal light stripe from snout tip to tail base; two paravertebral dark stripes from

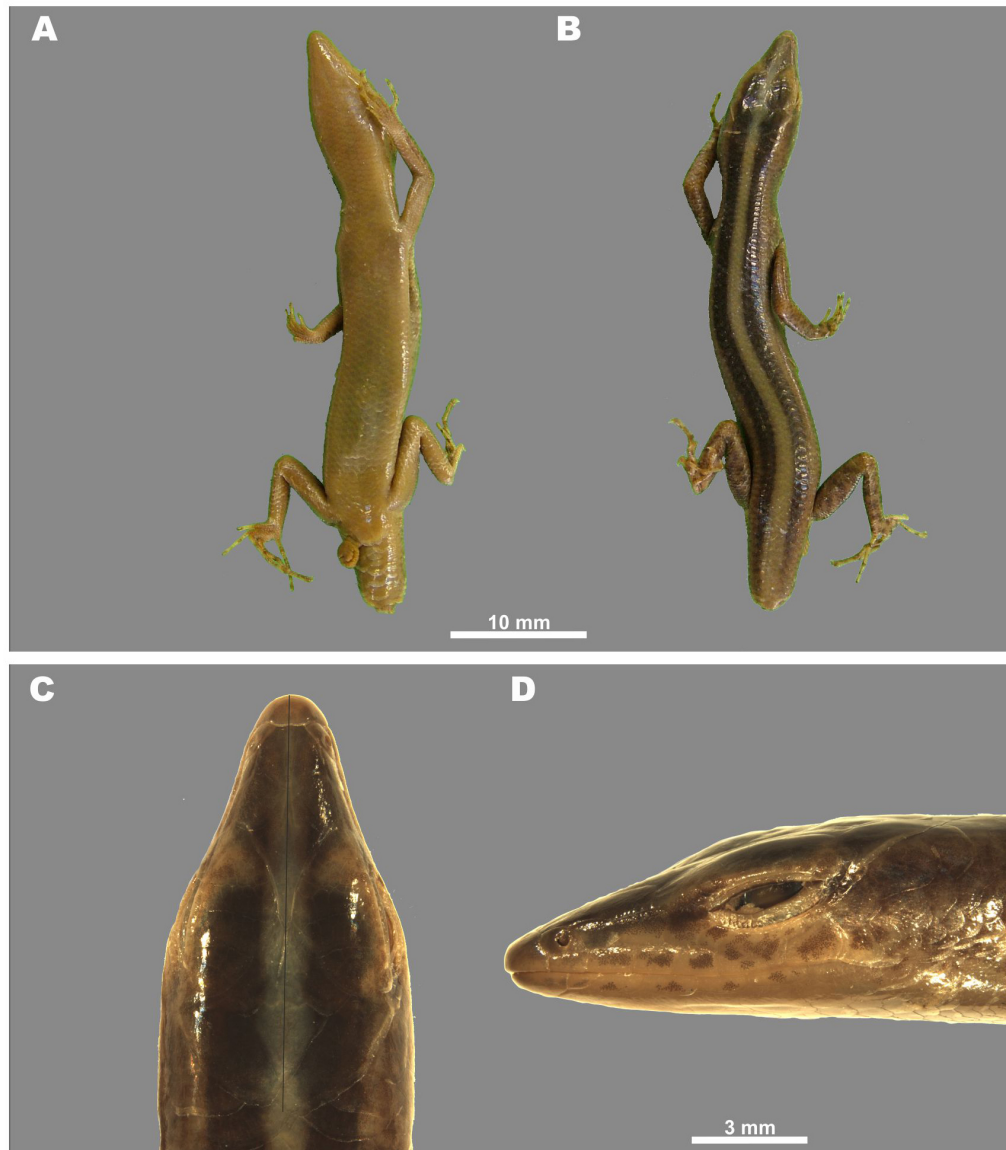


Figure 8 Holotype of *Lygosoma vittigerum* Boulenger, 1894 (MSNG 55855, male) in preservative

A: General ventral view; B: General dorsal view; C: Head dorsal view; D: Head lateral view. Photos by Giuliano Doria and André Koch.

supraoculars toward tail, continuing on anterior part of tail; flanks dotted brown, without any distinct dark or light stripes.

Etymology: Although not stated by Boulenger (1894), the species name "*vittigerum*" is derived from Latin "*vitta*" for a head band used by Roman priests during rituals and "*gero*" (to wear), as a reference to the banded dorsal pattern of this species. Due to the feminine gender of the genus name *Lipinia*, the species epithet has to be adapted to "*vittigera*".

Description of holotype: Measurements and counts of holotype are presented in detail in Table 2. Head scalation of holotype is detailed in Figure 7A–B.

SVL 36.9 mm (Figure 8), TaL 4.5 mm, largest parts

missing. Snout acute, SL 4.1 mm; nostrils oriented laterally, oval, situated closer to snout tip than to orbit, END 3.0 mm; head elongated, HL 10.1 mm, HW 4.8 mm, HL/HW ratio 2.1, flattened, HH 3.4 mm, HL/HH ratio 3.0; rostral broad, visible in dorsal view (Figure 7A–B); frontonasal almost as wide as long; frontal elongated, arrow-shaped, wider anteriorly; prefrontals large, not in contact medially, laterally and posteriorly in contact with loreals, first presupraocular, first supraocular, frontal and frontonasal; two frontoparietals in broad median contact; interparietal arrow-shaped, wider anteriorly; parietals in contact behind interparietal, anteriorly in contact with postsupraoculars, fourth supraocular, nuchals, and frontoparietals; seven nuchals; four supraoculars; three

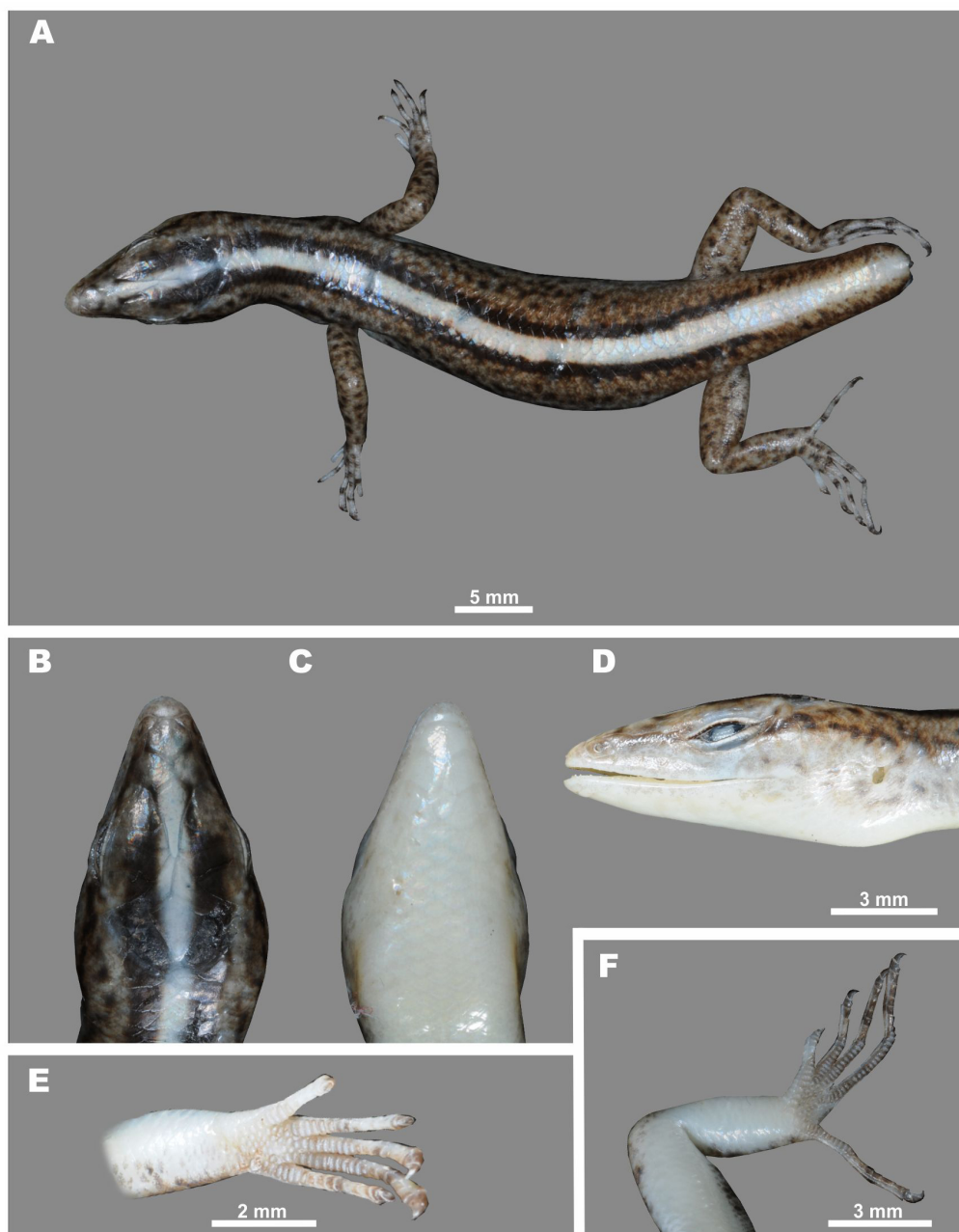


Figure 9 Specimen of *Lipinia* cf. *vittigera* (Boulenger, 1894) (ZMMU R14477, male) in preservative

A: General dorsal view; B: Head dorsal view; C: Head ventral view; D: Head lateral view; E: Left forelimb in volar view; F: Left hindlimb in thenar view. Photos by Nikolay A. Poyarkov.

presupraoculars, visible from above; seven supraciliaries; nostrils located within nasals; postnasal absent; two loreals, slightly elongated, second longer than first; two enlarged presuboculars, separating supralabials III and IV from eye; seven supralabials, supralabial V largest, in contact with orbit; two postsuboculars, separating supralabial VI from orbit; seven postsupraoculars (pretemporals); one primary temporal; two secondary temporals, dorsal largest; two

postsupralabials; lower eyelid bearing large transparent window; scales on upper row of lower eyelid small, 14 in number; mental wider than long; one postmental, in contact with first infralabial and anterior portion of second infralabial; seven infralabials; three pairs of chinshields, first pair in contact medially, second pair separated by one scale, third pair separated by three scales; external ear opening visible and subcircular (Figure 7A–B).

Table 2 Morphometric and meristic data of examined specimens of *Lipinia vittigera* species complex of Indochina and adjacent territories (All measurements are in mm)

No.	Species/Specimen	Sex	SVL	TaL	TrunkL	SVL/TL	HL	HW	HH	SL	STL	SFIL	END	EL
<i>Lipinia vittigera</i>														
1	MSNG 55855–holotype	M	37.8	5.4*	15.5	–	10.8	4.9	3.5	6.2	9.6	15.1	3.9	1.9
2	ZFMK 48542	M	35.5	–*	16.6	–	9.6	4.5	3.0	5.4	9.0	15.9	2.4	2.0
3	ZMMU R-14477	M	35.8	8.3*	17.8	–	7.6	4.7	3.7	3.8	8.6	15.5	1.9	2.1
<i>Lipinia microcercus</i> stat. nov.														
4	SMF14593–holotype	M	41.9	44.5	22.8	94.2%	9.8	5.1	3.3	6.2	8.6	14.2	2.5	2.2
5	ZFMK 90339	Juv.	19.6	18.8*	9.2	–	6.0	2.9	1.8	3.2	4.9	8.4	1.2	1.3
6	ZMMU R-10962	M	39.3	12.4*	18.5	–	8.0	4.8	3.3	3.7	8.6	14.7	2.3	1.7
7	ZFMK 88968	M	34.9	15.7*	15.5	–	8.5	4.8	3.1	5.5	7.9	13.9	2.5	1.8
8	ZFMK 88869	F	34.1	21.8*	16.3	–	8.7	4.6	3.6	4.9	7.5	13.6	2.5	2.0
9	ZMMU R-11475-1	F	34.6	46.9	16.9	73.8%	7.6	5.1	3.3	3.5	8.0	13.4	2.4	1.6
10	ZMMU R-11475-2	Juv.	19.9	28.3	9.2	70.2%	4.7	3.1	2.1	2.0	4.9	8.8	1.4	1.3
11	ZMMU R-11475-3	Juv.	21.6	35.8	10.3	60.2%	5.5	3.5	2.4	2.3	5.6	9.7	1.5	1.3
12	ZMMU R-13599-9	M	36.5	43.2	17.2	84.5%	8.1	5.0	3.6	3.5	8.1	14.3	2.2	1.8
13	ZMMU R-13599-74	M	38.3	6.3*	18.1	–	9.3	6.1	4.1	4.3	10.0	16.7	3.0	2.4
14	ZMMU R-07528	M	33.4	55.0	16.5	60.8%	7.1	4.7	3.2	3.2	7.4	11.6	2.0	1.9
15	ZMMU R-13337	M	34.2	4.1*	15.7	–	7.5	4.9	3.2	3.5	7.7	14.4	2.0	2.2
16	ZMMU R-13843	F	31.6	4.7*	16.1	–	6.7	4.0	2.6	2.8	6.9	12.6	2.1	1.9
17	ZMMU R-08319	F	31.2	47.9	14.4	65.2%	6.9	4.4	2.7	3.5	7.5	13.2	2.1	2.0
18	ZMMU R-11184	F	30.1	47.3	13.9	63.6%	7.4	4.1	2.7	3.1	7.1	12.4	2.2	1.9
19	ZMMU R-11165	Juv.	26.3	43.6	12.0	60.2%	6.0	3.6	2.5	2.9	6.5	11.5	2.0	1.7
20	ZMMU R-11178	Juv.	24.9	44.5	11.7	56.0%	6.3	3.7	2.5	2.6	6.3	11.3	2.0	1.6
21	ZMMU R-13698	F	33.9	49.9	16.7	67.9%	7.3	5.0	3.4	3.4	8.1	13.9	2.0	1.7
22	ZMMU NAP-04318	F	34.0	43.3	16.5	78.5%	8.2	5.1	3.7	3.5	8.0	13.9	2.3	1.8
23	ZMMU R-04613-1	F	37.5	58.6	17.0	64.1%	8.1	5.0	3.2	4.0	8.5	15.6	2.7	2.1
24	ZMMU R-04613-2	M	37.0	54.9	17.5	67.5%	8.2	4.8	3.1	3.8	8.4	15.3	2.5	1.9
25	ZMMU R-04613-3	M	37.7	28.1*	18.0	–	8.8	5.2	3.6	4.1	9.1	15.9	2.7	2.0
26	ZMMU R-04613-4	M	36.4	47.4	17.8	76.7%	8.1	4.7	3.0	3.7	7.6	14.2	2.3	2.0
<i>Lipinia trivittata</i> sp. nov.														
27	ZMMU R-13920-58–holotype	F	44.4	59.3	22.4	74.9%	9.2	5.3	3.6	4.2	9.4	17.3	2.5	2.0
28	ZMMU R-13449	M	42.0	46.6	21.4	90.2%	9.4	7.1	5.0	4.6	11.0	18.7	3.6	2.4
29	ZMMU R-13934-112	M	42.7	34.8	20.2	122.9%	10.0	6.3	4.3	4.7	10.7	17.4	3.2	2.3
30	ZMMU R-13934-101	Juv.	20.0	33.1	8.8	60.5%	4.8	3.2**	1.3**	1.8**	5.3**	9.3**	N/A**	N/A**
31	ZMMU R-13920-56	M	43.6	17.8*	20.4	–	9.7	6.4	4.6	4.6	10.7	18.4	2.8	2.2
32	ZMMU R-13920-57	M	32.0	41.4	15.4	77.2%	6.9	4.1	2.8	3.2	7.6	13.2	2.2	1.7
33	ZMMU R-13920-55	M	40.7	20.6*	18.8	–	9.5	5.8	4.3	4.2	10.0	16.2	2.6	2.0
34	ZMMU R-15199	M	31.8	52.3	15.8	60.8%	7.8	4.9	3.3	3.7	8.2	15.6	2.4	2.0
35	ZFMK 90419	M	39.7	39.1	20.4	101.5%	9.7	4.7	3.2	5.0	8.6	15.3	3.8	1.9
<i>Lipinia vassilievi</i> sp. nov.														
36	ZMMU R-14604–holotype	M	39.4	40.9	18.7	96.5%	9.1	6.1	4.3	4.4	9.8	16.1	3.1	2.6

													Continued
No.	Species/Specimen	TYD	FLL	HLL	FNW	PFC	FSO	SOC	FPS	Ncl	Scil	PSPO	PSBO
<i>Lipinia vittigera</i>													
1	MSNG 55855–holotype	0.4	8.9	10.9	N	N	1+2+3	4	3+4	4/3	7/7	6	2
2	ZFMK 48542	0.5	8.0	10.7	N	S	1+2+3	4	3+4	3/3	7/7	6	2
3	ZMMU R-14477	0.8	12.6	16.2	Y	Y	1+2	4	3+4	3/3	11/11	6	2
<i>Lipinia microcercus</i> stat. nov.													
4	SMF14593–holotype	0.6	8.0	10.5	Y	Y	1+2+3/1+2	4	3+4	3/3	7/7	6	2
5	ZFMK 90339	0.4	4.1	5.4	Y	Y	1+2+3	4	3+4	3/3	7/7	6	3
6	ZMMU R-10962	0.6	12.0	14.8	Y	Y	1+2	4	3+4	4/3	8/9	6	2
7	ZFMK 88968	0.6	7.4	9.5	Y	Y	1+2+3	4	3+4	3/3	7/7	6	3
8	ZFMK 88869	0.5	6.3	8.2	Y	Y	1+2	4	3+4	3/3	7/7	6	3
9	ZMMU R-11475-1	0.7	9.1	13.5	Y	Y	1+2	7/4	5+6+7/3+4	3/3	8/8	6	2
10	ZMMU R-11475-2	0.4	6.3	7.6	Y	Y	1+2	4	3+4	3/3	8/8	6	2
11	ZMMU R-11475-3	0.5	7.0	9.8	Y	Y	1+2	4	3+4	3/3	8/9	6	2
12	ZMMU R-13599-9	0.7	10.9	14.5	Y	Y	1+2	4	3+4	3/4	8/8	6/3	2
13	ZMMU R-13599-74	0.8	13.8	15.5	Y	Y	1+2+3	4	3+4	3/3	8/8	6	2
14	ZMMU R-07528	0.5	10.7	13.2	Y	Y	1+2+3	4	3+4	4/3	9/9	6	2
15	ZMMU R-13337	0.5	11.7	14.9	Y	Y	1+2+3	4	3+4	3/3	9/8	6	2
16	ZMMU R-13843	0.5	9.6	12.0	Y	Y	1+2	4	3+4	3/3	6/7	6	2
17	ZMMU R-08319	0.5	10.5	12.2	Y	Y	1+2+3	4	3+4	3/3	8/7	6	2
18	ZMMU R-11184	0.6	9.8	12.9	Y	Y	1+2+3	4	3+4	3/3	7/7	6	2
19	ZMMU R-11165	0.4	8.3	10.8	Y	Y	1+2+3	4	3+4	3/3	8/7	6	2
20	ZMMU R-11178	0.5	8.1	10.7	Y	Y	1+2	4	3+4	3/3	7/7	6	2
21	ZMMU R-13698	0.6	11.2	14.2	Y	Y	1+2	4	3+4	4/3	8/9	6	2
22	ZMMU NAP-04318	0.6	11.2	14.6	Y	Y	1+2	4	3+4	4/4	9/8	6	2
23	ZMMU R-04613-1	0.7	12.8	15.5	Y	Y	1+2+3	4	3+4	3/3	9/8	6	2
24	ZMMU R-04613-2	0.5	11.7	14.4	Y	Y	1+2+3	4	3+4	3/3	8/9	6	2
25	ZMMU R-04613-3	0.6	12.9	15.2	Y	Y	1+2+3	4	3+4	3/3	8/9	6	2
26	ZMMU R-04613-4	0.4	11.2	14.0	Y	Y	1+2+3/1+2+4	4/5	3+4/4+5	3/3	7/7	6	2
<i>Lipinia trivittata</i> sp. nov.													
27	ZMMU R-13920-58–holotype	0.5	13.4	17.9	Y	Y	1+2+3/1+2	4	3+4	3/3	9/8	6	2
28	ZMMU R-13449	0.8	15.0	18.6	Y	Y	1+2	4	3+4	3/3	7/8	6	2
29	ZMMU R-13934-112	0.6	14.3	17.8	Y	N	1+2	4	3+4	3/3	6/7	6	2
30	ZMMU R-13934-101	0.4	7.1	8.6	Y	S	1+2+3	4	3+4	3/3	7/7	6	2
31	ZMMU R-13920-56	0.8	14.6	18.5	Y	Y	1+2+3	4	3+4	3/3	10/9	6	2
32	ZMMU R-13920-57	0.6	11.3	13.0	Y	S	1+2	4	3+4	3/3	7/7	6	2
33	ZMMU R-13920-55	0.7	13.9	18.2	Y	Y	1+2+3	4	3+4	3/3	7/8	6	2
34	ZMMU R-15199	0.8	11.5	15.6	Y	Y	1+2+3	4	3+4	3/3	7/7	6	2
35	ZFMK 90419	0.7	8.8	10.3	Y	Y	1+2+3	4	3+4	3/3	7/7	6	3/4
<i>Lipinia vassilievi</i> sp. nov.													
36	ZMMU R-14604–holotype	0.7	12.8	17.3	Y	Y	1+2	4	3+4	3/3	10/11	6	2

Continued

No.	Species/Specimen	SLab	SLO	ILab	MSR	MdS	Vent	PrCl	SDL4F	SDL4T	LStr
<i>Lipinia vittigera</i>											
1	MSNG 55855–holotype	7/7	5+6	7/7	32	52	56	4	16/15	25/25	1
2	ZFMK 48542	8/7	5+6	7/7	30	48	56	2	16/16	22/22	1
3	ZMMU R-14477	7/7	5+6	7/7	28	50	56	4	16/16	26/25	1
<i>Lipinia microcercus</i> stat. nov.											
4	SMF14593–holotype	7/7	5+6	7/7	28	56	62	6	21/21	26/26	5
5	ZFMK 90339	7/7	5+6	7/7	28	50	62	4	20/20	24/24	5
6	ZMMU R-10962	7/7	5+6	7/7	30	56	60	4	20/21	29/29	5
7	ZFMK 88968	7/7	5+6	7/7	30	52	60	4	20/21	26/26	5
8	ZFMK 88869	7/7	5+6	7/6	28	48	64	4	18/19	25/25	5
9	ZMMU R-11475-1	7/7	5+6	7/7	28	50	62	4	21/20	25/24	5
10	ZMMU R-11475-2	7/7	5+6	6/6	26	58	60	4	18/18	24/–	5
11	ZMMU R-11475-3	7/7	5+6	7/7	30	52	60	4	19/18	28/28	5
12	ZMMU R-13599-9	7/7	5+6	7/7	32	50	60	4	22/21	26/29	5
13	ZMMU R-13599-74	7/7	5+6	7/6	28	50	54	4	21/21	32/32	5
14	ZMMU R-07528	7/7	5+6	7/7	30	52	60	4	18/18	24/24	5
15	ZMMU R-13337	7/7	5+6	7/7	28	52	60	4	19/20	27/27	5
16	ZMMU R-13843	7/7	5+6	7/7	26	50	62	4	20/21	26/27	5
17	ZMMU R-08319	7/7	5+6	7/7	32	54	62	4	21/21	30/29	5
18	ZMMU R-11184	7/7	5+6	7/7	28	54	62	4	20/20	31/27	5
19	ZMMU R-11165	7/7	5+6	7/7	32	52	62	4	19/20	25/24	5
20	ZMMU R-11178	7/7	5+6	7/7	30	48	54	4	19/17	27/27	5
21	ZMMU R-13698	7/7	5+6	7/7	32	52	64	4	18/18	28/30	5
22	ZMMU NAP-04318	7/7	5+6	7/7	32	50	62	4	23/21	29/29	5
23	ZMMU R-04613-1	7/7	5+6	7/7	30	50	62	4	17/18	26/26	5
24	ZMMU R-04613-2	7/7	5+6	7/7	28	54	60	4	19/19	25/26	5
25	ZMMU R-04613-3	7/7	5+6	7/7	30	50	58	4	20/20	29/28	5
26	ZMMU R-04613-4	7/7	5+6	7/7	30	52	58	4	21/21	30/29	5
<i>Lipinia trivittata</i> sp. nov.											
27	ZMMU R-13920-58–holotype	7/8	5+6/6+7	7/7	28	52	66	4	24/24	32/33	3
28	ZMMU R-13449	7/7	5+6	7/7	28	52	62	4	22/22	32/32	3
29	ZMMU R-13934-112	7/7	5+6	7/7	32	56	62	4	26/24	30/30	3
30	ZMMU R-13934-101	7/7	5+6	7/7	26	56	62	4	25/25	31/31	3
31	ZMMU R-13920-56	7/7	5+6	6/6	32	54	60	4	25/24	29/29	3
32	ZMMU R-13920-57	7/7	5+6	7/7	28	54	60	4	24/23	30/30	3
33	ZMMU R-13920-55	7/7	5+6	7/7	30	50	60	4	20/22	31/31	3
34	ZMMU R-15199	7/7	5+6	8/8	28	56	60	4	24/23	30/30	3
35	ZFMK 90419	7/7	5+6	8/8	32	58	58	4	18/18	26/26	3
<i>Lipinia vassilievi</i> sp. nov.											
36	ZMMU R-14604–holotype	7/7	5+6	7/7	28	56	66	4	15/14	21/19	3+2***

For character abbreviations see “Materials and Methods”. Character states and remarks: *: Tail broken; **: Head damaged; ***: Outer stripes broken, consisting of spots; Y: Yes; N: No; S: Slightly; –: Not available. F: Female; M: Male; Juv.: Juvenile.

Body slender (Figure 8), TrunkL 17.1 mm; head slightly distinct from neck and body; 56 middorsal scales from parietal to point above vent, scales in four median longitudinal rows enlarged; ventrals in 58 rows, counted from first postgular to preanal scales; body scales smooth, subcycloid; 30 scales around midbody; four slightly enlarged preanals; Limbs slender, pentadactyl, and clawed; forelimb and hindlimb meeting when adpressed; subdigital lamellae under finger IV: 15/16; subdigital lamellae under toe IV: 25/25; all subdigital lamellae enlarged.

Coloration in preservative: MDLS cream (Figure 8), from snout to tail base, widening at point above vent and merging into light dorsal coloration of tail. DTM indistinct dark mottling in temporal region (Figure 8D). MDLS on midbody about two scales wide. Two black PVDS from supraoculars to tail base, one scale wide at midbody, merging into brown lateral tail coloration. Outer margin of PVDS straight; flanks and gular region light fawn, dotted with small brown spots. Labials and surrounding of outer ear opening fawn with brown markings. Dorsal surface of remaining part of tail cream, becoming darker on lateral sides. Dorsal surface of limbs grayish fawn scattered with irregular brown spots. Toes and fingers light fawn with dark brown blotches on joints. Ventral surface of throat, trunk, limbs, and tail cream.

Coloration in life: Based on specimen (ZMMU R-14477, see Figure 5A–B) from Phanom District, Surat Thani Province, peninsular Thailand: MDLS fawn yellow on head, neck, and anterior half of trunk, gradually turning into fawn orange toward tail; PVDS brownish black; flanks and lateral surfaces of head light golden brown, scattered with lighter fawn and dark brown spots; dorsal surfaces of limbs golden brown with light orange complexion and small brown dots; digits fawn with dark brown spots on joints; labials fawn white; throat and belly white; tail fawn orange; lateral surfaces of tail marbled in brown. DTM, indistinct dark mottling in temporal region (Figure 5B, see Figure 9D for the same specimen in preservative).

Type locality: Sereinu Island (=Sipura), Mentawai Archipelago, west of Sumatra; see Boulenger (1894) and Bucklitsch et al. (2012) for discussion.

Variation: Measurements of the holotype and referred specimens are presented in Table 2. Certain morphological variation was found among the examined specimens. For example, the frontonasal width is smaller than its length in the holotype and specimen from Penang, Malaysia (ZFMK 48542), but width is greater than its length in the specimen from southern peninsular Thailand (ZMMU R-14477). In addition, the prefrontals are not in contact in the holotype, but are touching slightly in the Penang specimen (ZFMK 48542) and broadly contacting in the Thai specimen (ZMMU R-14477). The taxonomic value of these differences is unclear and requires broader molecular and morphological sampling from the Thai-Malay Peninsula and Sumatra.

Distribution: See Figure 1. In mainland Southeast Asia, *L.*

vittigera sensu stricto seems to be restricted to an area south of the Isthmus of Kra, though additional research on the Thai-Malay Peninsula populations is needed to confirm this assumption. Distribution of the species in peninsular Malaysia and its offshore islands was reviewed by Grismer (2011b). The species has been reported from: Peninsular Thailand: "Tasan, Isthmus of Kra" (Smith, 1935); Nakhon Si Thammarat Prov.: Khao Ram Rome Mt. (P. Pawangkhanant, personal communication); Surat Thani Prov.: Phanom (KUH 328480); Phanom Dist. (ZMMU R-14477; see material examined, Appendix I); Peninsular Malaysia: Pulau Pinang (Penang) (ZFMK 48542); Lata Tembaka, Terengganu; Jor, Perak, Kuala Teku, Pahang, Kepong and Ulu Langat, Selangor; and Endau Rompin and Gunung Panti, Johor (Denzer & Manthey, 1991; Grandison, 1972; Grismer, 2011b; Norsham & Ong, 2001; Onn et al., 2010; Smith, 1922; Tanner, 1953; Wood et al., 2004); Seribu Archipelago: Pulau Aur and Pulau Babi Besar, Johor, and Pulau Tioman, Pahang (Grismer et al., 2006); Singapore (Baker & Lim, 2008); Mentawai Archipelago (Boulenger, 1894) (MSNG 55855); as well as in Sumatra and northern Borneo (Das, 2010). Distribution records from north of the Isthmus of Kra often lack a clear assignment to one of the former subspecies, i.e., *L. v. vittigera* or *L. v. microcercus*. Thus, those records need further research to verify species assignment (see account on *L. microcercus* **stat. nov.**). Smith (1935) and Taylor (1963) published several records of *L. v. vittigera* from northern and eastern Thailand: "Chantaboon (= Chantaburi); Rehang district; Meh Lem, Meh Wang in N. Siam". However, without having seen the reference specimens, it is not possible to decide to which species of the *L. vittigera* complex those records belong.

Natural history: Grismer (2011a, 2011b) summarized several field observations from peninsular Malaysia and its offshore islands, with the species occurring in lowland and hill dipterocarp forests (primary and secondary) from 0 to 600 m a. s.l., and with a preferred microhabitat including trunks of large trees up to a height of 10 m. Reproduction was described by Goldberg & Grismer (2014): gravid females were recorded in March; females lay two to three eggs; hatchlings were observed in July.

Remarks: Our study suggests that the range of *L. vittigera sensu stricto* is restricted to the Mentawai Archipelago, Sumatra, the Thai-Malay Peninsula south of Kra Isthmus, and Borneo. The northern extent of its distribution is unknown and requires further studies. However, certain morphological variation was observed even within our limited sampling on *L. vittigera sensu stricto*. No data on variation of Bornean populations of *L. vittigera* are available. Grismer (2011b) reported color variation between specimens from Pulau Tioman, Pahang, which exhibited thin vertebral stripes only one scale wide, whereas specimens from peninsular Malaysia showed wider vertebral stripes, usually two scale rows wide. These data suggest that diversity of the *L. vittigera* complex in Peninsular Malaysia and Sundaland may still be

underestimated. Thus, further morphological and molecular studies are needed to address these questions.

Lipinia microcercus **stat. nov.** (= *Lygosoma microcercum*) (Boettger, 1901)

Figures 5C–H, 7C–F, 11–13; Tables 1–2.

Chresonymy

Lygosoma (*Leiopisma*) *microcercum* Boettger, 1901, p. 49;

Lygosoma pulchellum (partim) — Annandale, 1905, p. 145 (preliminary, see taxonomic comment below);

Leiopisma pulchellum (partim) — Taylor, 1922, p. 212;

Lygosoma vittigerum kronfanum Smith, 1922, p. 208 (see taxonomic comment below);

Leiopisma vittigerum kronfanum — Schmidt, 1928, p. 80;

Leiopisma pranensis Cochran, 1930, p. 18 (preliminary, see taxonomic comment below); Smith, 1930, p. 126;

Leiopisma vittigerum microcercum — Smith, 1935, p. 308; Bourret, 1939, p. 52; Taylor, 1963, p. 1030; Ho & Nguyen, 1981, p. 140; Semenov et al., 1983, p. 72; Bourret, 2009, p. 275;

Lipinia vittigerum microcercum — Bobrov, 1992, p. 19; Bobrov, 1995, p. 15;

Lygosoma microcercum — Bobrov, 1995, p. 15;

Scincella vittigerum (partim) — Nguyen & Ho, 1996, p. 40;

Scincella vittigerum kronfanum — Nguyen & Ho, 1996, p. 40;

Scincella vittigerum microcercum — Nguyen & Ho, 1996, p. 40;

Lipinia vittigera microcerca — Bobrov & Semenov, 2008, p. 64; Nguyen et al., 2009, p. 252; Bucklitsch et al., 2012, p. 325; Vassilieva et al., 2016, p. 175;

Lipinia vittigera microcercum — Grossmann, 2010, p. 2;

Lipinia vittigera (partim) — Nguyen et al., 2005, p. 59; Stuart et al., 2006, p. 147; Stuart & Emmet, 2006, p. 15; Grismer et al., 2008, p. 22; Hartmann et al., 2013b, p. 48; Jęstrzyski et al., 2013, p. 96; Grismer & Quah, 2019, p. 234;

Lipinia vittigera kronfanum — Das, 2010, p. 237 (treated as a valid subspecies).

Holotype: SMF 14593, adult male (Figure 10), collected by Hans Fruhstorfer from "Phuc-son in Annam" (=Phuoc Son District in Quang Nam Province), Vietnam (see comment below for discussion on type locality).

Paratypes: None.

Diagnosis: Small (SVL to 41.9 mm) species of *Lipinia*, differentiated from congeners by the following combination of external traits: external ear opening present; lower eyelid bearing large transparent spectacle; 28–32 midbody scale rows; 48–58 middorsal scales between parietals and point above vent; 18–21 subdigital lamellae under finger IV; 24–32 lamellae under toe IV; prefrontals in broad contact; seven supralabials, seven infralabials; thin middorsal light stripe from snout tip to tail base; two paravertebral dark stripes from supraoculars toward tail, continuing on anterior part of tail; two distinct dorsolateral light stripes; broad lateral dark stripe from

temporals to anterior part of tail; one distinct lateral light stripe, separated from belly by narrow ventrolateral dark stripe or longitudinal patch of dark spots.

Etymology: Referring to its short tail compared to other lygosomine skinks, Boettger (1901) provided the species epithet "*microcercum*". He treated this as a flexible adjective by adjusting it to the neutral gender of the genus name *Lygosoma*. However, such an adjective does not exist in the Latin language. The noun "*cercus*" is a Latinized version of the ancient Greek "κέρκος (*kérkos*)" in female gender, meaning "tail". When used as a noun in apposition, the species epithet cannot be reflected and therefore must be used as "*microcercus*".

Redescription of holotype: Measurements and counts of holotype are presented in detail in Table 2. Head scalation of holotype is detailed in Figure 7E–F. Adult male (Figure 10), SVL 41.9 mm, TaL 44.5 mm.

Snout acute, SL 6.2 mm; nostrils oriented laterally, oval, situated closer to snout tip than to orbit, END 2.5 mm; head long, almost twice as long as wide, HL 9.8 mm, HW 5.1 mm, HL/HW ratio 1.92, flattened, HH 3.3 mm, HL/HH ratio 2.97; rostral broad, visible in dorsal view, posterior border almost straight, contact zone with nasals slightly emarginated, frontonasal wider than long; frontal elongated, arrow-shaped, wider anteriorly; prefrontals large, in broad contact medially (Figure 7F), laterally and posteriorly in contact with loreals, enlarged presupraocular, first supraocular, frontal and frontonasal; two frontoparietals in broad median contact; interparietal arrow-shaped, wider anteriorly; parietals in contact behind interparietal, anteriorly in contact with postsupraoculars, nuchals, and frontoparietals; six nuchals; four supraoculars; one enlarged presupraocular, visible from above; seven supraciliaries; nostrils located within nasals; postnasal absent; two loreals, slightly elongated, second longer than first; two enlarged presuboculars, separating supralabials III and IV from eye; seven supralabials, supralabial V largest, in contact with orbit; three postsupoculars, separating supralabial VI from orbit; six postsupraoculars (pretemporals); one primary temporal; two secondary temporals, dorsal largest; two postsupralabials; lower eyelid bearing large transparent spectacle (Figure 10F); scales on upper row of lower eyelid small, 11 in number; mental wider than long; one postmental, in contact with first infralabial and anterior portion of second infralabial; seven infralabials; three pairs of chinshields, first pair in contact medially, second pair separated by one scale, third pair separated by three scales; external ear opening visible and subcircular (Figures 7E, 10E).

Body slender, TrunkL 22.8 mm; head slightly distinct from neck and body; 56 middorsal scales from parietal to point above vent, scales in four median longitudinal rows enlarged; ventrals in 58 rows, counted from first postgular to preanal scales; body scales smooth, subcycloid; 28 scales around midbody; six slightly enlarged preanals; tail relatively long, TaL/SVL ratio 0.94, tip rounded; tail gradually tapering to point;

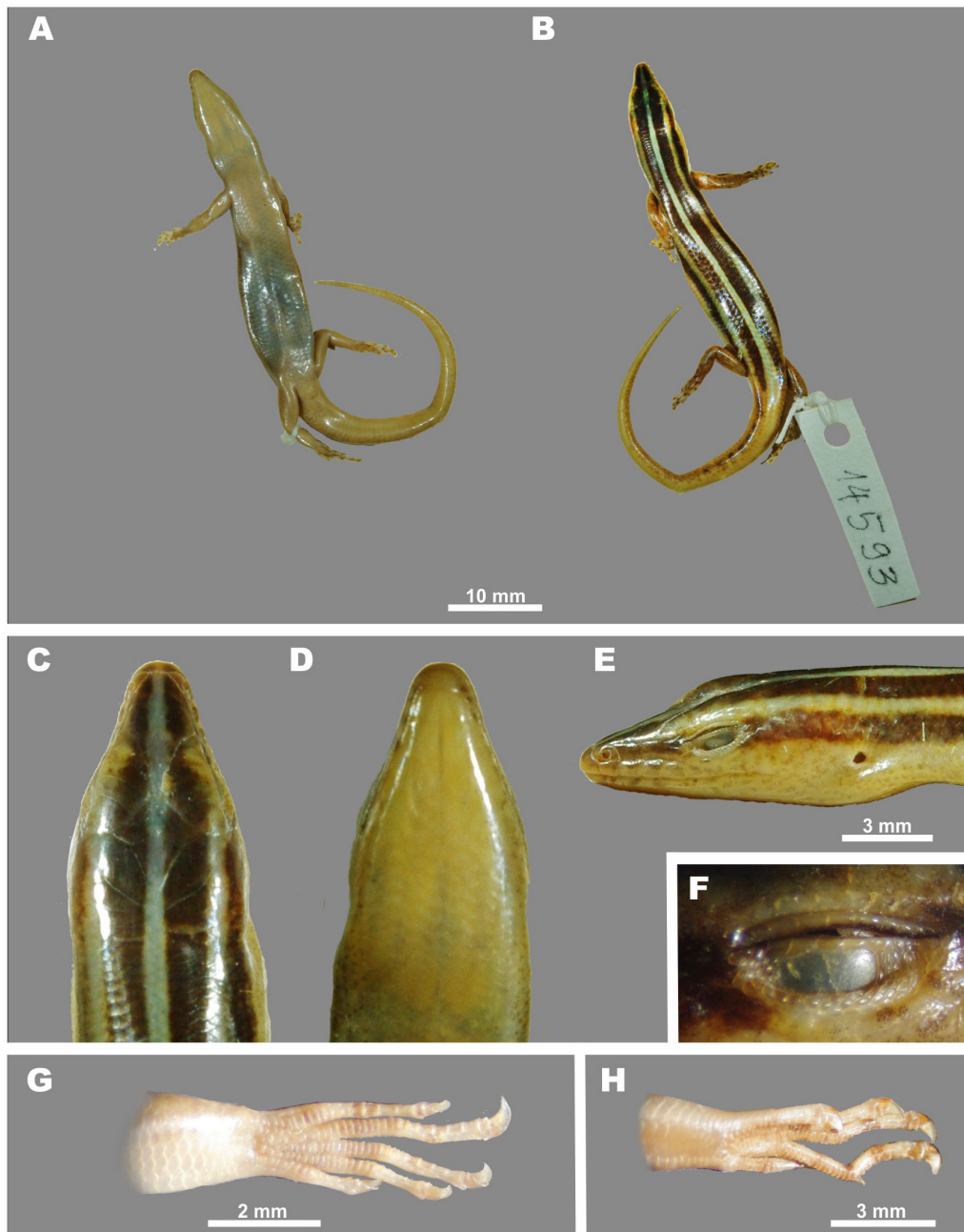


Figure 10 Holotype of *Lygosoma (Leiolopisma) microcercum* Bottger, 1901 (SMF 14593, male) in preservative

A: General ventral view; B: General dorsal view; C: Head dorsal view; D: Head ventral view; E: Head lateral view; F: Close-up of right eye showing translucent window in lower eyelid; G: Right forelimb in volar view; H: Right hindlimb in thenar view. Photos by Peter Geissler.

median row of subcaudals enlarged; Limbs slender, pentadactyl, and clawed; forelimb and hindlimb meeting when adpressed; Subdigital lamellae under finger IV: 21 (Figure 10G); subdigital lamellae under toe IV: 26 (Figure 10H); all subdigital lamellae enlarged (Figure 10G–H).

Coloration in preservative: See Figure 10; MDLS whitish,

from head to tail base, widening at point above vent and merging into light brownish coloration of tail. MDLS on midbody about one scale wide, covering interior halves of two paravertebral scale rows. Two brownish PVDS from snout to tail base, about two scales wide, continued by row of eight irregular brown blotches on both sides of anterior half of tail. Two fawn DLLS, starting on supraoculars, running down to

point above vent, merging with MDLS and light brownish tail coloration. Laterally, on flanks, stripes sharply bordered by blackish brown LDS, starting at nostrils, extending to hind margin of hindlimbs. Ventral margin of LDS less sharp, sometimes frayed. LLS cream, only separated from light cream ventral trunk surface by faint narrow patch of brown spots (VLDS) between axilla and groin. DTM as wide dark band, about two times wider than DLLS above, running from posterior margin of eye to temporal region and further posteriorly on body flanks, joining with LDS (Figure 10E). Labials and surrounding of outer ear opening fawn white with some faint irregular brown pigmentation. Dorsal surface of tail light brown, becoming darker on lateral sides. Anterior third of tail with eight dark brown lateral blotches flanking light brown median tail surface. Dorsal surface of limbs brown, scattered with irregular darker spots. Toes and fingers light fawn with dark brown blotches on joints. Ventral surface of throat, trunk, limbs, and tail fawn, somewhat darker on tail and posterior part of trunk than on throat.

Coloration in life: Description of life coloration is based on an adult male specimen (ZMMU R13698, Yok Don, Dak Lak, Vietnam), see Figure 5E–F. MDLS whitish beige on head and anterior parts of trunk, gradually turning light orange on tail; PVDS and LDS brownish black; DLLS whitish beige with light orange complexion toward tail base; LLS grayish white; VLDS grayish brown; limbs and digits dark brown, scattered with lighter beige and slightly orange spots; digits whitish with dark brown spots on joints; labials bright white with dark gray markings; throat and belly white; tail bright orange, with increasing intensity toward tail tip; lateral surfaces of tail orange, interrupted by partly connected dark brown patches.

Variation: To assess morphological variation, we investigated 23 recently collected specimens from central and southern Vietnam and from Cambodia. Selected traits and measurements are shown in Table 2. We also examined photos of type specimens of *Lygosoma vittigerum kronfanum* Smith, 1922 (Figure 11) and *Leiopisma pranensis* Cochran, 1930 (Figure 12). In general, all examined specimens correspond quite well to the description of the holotype, although certain variation was observed in number of supraoculars contacting frontal and number of superciliary scales. Coloration features appeared quite stable within *L. microcercus stat. nov.* (Figure 13). No statistically significant differences in morphological characters between sexes were observed.

Distribution: Distribution is shown in Figure 1. This species is known with certainty from central and southern Vietnam, Cambodia, and extreme south of Laos. As we tentatively synonymize *Leiopisma pranensis* Cochran, 1930 from Tenasserim with *L. microcercus stat. nov.*, its distribution may extend further westward to northern and western Thailand north of the Isthmus of Kra; occurrence of this species in easternmost Myanmar is expected (Figure 1).

It is likely that the records of "*L. vittigera*" from Tanintharyi

Division of Myanmar correspond to this species; it was recorded from the following localities: Tavoy (=Dawei, Dewei) (Annandale, 1905); Yepone, Yebyu Township, Dewei Dist., Tanintharyi Div., Myanmar (CAS 243723); and Kawthaung Township, Tanintharyi Div., Myanmar (CAS 229605). However, the taxonomic status of these populations needs to be clarified.

Records of the genus *Lipinia* from Thailand require further specimen examination for correct identification; members of the *L. vittigera* complex were recorded from all over the country, including: Phetchaburi Prov.: Kaeng Krachan NP; Prachuap Khiri Khan Prov.: Pran (=Pran Buri) (USNM 75591); Kui Buri NP; Uthai Thani Prov.: Huai Kha Khaeng WS; Chiang Mai Prov.: Doi Angka Mt. (USNM 76850); Chiang Mai (FMNH 177050); Doi Suthep-Pui NP, Mae Takhrui NP (P. Pawangkhanant, personal communication); Nakhon Ratchisima Prov.: Mueang Nakhon Ratchisima Dist. (KUH 328481); Khao Yai NP; Nan Prov.: Tambol Auan, Amphoe Pua (FMNH 270715); Loei Prov.: Phu Kradueng NP; Saraburi Prov.: Muak Lek, Chet Sao Noi NP; Sa Kaeo Prov.: Pang Sida NP; Ubon Ratchathani Prov.: Ubon (FMNH 177615) (P. Pawangkhanant, personal communication). Further studies are essential to clarify species identity of the Thai populations of the *L. vittigera* complex.

Records of *Lipinia* from Laos are poorly documented but include Xepian NBCA, Champasak Prov. (Teynié et al., 2004). In addition to the localities presented in Figure 1 (see Appendix I for details), existing records from Cambodia (as *L. vittigera*) include: Pursat Prov.: Veal Veang, Phnom Samkos WS (NCSM 80292); Kratie Prov.: Sambour, Koh Kring Island (MVZ 258369); Kampong Speu Prov.: Phnom Sruoch Dist. (FMNH 261862); Ratanakiri Prov.: Ta Veng Dist. (FMNH 262984); Koh Kong Prov., Thmar Baing Dist. (FMNH 263362); Sihanoukville Prov. (FMNH 270597) (Stuart & Emmet, 2006; Stuart et al., 2006, 2010). Hartmann et al. (2013a) also mentioned a photo record of a *Lipinia* specimen from northwestern Kulen Prum Tep WS (KPWS, Oddar Meanchey Province, Trapeang, Prasat District: ZFMK-PA SE 30; N14.7467°, E104.8100°, 99 m a.s.l.); based on coloration this specimen can be reliably assigned to *L. microcercus*.

In addition to the localities verified by genetic and morphological analyses (see Figure 1 and Appendix I for details), *L. microcercus stat. nov.* was documented as *L. v. microcercus* from the following localities in Vietnam: Thua Thien-Hue Prov.: A Luoi (AMNH R-154622), Hue environs; Da Nang: Hai Van mountain pass, Bach Ma NP; Quang Nam Prov.: Hien, Nam Giang, Tay Gianh, Phuoc Son, Ngoc Linh NP; Kon Tum Prov.: Ngoc Linh NP, Kon Tum; Gia Lai Prov.: Buon Luoi (FMNH 252169), K Bang: SOn Lang, Chu Se; Dak Lak Prov.: Buon Ma Thuot (MVZ 222200), Yok Don NP; Lam Dong Prov.: Lang Bian, Da Ban, Bao Loc (USNM 90386), Cat Loc; Khanh Hoa Prov.: Hon Ba NP; Binh Phuoc Prov.: Nghia Trung; Dong Nai Prov.: Cat Tien NP, Ma Da; Ba Ria - Vung Tau Prov.: Binh Chau-Phuok Buu NP; Tay Ninh NP: Lo Go-Xa Mat NP; Kien Giang Prov.: Phu Quoc NP (Bobrov & Semenov, 2008; Nguyen et al., 2009). The record of "*L. vittigera*" from Ha Tinh Prov. (Vu Kuang NP) by Semenov (2001) is doubtful;

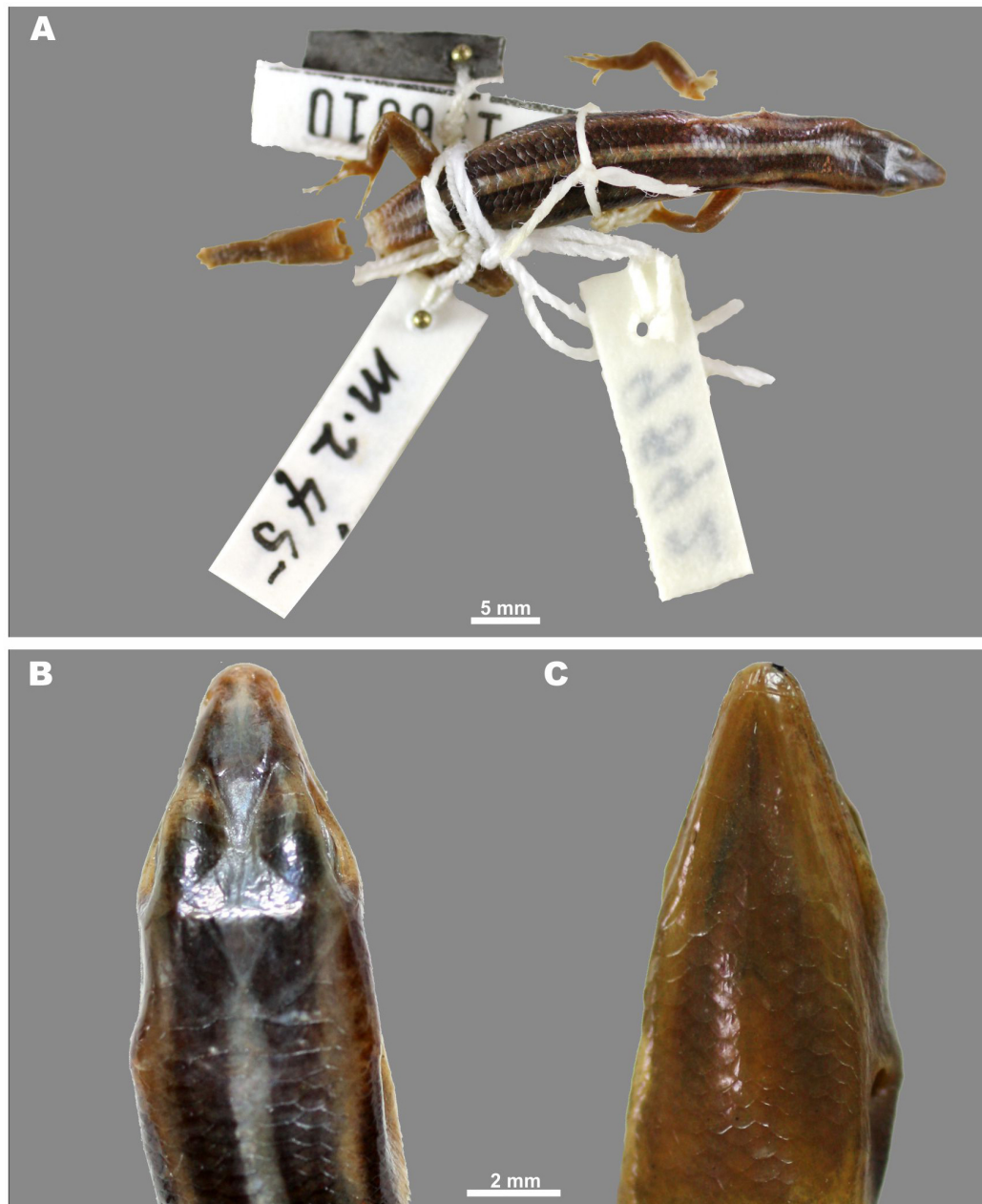


Figure 11 Paratype of *Lygosoma vittigerum kronfanum* Smith, 1922 (FMNH 196010, field number M.A. Smith 4514, male) in preservative A: General dorsal view; B: Head dorsal view; C: Head ventral view. Photos by Rachel Grill.

see Bobrov (1992, 1995) and Bobrov & Semenov (2008).

Natural history: A brief description of the biology of this species in Vietnam was presented by Bobrov & Semenov (2008) and Vassilieva et al. (2016). The species was recorded from diverse types of clear forest habitats, including disturbed areas and rural and suburban landscapes in lowland, hilly, and submontane regions up to 1 200 m a.s.l. (Vassilieva et al., 2016). It is an arboreal species, which can be quite common

locally. Specimens were usually observed during the day while the lizards foraged on trunks of large trees or, occasionally, on walls of wooden buildings located within the forest or at forest edges. Occasionally, specimens were observed on the ground, presumably crossing from one tree trunk to another. These lizards are active at temperatures above 20 °C, and usual hide under bark or in small tree hollows on rainy days (Bobrov & Semenov, 2008). Diet includes spiders and various small insects; in Cat Tien NP, a male specimen (ZFMK 88969)

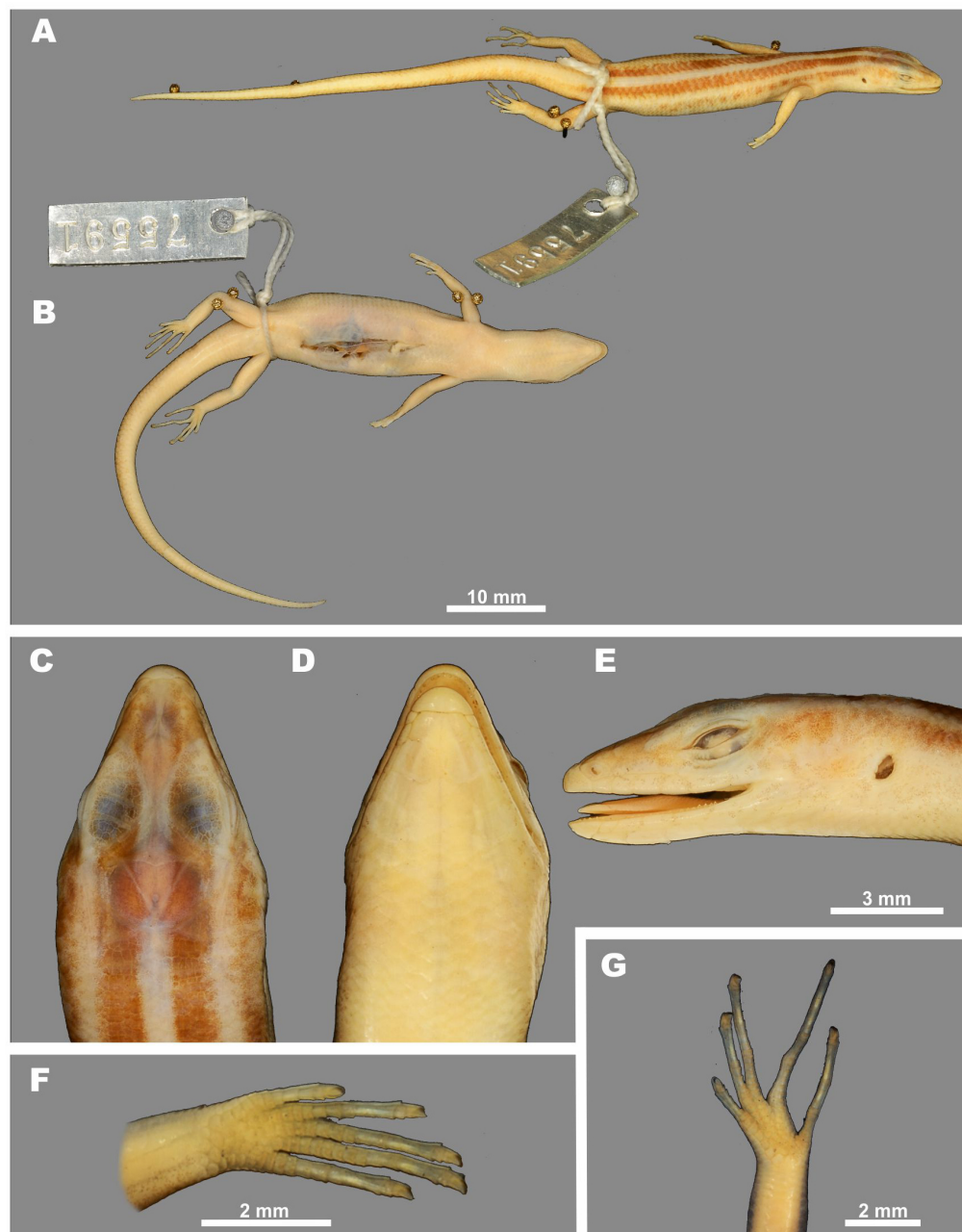


Figure 12 Holotype of *Leiolopisma pranensis* Cochran, 1930 (USNM75591, male) in preservative

A: General dorso-lateral view; B: General ventral view; C: Head dorsal view; D: Head ventral view; E: Head lateral view; F: Left forelimb in volar view; G: Left hindlimb in thenar view. Photos by James Poindexter.

was observed catching ants on the walls of a wooden stilt hut on the forest edge at Bau Sau Lake at a height of 5 m above ground. They are occasionally observed in groups of 2–3 on the same tree trunk. Waving movements of their brightly colored reddish or bright-orange tails is a commonly observed display behavior. They are oviparous, laying 2–4 eggs per clutch; hatching is observed during the rainy season. Sexual maturity is reached at the end of the first year, shedding

occurs in January (Vassilieva et al., 2016).

Comparisons: Comparisons are based on original descriptions or descriptions provided in broader faunal and taxonomic publications (citations in the Materials and Methods section above).

Morphological comparisons between the four members of the *L. vittigera* species complex from mainland Southeast Asia

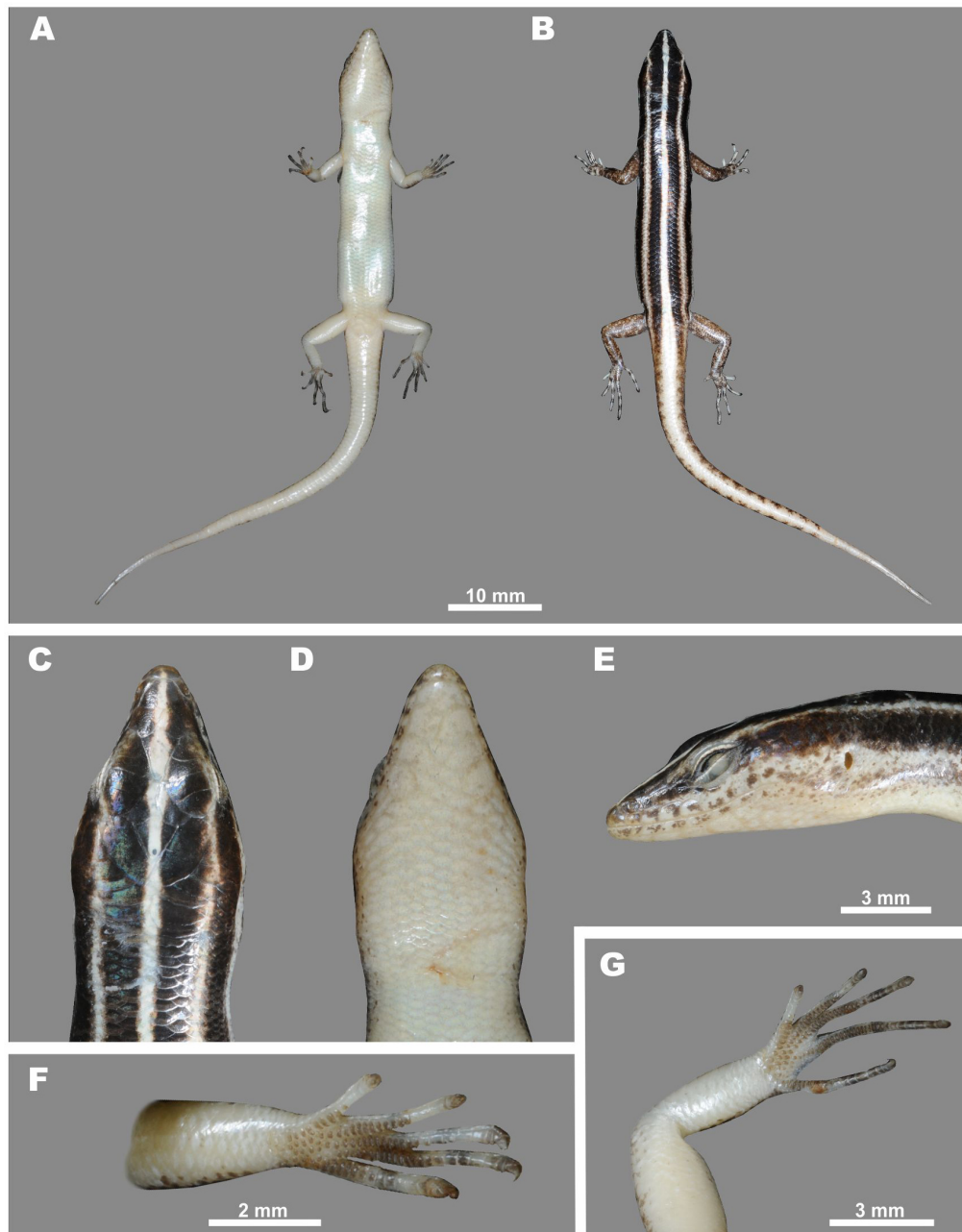


Figure 13 Specimen of *Lipinia microcercus* stat. nov. (Boettger, 1901) (ZMMU NAP-04318, male) in preservative

A: General ventral view; B: General dorsal view; C: Head dorsal view; D: Head ventral view; E: Head lateral view; F: Left forelimb in volar view; G: Left hindlimb in thenar view. Photos by Nikolay A. Poyarkov.

are summarized in Table 1. *Lipinia microcercus* stat. nov. can be differentiated from all other members of the *L. vittigera* species complex by the following opposing combination of characters (see Table 1 for details): *L. vittigera sensu stricto* (Boulenger, 1894) from Peninsular Malaysia, Mentawai Islands, Sumatra, and Borneo: 15–16 subdigital lamellae under finger IV; MDLS broad (two scales wide) from snout tip to tail; PVDS not as broad as MDLS; flanks with dark and pale

spots (LDS, LLS absent or indistinct); DTM present, indistinct dark mottling or spots; *Lipinia trivittata* sp. nov. (herein) from southern Vietnam, Cambodia, and eastern Thailand: 20–26 subdigital lamellae under finger IV; MDLS broad (two scales wide); PVDS not as broad as MDLS, not continuing on tail; LDS only present on anterior third of trunk; DTM as narrow black stripe about as wide as DLLS; *Lipinia vassilievi* sp. nov. (herein) from central Vietnam: 10–11 supraciliaries; 14–15

subdigital lamellae under finger IV; 19–21 subdigital lamellae under toe IV; MDLS broad (two scales wide); PVDS not as broad as MDLS; LDS and VDSL dissolving into two rows of irregular dark blotches; DTM narrow black stripe, about as wide as DLLS.

In the following, *L. microcercus* **stat. nov.** is compared with other congeners bearing a light middorsal stripe by listing their opposing character combinations: *L. albodorsalis* (Vogt) from New Guinea: SVL to 54 mm; 22–25 midbody scale rows; dorsum pale yellow with dark lateral stripe; *L. infralineolata* (Günther) from Sulawesi and Sangihe Islands: SVL to 49 mm; 22 midbody scale rows; *L. leptosoma* (Brown & Fehlmann) from Palau Islands: 7–10 lamellae under toe IV; *L. longiceps* (Boulenger) from New Guinea, Fergusson, Misima, and Trobriand Islands: 24 midbody scale rows; snout strongly elongated; dorsum light brown with two dorsolateral stripes converging on tail base; tail golden yellow; *L. macrotypanum* (Stoliczka) from Andaman and Nicobar Islands: 21–23 midbody scale rows; prefrontals separated; hindlimbs and forelimbs not meeting when adpressed; *L. miangensis* (Werner) from Pulau Miang, Kalimantan Timur, Borneo: 24 midbody scale rows; back golden with two dark brown longitudinal stripes from snout to tail; *L. nitens* (Peters) from Sarawak, Borneo: SVL to 33.6 mm; external ear opening replaced by scaly dimple; back metallic green with pale yellow vertebral stripe; *L. noctua* from South Pacific islands (allochthonous) and Indonesia: Maluku and Papua Province; Papua New Guinea, Admiralty Islands, Bismarck Islands, and Solomon Islands: dorsum brown with light vertebral stripe, starting with wide and contrasting light spot on head; dark paravertebral stripes with irregular borders, often broken into row of irregular dark blotches; *L. pulchella* from the Philippines: 22–26 midbody scale rows; 24–31 lamellae under toe IV; only one light whitish stripe present on dorsum, from snout to tail tip, becoming yellowish from midbody toward tail; *L. pulchra* (Boulenger) from New Guinea: dorsum black with five greenish light stripes; *L. rabori* (Brown & Alcalá) from the Philippines (Negros Island): SVL to 51.0 mm in males and 54.8 mm in females; 22 midbody scale rows; *L. relicta* (Vinciguerra) from Indonesia: Mentawai Archipelago, SVL to 56 mm; 20 midbody scale rows; 16–18 lamellae under toe IV; tail thick; light vertebral line present and labials each bearing small white spot; lateral dark stripe present from eye to insertion of hindlimbs; *L. rouxi* (Hediger) from New Ireland, northeast Papua New Guinea, and Bismarck Archipelago: dorsum brown, dark paravertebral stripes, with irregular borders, often broken into row of irregular dark blotches; *L. septentrionalis* Günther from Indonesia (Papua Province): 24–26 midbody scale rows; one cream vertebral stripe, broadening toward tail; *L. subvittata* (Günther) from Sulawesi, Java, the Philippines (Mindanao Island): SVL 47–56 mm; dorsal longitudinal stripes extending to forearm region; 22 midbody scale rows; *L. vulcania* from the Philippines (Mindanao and Luzon Islands): 17 lamellae under toe IV; limbs not meeting when adpressed; dorsum brownish, scattered with dark brown spots; dark lateral stripe, scattered with whitish or yellowish spots.

The following congeners can be distinguished from *L. microcercus* by the absence of a light middorsal stripe: *L. auriculata* (Taylor) from the Philippines (Negros and Masbate Islands); *L. cheesmanae* (Parker) from New Guinea; *L. inexpectata* Das & Austin from Borneo and its northern offshore islands; *L. nototaenia* (Boulenger) from West Papua; *L. occidentalis* Günther from Papua Province, New Guinea; *L. sekayuensis* Grismer, Ismail, Awangm, Rizal & Ahmad from Peninsular Malaysia; *L. semperi* (Peters) from the Philippines (Mindanao and Camiguin Islands); *L. surda* (Boulenger) from Peninsular Malaysia; *L. venemai* (Brongersma) from Indonesia: Papua Province; and *L. zamboangensis* (Brown & Alcalá) from the Philippines (Mindanao Island).

Remarks: *Lipinia microcercus* **stat. nov.** was ranked as a subspecies of *L. vittigera* (Boulenger, 1894) by Smith (1935). However, the genetic differentiation presented in this study as well as the morphological differentiation documented herein indicate that *L. microcercus* has to be treated as a valid species.

Remarks on type locality of *Lygosoma (Leiolopisma) microcercum* Boettger, 1901: Boettger (1901) noted the type locality as "Phuc-son in Annam". A recent literature review enabled an exact localization of this village. The type specimen belonged to a herpetological collection sent to Frankfurt by the German naturalist Hans Fruhstorfer in November and December 1899. Hans Fruhstorfer travelled through Indochina for about three years (1899–1901), visiting all provinces of the so-called Union Indochinoise (Lamas, 2005). Though mainly focused on collecting insects and molluscs, Fruhstorfer also noted in his published travelogue (Fruhstorfer, 1905) several reptiles and amphibians. In the case of the holotype specimen of *Lygosoma microcercum*, a concurrent reference in Fruhstorfer (1901) can be ascribed, where he mentions a remarkable lizard: "*Viel Aufsehen erregte der Fang einer Eidechse mit rothem Schwanz und drei goldenen Linien über dem Rücken, wahrscheinlich Lygosoma sanctum Dum.*" (p. 130) (translation: "The catch of a lizard caused a certain sensation. It had a red tail and three golden lines on its back, probably *Lygosoma sanctum* Dum."). This note, the only one which can be assigned to a specimen of the genus *Lipinia*, belongs to an entry from 24 November 1899 in "Phuc son, Gebiet der Moi" (Fruhstorfer, 1901). Fruhstorfer entered Annam at the harbor of Tourane (today Da Nang, Quang Nam Province) on 13 November 1899 and left for a collection trip (six weeks) into the hinterland of Tourane, to "Phuc son" and "Thu-bon" on 15 November 1899. Though Fruhstorfer's transcription of "Phuc son", which was adopted by Boettger (1901), slightly differs from the modern "Phuoc Son", it can be stated with certain reliability that the type locality of *Lygosoma microcercum* can be restricted to the modern Phuoc Son District in Quang Nam Province, Central Vietnam (Figure 1, locality 6).

Taxonomic status of *Lygosoma vittigerum kronfanum* Smith, 1922: Smith (1922) described the new subspecies

Lygosoma vittigerum kronfanum based on six specimens collected at "Daban, Langbian plateau, S. Annam in March 1918". However, all diagnostic characters provided by Smith (1922) are within the character range of *Lygosoma microcercus* Boettger, 1901: TL 93 mm; SVL 34 mm; midbody scale rows 28–32; limbs overlapping when adpressed; prefrontals in contact, forming broad median suture; five "well-defined light stripes". The description of coloration in preservative also fits the coloration pattern of *L. microcercus* **stat. nov.**, as described above: "Black above, with 5 greenish-white dorsal stripes, namely, a vertebral one from tip of the nose to the root of the tail, a dorsolateral pair from the upper eyelid to above the thigh, and a lateral pair from the upper lip to the groin" (Smith, 1922, p. 209).

Smith (1935) himself then placed *Lygosoma vittigerum kronfanum* into synonymy of *Leiolopisma vittigerum microcercus* (Boettger, 1901), referring to a personal comment of Robert Mertens (unpublished), the successor of Oskar Boettger in SMF in Frankfurt: "Dr. Mertens has compared my *kronfanum* with the type of *microcercus*, and has confirmed my suspicion that the two are identical" (Smith, 1935, p. 308). At least one paratype of *L. vittigerum kronfanum* is still present in today's FMNH collection. The handwritten labels indicate that FMNH 196010 (see Figure 11) is one of four paratypes (collection numbers: 2453–2456) present in the private collection of Smith). The fate of the holotype (Smith's private collection number 2417) and other paratypes remains unknown. Das (2010) erroneously listed *L. v. kronfanum* as a valid subspecies. Based on morphological accordance, we follow Smith (1935) in recognizing *L. v. kronfanum* as a junior synonym of *L. microcercus* (Boettger, 1901) **stat. nov.**

Taxonomic status of *Leiolopisma pranensis* Cochran, 1930: Cochran (1930) described *Leiolopisma pranensis* from Siam (now Thailand) based on two specimens, including the holotype USNM 75591 from Pran (now Pran Buri, Prachuap Khiri Khan Prov.) and paratype USNM 76850 from Doi Angka Mt. (Chiang Mai Prov.). Soon after, Smith (1935) synonymized this taxon with *Leiolopisma vittigerum vittigerum*, although without any justification for this decision. This opinion was later accepted by subsequent researchers (see Taylor, 1963, p. 1029).

We examined photos of the holotype (Figure 12) of *Leiolopisma pranensis* Cochran, 1930, and we doubt that this taxon is close to *L. vittigera sensu stricto*. In general, external morphology of the holotype USNM 75591 agrees well with *L. microcercus* **stat. nov.** (see Table 1 for comparison): SVL 38.0; TaL/SVL ratio 1.26; TrunkL/SVL ratio 0.53; SL/SVL ratio 0.12; STL/SVL ratio 0.24; SFIL/SVL ratio 0.37; FLL/SVL ratio 0.29; HLL/SVL ratio 0.39; frontonasal wider than long; prefrontals in contact (see Figure 7D); frontal contacting 1+2 supraoculars; frontoparietals contacting 2+3+4 supraoculars; supraciliaries 7–8; MSR 30; MDSR 54; ventrals 56. In coloration (Figure 12), the holotype of *Leiolopisma pranensis* is also similar to *L. microcercus* **stat. nov.** with narrow MDLS (one scale wide), PDS slightly wider than MDLS, not

continuing on tail (although coloration on tail is possibly faded as the specimen appears slightly bleached); DLLS distinct with regular borders, one scale wide.

However, the holotype of *Leiolopisma pranensis* shows some differences when compared with the holotype of *L. microcercus* **stat. nov.**: 14 subdigital lamellae under finger IV; 21 subdigital lamellae under toe IV; fifth supralabial not contacting orbit (Figure 7C); LDS dissolving into row of irregular dark blotches, not reaching groin; VLDS only present as narrow row of irregular small spots. Unfortunately, our phylogenetic analysis lacked samples from western Thailand, including the vicinity of the *Leiolopisma pranensis* type locality, so the taxonomic value of these differences is not clear and requires further study. Nevertheless, the available information indicates that *Leiolopisma pranensis* is notably different from *L. vittigera sensu stricto* and more closely resembles *L. microcercus* **stat. nov.** Further molecular and morphological data on *Lipinia* populations from western Thailand are needed for future research. We herein propose to place *Leiolopisma pranensis* Cochran, 1930 into tentative synonymy of *L. microcercus* (Boettger, 1901) **stat. nov.**

Lipinia trivittata **sp. nov.**

Figures 6A–D, 7G–H, 14; Tables 1, 2.

Chresonymy

Lygosoma vittigerum kronfanum (partim) — Smith, 1922, p. 209 (tentative chresonymy; see taxonomic comment below);

Lipinia vittigera (partim) — Mahony, 2008, p. 239(?); Grismer et al., 2011, p. 62(?); Vassilieva et al., 2016, p. 167.

Holotype: ZMMU R13920-58, adult female (Figure 14), collected by Eduard A. Galoyan from a tree trunk in a pine forest in Chu Yang Sin NP, Dak Lak Province, Vietnam (N12.40611°, E108.35361°; 950 m a.s.l.) on 30 March 2013.

Paratypes: ZMMU R13920-55–57, three adult males with same collection information as holotype; ZMMU R13449, adult male collected by Nikolay A. Poyarkov on the edge of a forest road in Dac Ca River valley, Bu Gia Map NP, Binh Phuok Province, Vietnam (N12.1931°, E107.2121°; 545 m a.s.l.) on 16 April 2009; ZMMU R13934-112, adult male, and ZMMU R13934-101, juvenile, collected by Eduard A. Galoyan and Anna B. Vassilieva from Loc Bac forest (operated by Loc Bac Forest Enterprise), Loc Bao Commune, Bao Lam District, Lam Dong Province, Vietnam (N11.73806°, E107.70694°; 850 m a.s.l.) on 7 April 2013; ZFMK 90419, adult female, collected by T. Hartmann from Kulen Prum Tep WS, Preah Vihear Province, Kulen District (N13.8851°, E104.8820°; 70 m a.s.l.) on 10 July 2009.

Diagnosis: Small (SVL up to 44.4 mm) species of *Lipinia*, differentiated from congeners by the following combination of external morphological traits: external ear opening present; lower eyelid bearing large transparent spectacle; 28–32 midbody scale rows; 48–58 middorsal scales between parietals and point above vent; 20–26 subdigital lamellae under finger IV; 29–33 lamellae under toe IV; prefrontals in

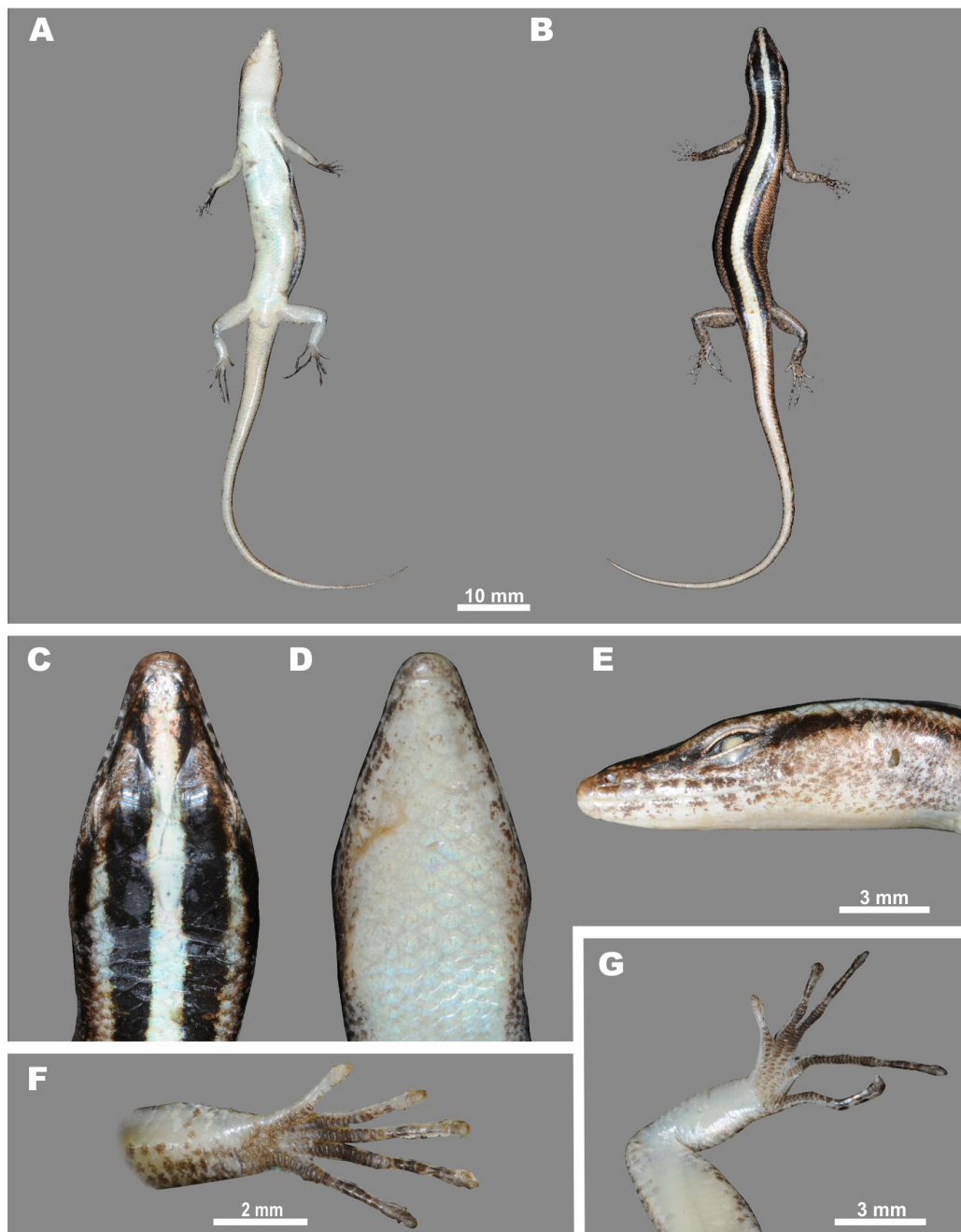


Figure 14 Holotype of *Lipinia trivittata* sp. nov. (ZMMU R13920-58, female) in preservative

A: General ventral view; B: General dorsal view; C: Head dorsal view; D: Head ventral view; E: Head lateral view; F: Left forelimb in volar view; G: Left hindlimb in thenar view. Photos by Nikolay A. Poyarkov.

broad contact; seven supralabials, seven infralabials; middorsal light stripe from snout tip to tail base; two paravertebral dark stripes, continuing on anterior part of tail; two dorsolateral light stripes, distinct on head and anterior third of trunk; narrow lateral dark stripe from loreals to anterior half of trunk.

Etymology: The species epithet is an adjective in nominative singular (feminine gender) derived from the Latin "*tri-*" for three and "*vitta*" for a head band (see above), referring to its prominent three stripes (one light middorsal stripe and two dark paravertebral stripes) in dorsal view.

Description of holotype: Measurements and counts of

holotype are presented in detail in Table 2. Adult female, SVL 44.4 mm (see Figure 14), TL 59.3 mm.

Snout acute, SL 4.2 mm; nostrils oriented laterally, oval, situated closer to snout tip than to orbit, END 2.5 mm; head long, almost twice as long as wide, HL 9.2 mm, HW 5.3 mm, HL/HW ratio 1.74, flattened, HH 3.7 mm, HL/HH ratio 2.5; rostral broad, visible in dorsal view, posterior border of rostral waved, contact zone with nasals slightly emarginated; frontonasal wider than long; frontal elongated, arrow-shaped, wider anteriorly; prefrontals large, in broad contact medially (Figure 7H), surrounded by loreals, enlarged presupraocular, frontal, first supraoculars (punctiform contact) and frontonasal; two frontoparietals in broad median contact; interparietal arrow-shaped, wider anteriorly; parietals in contact behind interparietal, surrounded by postsupraoculars, nuchals, interparietal, and frontoparietals; six nuchals; four supraoculars; one enlarged presupraocular, visible from above; nine/eight supraciliaries; nostrils located within nasals; postnasal absent; two loreals, slightly elongated, second longer than first; two enlarged presuboculars, separating supralabial III and IV from orbit; seven supralabials, supralabial V largest, in contact with orbit; three postsuboculars, separating supralabial VI from orbit; six postsupraoculars (pretemporals); one primary temporal; two secondary temporals, dorsal largest; two postsupralabials; lower eyelid bearing large transparent spectacle; scales on upper row of lower eyelid small, 10 in number; mental wider than long; one postmental, in contact with first infralabial and anterior portion of second infralabial; seven infralabials; three pairs of chinshields, first pair in contact medially, second pair separated by one scale, third pair separated by three scales; External ear opening visible and subcircular (Figure 7G).

Body slender (Figure 14A–B), TrunkL 22.4 mm; head slightly distinct from neck and body; 56 middorsal scales from parietal to point above vent, scales in four median longitudinal rows enlarged; ventrals in 66 rows, counted from first postgular to preanal scales; body scales smooth, subcycloid; 28 scales around midbody; four slightly enlarged preanals; Tail relatively long, TaL/SVL ratio 1.33, tip rounded; tail gradually tapering to point; median row of subcaudals enlarged; Limbs slender, pentadactyl, and clawed; forelimb and hindlimb meeting when adpressed; Subdigital lamellae under finger IV: 24 (Figure 14F); subdigital lamellae under toe IV: 32/33 (Figure 14G); all subdigital lamellae enlarged.

Coloration in preservative: MDLS whitish, from head to tail base, widening at point above vent and continuing on dorsal surface of tail. MDLS on midbody about two scale rows wide, covering both paravertebral scale rows. Two black PVDS from snout to tail base, about two scales wide, narrowing on tail base, running into thin brown stripe within anterior fourth of tail. Two fawn DLLS, starting on supraoculars, running down to point above forelimb insertion, merging with brownish flank on anterior part of trunk. LDS starting at nostrils, running out into diffuse stripe on anterior third of trunk. LLS and VLDS absent. DTM as narrow black stripe ca. same width as DLLS above, running from posterior margin of eye to temporal

region and further posteriorly on body flanks, joining with LDS (Figure 14E). Labials, gular region, and flanks cream, scattered with brown pigmentation, darker on head, becoming lighter on flanks. Dorsal surface of tail whitish, lateral surface light brown. Dorsal surface of limbs light brown, scattered with irregular darker spots on hands and feet. Toes and fingers light fawn with dark brown blotches on joints. Ventral surface of throat, trunk, limbs, and tail white. Subdigital lamellae and ventral scales on hands and feet dark brown.

Coloration in life: MDLS whitish beige on head and anterior parts of trunk, gradually turning into light orange beige on tail (Figure 6A). DLLS and flanks grayish brown, slightly golden. Limbs and digits light grayish, scattered with dark brown spots. Lateral surfaces of tail irregularly mottled in light brown and light orange beige. DTM as narrow dark brown stripe running from posterior corner of eye posteriorly (Figure 6B).

Variation: For variation of traits in paratypes see Table 2. In general, members of the type series well agree with the description of the holotype. Certain variation was observed in prefrontal positions, which are broadly contacting with each other in most specimens, but slightly touching each other in ZMMU R-13934-101 and ZMMU R-13920-57 and are not in contact in ZMMU R-13934-112. Paratype ZMMU R13449 has MDLS wider than PVDS and brighter orange coloration of tail, becoming light orange toward sacrum (Figure 6C). Paratype ZFMK 90419 shows a brighter coloration of light dorsal stripes, with dorsal tail surface being intensely orange. A specimen from Khao Soi Dao NP, Thailand (Figure 6D, not collected) shows a very similar coloration pattern, with even brighter orange-reddish coloration of tail and MDLS; based on this photo record, we assume that this specimen belongs to *Lipinia trivittata* **sp. nov.** We did not reveal any sexually dimorphic characters in this species.

Distribution: Distribution of the new species is presented in Figure 1. *Lipinia trivittata* **sp. nov.** is reliably reported from hilly and mountainous areas of southern Vietnam–Langbian Plateau and its foothills (Dak Lak, Lam Dong and Binh Phuok Provinces), as well as from the Bay Nui Hills in southern Vietnam (An Giang Province) and northern Cambodia: Kulen Prum Tep NP (Preah Vihear Province). Sequences of a tissue sample from a non-collected specimen originating from Phu Quoc Island of Vietnam confirm the presence of *Lipinia trivittata* **sp. nov.** on the island (Figure 1, locality 24). A photo record of *Lipinia trivittata* **sp. nov.** from Khao Soi Dao NP in Chanthaburi Province of eastern Thailand (Figure 6D) indicates that the range of the species is likely wider than currently known and possibly extends to the Cambodian part of the Cardamoms. Further studies are required to clarify the distribution of the new species.

Natural history: Forest arboreal species, occurring throughout primary and old secondary montane and hill dipterocarp forests to disturbed forests, bamboo groves, and pine montane forests, known from elevations of 300 to 1 100 m a. s. l. In the type locality (Chu Yang Sin NP, Dak Lak

Province, Vietnam), the new species was observed in montane pine forests dominated by *Pinus kesiya* Royle ex Gordon; and observed in the day climbing on logs or trunks of large trees while foraging for small insects (mostly ants). In Bu Gia Map NP, Binh Phuok Province, a specimen of the new species was collected on the ground while it was crossing a road in a bamboo grove at midday. In Cambodia, the female paratype was collected from the southeastern part of KPWS while it was actively foraging on a fallen tree trunk at midday in a disturbed semi-evergreen forest at 70 m a.s.l.; this locality is located ~60 km from the *L. microcercus* record in KPWS. Gravid females were not recorded. Juveniles were observed in May–June. Clutch size is unknown.

Comparisons: Comparisons are based on the original descriptions or descriptions provided in broader faunal and taxonomic publications (citations in the Materials and Methods section above). For distribution notes of each of the compared congeners, see the comparison section within the *L. microcercus* account above as well as Figure 1.

Morphological comparisons between the four members of the *L. vittigera* species complex from mainland Southeast Asia are summarized in Table 1. In general, *Lipinia trivittata* **sp. nov.** resembles the other members of the Southeast Asian *L. vittigera* complex. However, the new species can be differentiated based on the following opposing combination of characters (see Table 1 for details): *L. vittigera sensu stricto* (Boulenger, 1894): 15–16 subdigital lamellae under finger IV; flanks with dark and pale spots; LDS absent or indistinct; *Lipinia vassilievi* **sp. nov.** (herein): 10–11 supraciliaries; 14–15 subdigital lamellae under finger IV; 19–21 subdigital lamellae under toe IV; LDS and VDSL dissolving into two rows of irregular dark blotches; *L. microcercus* (Boettger, 1901) **stat. nov.**: MDLS narrow (one scale wide at midbody), PVDS continuing on tail; distinct LDS present from temporal region to anterior parts of tail.

Lipinia trivittata **sp. nov.** can be compared with other congeners bearing a middorsal light stripe by their opposing character combinations: *L. albodorsalis*: SVL up to 54 mm; 22–25 midbody scale rows; dorsum pale yellow with a dark lateral stripe; *L. infralineolata* (Günther): SVL to 49 mm; 22 midbody scale rows; *L. leptosoma*: 7–10 lamellae under toe IV; *L. longiceps*: 24 midbody scale rows; snout elongated; back light brown with two dorsolateral stripes converging on tail base; tail golden yellow; *L. macrotympanum*: 21–23 midbody scale rows; prefrontals separated; hindlimbs and forelimbs not meeting when adpressed; *L. miangensis*: 24 midbody scale rows; back golden with two dark brown longitudinal stripes from snout to tail; dark line from eye to insertion of forelimb; *L. nitens*: SVL to 33.6 mm; external ear opening replaced by scaly dimple; back metallic green with pale yellow vertebral stripe; *L. noctua*: dorsum brown with light vertebral stripe, starting with wide and contrasting light spot on head; dark paravertebral stripes with irregular borders, often broken into row of irregular dark blotches; *L. pulchella*: 22–26 midbody scale rows; and 24–31 lamellae under toe IV; only one light whitish stripe present on dorsum, from snout to tail tip,

becoming yellowish from midbody toward tail; *L. pulchra*: dorsum black with five greenish light stripes; *L. rabori*: SVL to 51.0 mm in males and 54.8 mm in females; 22 midbody scale rows; *L. relicta*: SVL to 56 mm; 20 midbody scale rows; 16–18 lamellae under toe IV; tail thick; light vertebral line present and labials each bearing small white spot; lateral dark stripe present from eye to insertion of hindlimbs; *L. rouxi*: dorsum brown, dark paravertebral stripes, with irregular borders, often broken into row of irregular dark blotches; *L. septentrionalis*: 24–26 midbody scale rows; light middorsal stripe as well as brown paravertebral stripes each bearing narrow black contour; *L. subvittata*: SVL 47–56 mm; dorsal longitudinal stripes extending to forearm region; 22 midbody scale rows; *L. vulcania*: 17 lamellae under toe IV; limbs not meeting when adpressed; dorsum brownish, scattered with dark brown spots; dark lateral stripe, scattered with whitish or yellowish spots.

Remaining congeners can be distinguished from *Lipinia trivittata* **sp. nov.** by absence of light middorsal stripe: *L. auriculata*; *L. cheesmanae*; *L. inexpectata*; *L. nototaenia*; *L. occidentalis*; *L. sekayuensis*; *L. semperi*; *L. surda*; *L. venemai*; and *L. zamboangensis*.

Remarks: In his description of *Lygosoma vittigerum kronfanum*, Smith (1922) reported on geographic variation in number of stripes on dorsum in Indochinese *Lipinia*: in addition to the typical form (*L. vittigera sensu stricto* from Sumatra and Malayan Peninsula) with one distinct vertebral stripe on dorsum and Indochinese form (now treated as *L. microcercus* **stat. nov.**) with five stripes on dorsum, he reported a juvenile specimen from northern Siam (now Thailand) with three dorsal light stripes and stated that further sampling may show this three-striped form to be taxonomically distinct. We were unable to locate and examine this specimen; however, we assume that it may possibly represent the first discovery of *Lipinia trivittata* **sp. nov.** Some records of *L. vittigera* from Cambodia (Grismer et al., 2011: 62; Mahony, 2008, p. 239) and southern Vietnam (Vassilieva et al., 2016, p. 167) may also correspond to this species, though this requires further confirmation.

Lipinia vassilievi **sp. nov.**

Figure 6E–F; Figure 7I–J; Figure 15; Tables 1, 2.

Holotype: ZMMU R14604, adult male (Figure 15), collected by Dmitry F. Fedorenko and Anna B. Vassilieva in a montane forest in Chu Mom Ray NP, Kon Tum Province, Vietnam (N14.49583°, E107.71947°; 810 m a.s.l.) on 30 March 2015.

Diagnosis: Small (SVL to 39.4 mm) species of *Lipinia*, differentiated from congeners by the following combination of external traits: external ear opening present; lower eyelid bearing large transparent spectacle; 30 midbody scale rows; 56 middorsal scales between parietals and point above vent; 15/14 subdigital lamellae under finger IV; 21/19 lamellae under toe IV; prefrontals in broad contact; seven supralabials, seven infralabials; broad middorsal light stripe from snout tip to tail base; two paravertebral dark stripes from supraoculars

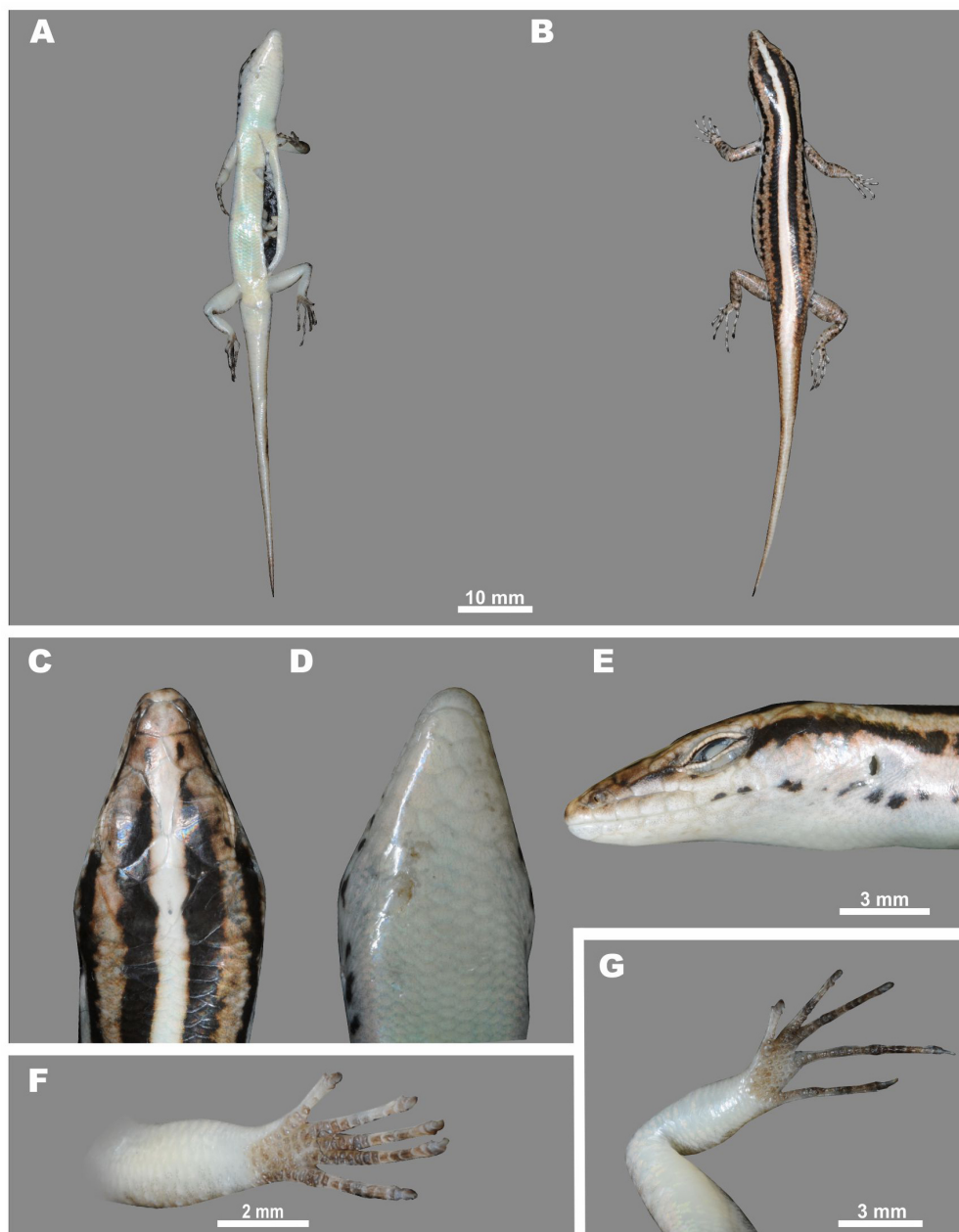


Figure 15 Holotype of *Lipinia vassilievi* sp. nov. (ZMMU R14604, male) in preservative

A: General ventral view; B: General dorsal view; C: Head dorsal view; D: Head ventral view; E: Head lateral view; F: Left forelimb in volar view; G: Left hindlimb in thenar view. Photos by Nikolay A. Poyarkov.

toward tail, continuing on anterior part of tail; two distinct dorsolateral light stripes; lateral dark stripe from temporals to groin dissolving into row of irregular black spots; one lateral light stripe, separated from belly by row of large black spots between ear opening and groin.

Etymology: The name of the new species is a Latinized patronymic adjective in genitive plural, possessive form of the family name Vassiliev. This species is named in honor of Prof.

Boris D. Vassiliev, a professor of herpetology from the Department of Vertebrate Zoology of Lomonosov Moscow State University for the last 50 years; he has nurtured and educated several generations of Russian herpetologists, including three co-authors of the present paper. In the last 30 years, he has participated in several expeditions to central and southern Vietnam.

Description of holotype: Adult male, SVL 39.4 mm (Figure

15A–B), TaL 44.5 mm; Snout acute, SL 4.4 mm; nostrils oriented laterally, oval, situated closer to snout tip than to orbit, END 3.1 mm; head elongated, HL 9.1 mm, HW 6.1 mm, HL/HW ratio 1.5, slightly flattened, HH 4.3 mm, HL/HH ratio 2.1; rostral broad, visible in dorsal view, posterior border almost straight, contact zone with nasals slightly emarginated, frontonasal wider than long; frontal elongated, arrow-shaped, wider anteriorly; prefrontals large, in contact medially (Figure 7J), laterally and posteriorly in contact with loreals, enlarged presupraocular, first supraocular, frontal, and frontonasal; two frontoparietals in broad median contact; interparietal arrow-shaped, wider anteriorly; parietals in contact behind interparietal, anteriorly in contact with postsupraoculars, fourth supraocular, nuchals, and frontoparietals; seven nuchals; four supraoculars; one enlarged presupraocular, visible from above; 10/11 supraciliaries; nostrils located within nasals; postnasal absent; two loreals, slightly elongated, second longer than first; two enlarged presuboculars, separating supralabials III and IV from eye; seven supralabials, supralabial V largest, in contact with orbit; two postsuboculars, separating supralabial VI from orbit; six postsupraoculars (pretemporals); one primary temporal; two secondary temporals, dorsal largest; two postsupralabials; lower eyelid bearing large transparent spectacle; scales on upper row of lower eyelid small, 12 in number; mental wider than long; one postmental, in contact with first infralabial and anterior portion of second infralabial; seven infralabials; three pairs of chinshields, first pair in contact medially, second pair separated by one scale, third pair separated by three scales; external ear opening visible and subcircular (Figure 7I).

Body slender (Figure 15A–B), TrunkL 18.7 mm; head slightly distinct from neck and body; 56 middorsal scales from parietal to point above vent, scales in four median longitudinal rows enlarged; ventrals in 66 rows, counted from first postgular to preanal scales; body scales smooth, subcycloid; 28 scales around midbody; four slightly enlarged preanals; Tail relatively long, TaL/SVL ratio 1.0, tip rounded; tail gradually tapering to point; median row of subcaudals enlarged; Limbs slender, pentadactyl, and clawed; forelimb and hindlimb meeting when adpressed; subdigital lamellae under finger IV: 15/14 (Figure 15F); subdigital lamellae under toe IV: 21/19 (Figure 15G); all subdigital lamellae enlarged.

Coloration in preservative: MDLS whitish, from head to tail base, widening at point above vent and merging into light dorsal coloration of tail (Figure 15B). MDLS on midbody about two scales wide. Two black PVDS from supraoculars to tail base, about one scale wide at midbody, merging into brown lateral tail coloration. Outer margin of PVDS frayed. Two grayish brown DLLS, from supraoculars to tail base, margins frayed. Two LDS, dissolving into series of irregular black blotches and markings, starting on loreals, running down to groin. LLS grayish white, separated from light cream ventral trunk surface by row of smaller irregular black spots (VLDS) between gular region and groin. DTM as narrow black stripe, about same width as DLLS above, running from posterior margin of eye to temporal region and terminating on neck

sides (Figure 15E). Labials and surrounding of outer ear opening fawn white. Dorsal surface of tail cream, becoming darker on lateral sides (Figure 15A). Dorsal surface of limbs grayish brown scattered with irregular light and dark spots. Toes and fingers light fawn with dark brown blotches on joints. Ventral surface of throat, trunk, limbs, and tail whitish.

Coloration in life: MDLS whitish beige on head and neck, gradually turning fawn orange over trunk toward tail (Figure 6E); PVDS, LDS, and VLDS spots brownish black; DLLS light brown; LLS grayish white; limbs and digits dark brown, scattered with lighter beige and dark brown spots; digits fawn with dark brown spots on joints; labials fawn white (Figure 6F); throat and belly white; tail fawn orange, with increasing intensity toward tail tip; lateral surfaces of tail orange brown.

Distribution: Figure 1 shows the known distribution of the new species. The type locality of *Lipinia vassilievi* **sp. nov.** is located in Chu Mom Ray NP in Kon Tum Province of Vietnam, a southern outcrop of the Central (or Kon Tum) Plateau of the central Annamites (=Truong Son mountains). Sequences of tissue samples from two non-collected specimens (tail tips) originating from Virachey NP, Ratanakiri Province in eastern Cambodia, confirm the presence of *Lipinia vassilievi* **sp. nov.** in the country (Figure 1, locality 19); the Cambodian locality is situated about 50 km SW from the type locality. It is likely that the new species has a wider distribution extending to other areas of the Central Plateau foothills in central Vietnam, northern Cambodia, and, possibly, southern Laos (Champasak and Attapeu Provinces). Further research is needed to clarify the distribution range of *Lipinia vassilievi* **sp. nov.**

Natural history: The holotype was collected under bark of a large tree close to a stream in a mixed montane polydominant forest at an elevation of 810 m a.s.l. Specimens from Virachey NP in Ratanakiri Province of Cambodia were recorded on the ground crossing a road.

Comparisons: The only specimen of *Lipinia vassilievi* **sp. nov.** we were able to examine morphologically was the holotype; the two other samples of this species from Ratanakiri Province of Cambodia included in the phylogenetic analyses were tissue samples (tail tips), the respective voucher specimens were not collected. Comparisons are based on original descriptions or descriptions provided in broader faunal and taxonomic publications (citations in the Materials and Methods section above). For distribution notes of each of the compared congeners, see the comparison section within the *L. microcercus* **stat. nov.** account above as well as Figure 1.

Morphological comparisons between the four members of the *L. vittigera* species complex from mainland Southeast Asia are summarized in Table 1. The members can be differentiated by the following opposing combination of traits: *L. vittigera sensu stricto* (Boulenger, 1894): PVDS with straight margins on both sides; flanks with dark and pale spots (LDS, LLS absent or indistinct); *Lipinia trivittata* **sp. nov.**: 20–

26 subdigital lamellae under finger IV; PVDS with straight margins on both sides, not continuing on tail; LDS only present on anterior third of trunk; *L. microcerus* (Boettger, 1901) **stat. nov.**: MDLS narrow (one scale wide at midbody), PVDS with straight margins on both sides, continuing on tail; LDS continuous, present from temporal region to anterior parts of tail.

Further, those congeners bearing a middorsal light stripe can be distinguished from *Lipinia vassilievi* **sp. nov.** by the following opposing traits: *L. albodorsalis*: SVL to 54 mm; 22–25 midbody scale rows; dorsum pale yellow with dark lateral stripe; *L. infralineolata*: SVL to 49 mm; 22 midbody scale rows; *L. leptosoma*: 7–10 lamellae under toe IV; *L. longiceps*: 24 midbody scale rows; snout strongly elongated; dorsum light brown with two dorsolateral stripes converging on tail base; tail golden yellow; *L. macrotympanum*: 21–23 midbody scale rows; prefrontals separated; hindlimbs and forelimbs not meeting when adpressed; *L. miangensis*: 24 midbody scale rows; back golden with two dark brown longitudinal stripes from snout to tail; *L. nitens*: SVL to 33.6 mm; external ear opening replaced by scaly dimple; back metallic green with pale yellow vertebral stripe; *L. noctua*: dorsum brown with light vertebral stripe, starting with wide and contrasting light spot on head; dark paravertebral stripes with irregular borders, often broken into row of irregular dark blotches; *L. pulchella*: 22–26 midbody scale rows; 24–31 lamellae under toe IV; only one light whitish stripe present on dorsum, from snout to tail tip, becoming yellowish from midbody toward tail; *L. pulchra*: dorsum black with five greenish light stripes; *L. rabori*: SVL to 51.0 mm in males and 54.8 mm in females; 22 midbody scale rows; *L. relicta*: SVL to 56 mm; 20 midbody scale rows; tail thick; light vertebral line present and labials each bearing small white spot; lateral dark stripe present from eye to insertion of hindlimbs; *L. rouxi*: dorsum brown, dark paravertebral stripes, with irregular borders, often broken into row of irregular dark blotches; *L. septentrionalis*: 24–26 midbody scale rows; one cream vertebral stripe, broadening toward tail; *L. subvittata*: SVL to 56 mm; dorsal longitudinal stripes extending to forearm region; 22 midbody scale rows; *L. vulcania* from the Philippines (Mindanao and Luzon Islands): 17 lamellae under toe IV; limbs not meeting when adpressed; dorsum brownish, scattered with dark brown spots; dark lateral stripe, scattered with whitish or yellowish spots.

The remaining congeners can be distinguished from *Lipinia vassilievi* **sp. nov.** by absence of light middorsal stripe: *L. auriculata*; *L. cheesmanae*; *L. inexpectata*; *L. miotis*; *L. nototaenia*; *L. occidentalis*; *L. sekayuensis*; *L. semperi*; *L. surda*; *L. venemai*; and *L. zamboangensis*.

DISCUSSION

Phylogenetic studies of the genus *Lipinia* have been long neglected; an unpublished PhD thesis of Linkem (2013) indicates that the genus represents a non-monophyletic assemblage of several distantly related lineages of sphenomorphine skinks. Grismer et al. (2016) approached the

phylogenetic relationships of *Lipinia* skinks by analyzing 1 035 bp of *ND2* mtDNA gene. Among other samples, they included three samples of "*L. vittigera*" in their analysis. Their study strongly suggested monophyly of the *L. vittigera* species complex and deep genetic divergence between the specimens examined, indicating that its taxonomy is likely incomplete. In the phylogeny of Grismer et al. (2016), the specimen of *L. vittigera* from Pinang (Malaysia) was more closely related to a specimen from Pursat (Cambodia) than to a specimen from Nan (Thailand). Thus, taxonomic affinities of these specimens require clarification.

In the present paper, we applied *COI* DNA-barcoding to assess the taxonomic diversity of members of the *L. vittigera* species complex from Indochina. The resulting phylogenetic tree is not resolved in a number of major basal nodes (Figure 3) and cannot be used to discuss phylogenetic relationships within *Lipinia*. However, our data clearly support the presence of at least four distinct and highly divergent mtDNA lineages within *Lipinia* in mainland Southeast Asia. Our study demonstrates that these lineages are also different in external morphology and coloration pattern and thus warrant recognition as separate species, two of which are new to science. It is remarkable that the presence of one of these new species was predicted almost 100 years ago (Smith, 1922).

Our study also raises many questions on the taxonomy and distribution of the *L. vittigera* species complex members in mainland Southeast Asia. Molecular and morphological differentiation of *L. vittigera sensu stricto* from Mentawai, Sumatra, Malaysia, southern Thailand, and Borneo need to be examined in greater detail; our preliminary data and previously published observations (Grismer, 2011b) suggest the presence of at least two morphologically distinct lineages within *L. vittigera sensu stricto*. Morphological examination of the type series of *Leiopisma pranensis* Cochran, 1930 suggests that this taxon is more closely related to *L. microcerus* **stat. nov.** rather than to *L. vittigera sensu stricto*, as suggested earlier (Smith, 1935; Taylor, 1963). However, samples from western and northern Thailand were lacking in our analysis. The phylogenetic position and taxonomic status of *Lipinia* populations from mainland Thailand and Myanmar require further molecular and morphological studies. We assume that the geographic border between the ranges of *L. vittigera sensu stricto* and other members of the species complex in Indochina probably coincides with the Isthmus of Kra; however, this assumption needs to be verified by further studies. *Lipinia microcerus* **stat. nov.** is assumed to be the most widespread *Lipinia* species in Indochina. However, while its range in Vietnam and Cambodia is well documented, its distribution in Thailand and Laos requires further study.

Our preliminary research revealed the presence of three distinct mtDNA lineages within *Lipinia trivittata* **sp. nov.**, corresponding to populations from Cambodia, Phu Quoc, and mainland Vietnam (Figure 3). Though the ranges of the three species in the *L. vittigera* species complex recorded in Indochina are largely overlapping, none have yet been found in sympatry. In KPWS in Cambodia, *L. microcerus* **stat. nov.**

and *Lipinia trivittata* **sp. nov.** were recorded in different sectors of the WS, ca. 60 km from each other. In the Langbian Plateau, records of *L. microcercus* **stat. nov.** (from Bao Loc) and *Lipinia trivittata* **sp. nov.** (from Loc Bao) are separated by a distance of ca. 45 km. Future research is needed to clarify the actual distribution patterns and habitat preferences of Indochinese *Lipinia* species as well as possible sympatry.

Our study raises the total number of *Lipinia* species known for mainland Southeast Asia to six. This underscores that many widely distributed lizard species in Indochina actually represent species complexes (Grismer et al., 2012, 2018; Murdoch et al., 2019 and references therein). Our work provides further evidence that the herpetofaunal diversity of Indochina is currently underestimated. As deforestation and habitat destruction are progressing at an increasing rate in Southeast Asia (Meyfroidt & Lambin, 2008), further herpetological surveys and taxonomic expertise are urgently needed to catalog its biodiversity before elimination.

Key to species of *Lipinia* Gray, 1845 from mainland Southeast Asia

The following preliminary key can be used as a guide for the identification of *Lipinia* species occurring in mainland Southeast Asia and its offshore islands.

- 1a) Dorsum uniformly brown, outer ear opening covered with scales 2
- 1b) Dorsum bearing light middorsal stripe, flanked by two dark paravertebral stripes 3
- 2a) 56 paravertebral scale rows; 65 ventral scale rows; 10 subdigital lamellae under finger IV; 15 subdigital lamellae under toe IV; subcaudals slightly enlarged
..... *L. sekayuensis* from Peninsular Malaysia
- 2b) 64–65 paravertebral scale rows; 75 ventral scale rows; 13–14 subdigital lamellae under finger IV; 17–20 subdigital lamellae under toe IV; subcaudals not enlarged
..... *L. surda* from Peninsular Malaysia and islands of Seribu Archipelago
- 3a) Lateral dark stripe on trunk continuous line or row of larger dark spots 4
- 3b) Lateral dark stripe on trunk absent; middorsal light stripe broad (two scales wide at midbody); 15–16 subdigital lamellae under finger IV; no distinct dark or light stripes present on trunk
..... *L. vittigera sensu stricto* from Peninsular Malaysia, Southern Thailand (south of Isthmus of Kra), Mentawai Islands, Sumatra, and Borneo
- 4a) Width of paravertebral dark stripes subequal to middorsal light stripe 5
- 4b) Paravertebral dark stripes broader than middorsal light stripe
..... *L. microcercus* **stat. nov.** from southern Vietnam, Cambodia, and Thailand
- 5a) Lateral dark stripe and ventrolateral dark stripe dissolving into series of distinct dark spots, present between axilla and groin; 19–21 subdigital lamellae under toe IV
..... *Lipinia vassilievi* **sp. nov.** from central Vietnam.
- 5b) Lateral dark stripe on trunk not reaching groin, distinct on

anterior third of trunk, dissolving into faint, indistinct spots on second third of trunk; 29–33 subdigital lamellae under toe IV

..... *Lipinia trivittata* **sp. nov.** from southern Vietnam, Cambodia and eastern Thailand

NOMENCLATURAL ACTS REGISTRATION

The electronic version of this article in portable document format represents a published work according to the International Commission on Zoological Nomenclature (ICZN), and hence the new names contained in the electronic version are effectively published under that Code from the electronic edition alone (see Articles 8.5–8.6 of the Code). This published work and the nomenclatural acts it contains have been registered in ZooBank, the online registration system for the ICZN. The ZooBank LSIDs (Life Science Identifiers) can be resolved and the associated information can be viewed through any standard web browser by appending the LSID to the prefix <http://zoobank.org/>.

Publication LSID:

urn: lsid: zoobank. org: pub: 912E2BBD-C51D-4B07-88CF-FAD604E38DD3.

Lipinia trivittata LSID:

urn: lsid: zoobank. org: act: 85F0D2A2-1794-4AA5-98F2-14EEC8DDEE9D.

Lipinia vassilievi LSID:

urn: lsid: zoobank. org: act: C57629D5-D4C5-4FF9-BD0A-D4006499F1B5.

SCIENTIFIC FIELD SURVEY PERMISSION INFORMATION

Fieldwork in Vietnam was funded by the Joint Russian-Vietnamese Tropical and Technological Center (JRV TTC) and was conducted under permission of the Department of Forestry, Ministry of Agriculture and Rural Development of Vietnam (permit numbers 170/TCLN–BTTN, issued 7 February 2013; 831/TCLN–BTTN, issued 5 July 2013; 400/TCLN–BTTN, issued 26 March 2014; 547/TCLN–BTTN, issued 21 April 2016, 432/TCLN–BTTN, issued 30 March 2017). Forest Protection Departments of the Peoples' Committee of Local Administration provided permits for fieldwork and sample collection (Gia Lai Province: permit numbers 1951/UBND–NV, issued 4 May 2016, and 142/SNgV–VP, issued 11 April 2017; Lam Dong Prov.: No. 5832/UBND–LN, issued 22 October 2012). In Cat Tien NP, fieldwork was conducted in accordance with Agreement No. 37/HD on the scientific cooperation between Cat Tien NP and JRV TTC; in Bu Gia Map NP, fieldwork was conducted in accordance with Agreement No. 137/HD NCKH of 23 June 2010 on the scientific cooperation between Bu Gia Map NP and JRV TTC. In Thailand, specimens collection protocols were approved by the Institutional Ethical Committee of Animal Experimentation of the University of Phayao (certificate number 610104022); specimens were collected under approval from the Institute of Animal for Scientific Purposes Development (IAD), which

issued fieldwork permission (No. U1-01205-2558) in Thailand and export permits. In Kulen Prum Tep WS and Phom Kulen NP, fieldwork was conducted in accordance with GDANCP/MoE no: 277.

SUPPLEMENTARY DATA

Supplementary data to this article can be found online.

COMPETING INTERESTS

The authors declare that they have no competing interests.

AUTHORS' CONTRIBUTIONS

N.A.P. and P.G. designed the study; N.A.P., P.G., T.H., C.S., and E.A.D. collected materials for study; N.A.P., P.G., V.A.G., T.H., C.S., and E.A.D. discussed the results; P.G. and N.A.P. prepared the manuscript; N.A.P., P.G., and E.A.D. provided photographs and figures; P.G., V.A.G., N.A.P., and E.A.D. performed morphological analyses; V.A.G. and N.A.P. performed molecular and phylogenetic analyses; N.A.P., T.H., C.S., and P.G. provided funding and permits and revised the manuscript. All authors read and approved the final manuscript.

ACKNOWLEDGEMENTS

We are very grateful to Valentina Orlova (Zoological Museum, Moscow State University) and Gunther Köhler (Senckenberg Museum Frankfurt) for providing working facilities and permission to examine specimens under her care. We are indebted to Anna B. Vassilieva (Moscow/Ho Chi Minh City) and Eduard A. Galoyan (Moscow) for help in the field and permanent support. N.A.P. thanks Andrei N. Kuznetsov and Leonid P. Korzoun for support and organization of their work in Vietnam. We are indebted to Neang Thy for field-work support in Cambodia. P.G. is grateful to Wolfgang Böhme, Thomas Ziegler, and Nguyen Quang Truong, who provided initiation for the taxonomic study of scincid lizards in Southeast Asia. Wolfgang Böhme also contributed important comments on zoological nomenclature and etymology of *Lipinia microcercus*. We are extremely grateful to Parinya Pawangkhanant, Justin Lee and Olivier Pauwels for useful comments that helped improve the earlier version of this manuscript and to Giuliano Doria, Eduard A. Galoyan, Rachel Grill, André Koch, James Poindexter, David Sargeant/North Thailand Birding, and Vitaly L. Trounov for providing their photos for this publication.

REFERENCES

Adler GH, Austin CC, Dudley R. 1995. Dispersal and speciation of skinks among archipelagos in the tropical Pacific Ocean. *Evolutionary Ecology*, **9**(5): 529–541.

Annandale N. 1905. Contributions to Oriental Herpetology. Suppl. III. Notes on the Oriental lizards in the Indian Museum, with a list of the species recorded from British India and Ceylon. *Journal of the Asiatic Society of Bengal*, **2**(1): 139–151.

Austin CC. 1998. Phylogenetic relationships of *Lipinia* (Scincidae) from New Guinea based on DNA sequence variation from the mitochondrial 12S rRNA and nuclear c-mos genes. *Hamadryad*, **23**: 93–102.

Austin CC. 1999. Lizards took express train to Polynesia. *Nature*, **397**(6715): 113–114.

Baker N, Lim K. 2008. Wild Animals of Singapore. A Photographic Guide to Mammals, Reptiles, Amphibians and Freshwater Fishes. Pte. Ltd. and Nature Society, Singapore: Draco Publishing and Distribution, 180.

Barbour T. 1912. A contribution to the zoogeography of the East Indian islands. *Memoirs of the Museum of Comparative Zoology at Harvard College*, **44**(1): 1–204.

Bobrov VV. 1992. Notes on lizards (Reptilia, Sauria) from Southern Vietnam. *Journal of Bengal Natural History Society: New Series*, **2**(1): 17–24.

Bobrov VV. 1995. Checklist and bibliography of the lizards of Vietnam. *Smithsonian Herpetological Information Service*, (105): 1–28.

Bobrov VV, Semenov DV. 2008. Lizards of Vietnam. *Moscow, KMK*, 236. (in Russian)

Boettger O. 1901. Aufzählung einer liste von reptilien und batrachiern aus Annam. *Bericht der Senckenbergischen Naturforschenden Gesellschaft*, **1901**: 45–53. (in German)

Boulenger GA. 1894. A list of reptiles and batrachians collected by Dr. E. Modigliani on Sereinu (Sipora), Mentawai Islands. *Annali del Museo civico di storia naturale di Genova*, 613–618.

Bourret R. 1939. Notes herpétologiques sur l'Indochine française. XX. Liste des reptiles et batraciens actuellement connus en Indochine française. *Bulletin Général de l'Instruction Publique Hanoi*, **4**: 49–60. (In French)

Bourret R. 2009. Les Lézards de l'Indochine. Edition Chimaira, Frankfurt am Main, 624. (in French)

Brongersma LD. 1942. Notes on scincid lizards. *Zoologische Mededelingen*, **24**(5): 125–152.

Bucklitsch Y, Geissler P, Hartmann T, Doria G, Koch A. 2012. Rediscovery and re-description of the holotype of *Lygosoma vittigerum* (= *Lipinia vittigera*) Boulenger, 1894. *Acta Herpetologica*, **7**(2): 325–329.

Chan-ard T, Parr JWK, Nabhitabhata J. 2015. A field guide to the reptiles of Thailand. NY, USA: Oxford University Press, 352.

Cochran DM. 1930. The herpetological results made by Dr. Hugh Smith in Siam from 1923 to 1929. *Proceeding of the United States National Museum*, **77**(11): 1–39.

Cox MJ, van Dijk PP, Nabhitabhata J, Kumthorn T. 1998. A Photographic Guide to Snakes and Other Reptiles of Peninsular Malaysia, Singapore and Thailand. *Ralph Curtis Publishing*, 144.

Das I. 1997. Rediscovery of *Lipinia macrotympanum* (Stoliczka, 1873) from the Nicobar Islands, India. *Asiatic Herpetological Research*, **7**: 23–26.

Das I. 2010. A field guide to the reptiles of South-East Asia. London: New Holland Publishers, 376.

Das I, Austin CC. 2007. New species of *Lipinia* (Squamata: Scincidae) from Borneo, revealed by molecular and morphological data. *Journal of Herpetology*, **41**(1): 61–71.

Das I, Greer AE. 2002. *Lipinia nitens* (Peters, 1871): discovery of a second specimen and a redescription of the holotype. *Raffles Bulletin of Zoology*, **50**(2): 483–485.

de Rooij N. 1915. The Reptiles of the Indo-Australian Archipelago. I. Lacertilia, Chelonia, Emydosauria. Leiden (E. J. Brill), xiv+384.

Denzer W, Manthey U. 1991. A nominal checklist of the lizards inhabiting Peninsular Malaysia and Singapore. *Raffles Bulletin of Zoology*, **39**(2): 309–322.

- Felsenstein J. 1985. Confidence limits on phylogenies: an approach using the bootstrap. *Evolution*, **39**(4): 783–791.
- Felsenstein J. 2004. Inferring Phylogenies. Sunderland: Sinauer Associates.
- Fruhstorfer H. 1901. Tagebuchblätter. *Insekten-Börse*, **17**: 130–131. (in German)
- Fruhstorfer H. 1905. Tagebuchblätter. Leipzig, Frankestein & Wagner, i+721. (in German)
- Goldberg SR, Grismer LL. 2014. *Lipinia vittigera* (yellow-striped tree skink) reproduction. *Herpetological Review*, **45**(4): 697–698.
- Grandison AGC. 1972. The Gunong Benom Expedition 1967. 5. Reptiles and amphibians of Gunong Benom with a description of a new species of *Macrocalamus*. *Bulletin of the British Museum (Natural History)*, London, **23**: 45–101.
- Greer AE. 1974. The genetic relationships of the scincid lizard genus *Leiopisma* and its relatives. *Australian Journal of Zoology Supplementary Series*, **22**(31): 1–67.
- Grismer LL. 2011a. Field Guide to the Amphibians and Reptiles of the Seribuat Archipelago, Peninsular Malaysia. Edition Chimaira, Frankfurt am Main, 239.
- Grismer LL. 2011b. Lizards of Peninsular Malaysia, Singapore and Their Adjacent Archipelagos. Frankfurt: Edition Chimaira, 728.
- Grismer LL, Grismer JL, Wood PL Jr, Ngo VT, Thy N, Onn CK. 2011. Herpetology of the fringes of the Sunda Shelf: a discussion of discovery, taxonomy, and biogeography. *Bonner Zoologische Monographien*, **57**: 57–97.
- Grismer LL, Lukman HBI, Awang MT, Rizal SA, Ahmad AB. 2014. A new species of lowland skink (genus *Lipinia* Gray, 1845) from northeastern Peninsular Malaysia. *Zootaxa*, **3821**(4): 457–464.
- Grismer LL, McGuire JA, Sosa RA, Kaiser H. 2002. Revised checklist and comments on the terrestrial herpetofauna of Pulau Tioman, Peninsular Malaysia. *Herpetological Review*, **33**(1): 26–29.
- Grismer LL, Neang T, Chav T, Wood PL Jr, Oaks JR, Holden J, Grismer JL, Szutz TR, Youmans TM. 2008. Additional amphibians and reptiles from the Phnom Samkos Wildlife Sanctuary in Northwestern Cardamom Mountains, Cambodia, with comments on their taxonomy and the discovery of three new species. *The Raffles Bulletin of Zoology*, **56**(1): 161–175.
- Grismer LL, Quah ESH. 2019. An updated and annotated checklist of the lizards of Peninsular Malaysia, Singapore, and their adjacent archipelagos. *Zootaxa*, **4545**(2): 230–248.
- Grismer LL, Wood PL Jr, Quah ESH, Anuar S, Muin MA, Sumontha M, Ahmad N, Bauer AM, Wangkulangkul S, Grismer JL, Pauwels OSG. 2012. A phylogeny and taxonomy of the Thai-Malay Peninsula Bent-toed Geckos of the *Cyrtodactylus pulchellus* complex (Squamata: Gekkonidae): combined morphological and molecular analyses with descriptions of seven new species. *Zootaxa*, **3520**: 1–55.
- Grismer LL, Wood PL Jr, Syafiq MF, Badli-Sham BH, Rizal SA, Ahmad AB, Quah ESH. 2016. On the taxonomy and phylogeny of the skinks *Lipinia sekayuensis* Grismer, Ismail, Awang, Rizal, & Ahmad and *Lipinia surda* Boulenger from Peninsular Malaysia. *Zootaxa*, **4147**(1): 59–66.
- Grismer LL, Wood PL Jr, Thura MK, Zin T, Quah ESH, Murdoch ML, Grismer MS, Lin A, Kyaw H, Lwin N. 2018. Twelve new species of *Cyrtodactylus* Gray (Squamata: Gekkonidae) from isolated limestone habitats in east-central and southern Myanmar demonstrate high localized diversity and unprecedented microendemism. *Zoological Journal of the Linnean Society*, **182**(4): 862–859.
- Grismer LL, Youmans TM, Wood PL, Grismer JL. 2006. Checklist of the herpetofauna of the Seribuat Archipelago, West Malaysia with comments on biogeography, natural history, and adaptive types. *The Raffles Bulletin of Zoology*, **54**(1): 157–180.
- Grossmann W. 2010. *Lipinia vittigera vittigera* (Boulenger 1894). *Sauria*, **32**(1): 2. (in German)
- Günther R. 2000. In alten Sammlungen aus Neuguinea entdeckt: Zwei neue Arten der Gattung *Lipinia* (Squamata: Scincidae). *Salamandra*, **36**(3): 157–174. (in German)
- Hall TA. 1999. BioEdit: a user-friendly biological sequence alignment editor and analysis program for Windows 95/98/NT. *Nucleic Acids Symposium Series*, **41**: 95–98.
- Hartmann T, Ihlow F, Edwards S, Sovath S, Handschuh M, Böhme W. 2013a. A preliminary annotated checklist of the amphibians and reptiles of the Kulen Promtep Wildlife Sanctuary in Northern Cambodia. *Asian Herpetological Research*, **4**(1): 36–55.
- Hartmann T, Geissler P, Poyarkov NA Jr, Ihlow F, Galoyan EA, Rödder D, Böhme W. 2013b. A new species of the genus *Calotes* Cuvier, 1817 (Squamata: Agamidae) from southern Vietnam. *Zootaxa*, **3599**(3): 246–260.
- Hillis DM, Moritz C, Mable BK. 1996. Molecular Systematics (2nd edition). Sunderland, MA: Sinauer Associates.
- Ho TC, Nguyen VS. 1981. Preliminary results of survey on amphibians and reptiles in Tay Nguyen region. *Bao Cao Nguyen Cuu Khoa Hoc Sinh Vat Hoc, Ha Noi*, 136–144. (in Vietnamese)
- Huelsenbeck JP, Hillis DM. 1993. Success of phylogenetic methods in the four-taxon case. *Systematic Biology*, **42**(3): 247–264.
- Huelsenbeck JP, Ronquist F. 2001. MRBAYES: Bayesian inference of phylogenetic trees. *Bioinformatics*, **17**(8): 754–755.
- Jestrzanski D, Schütz S, NguyenTQ, Ziegler T. 2013. A survey of amphibians and reptiles in Chu Mom Ray National Park, Vietnam, with implications for herpetofaunal conservation. *Asian Journal of Conservation Biology*, **2**(2): 88–110.
- Katoh K, Misawa K, Kuma K, Miyata T. 2002. MAFFT: a novel method for rapid multiple sequence alignment based on fast Fourier transform. *Nucleic Acids Research*, **30**(14): 3059–3066.
- Koch A. 2012. Discovery, Diversity, and Distribution of the Amphibians and Reptiles of Sulawesi and Its Offshore Islands. *Edition Chimaira*, 374.
- Kumar S, Stecher G, Tamura K. 2016. MEGA7: Molecular evolutionary genetics analysis Version 7.0 for Bigger Datasets. *Molecular Biology and Evolution*, **33**(7): 1870–1874.
- Lamas G. 2005. A bibliography of the zoological publications of Hans Fruhstorfer (1866*–1922†). *Entomofauna*, **26**(6): 57–100.
- Leviton AE, Anderson SC, Gibbs RH. 1988. Standards in herpetology and ichthyology. Part I. Standard symbolic codes for institutional resource collections in herpetology and ichthyology. Supplement 1. Additions and corrections. *Copeia*, **1988**: 280–282.
- Leviton AE, Gibbs RH, Heal E, Dawson CE. 1985. Standards in herpetology and ichthyology: Part I. Standard symbolic codes for institutional resource collections in herpetology and ichthyology. *Copeia*, **1985**(3): 802–832.
- Linkem CW. 2013. Molecular Phylogenetics and Biogeography of Sphenomorphini (Squamata: Scincidae). Ph.D. Dissertation. Department of Ecology and Evolutionary Biology, University of Kansas, 250.
- Loveridge A. 1948. New Guinean reptiles and amphibians in the Museum of Comparative Zoology and United States National Museum. *Bulletin of the*

- Museum of Comparative Zoology Harvard, **101**(2): 305–430.
- Mahony S. 2008. *Lipinia vittigera*. *Herpetological Review*, **39**(2): 239.
- Manthey U, Grossmann W. 1997. Amphibien & Reptilien Südostasiens. Natur und Tier Verlag (Münster), 512. (in German)
- Meyfroidt P, Lambin EF. 2008. The causes of the reforestation in Vietnam. *Land Use Policy*, **25**(2): 182–197.
- Mittleman MB. 1952. A generic synopsis of the lizards of the subfamily Lygosominae. *Smithsonian Miscellaneous Collections*, **117**: 1–35.
- Mulcahy DG, Lee JL, Miller AH, Chand M, Thura MK, Zug GR. 2018. Filling the BINs of life: Report of an amphibian and reptile survey of the Tanintharyi (Tenasserim) region of Myanmar, with DNA barcode data. *ZooKeys*, **757**: 85–152.
- Murdoch ML, Grismer LL, Wood PL Jr, Neang T, Poyarkov NA, Ngo VT, Nazarov RA, Aowphol A, Pauwels OSG, Nguyen HN, Grismer JL. 2019. Six new species of the *Cyrtodactylus intermedius* complex (Squamata: Gekkonidae) from the Cardamom Mountains and associated highlands of Southeast Asia. *Zootaxa*, **4554**(1): 1–62.
- Murphy RW, Crawford AJ, Bauer AM, Che J, Donnellan SC, Fritz U, Haddad CFB, Nagy ZT, Poyarkov NA, Vences M, Wang WZ, Zhang YP. 2013. Cold code: the global initiative to DNA barcode amphibians and nonavian reptiles. *Molecular Ecology Resources*, **13**(2): 161–167.
- Nagy ZT, Sonet G, Glaw F, Vences M. 2012. First large-scale DNA barcoding assessment of reptiles in the biodiversity hotspot of Madagascar, based on newly designed COI primers. *PLoS One*, **7**(3): e34506.
- Nazarov RA, Poyarkov NA, Orlov NL, Phung TM, Nguyen TT, Hoang DM, Ziegler T. 2012. Two new cryptic species of the *Cyrtodactylus irregularis* complex (Squamata: Gekkonidae) from southern Vietnam. *Zootaxa*, **3302**(1): 1–24.
- Nazarov RA, Poyarkov NA Jr, Orlov NL, Nguyen NS, Milto KD, Martynov AA, Konstantinov EL, Chulisev AS. 2014. A review of genus *Cyrtodactylus* (Reptilia: Sauria: Gekkonidae) in fauna of Laos with description of four new species. *Proceedings of the Zoological Institute RAS*, **318**(4): 391–423.
- Neang T, Chan S, Poyarkov NA Jr. 2018. A new species of smooth skink (Squamata: Scincidae: *Scincella*) from Cambodia. *Zoological Research*, **39**(3): 220–240.
- Nguyen VS, Ho TC. 1996. Reptiles and Amphibians of Vietnam. Ha Noi: Nha Xuat Ban Khoa Hoc Va Ky Thuat, 264. (in Vietnamese)
- Nguyen VS, Ho TC, Nguyen QT. 2005. A Checklist of Amphibians and Reptiles of Vietnam. Hanoi: Agricultural Publishing House, 180. (in Vietnamese)
- Nguyen VS, Ho TC, Nguyen TQ. 2009. Herpetofauna of Vietnam. Edition Chimaira, Frankfurt am Main, 768.
- Norsham Y, Ong T. 2001. Vertebrate fauna of compartment 14, Sungai Lalang Forest Reserve, Selangor. *Journal of Wildlife and Parks*, **19**: 99–108.
- Okamoto T, Hikida T. 2012. A new cryptic species allied to *Plestiodon japonicus* (Peters, 1864) (Squamata: Scincidae) from eastern Japan, and diagnoses of the new species and two parapatric congeners based on morphology and DNA barcode. *Zootaxa*, **3436**(1): 1–23.
- Onn CK, van Rooijen J, Grismer LL, Belabut D, Muin MA, Akil M, Jamaludin H, Gregory R, Ahmad N. 2010. First report on the herpetofauna of Pulau Pangkor, Perak, Malaysia. *Russian Journal of Herpetology*, **17**(2): 139–146.
- Pauwels OSG, David P, Chimsunchart C, Thirakhupt K. 2003. Reptiles of Phetchaburi Province, Western Thailand: a list of species, with natural history notes, and a discussion on the biogeography at the Isthmus of Kra. *Natural History Journal of Chulalongkorn University*, **3**(1): 23–53.
- Posada D, Crandall KA. 1998. MODELTEST: testing the model of DNA substitution. *Bioinformatics*, **14**(9): 817–818.
- Rambaut A, Drummond AJ. 2007. Tracer v1. 5. <http://beast.bio.ed.ac.uk/Tracer>.
- Ronquist F, Huelsenbeck JP. 2003. MrBayes 3: Bayesian phylogenetic inference under mixed models. *Bioinformatics*, **19**(12): 1572–1574.
- Schmidt KP. 1928. Notes on the herpetology of Indo-China. *Copeia*, (168): 77–80.
- Semenov DV. 2001. Herpetological observations in Vu Quang National Park, Ha Tinh Province, Vietnam (Vertebrata: Amphibia et Reptilia). In: Materialy zoologo-botanicheskikh issledovaniy v Natsionalnom parke Vu Kuang (provintsiya Ha Tinh, Vyetnam) (Materials of zoological and botanical studies in Vu Quang National Park (Ha Tinh Province, Vietnam)), Moscow–Hanoi, 332–347. (in Russian)
- Semenov DV, Smirnov SV, Ho TC. 1983. Herpetofauna of Buon Luoi Station vicinity: winter ecology of scincid lizards. In: Fauna i Ecologia Zhivotnykh Vietnam (Fauna and Animal Ecology in Vietnam), Moscow, Nauka, 71–76. (in Russian)
- Smith AM, Poyarkov NA Jr, Hebert PDN. 2008. CO1 DNA barcoding amphibians: take the chance, meet the challenge. *Molecular Ecology Resources*, **8**(2): 235–246.
- Smith MA. 1922. Notes on reptiles and batrachians from Siam and Indo-China (No. 1). *Journal of Natural History Society Siam*, **4**: 203–214.
- Smith MA. 1930. The reptilia and amphibia of the Malay Peninsula from the Isthmus of Kra to Singapore, including the adjacent Islands. A Supplement to G. A. Boulenger's Reptilia and Batrachia, 1912. *Bulletin of the Raffles Museum*, **3**: 1–149.
- Smith MA. 1935. The Fauna of British India, including Ceylon and Burma. Reptilia and Amphibia. Volume II. Sauria. London: Taylor & Francis, 440.
- Smith MA. 1937. A review of the genus *Lygosoma* (Scincidae: Reptilia) and its allies. *Records of the Indian Museum*, **39**(3): 213–234.
- Solovyeva EN, Poyarkov NA, Dunayev EA, Duysebayeva TN, Bannikova AA. 2011. Molecular differentiation and taxonomy of the sunwatcher toad-headed agama species complex *Phrynocephalus* superspecies *helioscopus* (Pallas 1771) (Reptilia: Agamidae). *Russian Journal of Genetics*, **47**(7): 842–856.
- Solovyeva EN, Lebedev VS, Dunayev EA, Nazarov RA, Bannikova AA, Che J, Murphy RW, Poyarkov NA. 2018. Cenozoic aridization in Central Eurasia shaped diversification of toad-headed agamas (*Phrynocephalus*; Agamidae, Reptilia). *PeerJ*, **6**: e4543.
- Stamatakis A, Hoover P, Rougemont J. 2008. A rapid bootstrap algorithm for the RAxML web servers. *Systematic Biology*, **57**(5): 758–771.
- StatSoft, Inc. 2007. STATISTICA (data analysis software system), version 8.0. www.statsoft.com.
- Stuart BL. 1999. Amphibians and reptiles. In: Duckworth JW, Salter RE, Khounbolin K. Wildlife in Lao PDR: 1999 Status Report: 43–67, Pls. 8–10. IUCN-The World Conservation Union - Wildlife Conservation Society - Centre for Protected Areas and Watershed Management, Vientiane.
- Stuart BL, Emmett DA. 2006. A collection of amphibians and reptiles from the Cardamom Mountains, southwestern Cambodia. *Fieldiana Zoology*, (109): 1–27.
- Stuart BL, Sok K, Neang T. 2006. A collection of amphibians and reptiles from hilly eastern Cambodia. *The Raffles Bulletin of Zoology*, **54**(1):

129–155.

Stuart BL, Rowley JLL, Neang T, Emmett DA, Som S. 2010. Significant new records of amphibians and reptiles from Virachey National Park, northeastern Cambodia. *Cambodian Journal of Natural History*, **2010**: 38–47.

Sworder GH. 1933. Notes on some reptiles from the Malay Peninsula. *Bulletin of the Raffles Museum*, **8**: 101–105.

Tanner VM. 1953. Pacific island herpetology no. VII, Ulu Langat, state of Selangor, Malay. *Great Basin Naturalist*, **8**: 1–7.

Taylor EH. 1917. Snakes and lizards known from Negros, with descriptions of new species and subspecies. *Philippine Journal of Science*, **12**: 353–381.

Taylor EH. 1922. The lizards of the Philippine Islands. Department of Agriculture and Natural Resources, Bureau of Science, Government of the Philippine Islands, Manila, Publication no. 17, 269.

Taylor EH. 1935. A taxonomic study of the cosmopolitan scincoid lizards of the genus *Eumeces* with an account of the distribution and relationships of its species. *Kansas University Science Bulletin*, **23**: 1–643.

Taylor EH. 1963. The Lizards of Thailand. *The University of Kansas Science Bulletin*, **44**(14): 687–1077.

Teo RCH, Rajathurai S. 1997. Mammals, reptiles and amphibians in the

Nature Reserves of Singapore - diversity, abundance and distribution. *The Gardens' Bulletin Singapore*, **49**(4): 353–425.

Teynié A, David P, Ohler A, Launglath K. 2004. Notes on a collection of amphibians and reptiles from southern Laos, with a discussion of the occurrence of Indo-Malayan species. *Hamadryad*, **29**(1): 33–62.

Uetz P, Hošek J. 2019 (2019-1-22).. The Reptile Database. <http://www.reptile-database.org>.

Vassilieva AB, Galoyan EA, Poyarkov NA, Geissler P. 2016. A Photographic Field Guide to the Amphibians and Reptiles of the Lowland Monsoon Forests of Southern Vietnam. Frankfurt Contributions to Natural History Vol. 36, Frankfurt: Edition Chimaira, 319.

Werner F. 1910 (1909). Über neue oder seltene Reptilien des Naturhistorischen Museums in Hamburg. II. Eidechsen. *Jahrbuch der Hamburgischen Wissenschaftlichen Anstalten*. **27**(2): 1–46.

Wood PL Jr, Kaiser H, Looper S, Youmans TM, Grismer JL, Grismer LL. 2004. A first report on the herpetofauna of Pulau Besar, Johor, West Malaysia. *Hamadryad*, **28**(1–2): 106–109. (in German)

Zweifel RG. 1979. Variation in the scincoid lizard *Lipinia noctua* and notes on other *Lipinia* from the New Guinea region. *American Museum Novitates*, **2676**: 1–21.

APPENDIX I

Material examined morphologically.

Lipinia vittigera sensu stricto:

(1) MSNG 55855, Indonesia, West Sumatra, Mentawai Isl., male (holotype of *Lygosoma vittigerum* Boulenger, 1894); (2) ZFMK 48542, Malaysia, Penang, Penang Isl., male; (3) ZMMU R14477, Thailand, Surat Thani, Phanom Dist., male.

Lipinia microcercus **stat. nov.**:

(4) USNM 75591, Thailand, Prachuap Khiri Khan, Pran, male (holotype of *Leiopisma pranensis* Cochran, 1930); (5) USNM 76850, Thailand, Chiang Mai, Doi Angka, male (paratype of *Leiopisma pranensis* Cochran, 1930); (6) SMF 14593, Vietnam, Quang Nam, Phuoc Son, male (holotype of *Lygosoma microcercum* Boettger, 1901); (7) FMNH 196010, "peninsular Siam", male (paratype of *Lygosoma vittigerum kronfanum* Smith, 1922; field number M.A. Smith 4514); (8) ZFMK 90339, Cambodia, Siem Reap, Phnom Kulen NP, juvenile; (9) ZMMU R10962, Cambodia, Kampong Speu, Kirirom NP, male; (10) ZFMK 88968, Vietnam, Dong Nai, Cat Tien NP, male; (11) ZFMK 88869, Vietnam, Dong Nai, Cat Tien NP, female; (12) ZMMU R11475-1, Vietnam, Dong Nai, Cat Tien NP, female; (13) ZMMU R11475-2, Vietnam, Dong Nai, Cat Tien NP, juvenile; (14) ZMMU R11475-3, Vietnam, Dong Nai, Cat Tien NP, juvenile; (15) ZMMU R13599-9, Vietnam, Dong Nai, Cat Tien NP, male; (16) ZMMU R13599-74, Vietnam, Dong Nai, Cat Tien NP, male; (17) ZMMU R7528, Vietnam, Dong Nai, Ma Da (Vinh Cuu), male; (18) ZMMU R13337, Vietnam, Dong Nai, Cat Tien NP, male; (19) ZMMU R13843, Vietnam, Dong Nai, Ma Da (Vinh Cuu), female; (20) ZMMU R8319, Vietnam, Lam Dong, Bao Loc, female; (21) ZMMU R11184, Vietnam, Lam Dong, Cat Loc NR, female; (22) ZMMU R11165, Vietnam, Tay Ninh, Lo Go-Xa Mat NP, juvenile; (23) ZMMU R11178, Vietnam, Tay Ninh, Lo Go-Xa Mat NP, juvenile; (24) ZMMU R13698, Vietnam, Dak Lak, Yok Don NP, female; (25) ZMMU NAP-04318, Vietnam, Dak Lak, Yok Don NP, female; (26) ZMMU R4613-1, Vietnam, Gia Lai, Buon Luoi, female; (27) ZMMU R4613-2, Vietnam, Gia Lai, Buon Luoi, male; (28) ZMMU R4613-3, Vietnam, Gia Lai, Buon Luoi, male; (29) ZMMU R4613-4, Vietnam, Gia Lai, Buon Luoi, male.

Lipinia trivittata **sp. nov.**:

(30) ZMMU R13449, Vietnam, Binh Phuok, Bu Gia Map NP, male (paratype); (31) ZMMU R13934-112, Vietnam, Lam Dong, Loc Bao, male; (32) ZMMU R13934-101, Vietnam, Lam Dong, Loc Bao, juvenile; (33) ZMMU R13920-56, Vietnam, Dak Lak, Chu Yang Sin NP, male (paratype); (34) ZMMU R13920-58, Vietnam, Dak Lak, Chu Yang Sin NP, female, (holotype); (35) ZMMU R13920-57, Vietnam, Dak Lak, Chu Yang Sin NP, male (paratype); (36) ZMMU R13920-55, Vietnam, Dak Lak, Chu Yang Sin NP, male (paratype); (37) ZMMU R15199, Vietnam, An Giang, Nui Cam, male; (38) ZFMK 90419, Cambodia, Preah Vihear, Kulen Prum Tep NP, male.

Lipinia vassilievi **sp. nov.**:

(39) ZMMU R14604, Vietnam, Kon Tum, Chu Mom Ray NP, male (holotype).

Synchronization between frontal eye field and area V4 during free-gaze visual search

Ting Yan^{1,*}, Hui-Hui Zhou^{1,*}

¹ Shenzhen Institutes of Advanced Technology, Chinese Academy of Sciences, Shenzhen Guangdong 518055, China

ABSTRACT

Information flow between the prefrontal and visual cortices is critical for visual behaviors such as visual search. To investigate its mechanisms, we simultaneously recorded spike and local field potential (LFP) signals in the frontal eye field (FEF) and area V4 while monkeys performed a free-gaze visual search task. During free-gaze search, spike-LFP coherence between FEF and V4 was enhanced in the theta rhythm (4–8 Hz) but suppressed in the alpha rhythm (8–13 Hz). Cross-frequency couplings during the Cue period before the search phase were related to monkey performance, with higher FEF theta-V4 gamma coupling and lower FEF alpha-V4 gamma coupling associated with faster search. Finally, feature-based attention during search enhanced spike-LFP coherence between FEF and V4 in the gamma and beta rhythms, whereas overt spatial attention reduced coherence at frequencies up to 30 Hz. These results suggest that oscillatory coupling may play an important role in mediating interactions between the prefrontal and visual cortices during visual search.

Keywords: Synchronization; Frontal eye field (FEF); V4; Visual search

INTRODUCTION

Visual search, which incorporates active scanning of the

visual environment for a particular object (target) among other objects (distracters), is important in our daily life. Its neural mechanisms have been investigated extensively in the visual cortex, including the V1 (Dougherty et al., 2017; Spaak et al., 2012), V2 (Huang et al., 2018), and V4 (Mazer & Gallant, 2003; Motter, 2018); inferior temporal cortex (IT) (Mruczek & Sheinberg, 2007); oculomotor areas, including the frontal eye field (FEF) (Mirpour et al., 2018), lateral intraparietal area (LIP) (Ong et al., 2017), supplementary eye field (SEF) (Purcell et al., 2012), and superior colliculus (SC) (Reppert et al., 2018); and other cortical areas such as the dorsal lateral prefrontal cortex (dlPFC) (Katsuki & Constantinidis, 2012). Although many studies have focused on individual brain areas, few studies have investigated the interactions among these areas in visual search (Buschman & Miller, 2007; Ibos et al., 2013; Sapountzis et al., 2018; Zhou & Desimone, 2011).

Oscillation coupling is an important mechanism underlying neuronal interactions among brain regions (Salinas & Sejnowski, 2001; Zanos et al., 2018). A number of studies have shown that coherence across brain areas mediates important brain functions, such as selective attention (Das & Ray, 2018; Mock et al., 2018; Zhou et al., 2016), learning and memory (Liebe et al., 2012), decision-making (Amemiya & Redish, 2018; Pesaran et al., 2008), and sensory-motor processes (Yanagisawa et al., 2012). For example, covert

Received: 04 January 2019; Accepted: 29 July 2019; Online: 06 August 2019

Foundation items: This study was supported by the National Key R&D Program of China (2017YFC1307500), the National Natural Science Foundation of China (31800900), the CAS-Iranian Vice presidency for Science and Technology Joint Research Project (172644KYSB2016 0175), Guangdong Innovative and Entrepreneurial Research Team Program (2014ZT05S020), Shenzhen Municipal Grants (KQJSCX 20170731164702657, JCYJ20151030140325151, JCYJ20170413165 053031, GJHZ20160229200136090, KQTD20140630180249366)

*Corresponding authors, E-mail: ting.yan@siat.ac.cn; huihui.zhou@siat.ac.cn

DOI: 10.24272/j.issn.2095-8137.2019.055

Open Access

This is an open-access article distributed under the terms of the Creative Commons Attribution Non-Commercial License (<http://creativecommons.org/licenses/by-nc/4.0/>), which permits unrestricted non-commercial use, distribution, and reproduction in any medium, provided the original work is properly cited.

Copyright ©2019 Editorial Office of Zoological Research, Kunming Institute of Zoology, Chinese Academy of Sciences

spatial attention causes spike and local field potential (LFP) coherence to increase at the gamma band but to decrease at low frequency between the V4 and FEF (Gregoriou et al., 2009, 2012). During visual search, attention enhances spike-LFP coherence at the gamma frequency in V4 (Bichot et al., 2005), and LFP-LFP coherence at beta frequency between the prefrontal and posterior parietal cortices (Buschman & Miller, 2009). To the best of our knowledge, however, the role of coherence between the prefrontal and visual cortices during free-gaze visual search remains unknown.

In addition to phase coherence, cross-frequency phase-amplitude coupling, which measures the coupling of two oscillations with different frequencies, has also been proposed as a mechanism underlying coordination of neural activity across different brain regions (Canolty & Knight, 2010; Sweeney-Reed et al., 2014). Theta-gamma coupling, in which the phase of theta oscillation biases the power of the gamma waves, is the most common pattern found among cross-frequency couplings. Gamma power can also be modulated by alpha (Osipova et al., 2008), beta (Richter et al., 2017), and delta oscillations (Whittingstall & Logothetis, 2009). These cross-frequency couplings observed within brain areas are involved in multi-unit spike firing (Whittingstall & Logothetis, 2009) and attentional selection (Lakatos et al., 2008). Thus far, however, the role of cross-frequency coupling among different brain regions, such as the prefrontal and visual cortices, has not been investigated during free-gaze visual search.

In the current study, we recorded multi-unit and LFP signals in the FEF and V4 simultaneously while monkeys performed a free-gaze visual search task. We examined spike-LFP coherence and cross-frequency phase-amplitude coupling in the two brain regions.

MATERIALS AND METHODS

General procedures

This study was carried out in strict accordance with the guidelines for the National Care and Use of Animals (China) as approved by the Institutional Animal Care and Use Committee (IACUC) of the Shenzhen Institutes of Advanced Technology, Chinese Academy of Sciences (approval ID: SIAT-IRB-160223-NS-ZHH-A0187-003).

Two male rhesus monkeys (*Macaca mulatta*) weighing 11–15 kg were implanted under aseptic conditions with a post to fix the head and two recording chambers, one over the FEF and one over the V4 area. The location coordinates were obtained based on magnetic resonance imaging (MRI) scans. Visual stimulation and behavioral control were performed using Cortex software.

Visual stimuli and tasks

We used a feature-based attention paradigm (see details in Zhou & Desimone (2011)) in the present study. Briefly, a cell's receptive field (RF) and stimulus selectivity were first mapped using a memory-guided saccade task, with a stimulus flashed in one of 20 positions on the search array used in the visual

search task. In the task, the monkeys exhibited fixation on a central spot for 400 ms. A central cue identical to the search target was then presented for 200–2 500 ms randomly, followed by a search array with 20 stimuli. After the onset of the array, the monkeys had 4 s to find the target identical to the central cue. There were 64 stimuli in this experiment, which were combinations of one of eight colors and one of eight shapes. Each stimulus was $1.1^\circ \times 1.1^\circ$.

Recording

Multi-unit spikes and local field potentials (LFPs) were recorded from the FEF and V4 simultaneously using a Multichannel Acquisition Processor system (Plexon Inc., Dallas, USA). Up to four tungsten microelectrodes (FHC Inc., Bowdoin, USA) were used in each area. Electrodes within an area were spaced 650 or 900 μm apart. Neural signals were filtered between 250 Hz and 8 kHz, amplified and digitized at 40 kHz to obtain spike data, and filtered between 0.7 and 170 Hz to obtain LFP signals. In both monkeys, we electrically ($<50 \mu\text{A}$) stimulated the FEF and elicited eye movements. Eye movements were recorded by an infrared eye tracking system (Eye Link II, SR Research Ltd. Ontario, Canada) at a sampling rate of 500 Hz.

Data analysis

Recording sites that showed a significant visual response (Wilcoxon rank-sum test, $P < 0.05$) were included for analysis. The interval used for statistical comparisons was 50 to 250 ms after stimulus onset for the post-stimulus period and –200 to 0 ms before stimulus onset for the pre-stimulus period. Firing rates were calculated with 10 ms non-overlapping bins.

The LFP signals were pre-processed for removal of the powerline artifact and phase correction. The powerline artifact was removed as described in our previous study (Fries et al., 2008). For each LFP epoch of interest, we took a 10 s epoch out of the continuous signal with the epoch of interest in the middle and calculated the discrete Fourier transform (DFT) of the 10 s epoch at 60 Hz without any tapering. We then constructed a 60 Hz sine wave with the amplitude and phase as estimated by the DFT and subtracted this sine wave (estimated powerline artifact) from the 10 s epoch. LFP phase shifts through the headstage and preamplifier were corrected as described before (Gregoriou et al., 2009). Briefly, sinusoidal signals of known frequencies (from 0.5 Hz to 400 Hz) were injected into two channels, one through the headstage and preamplifier used in the recordings and one going directly to an A/D channel with no filtering.

The mean phase difference between the two signals was calculated for each frequency using the Hilbert transform and filter response function was determined. The empirically derived digital filter was applied to the recorded data in time reverse order to cancel potential time delays caused by the original filters. We also used the utility program provided by Plexon Inc (USA) to correct for any filter-induced time delays (FPAlign, www.plexoninc.com). Results from the two methods were similar.

We used different tapers for analysis of low and high

frequencies as described in earlier research (Fries et al., 2008). For frequencies up to 25 Hz, we used a single Hanning taper and applied fast Fourier transform to the Hanning-tapered trials. For frequencies beyond 25 Hz, we used multi-taper methods to achieve the optimal spectral concentration (Jarvis & Mitra, 2001; Mitra & Pesaran, 1999; Pesaran et al., 2002). All coherence calculations used data from the two different electrodes to preclude the possibility that spikes contributed to the LFPs recorded on the same electrode.

To investigate how visual search influenced the interactions between the FEF and V4, we calculated coherence during a 'Cue' period and 'Search' period. The Cue period was from 150 ms after cue onset to search array onset and the Search period was 150 ms after search onset to 150 ms after fixation on the target. Minimum data length for analysis was 500 ms. The trial number and length of data for the two periods were equalized to eliminate possible bias from differing sample sizes.

To isolate the effects of feature-based attention, we divided fixation during the Search period into 'Target' and 'Distracter'. During the Target-in-RF fixations, a searched-for target with at least one preferred feature of the recorded site was in its RF. During the Distracter-in-RF fixations, no stimulus sharing color or shape with the target was in the RF. To avoid the influence of saccades, only fixations followed by a saccade away from the RF were included for analysis. We also matched the stimuli in the RF across two compared conditions using the method described in our previous study (Zhou & Desimone, 2011). If the RF contained only one of the 20 stimuli in the search array, we selected fixation periods in which the stimulus in the RF was the same in the two compared conditions. If the RF contained more than one stimulus, we first selected fixation periods in which the RF contained only one stimulus that shared at least one stimulus feature with the target in the attended conditions, with no other stimuli in the RF sharing any feature with the target. We then selected no-share fixations with the same stimulus as the stimulus with the target feature for the attended trials in the same location in the RF. Only matched trials were included for analysis. Coherence was calculated in a 200 ms time window starting from the onset of the Target-in-RF or Distracter-in-RF fixations. To eliminate the effect of spike number on coherence measures, we first calculated coherence after randomizing the LFPs and spike trains across fixations within the Target-in-RF and Distracter-in-RF fixations. As coherence can include bias caused by spike number, we subtracted coherences from coherences calculated without randomization, respectively.

To isolate the effects of overt spatial attention or saccade selection, we compared coherences during 'Saccade to RF' and 'Saccade out of RF' fixations. During a Saccade to RF fixation, the saccade following fixation was toward the RF. During a Saccade out of RF fixation, the saccade following fixation was away from the RF. We selected fixations and kept the stimulus in the RF, in which the saccade ended following the Saccade to RF fixation, the same as the stimulus in the same location in the RF during the Saccade out of fixation. Coherences were calculated in a 200 ms time window starting

from the onset of the two types of fixations. To eliminate the effect of spike number on coherence, we also calculated coherences after randomizing the LFPs and spike trains across fixations within the Saccade to RF and Saccade out of RF fixations and subtracted them from the coherences calculated without randomization, respectively.

To investigate the role of cross-frequency coupling in visual search, we divided trials into 'Fast search' and 'Slow search'. In Fast search trials, monkeys took one saccade to find the target. In Slow search trials, monkeys took at least three saccades to find the target. Theta phase-gamma power and alpha phase-gamma power cross-frequency couplings in the Cue period of Fast and Slow search trials were calculated and compared. In all selected trials, cell RFs were located at the peripheral regions of the screen, therefore the cue was not in the RF. Trial number and length of data for the two conditions were equalized to eliminate possible bias from differing sample sizes.

For theta-gamma cross-frequency couplings, we used a similar method as described previously (Canolty et al., 2006). Using a two-way least-squares FIR filter (eegfilt.m from the EEGLAB toolbox), the raw LFP signal was separated into bands with center frequencies ranging from 30 Hz to 50 Hz, in 2 Hz steps with 4 Hz bandwidths. This created a set of band-pass filtered signals. Each of these signals was normalized by subtracting the temporal mean and dividing by the temporal standard deviation to create a set of normalized band-passed signals. This normalization was used to facilitate comparison between different frequency bands. Hilbert transform was applied to calculate the instantaneous amplitude and power of each normalized band-pass signal. Epochs (500 ms) centered on the time points of theta troughs were extracted from the power time series and averaged within each band across trials to produce the theta trough-triggered mean instantaneous power across gamma frequencies. To detect the theta trough, the raw LFP signals were 4–8 Hz band-pass filtered by the FIR filter. Hilbert transform was applied to calculate the instantaneous phases of the theta band. The theta trough was identified as the time point where the phase value was larger by more than five radians than the phase value of its following time point.

To quantify amplitude modulation by phase, we calculated a modulation index (*MI*) using a similar method as Tort et al. (2008). Instantaneous gamma power across 30–50 Hz was averaged and binned into 18 groups based on its associated theta phase (0–360 deg, 20 deg/bin). Gamma power within each bin was averaged. We denoted $P(j)$ as the mean gamma power at bin j . We then applied the entropy measure H , defined by:

$$H = - \sum_{j=1}^N f(j) \log f(j) \quad (1)$$

where, $N=18$ (number of bins) and $f(j)$ is given by:

$$f(j) = \frac{p(j)}{\sum_{j=1}^N p(j)} \quad (2)$$

MI is finally obtained by normalizing H by the maximum possible entropy value (H_{\max}) obtained for uniform

distribution $f(j)=1/N$ (hence H_{\max} is $\log N$):

$$MI = \frac{H_{\max} - H}{H_{\max}} \quad (3)$$

A MI value of 0 indicates a lack of phase-to-amplitude modulation and larger MI values represent stronger phase-to-amplitude couplings. To assess the statistical significance of the MI values, we calculated 200 surrogate MI values after shuffling gamma power and theta phase time series across trials. We subsequently calculated the MI value and permutation distribution to determine what percentage of data points in the permutation distribution was equal to or greater than the observed MI value (P).

To compare couplings between Fast and Slow conditions, we first calculated MI based on the data of population averages. Hilbert transform was applied to the population average of the theta trough-triggered LFPs to calculate the instantaneous theta phase. The population average of gamma power was averaged across 30–50 Hz and binned into 18 groups based on the theta phase. We calculated the differences between MI values in the two conditions ($\Delta MI_{\text{real}} = MI_{\text{Fast}} - MI_{\text{Slow}}$). We then repeated the resampling process 1 000 times and obtained the generated distribution of 1 000 values of ΔMI . Finally, we determined the percent of ΔMIs that are equal to or larger than the MI difference we actually observed (ΔMI_{real}) in the 1 000 generated ΔMIs (P). The absolute values of the MI differences were used in the above comparison.

We also calculated the alpha-gamma cross-frequency couplings. Hilbert transform was applied to the alpha (8–13 Hz) band of the LFP signals to calculate the instantaneous phases of this band. All other analyses, including alpha trough identification, data averaging, MI calculation, and statistics, were the same as those used for theta-gamma couplings.

RESULTS

Spike-LFP coherences during Cue and Search periods

Spike-LFP coherence is considered an important mechanism underlying neuronal interactions across brain regions (Zanos et al., 2018). The influence of brain functions on neuronal interactions can be reflected by changes in spike-LFP coherence (Das & Ray, 2018; Zhou et al., 2016). To investigate how visual search influenced the interactions between FEF and V4, we used multi-taper spectral methods to calculate spike-LFP coherences between the two areas and during Cue and Search periods in the visual search task. During the Cue period, V4 spikes and FEF LFPs showed peak coherence in the alpha rhythm (8–13 Hz; Figure 2A). In contrast, during the Search period, V4 spikes and FEF LFPs showed peak coherence in the theta rhythm (4–8 Hz) (Figure 2A). Furthermore, the FEF spike-V4 LFP coherences showed similar changes to the V4 spike-FEF LFP coherences during the two periods (Figure 2B). These data illustrated distinct patterns of oscillation coupling during the Cue and Search periods in the FEF and V4. In the Cue period, coherence dominated in the alpha rhythm, whereas, in the Search period,

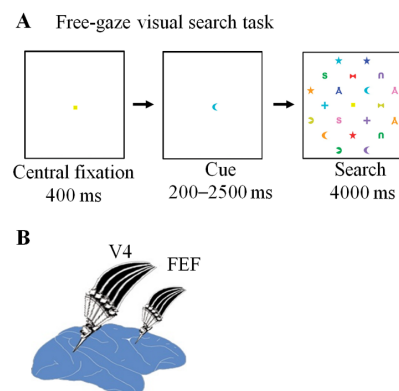


Figure 1 Task and recording sites

A: Illustration of visual search task. After center fixation for 400 ms, the monkeys were presented with a central cue identical to the searched-for target. The cue stayed on for 200–2 500 ms randomly, after which a search array with 20 stimuli was presented, and the center cue was replaced by the center fixation spot. Monkeys were allowed to make saccades after array onset and had 4 s to find the target. Monkeys had to fixate the target stimulus for 700 ms continuously to receive a juice reward. B: Illustration of simultaneous recording sites in FEF and V4.

coherence dominated in the theta rhythm.

Spike-LFP coherences within brain regions were also calculated. In the V4, the spike-LFP coherence during the Cue period was significantly stronger than the coherence during the Search period in the alpha rhythm, but significantly weaker in the theta rhythm (Figure 2C; Wilcoxon signed rank test, $P < 0.05$). Furthermore, in the FEF, coherence during the Cue period was significantly stronger than coherence during the Search period in the alpha band (Figure 2D; $P < 0.05$), but not significantly different in the theta band (Figure 2D; $P > 0.05$).

Cross frequency couplings during Cue period and search behaviors

Cross-frequency coupling has been implicated as a mechanism for coordinating local activities in different areas in cortical operations (Canolty & Knight, 2010). To examine the functional role of cross-frequency couplings in visual search, we calculated and compared the cross-frequency couplings (theta phase-gamma power and alpha phase-gamma power) in the Cue period during Fast search and Slow search trials. Figure 3A and B show the population averages of FEF theta-V4 gamma couplings in the Fast and Slow search trials, respectively. The population average was significantly stronger in the Fast search trials than in the Slow search trials (Figure 3C, two-sided permutation test, $P < 0.05$). The population averages of the theta trough-triggered FEF LFPs were the same in the Fast and Slow search trials (Figure 3C), indicating that coupling changes could not be explained by FEF theta power changes in the two trials. MI was used to quantify amplitude modulation by phase. Figure 3D shows the MI values from the two types of trials. There were no significant differences between MI values in the Fast and Slow search trials (Wilcoxon signed rank test, $P > 0.05$), suggesting

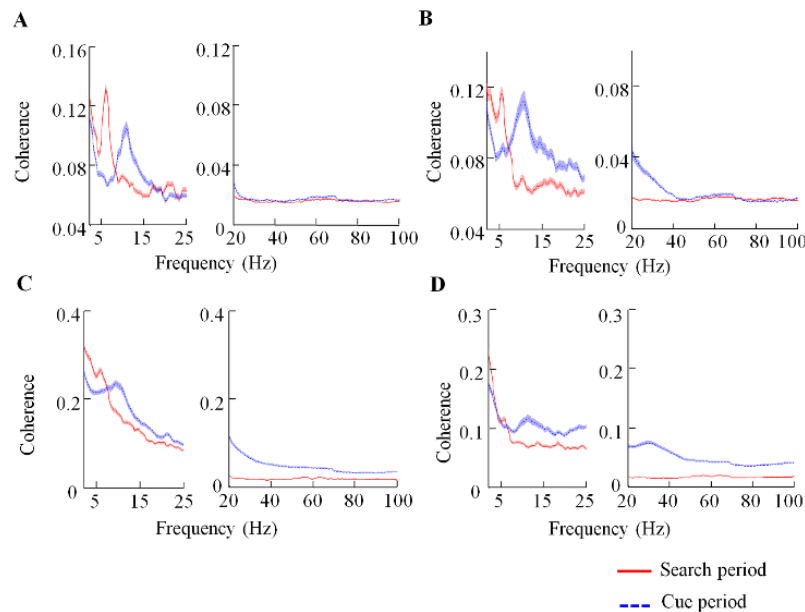


Figure 2 Spike-LFP coherences during Cue and Search periods

A: Population averages of V4 spike-FEF LFP coherences during Cue and Search periods. B: Population averages of FEF spike-V4 LFP coherences. C: Population averages of V4 spike-V4 LFP coherences. D: Population averages of FEF spike-FEF LFP coherences. SEM of population averages are marked by shading above and below averages.

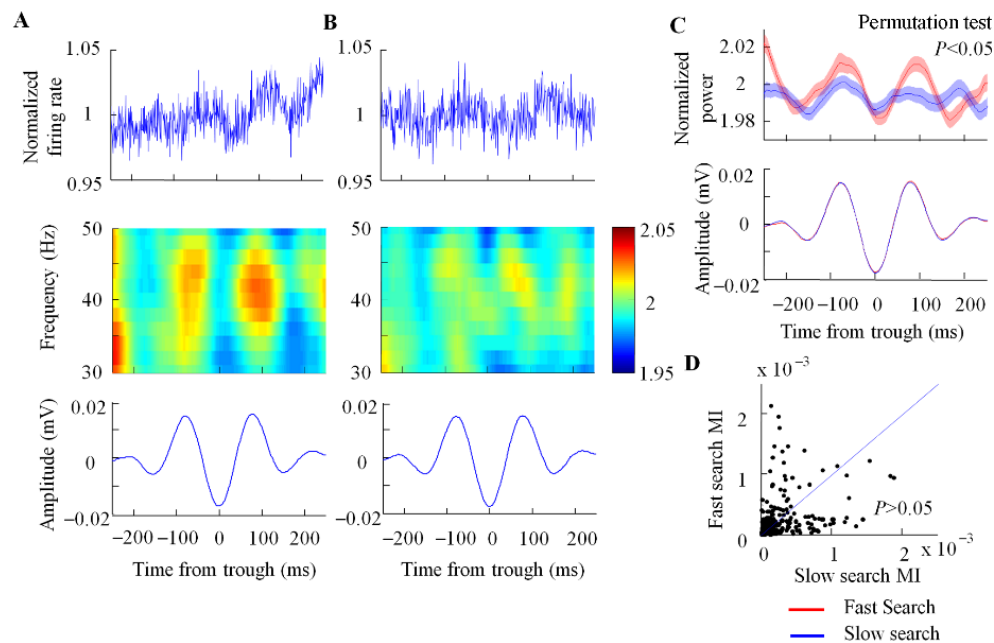


Figure 3 FEF theta-V4 gamma couplings during Cue period

A: Population average of couplings in Fast search trials. Low: Population average of FEF theta trough-triggered average of FEF LFPs. Middle: Population average of normalized V4 gamma powers aligned in FEF theta trough. Up: Population average of normalized V4 firing rates aligned in FEF theta trough. B: Population average of couplings in Slow search trials. C: Comparison of couplings in Fast and Slow search trials. Low: Population average of FEF theta trough-triggered average of FEF LFPs in Fast and Slow search trials. Up: Population average of gamma powers (averaged across 30–50 Hz) aligned in FEF theta-trough in Fast and Slow search trials. SEM of population averages are marked by shading above and below averages. D: Distribution of modulation index (*MI*) in Slow trials (X-axis) vs. Fast trials (Y-axis). *P* value is based on the Wilcoxon signed rank test.

that the increased population average of coupling in the Fast search trials may be due to a more consistent temporal relationship between V4 gamma powers and the FEF theta phase in these trials across LFP pairs. In contrast to the FEF theta-V4 gamma couplings, the FEF alpha-V4 gamma couplings were weaker in the Fast search trials than in the Slow search trials (Figure 4). Together, the cross-frequency couplings in the Cue period were related to the monkeys' search behaviors, with the higher FEF theta-V4 gamma coupling and lower FEF alpha-V4 gamma coupling associated with faster search.

Effects of attention on coherence between FEF and V4

Feature-based attention enhances spike-LFP coherence in the V4 for the attended preferred stimulus (Bichot et al., 2005). To investigate the mechanisms underlying the interaction between FEF and V4 during feature-based attention, we calculated spike-LFP coherences during fixation periods when a stimulus in the RF was the searched-for target with at least one good feature (Target-in-RF fixation) and when the same stimulus was in the RF, but shared nothing with the target (Distracter-in-RF fixation). All saccades following the Target-in-RF and Distracter-in-RF fixations were moved away from the RF to exclude the influence of spatial attention. The population averages of V4 spike-FEF LFP coherences are shown in Figure 5A. During the Target-in-RF fixations, the V4 spike-FEF LFP coherences were enhanced in the beta (~20 Hz) and gamma (~60 Hz) rhythms (Wilcoxon signed rank test, $P < 0.05$), but were suppressed at low frequencies (<15 Hz). Similar coherence changes were also observed in the FEF spike-V4 LFP (Figure 5B) and V4 spike-

V4 LFP coherences (Figure 5C). No coherence enhancement at the beta and gamma frequencies was observed within the FEF (Figure 5D). These results suggest that gamma, beta, and low frequency (<15 Hz) oscillation coupling changes were involved in the interaction between FEF and V4 during feature-based attention.

To investigate the effect of the overt spatial attention, we sorted the fixations based on the following saccade direction. Spike-LFP coherences during fixations followed by a saccade to the RF ('Saccade to RF') and fixations followed by a saccade outside of the RF ('Saccade out of RF') were calculated and compared. As shown in Figure 6, the main effect was de-synchronization at frequencies up to 30 Hz (Wilcoxon signed rank test, $P < 0.05$) under the Saccade to RF condition compared to the Saccade out of RF condition, suggesting that overt spatial attention desynchronized the oscillation coupling between FEF and V4 at low frequencies (<30 Hz).

DISCUSSION

Although neural mechanisms in the visual cortex, including the V4, IT, and prefrontal cortex, have been investigated extensively, the interactions among brain regions in visual search remain unclear. In this study, we simultaneously recorded neuronal activities in lower (V4) and higher cortical areas (FEF) while monkeys performed a visual search task. We showed that oscillation couplings between the two regions were selectively enhanced in the theta, beta, and gamma bands, but suppressed in the alpha band during the task.

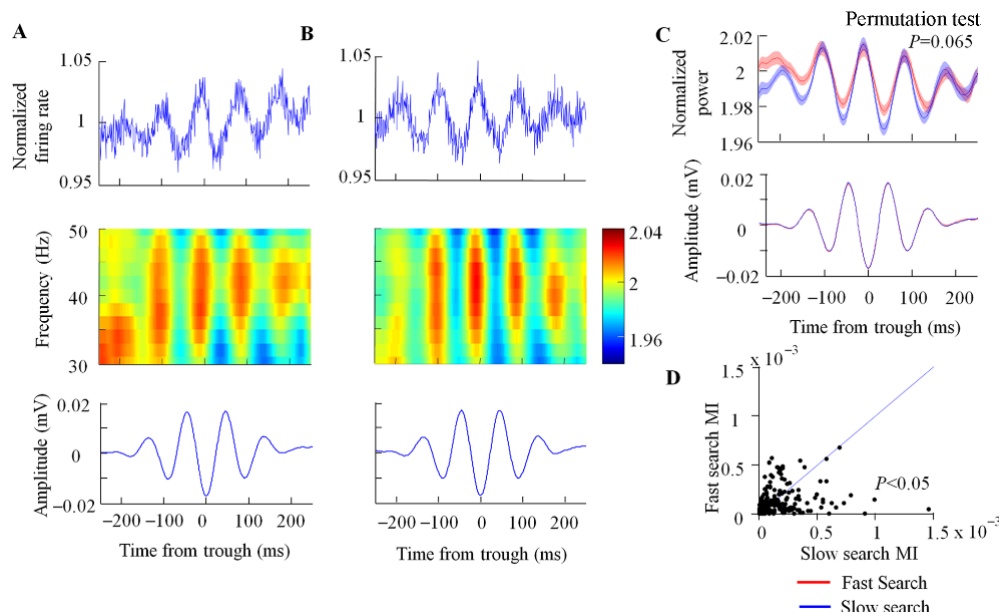


Figure 4 FEF alpha-V4 gamma couplings during Cue period

A: Population average of couplings in Fast search trials. B: Population average of couplings in Slow search trials. C: Comparison of couplings in Fast and Slow search trials. D: Distribution of modulation index (MI) in Slow trials (X-axis) vs. Fast trials (Y-axis). P value is based on Wilcoxon signed rank test.

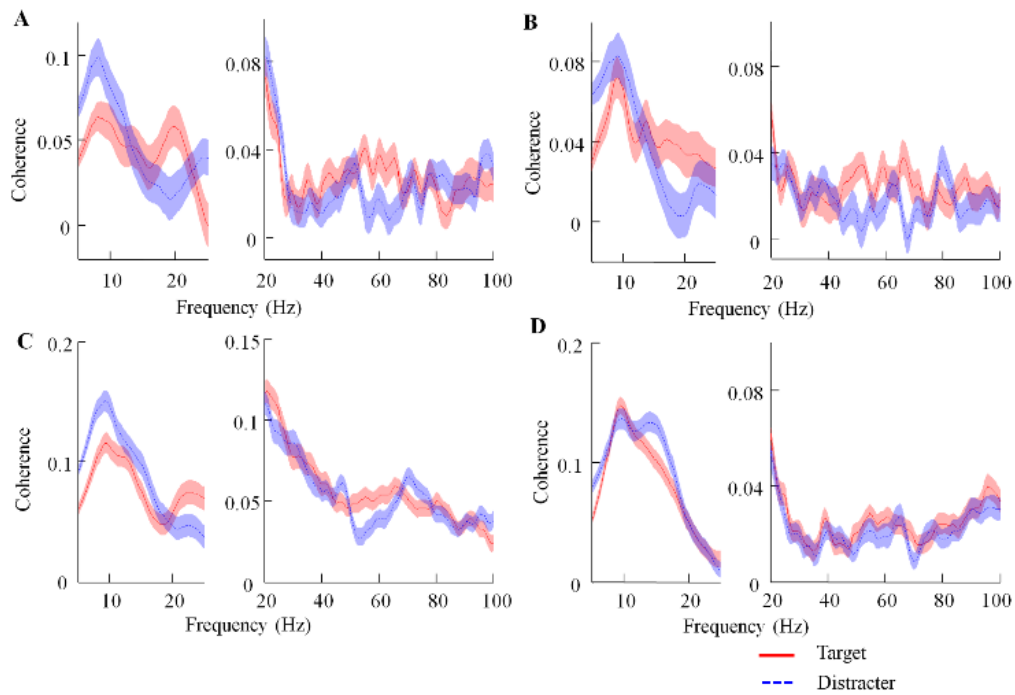


Figure 5 Spike-LFP coherences and feature-based attention

A: Population averages of V4 spike-FEF LFP coherences during target and distracter fixations. B: Population averages of FEF spike-V4 LFP coherences. C: Population averages of V4 spike-V4 LFP coherences. D: Population averages of FEF spike-FEF LFP coherences. SEM of population averages are marked by shading above and below averages.

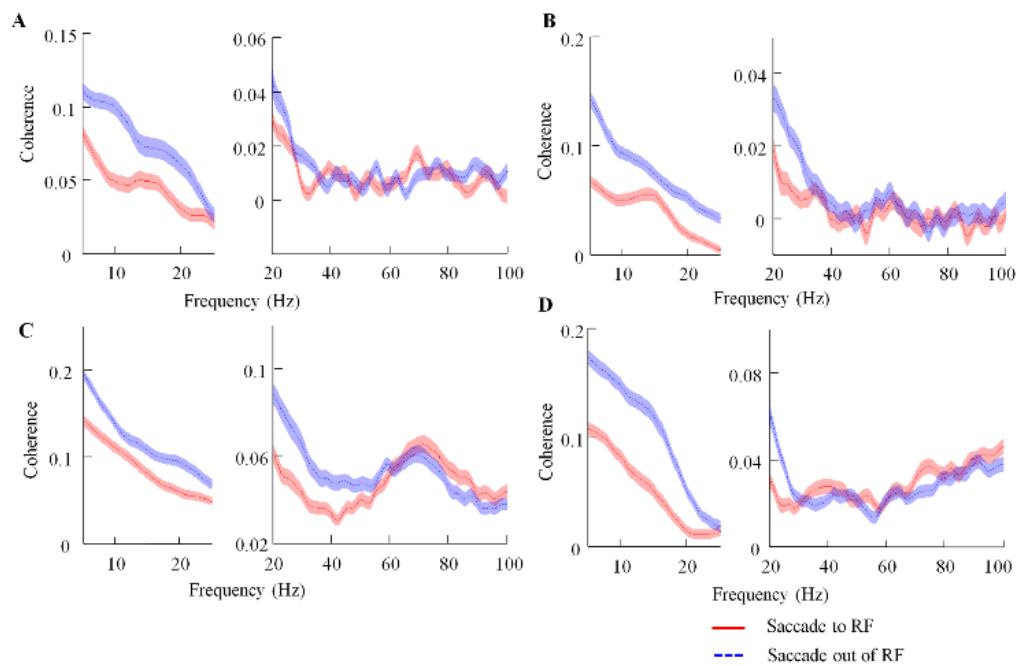


Figure 6 Spike-LFP coherences and saccade selection

A: Population averages of V4 spike-FEF LFP coherences during Saccade to RF and Saccade out of RF conditions. B: Population averages of FEF spike-V4 LFP coherences. C: Population averages of V4 spike-V4 LFP coherences. D: Population averages of FEF spike-FEF LFP coherences. SEM of population averages are marked by shading above and below averages.

Our results also showed that the dominant spike-LFP coherence between the FEF and V4 changed from the alpha rhythm during the Cue period to the theta rhythm during the Search period, suggesting that visual search enhanced spike-LFP coherence between the two regions in the theta band, but suppressed it in the alpha band. As saccades occurred during the Search period, they may also facilitate the dominant-coherence change. Neurophysiological studies suggest that changes in oscillation couplings occur to attain specific functional roles. For example, desynchronized alpha band oscillations (O'Connell et al., 2009) are considered as possible mechanisms to promote top-down attention, and gamma-band synchronization (Fries, 2015) is generally associated with bottom-up stimulus salience. These neural activities can be used to predict behavior. By recording the activities of V4 neurons when monkeys performed a change-detection task, Womelsdorf et al. (2006) found a positive relationship between the degree of gamma-band synchronization and monkey reaction time to stimulus change. Moreover, Dezfouli et al. (2018) found reaction time to be positively correlated with the amplitude of the LFPs long before (>2 s) a behavioral response. In addition, in multi-region electrophysiological studies, visual attention is reportedly related to reduced alpha oscillations between V1 and LGN (Bollimunta et al., 2011; Mock et al., 2018) and enhanced theta rhythm between V4 and TEO (Spyropoulos et al., 2018). In the present study, we extend previous findings by showing suppressed alpha and enhanced theta rhythms between FEF and V4 during the Search period, which thus promote our understanding of corticocortical communication.

In addition to spike-LFP phase coupling, we found that cross-frequency couplings during the Cue period play a key role in regulating monkey search behaviors, with the higher FEF theta-V4 gamma coupling and lower FEF alpha-V4 gamma coupling associated with faster search. In the visual system, oscillations in the gamma-frequency are thought to subserve between-area coordination (Bollimunta et al., 2011). Several cross-frequency studies have reported gamma power to be modulated with theta phase. For example, in an electrophysiological experiment, successful attention shift was accompanied by robust increases in theta-gamma phase-amplitude correlation between the anterior cingulate and prefrontal cortex (Vолоh et al., 2015). Increased theta-gamma coupling during spatial attention was also observed within the frontoparietal network (Fiebelkorn et al., 2018). As with these studies, previously described theta-gamma increase in the human visual cortex during spatial attention is related to improved behavioral performance (Landau et al., 2015). Similar to these results, the present data suggest that an increase in theta-gamma coupling is associated with enhanced visual search. Recently, however, selective attention related to theta-gamma coupling in the visual cortex has been reported (Spyropoulos et al., 2018). By recording neural activities in the MT area, Esghaei et al. (2015) reported a spatial attentional suppression of couplings between low-frequencies oscillation (1–8 Hz) and gamma (30–120 Hz) power. This spatial attention-related decrease in coupling

contrasts with our present results. This discrepancy may be due to the different tasks used in the two papers (Esghaei et al., 2015; Spyropoulos et al., 2018) and the present study. The previous studies on spatial attention applied two or three moving stimuli around the moving cue, and one stimulus overlap neuron receptive field. In the present study, however, there was no stimulus around the cue. Furthermore, the location of the target was unknown before the appearance of the search array containing 20 stimuli and monkeys had to focus on the feature property of the cue to find the target (feature-based attention). In addition, the above studies differed from our research in regard to the theta-gamma coupling relationship. The previous studies described a relationship between spatial attention and decreased theta-gamma coupling in the visual cortex, whereas we described a relationship between visual search behavior and increased theta-gamma couplings between the FEF and V4. Thus, future research is needed to clarify the above differences. Overall, we reported that gamma modulated with theta and alpha phases during the Cue period facilitated monkey search behavior. Thus, cross-frequency coupling occurred between the FEF and V4 for transmission of sensory inputs to motor responses.

Feature-based attention is a process of focusing on a specific attribute of an object. Studies examining the neural mechanisms of feature-based selection signals have found that attention to target features enhances responses to stimuli that share the target features in the ventral pre-arcuate (VPA) region of the prefrontal cortex, FEF, LIP, and V4 (Bichot et al., 2005, 2015; Ruff & Born, 2015). Moreover, when monkeys performed a task allocating attention to a color or motion signal of a moving stimulus, Katzner et al. (2009) reported a clear modulation of feature-based attention on the activities of MT neurons, which initially showed poor tuning for the object feature (color). This feature enhancement is actually used to select stimuli, or find a target, during visual search (Zhou & Desimone, 2011). In the FEF and V4, neurons synchronize their activity in the gamma frequency range during spatial attention (Gregoriou et al., 2009). In the present study, we demonstrated that these areas play similar roles during feature-based attention, as enhanced spike-LFP coherences in the gamma and beta bands and suppressed spike-LFP coherences at lower frequencies were observed between the FEF and V4.

By investigating the interactions between the FEF and V4, we demonstrated that selectively enhanced and suppressed oscillation couplings in different bands between the two regions were important for visual search. Moreover, we showed that feature-based attention modulated these couplings, thus providing insight into how visual and cognitive signals are communicated between neuronal populations.

COMPETING INTERESTS

The authors declare that they have no competing interests.

AUTHORS' CONTRIBUTIONS

H.H.Z. and T.Y. designed the study. T.Y. conducted the experiments. T.Y. drafted the manuscript with assistance from H.H.Z. All authors read and approved the final version of the manuscript.

REFERENCES

- Amemiya S, Redish AD. 2018. Hippocampal theta-gamma coupling reflects state-dependent information processing in decision making. *Cell Reports*, **22**(12): 3328–3338.
- Bichot NP, Rossi AF, Desimone R. 2005. Parallel and serial neural mechanisms for visual search in macaque area V4. *Science*, **308**(5721): 529–534.
- Bichot NP, Heard MT, Degennaro EM, Desimone R. 2015. A source for feature-based attention in the prefrontal cortex. *Neuron*, **88**(4): 832–844.
- Bollimunta A, Mo J, Schroeder CE, Ding M. 2011. Neuronal mechanisms and attentional modulation of corticthalamic alpha oscillations. *The Journal of Neuroscience*, **31**(13): 4935–4943.
- Buschman TJ, Miller EK. 2007. Top-down versus bottom-up control of attention in the prefrontal and posterior parietal cortices. *Science*, **315**(5820): 1860–1862.
- Buschman TJ, Miller EK. 2009. Serial, covert shifts of attention during visual search are reflected by the frontal eye fields and correlated with population oscillations. *Neuron*, **63**(3): 386–396.
- Canolty RT, Knight RT. 2010. The functional role of cross-frequency coupling. *Trends in Cognitive Sciences*, **14**(11): 506–515.
- Canolty RT, Edwards E, Dalal SS, Soltani M, Nagarajan SS, Kirsch HE, Berger MS, Barbaro NM, Knight RT. 2006. High gamma power is phase-locked to theta oscillations in human neocortex. *Science*, **313**(5793): 1626–1628.
- Das A, Ray S. 2018. Effect of stimulus contrast and visual attention on spike-gamma phase relationship in macaque primary visual cortex. *Frontiers in Computational Neuroscience*, **12**: 66.
- Dezfouli MP, Khamechian MB, Treue S, Esghaei M, Daliri MR. 2018. Neural activity predicts reaction in primates long before a behavioral response. *Frontiers in Behavioral Neuroscience*, **12**: 207.
- Dougherty K, Cox MA, Ninomiya T, Leopold DA, Maier A. 2017. Ongoing alpha activity in V1 regulates visually driven spiking responses. *Cerebral Cortex*, **27**(2): 1113–1124.
- Esghaei M, Daliri MR, Treue S. 2015. Attention decreases phase-amplitude coupling, enhancing stimulus discriminability in cortical area MT. *Frontiers in Neural Circuits*, **9**: 82.
- Fiebelkorn IC, Pinsk MA, Kastner S. 2018. A dynamic interplay within the frontoparietal network underlies rhythmic spatial attention. *Neuron*, **99**(4): 842–853.
- Fries P. 2015. Rhythms for cognition: Communication through coherence. *Neuron*, **88**(1): 220–235.
- Fries P, Womelsdorf T, Oostenveld R, Desimone R. 2008. The effects of visual stimulation and selective visual attention on rhythmic neuronal synchronization in macaque area V4. *The Journal of Neuroscience*, **28**(18): 4823–4835.
- Gregoriou GG, Gotts SJ, Desimone R. 2012. Cell-type specific synchronization of neural activity in FEF with V4 during attention. *Neuron*, **73**(3): 581–594.
- Gregoriou GG, Gotts SJ, Zhou H, Desimone R. 2009. High-frequency, long-range coupling between prefrontal and visual cortex during attention. *Science*, **324**(5931): 1207–1210.
- Huang G, Ramachandran S, Lee TS, Olson CR. 2018. Neural correlate of visual familiarity in macaque area V2. *The Journal of Neuroscience*, **38**(42): 8967–8975.
- Ibos G, Duhamel JR, Hamed SB. 2013. A functional hierarchy within the parietofrontal network in stimulus selection and attention control. *The Journal of Neuroscience*, **33**(19): 8359–8369.
- Jarvis MR, Mitra PP. 2001. Sampling properties of the spectrum and coherency of sequences of action potentials. *Neural Computation*, **13**(4): 717–749.
- Katsuki F, Constantinidis C. 2012. Early involvement of prefrontal cortex in visual bottom-up attention. *Nature Neuroscience*, **15**(8): 1160–1166.
- Katzner S, Busse L, Treue S. 2009. Attention to the color of a moving stimulus modulates motion-signal processing in macaque area MT: Evidence for a unified attentional system. *Frontiers in Systems Neuroscience*, **3**: 12.
- Lakatos P, Karmos G, Mehta AD, Ulbert I, Schroeder CE. 2008. Entrainment of neuronal oscillations as a mechanism of attentional selection. *Science*, **320**(5872): 110–113.
- Landau AN, Schreyer HM, Van Pelt S, Fries P. 2015. Distributed attention is implemented through theta-rhythmic gamma modulation. *Current Biology*, **25**(17): 2332–2337.
- Liebe S, Hoerzer GM, Logothetis NK, Rainer G. 2012. Theta coupling between V4 and prefrontal cortex predicts visual short-term memory performance. *Nature Neuroscience*, **15**(3): 456–462.
- Mazer JA, Gallant JL. 2003. Goal-related activity in V4 during free viewing visual search: Evidence for a ventral stream visual salience map. *Neuron*, **40**(6): 1241–1250.
- Mirpour K, Bolandnazar Z, Bisley JW. 2018. Suppression of frontal eye field neuronal responses with maintained fixation. *Proceedings of the National Academy of Sciences of the United States of America*, **115**(4): 804–809.
- Mitra PP, Pesaran B. 1999. Analysis of dynamic brain imaging data. *Biophysical Journal*, **76**(2): 691–708.
- Mock VL, Luke KL, Hembrook-Short JR, Briggs F. 2018. Dynamic communication of attention signals between the LGN and V1. *Journal of Neurophysiology*, **120**(4): 1625–1639.
- Motter BC. 2018. Saccadic momentum and attentive control in V4 neurons during visual search. *Journal of Vision*, **18**(11): 16.
- Mruczek REB, Sheinberg DL. 2007. Activity of inferior temporal cortical neurons predicts recognition choice behavior and recognition time during visual search. *The Journal of Neuroscience*, **27**(11): 2825–2836.
- O'Connell RG, Dockree PM, Robertson IH, Bellgrove MA, Foxe JJ, Kelly SP. 2009. Uncovering the neural signature of lapsing attention: electrophysiological signals predict errors up to 20 s before they occur. *The Journal of Neuroscience*, **29**(26): 8604–8611.
- Ong WS, Mirpour K, Bisley JW. 2017. Object comparison in the lateral intraparietal area. *Journal of Neurophysiology*, **118**(4): 2458–2469.
- Osipova D, Hermes D, Jensen O. 2008. Gamma power is phase-locked to posterior alpha activity. *PLoS One*, **3**(12): e3990.
- Pesaran B, Nelson MJ, Andersen RA. 2008. Free choice activates a decision circuit between frontal and parietal cortex. *Nature*, **453**(7193): 1069–1073.

406–409.

- Pesaran B, Pezaris JS, Sahani M, Mitra PP, Andersen RA. 2002. Temporal structure in neuronal activity during working memory in macaque parietal cortex. *Nature Neuroscience*, **5**(8): 805–811.
- Purcell BA, Weigand PK, Schall JD. 2012. Supplementary eye field during visual search: salience, cognitive control, and performance monitoring. *The Journal of Neuroscience*, **32**(30): 10273–10285.
- Reppert TR, Servant M, Heitz RP, Schall JD. 2018. Neural mechanisms of speed-accuracy tradeoff of visual search: saccade vigor, the origin of targeting errors, and comparison of the superior colliculus and frontal eye field. *Journal of Neurophysiology*, **120**(1): 372–384.
- Richter CG, Thompson WH, Bosman CA, Fries P. 2017. Top-Down beta enhances bottom-up gamma. *The Journal of Neuroscience*, **37**(28): 6698–6711.
- Ruff DA, Born RT. 2015. Feature attention for binocular disparity in primate area MT depends on tuning strength. *Journal of Neurophysiology*, **113**(5): 1545–1555.
- Salinas E, Sejnowski TJ. 2001. Correlated neuronal activity and the flow of neural information. *Nature Reviews Neuroscience*, **2**(8): 539–550.
- Sapountzis P, Paneri S, Gregoriou GG. 2018. Distinct roles of prefrontal and parietal areas in the encoding of attentional priority. *Proceedings of the National Academy of Sciences of the United States of America*, **115**(37): E8755–E8764.
- Spaak E, Bonnefond M, Maier A, Leopold DA, Jensen O. 2012. Layer-specific entrainment of gamma-band neural activity by the alpha rhythm in monkey visual cortex. *Current Biology*, **22**(24): 2313–2318.
- Spyropoulos G, Bosman CA, Fries P. 2018. A theta rhythm in macaque visual cortex and its attentional modulation. *Proceedings of the National Academy of Sciences of the United States of America*, **115**(24): E5614–E5623.
- Sweeney-Reed CM, Zaehle T, Voges J, Schmitt FC, Buentjen L, Kopitzki K, Esslinger C, Hinrichs H, Heinze HJ, Knight RT, Richardson-Klavehn A. 2014. Corticothalamic phase synchrony and cross-frequency coupling predict human memory formation. *eLife*, **3**: e05352.
- Tort AB, Kramer MA, Thorn C, Gibson DJ, Kubota Y, Graybiel AM, Kopell NJ. 2008. Dynamic cross-frequency couplings of local field potential oscillations in rat striatum and hippocampus during performance of a T-maze task. *Proceedings of the National Academy of Sciences of the United States of America*, **105**(51): 20517–20522.
- Voloh B, Valiante TA, Everling S, Womelsdorf T. 2015. Theta-gamma coordination between anterior cingulate and prefrontal cortex indexes correct attention shifts. *Proceedings of the National Academy of Sciences of the United States of America*, **112**(27): 8457–8462.
- Whittingstall K, Logothetis NK. 2009. Frequency-band coupling in surface EEG reflects spiking activity in monkey visual cortex. *Neuron*, **64**(2): 281–289.
- Womelsdorf T, Fries P, Mitra PP, Desimone R. 2006. Gamma-band synchronization in visual cortex predicts speed of change detection. *Nature*, **439**(7077): 733–736.
- Yanagisawa T, Yamashita O, Hirata M, Kishima H, Saitoh Y, Goto T, Yoshimine T, Kamitani Y. 2012. Regulation of motor representation by phase-amplitude coupling in the sensorimotor cortex. *The Journal of Neuroscience*, **32**(44): 15467–15475.
- Zanos S, Rembado I, Chen D, Fetz EE. 2018. Phase-locked stimulation during cortical beta oscillations produces bidirectional synaptic plasticity in awake monkeys. *Current Biology*, **28**(16): 2515–2526.
- Zhou H, Desimone R. 2011. Feature-based attention in the frontal eye field and area V4 during visual search. *Neuron*, **70**(6): 1205–1217.
- Zhou H, Schafer RJ, Desimone R. 2016. Pulvinar-cortex interactions in vision and attention. *Neuron*, **89**(1): 209–220.

A soluble FcγR homolog inhibits IgM antibody production in ayu spleen cells

Kai Chen¹, Yu-Hong Shi^{1,2,*}, Jiong Chen^{1,2,*}, Ming-Yun Li¹

¹ Laboratory of Biochemistry and Molecular Biology, School of Marine Sciences, Ningbo University, Ningbo Zhejiang 315832, China

² State Key Laboratory for Quality and Safety of Agro-products, Ningbo University, Ningbo Zhejiang 315211, China

ABSTRACT

Classical Fc receptors (FcRs) mediate the binding to and recognition of the Fc portion of antibodies and play an important role during immune responses in mammals. Although proteins similar to soluble FcRs have been identified in fish, little is known about the role of such proteins in fish immunity. Here, we cloned a cDNA sequence encoding a soluble Fc receptor for an immunoglobulin G (FcγR) homolog from ayu (*Plecoglossus altivelis*) (PaFcγRI). The predicted protein was composed of two immunoglobulin C2-like domains but lacked a transmembrane segment and a cytoplasmic tail. The PaFcγRI transcripts were distributed at low levels in all tested tissues, but significantly increased after *Vibrio anguillarum* infection. The PaFcγRI protein was expressed in the head kidney, trunk kidney, and neutrophils. Recombinant PaFcγRI (rPaFcγRI) was secreted when transfected into mammalian cells and the native protein was also detected in serum upon infection. rPaFcγRI was also demonstrated to bind to ayu IgM, as assessed by cell transfection. Suppressive activity of the recombinant mature protein of PaFcγRI (rPaFcγRI_m) on *in vitro* anti-sheep red blood cell (SRBC) responses was detected by a modified hemolytic plaque forming cell assay. In conclusion, our study revealed that PaFcγRI is closely involved in the negative regulation of IgM production in the ayu spleen.

Open Access

This is an open-access article distributed under the terms of the Creative Commons Attribution Non-Commercial License (<http://creativecommons.org/licenses/by-nc/4.0/>), which permits unrestricted non-commercial use, distribution, and reproduction in any medium, provided the original work is properly cited.

Copyright ©2019 Editorial Office of Zoological Research, Kunming Institute of Zoology, Chinese Academy of Sciences

Keywords: Soluble FcγR homolog; Sequence characterization; IgM-binding protein; Inhibition of IgM production; *Plecoglossus altivelis*

INTRODUCTION

Antibodies are key components of the immune system, linking both innate and adaptive immunity (Bournazos & Ravetch, 2015). The variable Fab region of an antibody mediates specificity and dictates to what antigen and with what affinity the antibody will bind to its target. Antibodies also contain a constant region, termed the Fc domain, which engages diverse cellular receptors, thereby triggering antibody-mediated effector functions in innate and adaptive immunity (Dilillo & Ravetch, 2015). As members of the immunoglobulin (Ig) superfamily, Fc receptors (FcRs) are broadly expressed on the surface of various myeloid leukocytes and mediate binding and recognition of the Fc portion of antibodies (Davis, 2007). Since their identification three decades ago, our understanding of the biological consequences of FcRs has continued to evolve. FcRs mediate various functions including phagocytosis, antibody-dependent cell-mediated cytotoxicity, lymphocyte proliferation, mast cell degranulation, release/secretion of cytokines and chemokines, antigen presentation,

Received: 18 February 2019; Accepted: 26 June 2019; Online: 23 July 2019

Foundation items: This project was supported by the Program for the National Natural Science Foundation of China (31772876; 31402323; 31372555), Natural Science Foundation of Zhejiang Province (LZ18C190001; LY14C190007), Scientific Innovation Team Project of Ningbo (2015C110018), Natural Science Foundation of Ningbo City of China (2018A610225), Ningbo Science and Technology “Fumin Engineering” Project (2017C10037), and K.C. Wong Magna Fund in Ningbo University

*Corresponding authors, E-mail: shiyuhong0517@163.com; jchen1975@163.com

DOI: 10.24272/j.issn.2095-8137.2019.056

regulation of antibody production, clearance of immune complexes, and Ig transport (Bournazos & Ravetch, 2015; Nayak et al., 2010).

Mammals express six different Ig classes: i.e., IgG, IgM, IgD, IgE, IgA, and IgO. Correspondingly, four major classical FcRs have been identified for IgG (FcγRI, FcγRII, FcγRIII, and FcγRIV), as well as one for IgE (FcεRI), one for both IgM and IgA (FcαμR), one for IgM (FcμR), and one for IgA (FcαRI) in most previously studied placental mammals (Akula et al., 2014). The α chains of these receptors, which are Ig-binding subunits, are all related in structure, thus suggesting an origin from one or a few common early ancestors via successive gene duplications (Davis et al., 2005). In most instances, classical mammalian FcR genes consist of extracellular C2 Ig domains as well as a transmembrane (TM) segment and a cytoplasmic tail (CYT), which may contain signaling motifs (Stafford et al., 2006).

Soluble forms of FcRs (sFcRs) have been identified in the sera and supernatants of activated cells, including T cells, B cells, fibroblasts, macrophages, NK cells, and Langerhans cells (Esposito-Farese et al., 1995). sFcRs are produced either by cleavage at the cell membrane or by secretion of molecules generated by splicing of the TM-encoding exon. Soluble forms exist in the extracellular portion of the receptor or extracellular region linked to the intracytoplasmic portion of the receptor (Rosales & Uribe-Querol, 2013). sFcRs have been described for FcγRI, FcγRII, FcγRIII, FcεRII, and FcαRI (Daëron et al., 1989; Matt et al., 2015; Sarfati et al., 1996; van der Boog et al., 2002). Among these sFcRs, soluble FcγRs (sFcγRs) are relatively well studied and shown to play a regulatory role in immune responses. For example, sFcγRs bind to the Fc domains of IgG to exert immunoregulatory activities *in vivo* and *in vitro*, including the inhibition of IgG and IgM antibody production (Fridman et al., 1992) and immune complex precipitation (Gavin et al., 1995). In addition, sFcγRs are also reported to function in the inhibition of C1q binding and complement activation, antibody dependent cellular cytotoxicity, and antigen-antibody uptake (Molenaar et al., 1977).

To date, four classes of Ig have been reported in teleosts, including IgM, IgD, IgZ/IgT, and IgM-IgZ chimera, with IgM reported first (Tian et al., 2009). Of the classical Ig-binding FcR homologs, however, only FcεRIγ has been identified in teleosts, which has limited our understanding not only of the evolutionary history of FcRs but also their functional significance in ectotherms (Akula et al., 2014). Interestingly, FcR homologs without a TM or CYT have been identified in teleosts by genomic/transcriptomic analysis, with the first reported in channel catfish (*Ictalurus punctatus*) (i.e., IpFcRI) (Stafford et al., 2006). IpFcRI is structurally conserved, containing extracellular domains, as found in classical FcRs, and maintaining three Ig domains and Fc-binding sites for antibody recognition (Stafford et al., 2006). Furthermore, IpFcRI binds to IgM as a soluble protein in serum (Nayak et al., 2010; Stafford et al., 2006). Such proteins are also found in many other bony fish, e.g., zebrafish (*Danio rerio*), rainbow trout (*Oncorhynchus mykiss*), tiger puffer (*Takifugu rubripes*),

and spotted green pufferfish (*Tetraodon nigroviridis*) (Akula et al., 2014; Stafford et al., 2006). To date, however, little is known about the function of these receptors.

Ayu (*Plecoglossus altivelis*) is an economically important fish in East Asia (Nishimori et al., 2000). Recently, however, the development of ayu aquaculture in China has been severely challenged by *Vibrio anguillarum* infection, which has resulted in both production and animal welfare problems (Li et al., 2009; Nishimori et al., 2000; Xiong et al., 2018). Given the importance of FcRs in innate immunity, understanding the function and mechanism of action of ayu FcRs would be helpful for disease control and prevention. In this study, a novel sFcγR-like gene (PaFcγRI) was identified from ayu. The mRNA expression profiles of PaFcγRI in healthy and *V. anguillarum*-infected tissues were determined. The IgM-binding activity of PaFcγRI and its effect on IgM antibody production in spleen cells were also preliminarily characterized.

MATERIALS AND METHODS

Molecular characterization of PaFcγRI

The cDNA sequence of PaFcγRI was obtained from transcriptome data of ayu head kidney-derived monocytes/macrophages (MO/MΦ) using a BLAST search (<http://blast.ncbi.nlm.nih.gov/Blast.cgi>). The sequence was then used to design primers for specific amplification of the objective gene sequence from cDNA, with the amplicons sequenced on an ABI 3730 automated sequencer (Invitrogen, Shanghai, China) to confirm the correctness of the PaFcγRI sequence. SignalP v4.1 (<http://www.cbs.dtu.dk/services/SignalP/>) was used to predict the cleavage sites of the signal peptides. The molecular weights (MW) and isoelectric points (pI) were predicted using the Compute pI/Mw tool (http://web.expasy.org/compute_pi/). The N-glycosylation sites were predicted using the NetNGlyc 1.0 server (<http://www.cbs.dtu.dk/services/NetNGlyc/>). The SMART program (<http://smart.embl-heidelberg.de/>) was used to predict the domain architecture of the putative protein. Multiple sequence alignment was analyzed using ClustalW (<http://clustalw.ddbj.nig.ac.jp/>), and phylogenetic analyses were conducted using MEGA v7.0 (Kumar et al., 2016). Sequences used in this study are listed in Table 1.

Fish and *V. anguillarum* infection challenge

Healthy fish weighing 50–60 g each were purchased from a commercial farm in Ninghai County, China, and maintained in 100 L tanks at 20–22 °C with regular feeding, as described previously (Chen et al., 2016). The fish were acclimatized to laboratory conditions for two weeks before experiments were conducted. All experiments were performed according to the Experimental Animal Management Law of China and approved by the Animal Ethics Committee of Ningbo University.

The *V. anguillarum* artificial infection experiment was carried out as reported previously (Chen et al., 2016). Briefly, bacteria were grown in nutrient broth on a rotary shaker at 28 °C and

Table 1 Sequences of FcγR used in the study

GenBank accession No.	Species		Protein
	Latin name	English name	
XM022404314	<i>Canis lupus familiaris</i>	Dog	FcγRI
L03418	<i>Homo sapiens</i>	Human	FcγRI
EU589389	<i>Ovis aries</i>	Sheep	FcγRII
NM001136219	<i>H. sapiens</i>	Human	FcγRIIA
NM001002274	<i>H. sapiens</i>	Human	FcγRIIB
DQ026064	<i>Sus scrofa</i>	Pig	FcγRIIB
NM201563	<i>H. sapiens</i>	Human	FcγRIIC
NM010188	<i>Mus musculus</i>	Mouse	FcγRIII
EU589390	<i>O. aries</i>	Sheep	FcγRIII
AF132036	<i>Bos taurus</i>	Cow	FcγRIII
NM001127596	<i>H. sapiens</i>	Human	FcγRIII
BC027310	<i>M. musculus</i>	Mouse	FcγRIV
NM004106	<i>H. sapiens</i>	Human	FcεRγ
XM018231525	<i>Xenopus laevis</i>	African clawed frog	FcRL5
XM018096520	<i>Xenopus tropicalis</i>	Tropical clawed frog	FcRL5
NM001184866	<i>H. sapiens</i>	Human	FcRLA
MG687271	<i>Plecoglossus altivelis</i>	Ayu	FcγRI
XM019102455	<i>Cyprinus carpio</i>	Common carp	FcεRαL
XM011608346	<i>Takifugu rubripes</i>	Tiger pufferfish	FcεRα
XM021478104	<i>Danio rerio</i>	Zebrafish	FcRL5
XM012871848	<i>Fundulus heteroclitus</i>	Mummichog	FcRLA
XM014331816	<i>Haplochromis burtoni</i>	African cichlid fish	FcRLA
CAF97406	<i>Tetraodon nigroviridis</i>	Spotted green pufferfish	FcR
DQ286290	<i>Ictalurus punctatus</i>	Channel catfish	FcRI
XM010738182	<i>Larimichthys crocea</i>	Large yellow croaker	FcRLA
XM018702142	<i>Lates calcarifer</i>	Asian seabass	FcγRIL
XM020503104	<i>Oncorhynchus kisutch</i>	Coho salmon	FcγRIL
XM021587750	<i>Oncorhynchus mykiss</i>	Rainbow trout	FcγRIL
XM019367764	<i>Oreochromis niloticus</i>	Nile tilapia	FcγRIIIA
XM011482503	<i>Oryzias latipes</i>	Japanese ricefish	FcγRIVL
XM015041400	<i>Poecilia latipinna</i>	Sailfin molly	FcRL4
XM014162558	<i>Salmo salar</i>	Atlantic salmon	FcγRIL
XM020928651	<i>Boleophthalmus pectinirostris</i>	Mudskipper	FcγRIVL

harvested in the logarithmic phase of growth, as monitored by optical density assay. The *V. anguillarum* cells were washed, resuspended, and diluted to an appropriate concentration in sterile phosphate buffer saline (PBS). Fish were challenged by intraperitoneal injection with 1.2×10^4 colony forming units (CFUs) of live *V. anguillarum* (in 100 μL PBS) per fish, with PBS alone used as the control. At 4, 8, 12, and 24 h post-infection (hpi), tissue samples were collected and immediately snap-frozen in liquid nitrogen. Blood samples were allowed to clot overnight, after which serum was collected by centrifugation at 13 000 r/min for 15 min at 4 °C. All tissues and sera were preserved at –80 °C until subsequent use.

Real-time quantitative polymerase chain reaction (RT-qPCR)

Total RNA extraction, first strand cDNA synthesis, and RT-qPCR were carried out as reported previously (Ren et al., 2019). The tPaFcγRI(+) and tPaFcγRI(–) primers were used to produce a 227 bp fragment ("t" in the primer name stands for "test") (Table 2). The Pa18S rRNA(+) and Pa18S rRNA(–) primers were used to produce a 116 bp fragment of the housekeeping 18S rRNA gene, which is widely used as an internal control (Table 2). The RT-qPCR protocol was: 94 °C for 5 min, 40 cycles of 94 °C for 30 s, 60 °C for 30 s, and 72 °C for 30 s in a RT-Cycler™ real-time fluorescence quantitative

PCR thermocycler (CapitalBio, Beijing, China). The mRNA expression of PaFcγRI was normalized against that of 18S rRNA, and the quantitative differences between expression levels were calculated using the $2^{-\Delta\Delta Ct}$ method in the V.

anguillarum infection challenge assay (Livak & Schmittgen, 2001). All data were analyzed by one-way analysis of variance (ANOVA) with SPSS (v13.0, Chicago, IL, USA). $P < 0.05$ was considered statistically significant.

Table 2 Primers used in the study

Primer	Gene	GenBank accession No.	Nucleotide sequence (5'–3')	Length (bp)
tPaFcRI(+)	PaFcγRI	MG687271	CAGAGCAGCAGAGTCACAGC	227
tPaFcRI(–)			TGGGGACGAAGATTGAGTTC	
Pa18S rRNA (+)	Pa18S rRNA	FN646593	GAATGTCTGCCCTATCAACT	116
Pa18S rRNA (–)			GATGTGGTAGCCGTTTCT	
rPaFcγRI(+)	PaFcγRI	MG687271	CAAGCTTATGTTCACTGTATGTTGTGAC ^a	926
rPaFcγRI(–)			TTGCGGCCGCCCTACACAGTGGTGATCTCAC ^b	
rPaFcγRI _m (+)	PaFcγRI	MG687271	GGGAATTCAGACCTTCTGGCTGAAGTCC ^c	810
rPaFcγRI _m (–)			CCTCGAGCTACACAGTGGTGATCTCAC ^d	
rPalgM-Fc(+)	PalgM-Fc	AB703441	GGAATTC AATAAGACGGCTTCCTTCG C ^e	1011
rPalgM-Fc (–)			CCTCGAGCTACTGGGCTATGCAGGAGG ^d	
TM-PalGM-P1(+)	PaCTLRC	KP329196	CGGGATCCCAGGGGGGTCAGGGGCCCTA ^e	111
TM-PalGM-P1(–)			CAGGCTCCTGTAGCGGGCAC	
TM-PalGM-P2(+)	PalgM	AB703441	GTGCCCGCTACAGGAGCCTGATGTTCTCTGTTTCGCTGCT	1761
TM-PalGM-P2(–)			CGGAATTCCTACTGGGCTATGCAGGAG ^a	
TM-P1(+)	PaCTLRC	KP329196	CGGGATCCCAGGGGGGTCAGGGGCCCTA ^e	117
TM-P1(–)			CGGAATTCCTACAGGCTCCTGTAGCGGGCAC ^a	

a, b, c, d and e: Underlined regions indicate restriction enzyme sites *Hind* III, *Not* I, *Eco* R I, *Xho* I, and *Bam* H I, respectively.

Prokaryotic expression and purification of recombinant proteins

In this study, the recombinant mature proteins of PaFcγRI (rPaFcγRI_m) and the Fc portion of the ayu IgM (rPalgM-Fc) were prokaryotically expressed. The primers for amplification of the two genes are listed in Table 2. The prokaryotic expression and purification have been described previously (Zhang et al., 2011). Briefly, amplicons of expected size were digested by *Eco*R I and *Xho* I, and subsequently inserted into the pET30a(+) vector. The recombinant plasmids were then transformed into *Escherichia coli* BL21 (DE3) for overexpression. After overexpression was identified by SDS-PAGE analysis, the isopropyl β-D-thiogalactoside (IPTG)-induced cultures were harvested, and the cell pellets were resuspended in 20 mL of sonication buffer. After sonication, the inclusion bodies were recovered and resuspended in 2 mL of buffer A (0.1 mol/L Tris-HCl, 0.5 mol/L NaCl, 10 mmol/L imidazole, and 8 mol/L urea, pH 7.5). The purification of solubilized recombinant proteins was performed on a HisTrap™ FF (GE Healthcare, Shanghai, China) and gradient eluted with buffer B (0.1 mol/L Tris-HCl, 0.5 mol/L NaCl, 500 mmol/L Imidazole and 8 mol/L urea, pH 7.5) increasing from 0 to 100%. The peak fractions were pooled and dialyzed with solubilization buffer (50 mmol/L KH₂PO₄, 1 mmol/L EDTA, and 300 mmol/L KCl, containing 8 mol/L urea and 0.2 mol/L DTT, pH 8.0) and then concentrated using a 10 000 NMWL spin filter (Millipore, Shanghai, China). Refolding of solubilized recombinant proteins by 8 to 2 mol/L urea gradient size-

exclusion chromatography was performed on an XK 16/100 column packed with Superdex 75 gel media (GE Healthcare). The concentrated peak fractions were desalted on a 5 mL Bio-Gel P-6 desalting column (Bio-Rad, Shanghai, China). All procedures were carried out at 4 °C. The purified proteins were lyophilized and stored at –80 °C before use.

Antibody preparation and Western blot analysis

Antibody preparation was performed as reported previously (Ren et al., 2019). In brief, purified recombinant proteins, dissolved in PBS and emulsified with Freund's incomplete adjuvant, were used to immunize mice by intraperitoneal injection once every 7 d for a total of four injections. Control mice were injected with incomplete Freund's adjuvant. Whole blood was collected and centrifuged at 13 000 r/min for 15 min at 4 °C to obtain serum. Anti-PaFcγRI_m, anti-PalGM-Fc, and control isotype antisera were purified by protein G chromatography media (Bio-Rad). Antiserum quality was tested by Western blot analysis as described previously (Ren et al., 2019), and visualized using an enhanced chemiluminescence (ECL) kit (Advansta, Menlo Park, USA). The antiserum with 0.2% sodium azide was kept at –20 °C until use. For the determination of PaFcγRI glycosylation, PNGase F (New England Biolabs, Beverly, MA, USA) was used to digest kidney proteins followed by Western blot analysis.

The monocytes/macrophages (MO/MΦ), lymphocytes, and neutrophils were isolated and enriched as described below

(Chen et al., 2016, 2018). Ayu head kidney was aseptically extracted and pushed with a glass rod through a 100 μ m wire mesh. The resultant single-cell suspension was layered onto Ficoll-Hypaque PREMIUM (1.077 g/mL) (GE Healthcare). After centrifugation at 400 g for 25 min at room temperature, the buffy layer above the Ficoll was collected and washed with RPMI 1640 medium (Invitrogen) supplemented with 2% fetal bovine serum (FBS; Invitrogen), penicillin (100 U/mL), streptomycin (100 U/mL), and heparin (20 U/mL). Cells were cultured for 12 h, with the attached cells identified as enriched MO/M Φ . Blood samples were collected and layered onto Ficoll-Hypaque PREMIUM (1.077 g/mL) at a density gradient, then centrifuged at room temperature for 25 min at 400 g. Neutrophils below the Ficoll (containing erythrocytes) were subjected to hypotonic lysis treatment with ice-cold ACK lysis buffer. The non-adherent lymphocytes were collected from the buffy layer by differential adherence to exclude MO/M Φ . PaFc γ RI expression in tissues (liver, spleen, and kidney) and cells (MO/M Φ , lymphocytes, and neutrophils) was determined by Western blot analysis.

In vitro secretion

To test whether the native leader of PaFc γ RI could generate a secreted protein, PaFc γ RI was amplified using the primers listed in Table 2. The amplified product was cloned into the pcDNA3.1 mammalian expression vector (Invitrogen) and then transiently transfected into HEK293 cells using FuGENE[®] 6 Transfection Reagent (Promega, Madison, USA). The HEK293 cells were grown at 37 °C in a humidified incubator in the presence of 5% CO₂. The complete medium for the HEK293 cells was Dulbecco's modified Eagle's medium supplemented with 10% FBS. After 24 h, the supernatants and cell lysates were examined for recombinant PaFc γ RI (rPaFc γ RI) (containing signal peptide) by Western blotting using the anti-PaFc γ RI antiserum. To further demonstrate the secretion characteristics of PaFc γ RI, Western blotting was used to detect the native protein in ayu serum.

Interaction between PaFc γ RI and ayu IgM (PalgM) identified by flow cytometry

The interaction between two recombinant proteins was identified by flow cytometry, as described in Seijsing et al. (2013). Firstly, a recombinant TM protein, with mCherry on its N-terminal and PalgM heavy chain on its C-terminal (mCherry-TM-PalGM), was expressed on the HEK293 cell membrane. The TM-PalGM fragment (111 bp+1 761 bp=1 872 bp) was obtained by overlap extension PCR. The primers for amplifying TM were designed according to the TM domain (aa 53–75) of the ayu C-type lectin receptor gene (Table 2). The control protein (mCherry-TM) was a recombinant TM protein with mCherry on the C-terminal. To construct the recombinant plasmids, amplicons of expected size were digested by *Bam*H I and *Eco*R I, and subsequently inserted into the pCMV-N-mCherry vector (Beyotime Biotechnology, Shanghai, China). The recombinant plasmid was then constructed and transfected into the HEK293 cell line by FuGENE[®] 6 Transfection Reagent. The expression of recombinant

mCherry-TM-PalGM and mCherry-TM were visualized using a Nikon Eclipse Ti-U fluorescence microscope. Their expression levels were also detected using anti-mCherry antibody by Western blot analysis.

The HEK293 cells expressing mCherry-TM-PalGM or mCherry-TM were incubated with anti-PalGM-Fc antiserum for 1 h at 37 °C. After washing, the cells were incubated with secondary antibody, FITC-labeled goat anti-mouse IgG (Beyotime Biotechnology), for 1 h at 37 °C. Finally, the cells were washed and analyzed by a Gallios flow cytometer (Beckman Coulter, California, USA).

The HEK293 cells expressing mCherry-TM-PalGM or mCherry-TM were respectively incubated with rPaFc γ RI for 1 h at 37 °C, and then washed and incubated with anti-PaFc γ RI antiserum for 1 h at 37 °C. After this, the cells were washed and incubated with FITC-labeled goat anti-mouse IgG (Beyotime Biotechnology) for 1 h at 37 °C, then washed and resuspended in PBS supplemented with 1% bovine serum albumin (BSA). Cells were analyzed in a Gallios flow cytometer and 10 000 events per sample were recorded. The data were processed using Kaluza software (Beckman Coulter).

Primary anti-sheep red blood cell (SRBC) responses in vitro

The biological activity of rPaFc γ RI was tested on primary anti-SRBC responses *in vitro* using a modified hemolytic plaque-forming cell (PFC) assay (Jacobson et al., 2003; Kaattari et al., 1986; Smith, 1998; Varin et al., 1989). Anesthetized fish were sacrificed and placed on ice. The spleens were excised under sterile conditions and immediately placed into 2 mL of cold Hank's balanced salt solution (HBSS) (Sangon Biotech, Shanghai, China) in sterile plastic 2 cm petri dishes. Spleen cells were separated by gentle maceration over a 100 μ m nylon screen, transferred to 15 mL conical tubes, and incubated with ACK Lysis Buffer (Beyotime Biotechnology) for 5 min at room temperature. The spleen cells were washed twice with cold HBSS and centrifuged at 2 000 r/min for 10 min at 4 °C. The resulting cellular pellet was resuspended in 2 mL cold complete media (RPMI 1640, 10% FBS, 100 U/mL penicillin, and 100 mg/mL streptomycin). A 50 μ L aliquot was removed and combined with 450 μ L of 10% trypan blue for lymphocyte differentiation, enumeration, and viability in a hemocytometer at 40 \times . Each sample was diluted to 8 \times 10⁶ cells per mL in complete media, after which 50 μ L of 20% SRBCs per mL was added and the sample was cultured for 3 d at 24 °C and 5% CO₂. At day 3, purified rPaFc γ RI was added, which was serially diluted (1: 2) (original concentration 5 μ g/mL) to a 100 μ L final volume, with a sample without rPaFc γ RI used as the control. At day 5, each sample (250 μ L) was combined with 0.15 mL of 20% SRBCs and 0.8 mL of 45 °C 0.7% agar solution, then mixed quickly and poured into 5 cm plastic petri dishes and allowed to solidify. Plates were incubated for 2 h with humidity at 24 °C to allow specific lymphocyte recognition of SRBCs and subsequent antibody production and binding. After this, 1 mL of 10% complement source serum (diluted by HBSS)

was added and the plates were incubated overnight at 24 °C to allow complement-mediated lysis of the SRBCs. Plaques were enumerated and evaluated for approximate size manually via a low-powered Guiguang XTL-400 dissecting microscope with 10× ocular strength. Inhibition >30% was considered significant in view of the variability of this technique.

RESULTS

Cloning and sequence analysis of PaFcγRI

The cDNA sequence of PaFcγRI was 1 113 nucleotides (nts) in length, comprising a 5'-UTR of 79 nts, 3'-UTR of 125 nts, and open reading frame of 79 nts, and encoding a polypeptide of 302 amino acids (aa) with a predicted molecular weight (MW) of 34.1 kDa. BLAST searching revealed that this sequence was homologous to mammalian FcγR and was thus tentatively named PaFcγRI. It was predicted to comprise of a signal peptide (aa 1–33) and two Ig domains: Ig domain 1 (D1) consisting of 80 aa (aa 43–122)

and Ig domain 2 (D2) consisting of 85 aa (aa 130–214). Both Ig domains contained two conserved cysteine residues (Cys), essential for the formation of disulfide bonds (predicted as Cys⁵⁸–Cys⁹⁸ and Cys¹⁴⁵–Cys¹⁹¹) (Figure 1). The two disulfide bonds were conserved in all selected mammalian and fish FcRs (Figure 1B). According to the features, such as the spacing of cysteine bridges and number of beta sheets, D1 and D2 were classified as C2 domains and shared homology with low-affinity receptor domains. Furthermore, PaFcγRI had three potential N-glycosylation sites: i.e., N¹¹²NS, N¹⁷⁷LT, and N¹⁸⁰LT.

Sequence comparison analysis showed that PaFcγRI was tightly grouped with previously reported Nile tilapia (*Oreochromis niloticus*) (identity 35.4%) and Japanese ricefish (*Oryzias latipes*) (identity 34.4%), suggesting an evolutionary relationship. Phylogenetic tree analysis revealed that PaFcγRI fell into a larger cluster that included fish FcRs, and also grouped with the mammalian FcγR subset (Figure 2A). In addition, each PaFcγRI domain had a related counterpart that variously occurred throughout the FcγRs (Figure 2B).

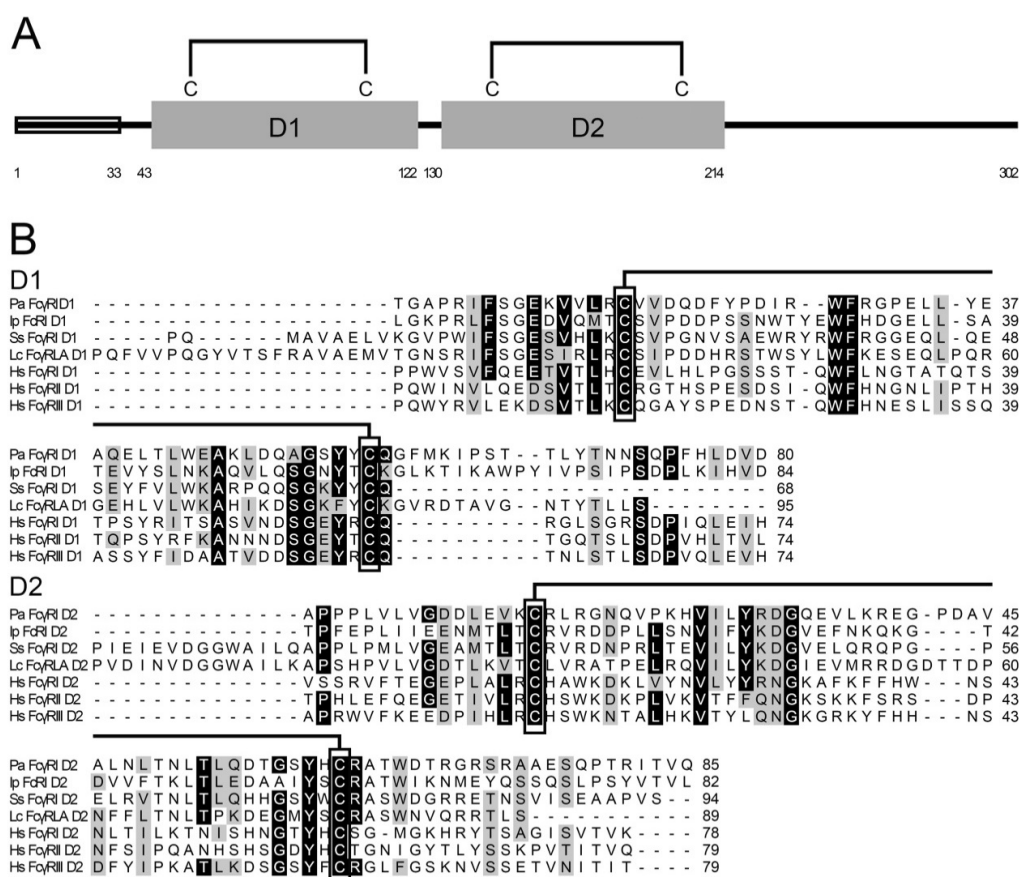


Figure 1 Schematic representation and multiple alignments of amino acid sequences

A: Schematic representation of PaFcγRI protein including signal peptide (box) and disulfide bonds (line). B: Amino acid alignments of D1 and D2 of ayu, channel catfish, Atlantic salmon, large yellow croaker, and representative human FcγRs. Hatched boxes indicate conserved cysteines and dashes (-) represent gaps. IpFcγRI: Channel catfish FcRI; SsFcγRI: Atlantic salmon FcRI; LcFcγRI: Large yellow croaker FcRI; HsFcγRI: Human FcRI; HsFcγRII: Human FcRII; HsFcγRIII: Human FcRIII. GenBank accession Nos. are listed in Table 1.

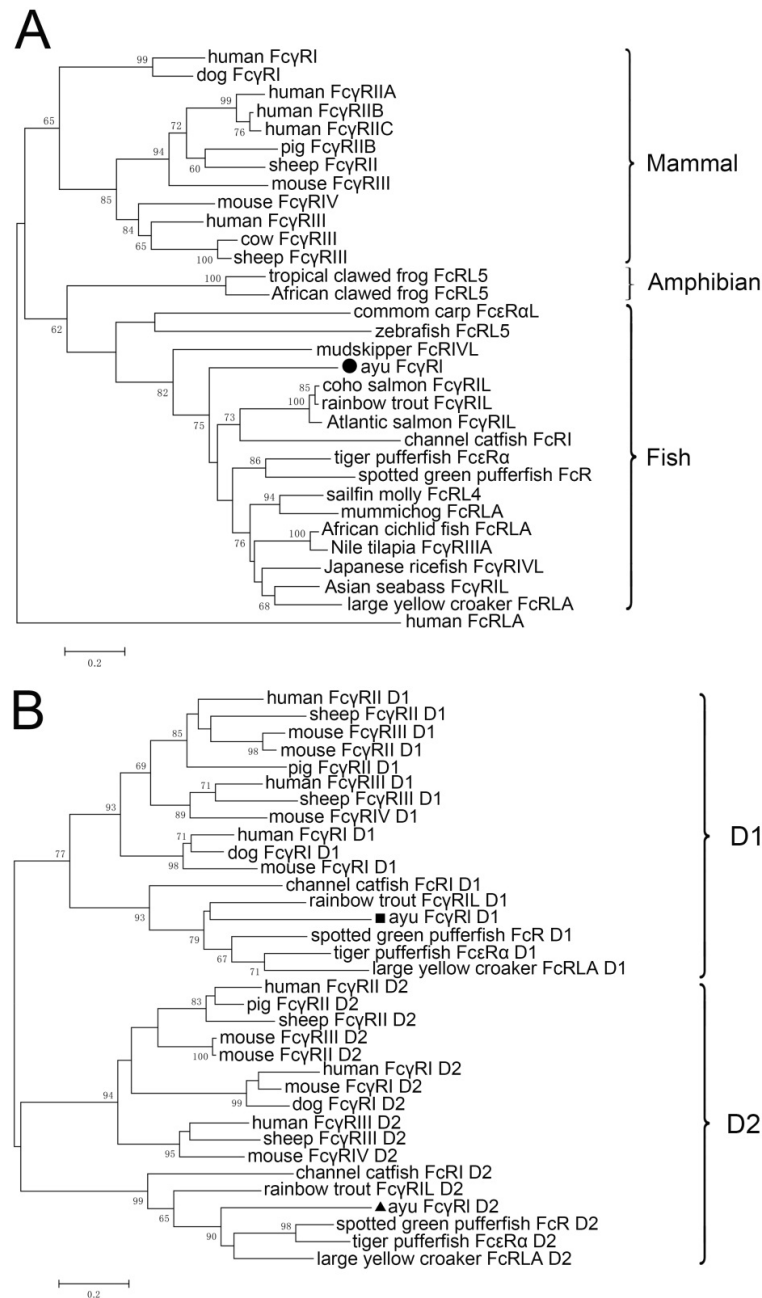


Figure 2 Phylogenetic analysis of full-length (A) and two Ig domain (B) amino acid sequences of PaFc γ RI and related FcRs using neighbor-joining method

Values at forks indicate percentage of trees in which this grouping occurred after bootstrapping (1 000 replicates; shown only when >60%) using MEGA7.0. Scale bar shows number of substitutions per base.

Tissue expression profiles of PaFc γ RI transcripts

PaFc γ RI mRNA was expressed in the liver, spleen, kidney, brain, intestines, muscle, and gill at low levels, with the highest expression detected in the gill of healthy ayu (Figure 3A). Following *V. anguillarum* infection, PaFc γ RI mRNA expression was up-regulated in all tested tissues (Figure 3B–

E). After stimulation with viable *V. anguillarum*, the up-regulation of PaFc γ RI expression in the liver and spleen demonstrated an inverted U-shaped tendency. The highest expression levels of PaFc γ RI in the liver, spleen, and kidney were detected at 8 hpi and in the gill were detected at 4 hpi. Furthermore, PaFc γ RI mRNA expression levels in the liver,

spleen, kidney, and gill were up-regulated by 19.30-fold, 16.05-fold, 19.01-fold, and 4.78-fold, respectively, after stimulation (Figure 3B–E).

Prokaryotic expression, purification, and antibody preparation of rPaFcyRI and rPalgM-Fc

After induction by IPTG, the recombinant proteins were all over-expressed in *E. coli* BL21 (DE3). The size of rPaFcyRI on the 12% SDS-PAGE gel was ~40 kDa, similar to the calculated MW of 39.8 kDa (34.1 kDa PaFcyRI plus 5.7 kDa His-tag) (Figure 4A). The size of rPalgM-Fc on the 12% SDS-PAGE gel was 44 kDa, similar to the calculated MW of 43.2 kDa (37.5 kDa rPalgM-Fc plus 5.7 kDa His-tag) (Figure 4C). The purifications of the two recombinant proteins were all greater than 95%.

Western blot analysis revealed that the MW of native PaFcyRI in the ayu kidney was ~47 kDa and after deglycosylation was ~34 kDa, similar to sequence calculations (34.1 kDa) (Figure 4B). Western blot analysis also revealed that the MW of the native PalgM heavy chains in ayu was ~70–80 kDa, similar to the MW of IgM heavy chains reported previously in fish (Wilson & Warr, 1992) (Figure 4D).

Furthermore, Western blot analysis revealed native protein expression in the healthy head kidney and trunk kidney, but not in the liver or spleen (Figure 4E). The detected cell types that expressed PaFcyRI were neutrophils, but not MO/MΦ or lymphocytes (Figure 4E).

In vitro secretion of rPaFcyRI

Results showed rPaFcyRI with the native leader was expressed in the HEK293 cells. As shown in Figure 5A,

rPaFcyRI was ~49 kDa (calculated MW 34.1 kDa), which might be caused by glycosylation, as expressed in HEK293 cells. rPaFcyRI was detected in both the supernatants and cell lysates of pcDNA3.1-PaFcyRI-transfected cells but not in the supernatants and cell lysates of the control cells transfected with pcDNA3.1, indicating that the native leader can indeed generate a secretory PaFcyRI. Native PaFcyRI in serum was also detected by Western blotting. In the sera of the healthy control and infected ayu, no obvious bands were observed at 4, 8, or 12 hpi, whereas an obvious band was observed in the infected ayu at 24 hpi (Figure 5B).

rPaFcyRI binding to PalgM

PalgM was expressed as a fusion protein, which included PalgM+TM+mCherry. Its expression was first detected in HEK293 cells by fluorescence microscopy. Results showed that mCherry was expressed in the cytoplasm, and the two recombinant proteins (mCherry-TM and mCherry-TM-PalM) were mainly localized on the plasma membrane (Figure 6A). Western blot analysis revealed that the MW of mCherry-TM was ~31 kDa, similar to the calculated MW of 30.5 kDa (3.8 kDa TM plus 26.7 kDa mCherry), and the MW of mCherry-TM-PalM was ~95 kDa, similar to the calculated MW of 95 kDa (68.3 kDa TM-PalM plus 26.7 kDa mCherry) (Figure 6B). Flow cytometry revealed that PalgM was identified with anti-PalM-Fc antiserum, suggesting that the PalgM part in mCherry-TM-PalM was mainly localized outside the HEK293 plasma membrane (Figure 6C). Finally, the interaction between rPaFcyRI and the PalgM Fc portion was detected by flow cytometry. Results showed that cells probed with FITC displayed a linear relationship between mCherry and FITC

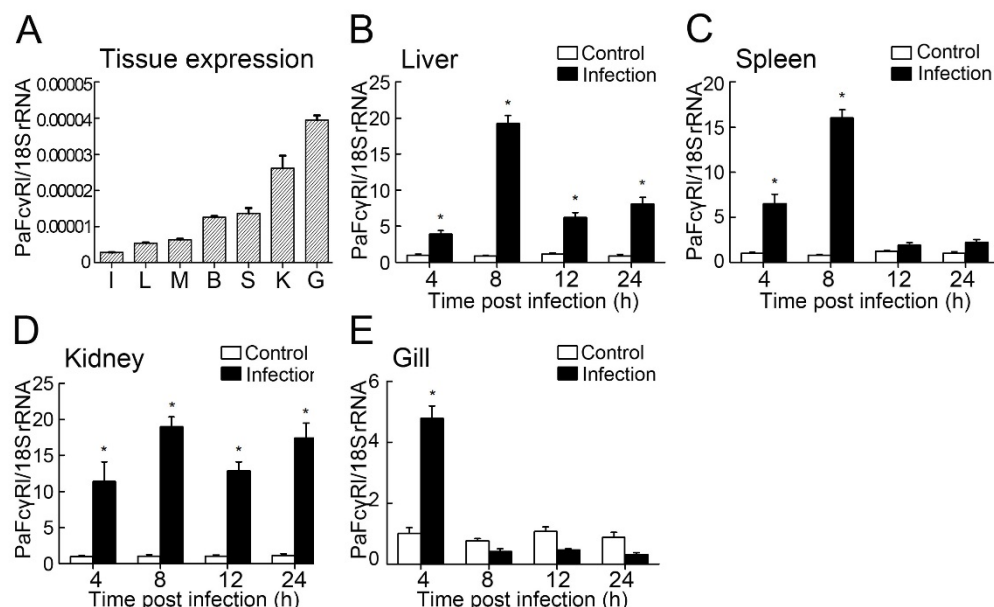


Figure 3 RT-qPCR detection of PaFcyRI expression in ayu tissues

A: Healthy tissues. L: Liver, S: Spleen, K: Kidney, B: Brain, G: Gill, I: Intestines, M: Muscle. B–E: PaFcyRI transcripts in ayu challenged with *V. anguillarum* infection. Tissues were collected at different time points post-infection. PaFcyRI transcript levels were normalized to Pa18S rRNA transcript levels. Data are means±SEM of the results from four fish. *: $P < 0.05$.

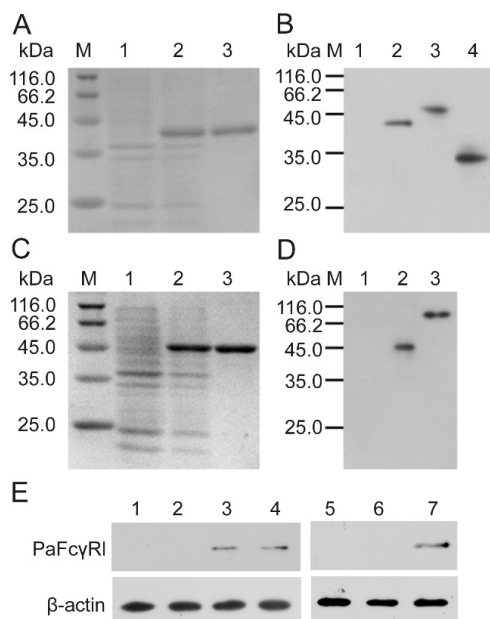


Figure 4 Prokaryotic expression and Western blot analysis

A: 12% SDS-PAGE analysis of bacterial lysates and purified rPaFcγRI. Lane M: Protein marker; 1: pET30a-PaFcγRI/BL21 before IPTG induction; 2: pET30a-PaFcγRI/BL21 after IPTG induction; 3: Purified rPaFcγRI. B: Western blot analysis of rPaFcγRI using anti-PaFcγRI antiserum. Lane M: Protein marker; 1: pET30a-PaFcγRI/BL21 before IPTG induction; 2: pET30a-PaFcγRI/BL21 after IPTG induction; 3: Ayu kidney lysates; 4: Ayu kidney lysates after deglycosylation by PNGase F. C: 12% SDS-PAGE analysis of bacterial lysates and purified rPalGM-Fc. Lane M: Protein marker; 1: pET30a-PalGM-Fc/BL21 before IPTG induction; 2: pET30a-PalGM-Fc/BL21 after IPTG induction; 3: Purified rPalGM-Fc. D: Western blot analysis of rPalGM-Fc using anti-PalGM-Fc antiserum. Lane M: Protein marker; 1: pET30a-PalGM-Fc/BL21 before IPTG induction; 2: pET30a-PalGM-Fc/BL21 after IPTG induction; 3: Ayu spleen lysates. E: Protein expression of PaFcγRI in different tissues and cell types. 1: Liver; 2: Spleen; 3: Head kidney; 4: Trunk kidney; 5: MO/MΦ; 6: Lymphocytes; 7: Neutrophils.

fluorescence, indicating a linear correlation between the amounts of mCherry-TM-PalGM and binding of rPaFcγRI (Figure 6D). The control (mCherry-TM and rPaFcγRI) did not show such a correlation (Figure 6D).

Suppressive activity of rPaFcγRI on *in vitro* IgM anti-SRBC antibody responses

The biological activity of rPaFcγRI on primary anti-SRBC antibody responses *in vitro* was tested. As shown in Figure 7, rPaFcγRI suppressed anti-SRBC antibody production in a dose-dependent fashion. About 1.70 μg/mL of rPaFcγRI was necessary to inhibit 50% of antibody production against SRBCs. This effect was not due to toxicity, as the addition of rPaFcγRI did not decrease viability of the spleen cells.

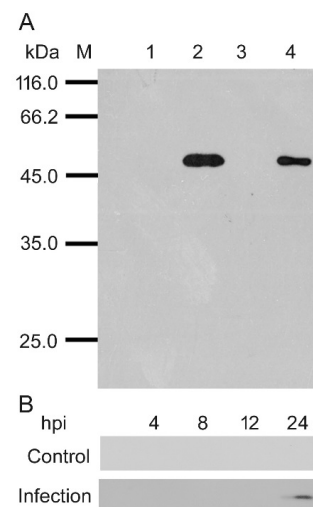


Figure 5 Secretion of rPaFcγRI

A: PaFcγRI was cloned into pcDNA3.1 and transiently transfected into HEK293 cells. After 24 h, supernatants and cell lysates were examined by Western blotting using anti-PaFcγRI antiserum. Lane M: Protein marker; 1: Supernatants of pcDNA3.1/HEK293, negative control; 2: Supernatants of pcDNA3.1-PaFcγRI/HEK293; 3: Cell lysates of pcDNA3.1/HEK293, negative control; 4: Cell lysates of pcDNA3.1-PaFcγRI/HEK293. B: Native PaFcγRI in ayu serum.

DISCUSSION

Myeloid leukocytes in humans and mice are equipped with a variety of receptors that enable their interaction with monomeric or aggregated immunoglobulins, antigen-antibody immune complexes, and opsonized antibody-coated particles or cells (Pierre & Friederike, 2015). FcγRs are receptors that induce diverse biological functions after binding to the Fc portion of antibodies mediated by extracellular domains. The extracellular domains of mammalian FcγRI contain three Ig domains (i.e., D1, D2, and D3), whereas FcγRII, FcγRIII, and FcγRIV only contain the first two (i.e., D1 and D2). D1 and D2 are highly homologous among species, whereas D3 shows a lower level of homology, although it is still clearly related to the Ig superfamily (Sears et al., 1990). Interestingly, there is a group of teleost proteins closely homologous to the extracellular domains of mammalian FcγRs (Stafford et al., 2006). Among such homologous proteins, most contain two Ig domains (D1, D2), although a few contain three or four. For example, IpFcRI contains three Ig domains (D1, D2, and D3), with D1 and D2 found clustered with high bootstrap values with mammalian FcR Ig-domain counterparts, but D3 not phylogenetically related to any mammalian FcR Ig domain (Stafford et al., 2006). Likewise, there are a different number of Ig domains in the FcR sequences of zebrafish, rainbow trout, tiger puffer, and spotted green pufferfish (Akula et al., 2014; Stafford et al., 2006). Here, we studied an FcγR-like gene, PaFcγRI, from ayu. Phylogenetic tree analysis showed that PaFcγRI and other fish FcRs were grouped together and

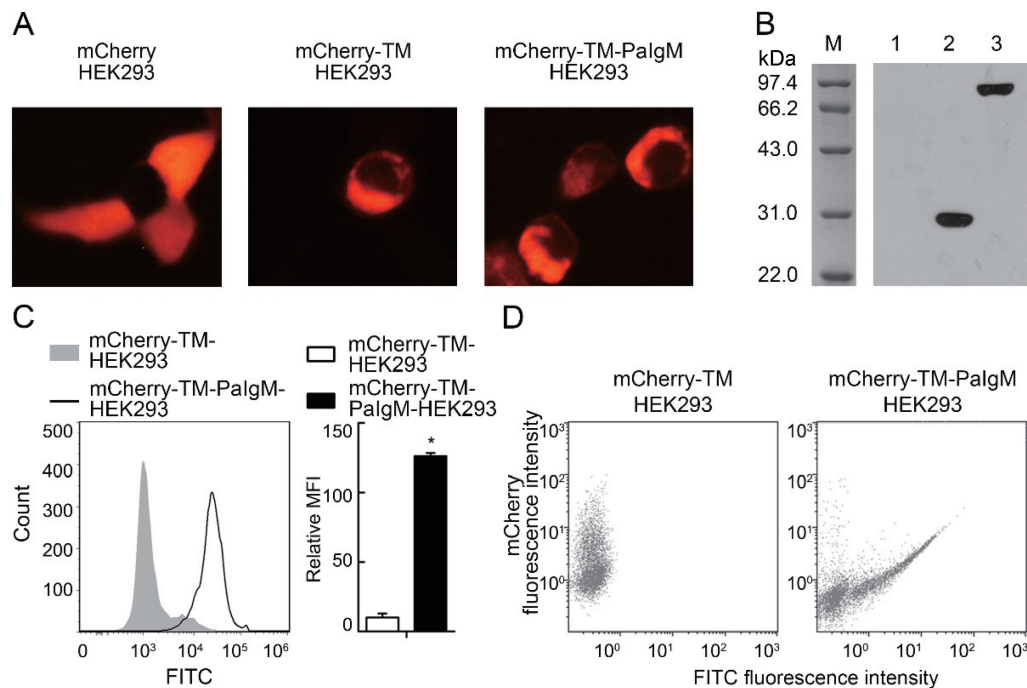


Figure 6 Interaction between rPaFcγRI and PalgM

A: Localization of mCherry, mCherry-TM, and mCherry-TM-PalgM in HEK293 cells observed by fluorescence microscopy. B: Western blot analysis of mCherry-TM and mCherry-TM-PalgM expression in HEK293 cells with anti-mCherry antibody. Lane M: Protein marker; 1: HEK293 cells, negative control; 2: mCherry-TM/HEK293; 3: mCherry-TM-PalgM/HEK293. C: Flow cytometry analysis of percentage of HEK293 cells expressing mCherry-TM-PalgM following incubation with anti-PalgM-Fc antiserum. Histogram showing percentage of mCherry-TM-PalgM-positive cells in mCherry-TM-PalgM/HEK293 and mCherry-TM-PalgM/HEK293 detected by flow cytometry analysis with anti-PalgM-Fc antiserum. Data are means \pm SEM of results from four assays. *: $P < 0.05$. D: Flow cytometry analysis of binding of rPaFcγRI to PalgM. HEK293 cells overexpressing mCherry-TM and mCherry-TM-PalgM were first probed with rPaFcγRI, then detected with anti-PaFcγRI antiserum produced in mice and stained with FITC-labeled goat anti-mouse IgG.

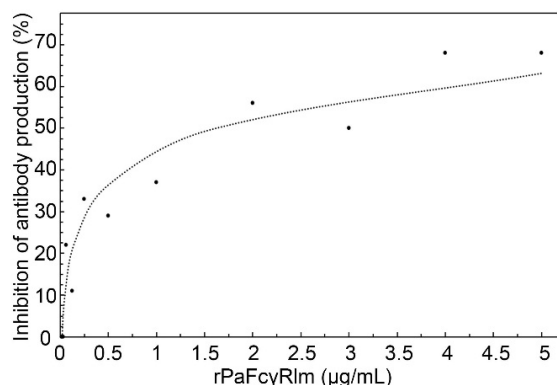


Figure 7 rPaFcγRI inhibits anti-SRBC antibody production

Various doses of rPaFcγRI were added at day 3 to cultures of spleen cells stimulated by SRBCs. Anti-SRBC antibody production was measured at day 5 by direct PFC assay.

were also clustered with the mammalian FcγR subset. In addition, PaFcγRI possessed only D1 and D2, which were classified into C2 sets and phylogenetically related to the corresponding domain of mammalian and fish FcγRs,

respectively.

Tissue and cellular mRNA expression of the FcγR homolog has been studied in channel catfish. Stafford et al. (2006) readily detected IpFcRI transcripts by Northern blot analysis in the spleen and hemopoietic kidney tissues of channel catfish, as well as in their peripheral blood leukocytes (PBLs) (predominantly in granulocytes). To date, however, no information regarding mRNA expression of FcγR homologs related to infection has been reported. Mammalian sFcγRs have been detected in biological fluids of mice and humans, with production found to be highly dependent on environmental factors, including pathogens. For example, mouse sFcγRII (Fcγ2b/γ1R) was reported to increase in culture medium after stimulation of spleen cells with lipopolysaccharide (LPS), which was attributed to B lymphocytes (Pure et al., 1984). Furthermore, a dramatic increase in circulating sFcγRII is also found in *Schistosoma mansoni*-infected mice (Khayat et al., 1986). In the current study, PaFcγRI mRNA was expressed at low levels in all tested tissues, with the highest expression found in the gill. Furthermore, expression in the liver, spleen, and kidney showed sensitive responses to *V. anguillarum* infection. With antiserum, the PaFcγRI protein was also detected in the head

kidney, trunk kidney, and neutrophils.

The teleost proteins mentioned in this study are soluble, thus differing from the mammalian membrane-bound Fc γ Rs. This suggests that this group of proteins may be secreted and/or intracellularly expressed, thus hinting at their function. In channel catfish, IpFcRI was identified as a secretory protein in the serum akin to sFcR found in mammals (Stafford et al., 2006). In this study, rPaFc γ RI was also found to be secreted in the supernatants of HEK293 cells. Native PaFc γ RI was also detectable in serum challenged with *V. anguillarum*.

The binding of the Fc region of IgG to Fc γ R is a critical step for the initiation and control of effector immune functions (Sib  ril et al., 2007). For the IgG ligands, Fc γ RI and Fc γ RIV are high-affinity receptors, whereas Fc γ RII and Fc γ RIII are low-affinity receptors (Qiu et al., 1990). Mouse and human sFc γ Rs bind to IgG subclasses with a binding profile identical to the corresponding membrane-associated receptors and exhibit immunomodulatory properties (Lynch et al., 1992). In fish, only IpFcRI has been identified to bind with IgM, as assessed by co-immunoprecipitation and cell transfection studies (Stafford et al., 2006). In our research, rPaFc γ RII was found to bind with IgM, which might provide a hint to its function in immunity.

As reported earlier, mammalian sFc γ Rs inhibit *in vitro* and *in vivo* immune responses. For instance, purified mouse sFc γ RIIB1 exerts dose-dependent suppressive activity on primary and secondary antibody responses when added to cultures of spleen cells stimulated with SRBCs, with the effect even more pronounced on IgG than on IgM responses (Varin et al., 1989). Saut  s et al. (1992) also found that sFc γ RIIB1 inhibits antibody *in vitro* responses to SRBCs in small B cell cultures stimulated by anti-IgM antibodies in the presence of IL-4 and IL-5. Moreover, intraperitoneal injection of this material into adult mice immunized with SRBCs decreases IgG antibody production in spleen cells, as measured by PFC assay, and in serum, as measured by antigen-specific ELISA (Saut  s et al., 1992). Furthermore, purified human sFc γ RIIIB (sCD16) inhibits IgM and IgG production of human peripheral blood mononuclear cells stimulated by pokeweed mitogen *in vitro* in a time and dose-dependent manner (Teillaud et al., 1993). sFc γ Rs are believed to function by competing with their membrane-bound counterparts for Ig (or immune complex) binding, which, in turn, down-regulates B cell proliferation and antibody production (Fridman et al., 1993). In our study, the PaFc γ RI protein was not detectable in the serum of healthy ayu but was up-regulated upon infection. We identified that rPaFc γ RII exerts suppressive activity on primary antibody responses *in vitro* at a relatively high concentration. Thus, we speculated that PaFc γ RI might be involved in the down-regulation of antibody levels at the late stage of infection.

In summary, we showed that PaFc γ RI exhibited sequence characteristics similar to classical FcRs with extracellular domains. Furthermore, we revealed that PaFc γ RI was a secretory protein bound to PaIgM. *In vitro*, PaFc γ RI likely plays a role in the regulation of IgM production.

COMPETING INTERESTS

The authors declare that they have no competing interests.

AUTHORS' CONTRIBUTIONS

Y.H.S. and J.C. drafted the experiments; K.C. and Y.H.S. performed the experiments; K.C., Y.H.S., J.C., and M.Y.L. analyzed the data and wrote the paper. All authors read and approved the final version of the manuscript.

REFERENCES

- Akula S, Mohammadamin S, Hellman L. 2014. Fc receptors for immunoglobulins and their appearance during vertebrate evolution. *PLoS One*, **9**(5): e96903.
- Bournazos S, Ravetch JV. 2015. Fc γ receptor pathways during active and passive immunization. *Immunological Reviews*, **268**(1): 88–103.
- Chen F, Lu XJ, Nie L, Ning YJ, Chen J. 2018. Molecular characterization of a CC motif chemokine 19-like gene in ayu (*Plecoglossus altivelis*) and its role in leukocyte trafficking. *Fish & Shellfish Immunology*, **72**: 301–308.
- Chen Q, Lu XJ, Li MY, Chen J. 2016. Molecular cloning, pathologically-correlated expression and functional characterization of the colonystimulating factor 1 receptor (CSF-1R) gene from a teleost, *Plecoglossus altivelis*. *Zoological Research*, **37**(2): 96–102.
- Da  ron M, Saut  s C, Bonnerot C, Blank U, Varin N, Even J, Hogarth PM, Fridman WH. 1989. Murine type II Fc gamma receptors and IgG-binding factors. *Chemical Immunology*, **47**: 21–78.
- Davis RS. 2007. Fc receptor-like molecules. *Annual Review of Immunology*, **25**: 525–560.
- Davis RS, Ehrhardt GRA, Leu CM, Hirano M, Cooper MD. 2005. An extended family of Fc receptor relatives. *European Journal of Immunology*, **35**(3): 674–680.
- DiLillo DJ, Ravetch JV. 2015. Fc-receptor interactions regulate both cytotoxic and immunomodulatory therapeutic antibody effector functions. *Cancer Immunology Research*, **3**(7): 704–713.
- Esposito-Farese ME, Saut  s C, de la Salle H, Latour S, Bieber T, de la Salle C, Ohlmann P, Fridman WH, Cazenave JP, Teillaud JL. 1995. Membrane and soluble Fc gamma RII/III modulate the antigen-presenting capacity of murine dendritic epidermal Langerhans cells for IgG-complexed antigens. *The Journal of Immunology*, **155**(4): 1725–1736.
- Fridman WH, Bonnerot C, Da  ron M, Amigorena S, Teillaud JL, Saut  s C. 1992. Structural bases of Fc γ receptor functions. *Immunological Reviews*, **125**(1): 49–76.
- Fridman WH, Teillaud JL, Bouchard C, Teillaud C, Astier A, Tartour E, Galon J, Mathiot C, Saut  s C. 1993. Soluble Fc gamma receptors. *Journal of Leukocyte Biology*, **54**(5): 504–512.
- Gavin AL, Wines BD, Powell MS, Hogarth PM. 1995. Recombinant soluble Fc gamma RII inhibits immune complex precipitation. *Clinical & Experimental Immunology*, **102**(3): 620–625.
- Jacobson KC, Arkoosh MR, Kagley AN, Clemons ER, Collier TK, Casillas E. 2003. Cumulative effects of natural and anthropogenic stress on immune function and disease resistance in juvenile Chinook Salmon. *Journal of Aquatic Animal Health*, **15**(1): 1–12.
- Kaattari SL, Irwin MJ, Yui MA, Tripp RA, Parkins JS. 1986. Primary *in vitro* stimulation of antibody production by rainbow trout lymphocytes. *Veterinary*

- Immunology and Immunopathology*, **12**(1–4): 29–38.
- Khayat D, Serban D, Dux Z, Schlomo Y, Jacquillat C. 1986. Role of infection in the modulation of mouse circulating soluble cell-free Fc γ 2b/ γ 1 receptor. *Scandinavian Journal of Immunology*, **24**(1): 83–91.
- Kumar S, Stecher G, Tamura K. 2016. MEGA7: molecular evolutionary genetics analysis version 7.0 for bigger datasets. *Molecular Biology and Evolution*, **33**(7): 1870–1874.
- Li CH, Chen J, Shi YH, Li MY. 2009. Characterization of *Listonella anguillarum* as the aetiological agent of vibriosis occurred in cultured ayu (*Plecoglossus altivelis*) in Ninghai country, China. *Acta Microbiologica Sinica*, **49**(7): 931–937.
- Livak KJ, Schmittgen TD. 2001. Analysis of relative gene expression data using real-time quantitative PCR and the 2^{- $\Delta\Delta$ CT} method. *Methods*, **25**(4): 402–408.
- Lynch A, Tartour E, Teillaud JL, Asselain B, Fridman WH, Sautès C. 1992. Increased levels of soluble low-affinity Fc γ receptors (IgG-binding factors) in the sera of tumour-bearing mice. *Clinical & Experimental Immunology*, **87**(2): 208–214.
- Matt P, Lindqvist U, Kleinau S. 2015. Elevated membrane and soluble cd64: a novel marker reflecting altered fc γ r function and disease in early rheumatoid arthritis that can be regulated by anti-rheumatic treatment. *PLoS One*, **10**(9): e0137474.
- Molenaar JL, Van Galen M, Hannema AJ, Zeijlemaker W, Pondman KW. 1977. Spontaneous release of Fc receptor-like material from human lymphoblastoid cell lines. *European Journal of Immunology*, **7**(4): 230–236.
- Nayak DK, Tang A, Wilson M, Miller NW, Bengtén E. 2010. Channel catfish soluble Fc μ R binds conserved linear epitopes present on C μ 3 and C μ 4. *Molecular immunology*, **47**(6): 1306–1316.
- Nishimori E, Kita-Tsukamoto K, Wakabayashi H. 2000. *Pseudomonas plecoglossicida* sp. nov., the causative agent of bacterial haemorrhagic ascites of ayu, *Plecoglossus altivelis*. *International Journal of Systematic and Evolutionary Microbiology*, **50**(1): 83–89.
- Pierre B, Friederike J. 2015. Mouse and human FcR effector functions. *Immunological Reviews*, **268**(1): 25–51.
- Puré E, Durie CJ, Summerill CK, Unkeless JC. 1984. Identification of soluble Fc receptors in mouse serum and the conditioned medium of stimulated B cells. *Journal of Experimental Medicine*, **160**(6): 1836–1849.
- Qiu WQ, de Bruin D, Brownstein BH, Pearse R, Ravetch JV. 1990. Organization of the human and mouse low-affinity Fc γ R genes: duplication and recombination. *Science*, **248**(4956): 732–735.
- Ren Y, Liu SF, Nie L, Cai SY, Chen J. 2019. Involvement of ayu NOD2 in NF- κ B and MAPK signaling pathways: Insights into functional conservation of NOD2 in antibacterial innate immunity. *Zoological Research*, **40**(2): 77–88.
- Rosales C, Uribe-Querol E. 2013. Antibody-Fc receptor interactions in antimicrobial functions. *Current Immunology Reviews*, **9**(1): 44–55.
- Sarfati M, Chevret S, Chastang C, Biron G, Stryckmans P, Delespesse G, Binet JL, Merle-Beral H, Bron D. 1996. Prognostic importance of serum soluble CD23 level in chronic lymphocytic leukemia. *Blood*, **88**(11): 4259–4264.
- Sautès C, Mazières N, Galinha A, Tartour E, Bonnerot C, Amigorena S, Teillaud C, Spagnoli R, Fridman WH. 1992. Murine soluble Fc γ receptors/IgG-binding factors (IgG-BF): Analysis of the relation to Fc γ RII and production of milligram quantities of biologically active recombinant IgG-BF. *Immunologic Research*, **11**(3–4): 181–190.
- Sears DW, Osman N, Tate B, McKenzie IF, Hogarth PM. 1990. Molecular cloning and expression of the mouse high affinity Fc receptor for IgG. *The Journal of Immunology*, **144**(1): 371–378.
- Seijsing J, Lindborg M, Löfblom J, Uhlén M, Gräslund T. 2013. Robust expression of the human neonatal Fc receptor in a truncated soluble form and as a full-length membrane-bound protein in fusion with eGFP. *PLoS One*, **8**(11): e81350.
- Sibérl S, Dutertre CA, Fridman WH, Teillaud JL. 2007. Fc γ R: The key to optimize therapeutic antibodies?. *Critical Reviews in Oncology/Hematology*, **62**(1): 26–33.
- Smith DA. 1998. The Development and Application of A Hemolytic Plaque Forming Cell Assay (PFC) and A Cytotoxic T-Lymphocyte Assay (CTL) in Tilapia (*Oreochromis niloticus*) for Immunotoxicity Risk Assessment of Environmental Contaminants. Ph.D. dissertation, Virginia Tech, 88–108.
- Stafford JL, Wilson M, Nayak D, Quiniou SM, Clem LW, Miller NW, Bengtén E. 2006. Identification and characterization of a FcR homolog in an ectothermic vertebrate, the channel catfish (*Ictalurus punctatus*). *The Journal of Immunology*, **177**(4): 2505–2517.
- Teillaud C, Galon J, Zilber MT, Mazières N, Spagnoli R, Kurrle R, Fridman WH, Sautès C. 1993. Soluble CD16 binds peripheral blood mononuclear cells and inhibits pokeweed-mitogen-induced responses. *Blood*, **82**(10): 3081–3090.
- Tian J, Sun B, Luo Y, Zhang Y, Nie P. 2009. Distribution of IgM, IgD and IgZ in mandarin fish, *Siniperca chuatsi* lymphoid tissues and their transcriptional changes after *Flavobacterium columnare* stimulation. *Aquaculture*, **288**(1–2): 14–21.
- van der Boog PJM, van Zandbergen G, de Fijter JW, Klar-Mohamad N, van Seggelen A, Brandtzaeg P, Daha MR, van Kooten C. 2002. Fc α RI/CD89 circulates in human serum covalently linked to IgA in a polymeric state. *The Journal of Immunology*, **168**(3): 1252–1258.
- Varin N, Sautès C, Galinha A, Even J, Hogarth PM, Fridman WH. 1989. Recombinant soluble receptors for the Fc γ portion inhibit antibody production *in vitro*. *European Journal of Immunology*, **19**(12): 2263–2268.
- Wilson MR, Warr GW. 1992. Fish immunoglobulins and the genes that encode them. *Annual Review of Fish Diseases*, **2**: 201–221.
- Xiong JB, Nie L, Chen J. 2019. Current understanding on the roles of gut microbiota in fish disease and immunity. *Zoological Research*, **40**(2): 70–76.
- Zhang RC, Chen J, Li CH, Lu XJ, Shi YH. 2011. Prokaryotic expression, purification, and refolding of leukocyte cell-derived chemotaxin 2 and its effect on gene expression of head kidney-derived macrophages of a teleost fish, ayu (*Plecoglossus altivelis*). *Fish & Shellfish Immunology*, **31**(6): 911–918.

Immunodetection of ephrin receptors in the regenerating tail of the lizard *Podarcis muralis* suggests stimulation of differentiation and muscle segmentation

Lorenzo Alibardi^{1,*}

¹ *Comparative Histolab Padova and Department of Biology, University of Bologna, Bologna 40126, Italy*

ABSTRACT

Ephrin receptors are the most common tyrosine kinase effectors operating during development. Ephrin receptor genes are reported to be up-regulated in the regenerating tail of the *Podarcis muralis* lizard. Thus, in the current study, we investigated immunolocalization of ephrin receptors in the *Podarcis muralis* tail during regeneration. Weak immunolabelled bands for ephrin receptors were detected at 15–17 kDa, with a stronger band also detected at 60–65 kDa. Labelled cells and nuclei were seen in the basal layer of the apical wound epidermis and ependyma, two key tissues stimulating tail regeneration. Strong nuclear and cytoplasmic labelling were present in the segmental muscles of the regenerating tail, sparse blood vessels, and perichondrium of regenerating cartilage. The immunolocalization of ephrin receptors in muscle that gives rise to large portions of new tail tissue was correlated with their segmentation. This study suggests that the high localization of ephrin receptors in differentiating epidermis, ependyma, muscle, and cartilaginous cells is connected to the regulation of cell proliferation through the activation of programs for cell differentiation in the proximal regions of the regenerating tail. The lower

immunolabelling of ephrin receptors in the apical blastema, where signaling proteins stimulating cell proliferation are instead present, helps maintain the continuous growth of this region.

Keywords: Lizard; Regenerating blastema; Ephrin receptors; Immunolabelling; Western blotting

INTRODUCTION

Among amniotes, only lizards regenerate a large organ such as their tail after loss (Alibardi, 2014, 2015, 2017a, 2018; Bellairs & Bryant, 1985; Cox, 1969; Fisher et al., 2012; Gilbert et al., 2015; Hughes & New, 1959; Lozito & Tuan, 2016). The process of tail regeneration in lizards occurs after the formation of a regenerative blastema over the injured tissue of the tail stump. The blastema comprises a soft mesenchyme rich in hyaluronate and is covered by an actively proliferating epidermis (Alibardi, 2017b, 2017c). While the growing tip of the blastema elongates the tail, the more proximal regions to the tail stump differentiate into axial tissues (Alibardi & Meyer-Rochow, 1989). The latter comprise a cartilaginous cylinder replacing the vertebral column and encasing the ependymal tube derived from the spinal cord and segmental myomeres of similar dimension (Figure 1). Regenerating muscles gradually grow from pro-muscle aggregates derived from the local fusion of myoblasts that give rise to elongating myotubes, while the segregated fibroblasts form the connective myosepta (Alibardi, 1995; Cox, 1969; Hughes & New, 1959).

Open Access

This is an open-access article distributed under the terms of the Creative Commons Attribution Non-Commercial License (<http://creativecommons.org/licenses/by-nc/4.0/>), which permits unrestricted non-commercial use, distribution, and reproduction in any medium, provided the original work is properly cited.

Copyright ©2019 Editorial Office of Zoological Research, Kunming Institute of Zoology, Chinese Academy of Sciences

Received: 13 January 2019; Accepted: 30 April 2019; Online: 16 May 2019

Foundation items: This study was mainly supported by the Comparative Histolab Padova and University of Bologna

*Corresponding author, E-mail: lorenzo.alibardi@unibo.it

DOI: 10.24272/j.issn.2095-8137.2019.046

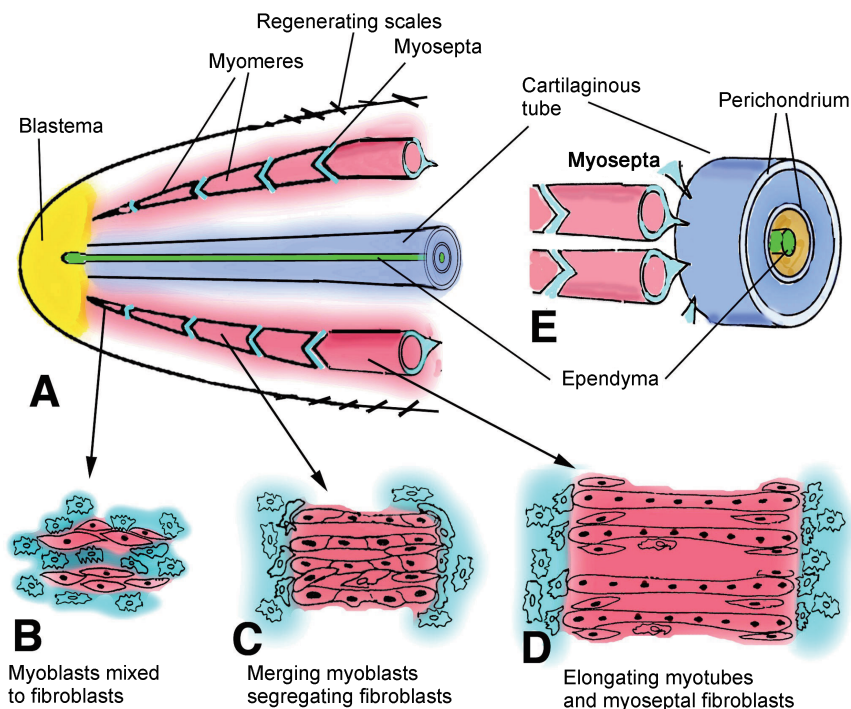


Figure 1 Schematic drawing

A: Regenerating tail at elongating cone stage showing main differentiating tissues formed in more proximal regions with respect to apical blastema (yellow). B–D: Process of myomere morphogenesis (red) separated by connective myosepta (light blue). E: Shape and attachment of two myomeres to cartilaginous tube (blue) containing regenerating ependymal (green).

Recent research has revealed the expression of numerous developmental genes in the regenerating tail of lizards (Hutchins et al, 2014; Liu et al., 2015). Comparison between up- and down-regulated genes in the tail with those in limbs has helped identify key genes responsible for tail regeneration (Vitulo et al., 2017a, 2017b). Previous studies have also detected the expression sites of these genes and their coded proteins (Alibardi, 2017a, 2017d). Thus, based on transcriptome analysis, it is now possible to determine the localization of specific, highly up-regulated proteins responsible for tail regeneration, avoiding a random search for signaling proteins, growth factors, oncogenes, and transcription factors.

One of the more up-regulated and tail-exclusive genes was coding for a receptor of ephrin proteins (erythropoietin producing hepatocellular carcinoma receptor), *ephrb6*, with 8–30-fold of expression in the regenerating blastema in comparison to the tissues present in the normal tail (Vitulo et al., 2017a). Ephrins are membrane-bound proteins that stimulate their specific tyrosine-kinase receptors located on the plasma membrane of a target cell, which respond by phosphorylation of cytoplasmic proteins for specific gene activation and cytoskeletal re-organization (Klein, 2012; Palmer & Klein, 2003; Park & Lee, 2015). Ephrin receptors comprise proteins inserted in a cell membrane that interact with ephrin membrane proteins and their physiological ligands, and are distinguished as sub-class A and B. These receptors comprise the highest number of protein kinases

present in cells of vertebrates, and are involved in numerous morphogenetic processes, including the development of paraxial segmentation, limb skeleton, and nervous system regionalization, as well as cancer and metastasis intervention (Durbin et al., 1998; Henkemeyer et al., 1994; Pasquale, 2010; Poliakov et al., 2004). These proteins and their receptors mediate the formation of cell junctions in external or internal epithelia, during neural tube development, in growing blood vessels, during formation of temporary junctions in migrating cells of the neural crest, and establishment of compartmentalization among different tissues, thus forming the basis for the development of distinct organs (Park & Lee, 2015).

In the regenerating tail of the common wall lizard (*Podarcis muralis*), where cell movement and tissue formation and re-organization are present, several genes coding for ephrin receptors are reported to be highly up-regulated (Vitulo et al., 2017a). However, the specific role of these genes and their main sites of expression in the regenerating tail remain undetermined. Therefore, based on immunohistochemical analysis, we detected the sites of ephrin receptor localization in the tail blastema-cone of *Podarcis muralis*.

MATERIALS AND METHODS

Procurement and maintenance of animals

Eight common wall lizards (*Podarcis muralis*), whose tail

tissues were prepared earlier for previous investigations, were used in the present study. Adult females and males were captured in the wild and were then maintained in cages at fluctuating temperatures of 25–30 °C. The lizards were fed three times weekly with maggots and mealworms and exposed to natural sunlight. All animal care and handling procedures followed Italian guidelines (Art. 5, DL 116/92). After inducing autotomy at about 1/3 proximal of the tail, a natural and painless process of tail amputation, the tail was regenerated at 25–30 °C until a 3–4-mm blastema-cone formed over the tail stump (~12–16 d later). We collected tissues from three adults with 3–4-mm long regenerated tails for protein extraction and successive electrophoretic analysis.

Western blotting

Tissues were homogenized in 8 mol urea and 50 mmol Tris-HCl at pH 7.6 containing 0.1 mol 2-mercaptoethanol, 1 mmol dithiothreitol, and 1% protease inhibitor (Sigma, St Louis, USA). The non-solubilized tissue components were removed by centrifugation at 10 000 g for 5 min at room temperature. Protein concentration was assayed by the Bradford method before electrophoresis.

For electrophoresis, the same amount of protein (35 µg) was loaded in each lane and separated in a gradient gel (8–250 kDa molecular weight (MW)) using the MiniProtein III electrophoresis apparatus (Bio-Rad, USA). For Western blotting, the separated proteins were transferred to nitrocellulose membranes, which were then stained with Ponceau red to verify protein transfer and incubated with primary mouse antibody against ephrin receptor. The primary antibody (CPTC-EPHB4-1) was induced in mice against an amino acid sequence within the Human Ephrin Receptor B4 protein (UniProt ID P54760). The antibody was produced by Clinical Proteomics Technologies for Cancer, National Cancer Institute, and maintained by the Hybridoma Developmental Study Bank, University of Iowa, USA, supported by the US NIH. For immunoblotting the antibody was utilized at 1:300 dilution in buffer, whereas the primary antibody was omitted in the controls. Detection of the separated and reactive protein bands was performed using enhanced chemiluminescence as per Amersham, which employed fluorescent secondary antibodies against mouse immunoglobulins (ECL, Plex Western Blotting System, GE Healthcare, UK).

Fixation and microscopic methods

The regenerating tissues were fixed for 8 h at 0–4 °C in 4% paraformaldehyde in 0.1 mol/L phosphate buffer at pH 7.4 and were then rinsed in buffer for 30 min, dehydrated in ethanol, clarified in xylene, and embedded in wax.

The tissues were sectioned (6–8 µm) using a microtome. The sections were then collected on chromolume-gelatin pre-coated slides and dried for 2–3 h on a warm plate. Representative sections were stained with Hematoxylin-Eosin (HE) or Mallory stain for histological examination. After de-waxing with xylene and hydration, the sections utilized for immunofluorescence were initially treated for antigen retrieval using a microwave-oven technique. The sections were

immersed in 0.1 mol/L citrate buffer at pH 5.6, and tissues were exposed to irradiation for 6 min. After this, sections were rinsed in Tris buffer 0.05 mol/L at pH 7.6 containing 5% bovine serum albumin and were pre-incubated for 20 min with buffer containing 2% normal goat serum to block non-specific antigens. The sections were incubated for 6 h at room temperature with primary mouse antibody (see above) at 1:50 dilution in buffer, whereas control sections were incubated with buffer only (omitting primary antibody). After rinsing in buffer for 10 min three times, the sections were incubated for 60 min at room temperature with fluorescein-isothiocyanate conjugated to an anti-mouse IgG (FITC, Sigma, USA), diluted 1:200 in buffer. The sections were again rinsed three times in buffer, mounted in anti-fading medium (Fluoroshield, Sigma, USA), and observed under a fluorescence microscope using a fluorescein filter. Pictures were taken using a digital camera and digitalized using the Adobe Photoshop Program v8.

RESULTS

Bioinformatics and Western blotting

Bioinformatics analysis using the Clustal-W Muscle Program showed that at least three ephrin-receptor proteins in the lizard *Anolis carolinensis* possessed possible epitopes recognized by the antibody employed here; in particular, ephrin receptor-B4 showed a higher identity in comparison to ephrin receptor-B2 and -B3 (Figure 2).

Immunoblot detection showed a main band at 60–65 kDa and weak bands at 130–140 and 17 kDa (Figure 3, first lane). Control blots showed lower labelling only at ~65 kDa, suggesting that this band also contained non-specific protein material packed with reactive antigen (Figure 3, second line).

Histology

The regenerating tail was composed of mesenchymal and loose connective tissues at the tip for 0.3–0.5 mm. This apical tissues were in continuation with a loose connective containing fibroblast-like cells in more proximal regions 0.5–1.0 mm from the tip (Figure 4A, B). The thick wound epidermis of the apical blastema consisted of numerous layers of keratinocytes covered by a thin corneous layer (Figure 4B). The apical epidermis was undulated and formed one or more small apical pegs. Numerous melanocytes were seen in the blastema and they also infiltrated the basal layer of the regenerating epidermis. Near the apical epidermis, a tube of ependymal cells, often forming a dilated ampulla, was present and surrounded by a cylinder of cartilage cells (Figure 4A). Around the cartilage, irregular loose connective tissue containing sparse blood vessels and nerves was present. The inner areas of connective tissue forming the future dermis contained bundles of regenerating muscles that were degrading into small pro-muscle aggregates toward the tip of the regenerating blastema (Figures 1, 4A). Moving proximally, the muscle aggregations formed segmented units made of bundles of myotubes separated by fibroblasts that gave rise to inter-muscle connective septa in more proximal, mature regions of the regenerating tail (Figures 1, 4C).

Ephrin type B receptor 4 XP_003230237.2 aa 429-525

```

ep -----SNAPPAVSDIRVTRSSPSSLAWAVPRAPSGAVLDYEVKYHEKGAEGPSS
eB4 SDSINASTNKDVQPVSIEQTSVSPNGVTLAWPPVQPPPTGTILDYEVKYHEKGVGGEM-
      .:. * **:*. * **.:*** :*::*****:***. **

ep VRFLKTSENRAELRGLKRGASYLVQVRARSEAGYGPFQEHHSQTQLD-----
eB4 --FVKTSKSRVTLTGLRQGATYGVQVRARSEAGYGGFPESAFQTQGNELGGGTEKLALI
      *::*:*. * **.:***:***** ** * ***:

```

XP_008116433.1 ephrin type-B receptor 3 isoform X2 aa 376-464

```

e -----SNAPPAVSDIRVTRSSPSSLAWAVPRAPSGAVLDYEVKYHEK
e3 KNPQNPFASVNITTNQAAPSATVTHLHGSGSSMTLSWEPKQNGIILDYEIKYFEK
      . **.*. :. : *::*:*. * *. *::*:***:***. **

e GAEGPSSVRFLKTSENRAELRGLKRGASYLVQVRARSEAGYGPF-----
e3 QGQGDGIASVTTSQKSMVRLEGKLPNAGYMIQVRARTVAGYQYSLPMEFRTPIEDGSSS
      .:* . . :.:.. . * *** .*:*****: ****:

```

XP_016854694.1 ephrin type-B receptor 2 aa 453-548

```

e -----SNAPPAVSDIRVTRSSPSSLAWAVP
e2 AHTQYTFEVQAVNGVTDQSPFSPQFASVNITTNQAAPSATVIMHQVSRVTSITLSWSQP
      . **.*. :. : .*:***: *

e RAPSGAVLDYEVKYHEKGAEGPSSVRFLKTSENRAELRGLKRGASYLVQVRARSEAGYGP
e2 DQPNGVILDYELQYYEDLSEFNGTA-VKSPTNTVTQNLKAGTIYVFQVRARTVAGYGR
      *.*:*****:***. . . . :*. * . :.* ** *:*:*****: ****

e FGQEHHSQTQLD-----
e2 FSGKMYFQTMTEAEYQTSIQEKLPLIIGSSAAGLVFLIALVVIVLCNSPPASRSARCS
      * . : * * :

```

Figure 2 Epitope regions, amino acid position within protein (aa), and GenBank accession No. for three ephrin receptors detected in NIH database for *Anolis carolinensis*

Regions with higher identity between epitope recognized by ephrin receptor antibody (ep) and lizard sequences are in green. Stars represent identities (same amino acid), colons indicate substitutive but conservative replacements (amino acids with similar 3D-shape, size, and solubility), and dots indicate semi-conserved substitutions (amino acids with similar size but different polarity).

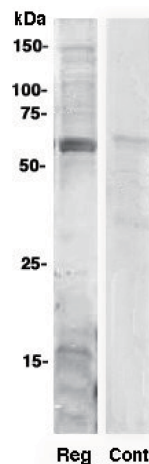


Figure 3 Western blotting of regenerating tail showing labelled bands

Reg: Regenerating sample; Cont: Control of regenerating sample (see text).

Immunofluorescence

The apical wound epidermis showed stronger immunolabelling in comparison to the mesenchymal blastema (Figure 5A). The numerous blood vessels fluoresced yellow, an indication of non-specific (auto-)fluorescence. Most suprabasal and external, pre-corneous keratinocytes were sparsely immunofluorescent, and the fluorescence appeared mainly localized along the peripheral cytoplasm (Figure 5B, C). Only basal cells in contact with the underlying blastema showed some nuclear labelling. Immunofluorescence decreased over the entire thickness of the proximal epidermis where scales were forming (Figures 5D, 6A). In the suprabasal layers of the regenerating scales, keratinocytes appeared in the course of differentiation to give rise to the spindle-shaped cells of the forming corneous layer. These differentiating cells also showed some labelling along their perimeter (Figure 6A).

The cells forming the enlarged ependymal ampulla showed variably intense immunolabelling in their cytoplasm and occasionally also in the nucleus, which appeared stronger in comparison to that seen in the mesenchymal cells of the surrounding blastema (Figure 6B, C). The differentiating

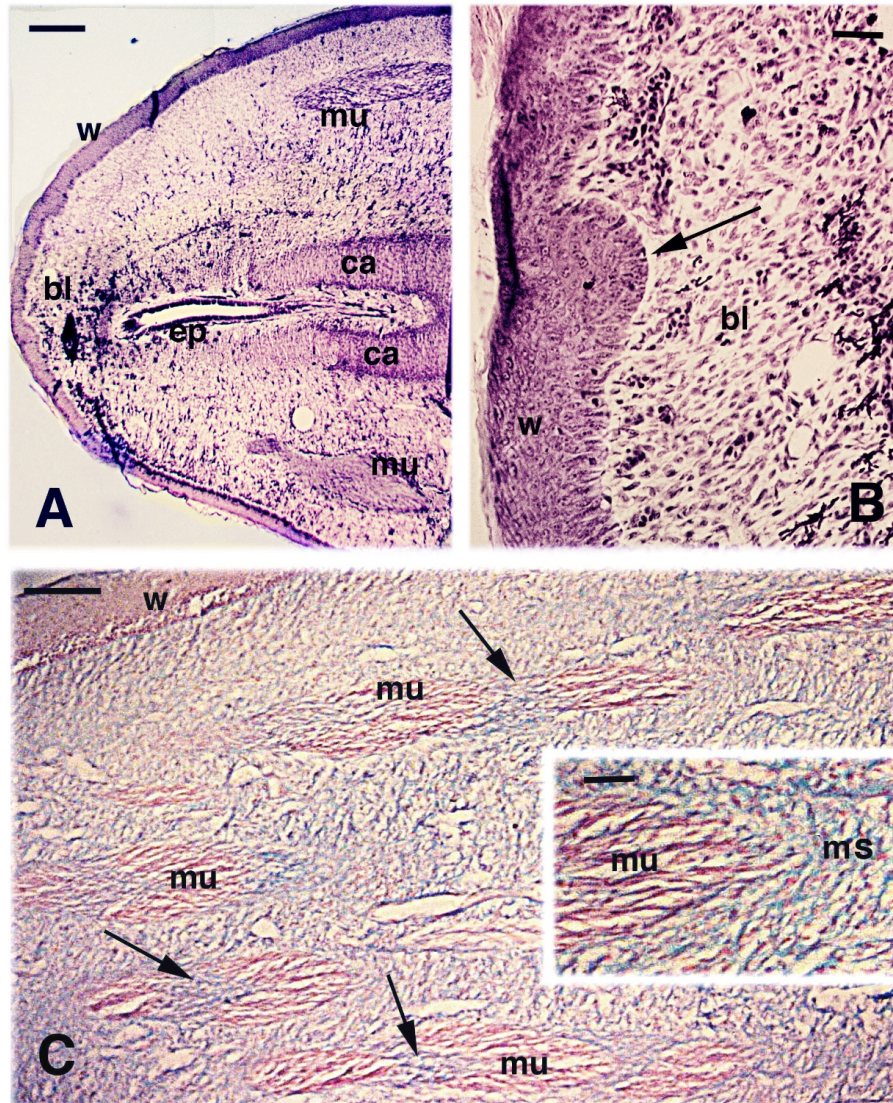


Figure 4 Histology of regenerating tail

A: Apical blastema with main regenerating tissues present. Hematoxylin-Eosin staining. Scale bar: 100 μ m. B: Wound epidermis with apical epidermal peg (arrow). Hematoxylin-Eosin staining. Scale bar: 25 μ m. C: Myomeres localized more proximally in an elongating cone and separated by myosepta (arrows). Mallory staining. Scale bar: 50 μ m, inset scale bar: 10 μ m. bl: blastema; ca: cartilaginous tube; ep: ependyma; ms: myoseptum; mu: regenerated muscles; w: wound (regenerating) epidermis.

cartilage cells surrounding the ependymal tube also showed more intense labelling than that in the cells of the peripheral mesenchyme (Figure 6B). Small as well as larger nerves entering the blastema also appeared more intensely labelled than the cells of the surrounding mesenchyme or of the loose connective tissue and forming dermis (Figure 6D). In more proximal regions, at 0.5–3 mm from the tail tip, the external region of the cartilaginous tube, the perichondrium, appeared intensely labelled but the labelling decreased in the fusiform chondrocytes localized in the more central regions of the cartilaginous tube (Figure 7A, B). In addition, the wall of the

large blood vessels (containing few or no erythrocytes) present in the loose connective tissue surrounding the cartilaginous tube, showed high immunofluorescence (Figure 7B). Erythrocytes fluoresced intensely yellow, especially when clustered within the lumen of the blood vessels, disturbing the green fluorescence of vessel walls.

The initial pro-muscle aggregates present at the apex of the regenerating blastema (Figures 1, 4A), appeared more immunofluorescent than the surrounding mesenchyme (Figure 7C). Strong immunolabelling was also noted in numerous nuclei of myoblasts of forming myomeres, and in their

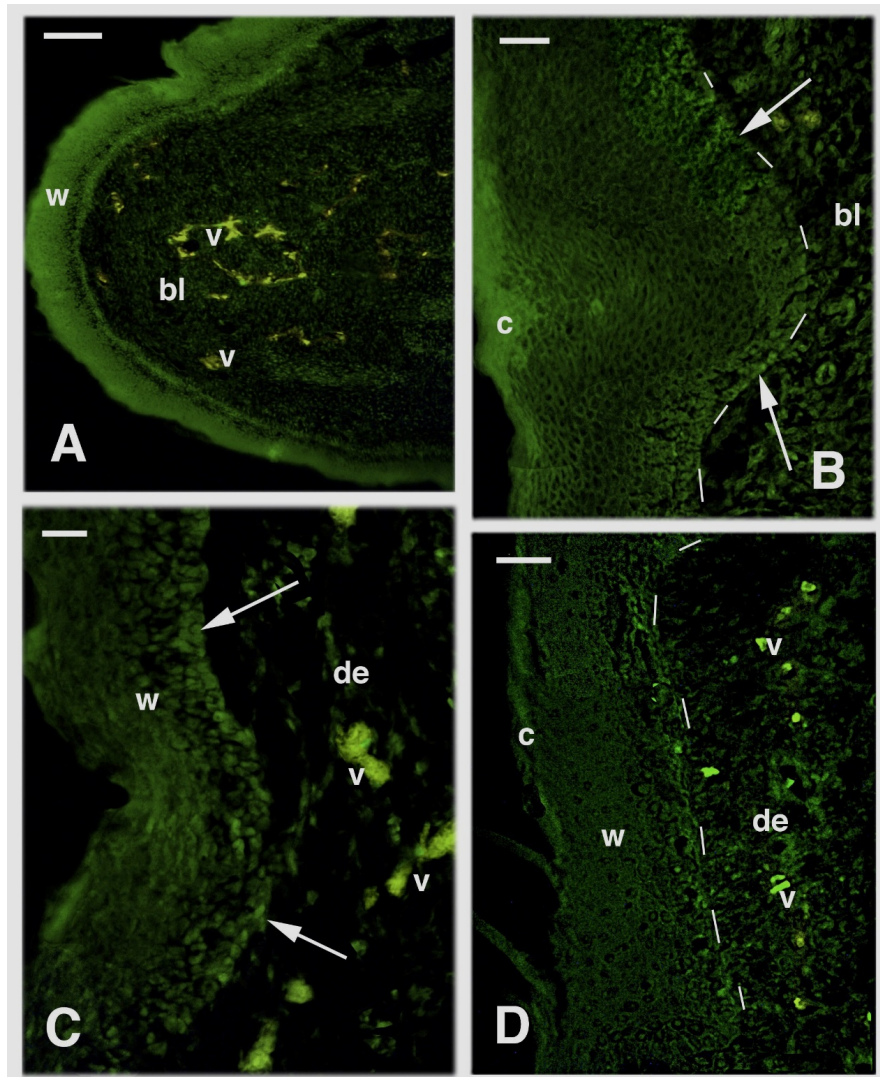


Figure 5 Immunofluorescence of blastema for ephrin receptors

A: Blastema tip showing higher immunofluorescence of wound epidermis over mesenchymal blastema. Scale bar: 50 μ m. B: Labelling on apical epidermal peg (arrows), especially in basal layers. Scale bar: 20 μ m. C: Weak labelling of waved epidermis in proximal areas of blastema with nuclear labelling in basal layers (arrows). Scale bar: 10 μ m. D: Low and even labelling present in proximal regenerated epidermis. Scale bar: 20 μ m. bl: blastema; c: corneous layer; de: dermis; v: blood vessels (auto-fluorescent in yellow). Dashes underline basal layer of epidermis.

cytoplasm (inset of Figure 7C). As the myoblasts merged into myotubes in more proximal regions of the regenerating tail, a segmented immunofluorescent pattern of the elongating myomeres became evident (Figure 7D). The inter-muscle fibroblasts appeared weakly labeled or unlabeled in comparison to the elongating myotubes forming the segmented myomeres (Figures 1, 7D, E). The immunofluorescence was nuclear but was also intensely localized in the cytoplasm and in the membranes of the growing muscle fibers. In the control sections, either weak or no labelling was detected in the epidermis, ependyma, muscles, and cartilage, aside from the yellowish autofluorescence present in sparse blood vessels (Figure 7F).

DISCUSSION

General considerations

Based on transcriptome data as well as the present bioinformatics, Western blotting, and immunohistochemical results, ephrin receptor-like proteins were present in the regenerating tail of *P. muralis*.

Previous transcriptome study of *P. muralis* has indicated that numerous ephrin receptor genes are variably up-regulated in the regenerating tail blastema, although their specific roles remain unknown (Vitulo et al., 2017a). They include *ephb6* (ENSACAG00000008000, 8.0-fold expression), *epha4* (ENSACAG00000005061, 6.8-fold), *ephb3* (ENSACAG

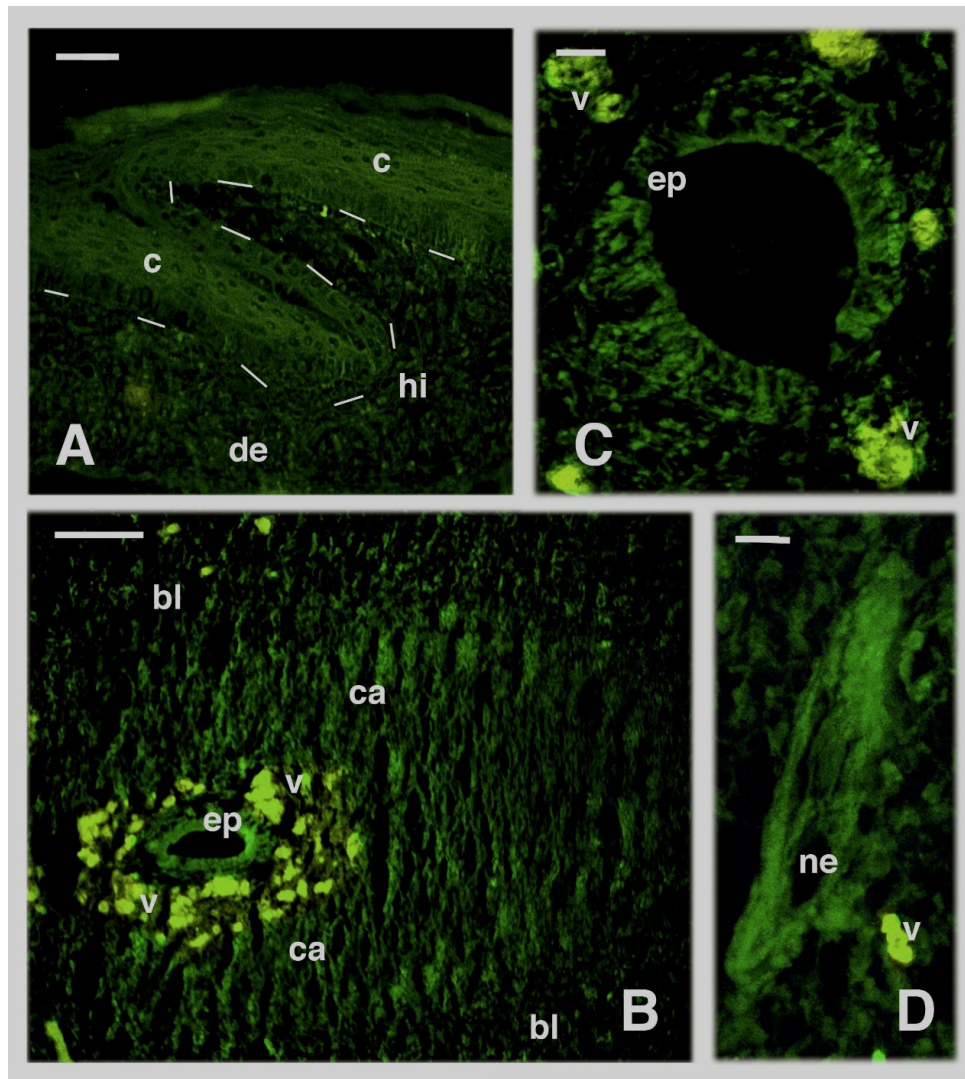


Figure 6 Immunofluorescence of tissues present in regenerating tail

A: Weak labelling in differentiating corneous layers of forming scales, located near tail stump. Dashes underline basal layer of epidermis. Scale bar: 20 μ m. B: Oblique section of apical ependymal ampulla surrounded by numerous, largely auto-fluorescent, blood vessels and from differentiating cartilaginous cells. Scale bar: 50 μ m. C: Obliquely-sectioned apical ependymal ampulla. Scale bar: 10 μ m. D: Regenerating nerves entering blastema. Scale bar: 10 μ m. bl: blastema; c: differentiating corneous layers; ca: regenerating cartilage; de: forming dermis; ep: ependymal; hi: hinge region; ne: nerve; v: blood vessels (yellowish autofluorescence).

00000007949, 3.7-fold), *ephb2* (ENSACAG00000022723, 5.8-fold), *ephb1* (ENSACAG00000009241, 3.6-fold), and an unclassified ephrin type B receptor kinase gene (ENSACAG 00000008140, 3.5-fold). Among the above receptors, *ephb6*, *ephb3*, *ephb2*, and *epha4* are tail exclusive and are not expressed in the scarring limb (Vitulo et al., 2017a). In the regenerating lizard tail, *ephrb6* has been hypothesized to function as a tumor suppressor and is considered to be a differentiating signaling protein that contrasts or regulates cell proliferation and induces differentiation in proximal areas of the regenerating blastema (Alibardi, 2017a, 2017d; Vitulo et al., 2017a). In the apical region of the blastema, numerous

Wnt genes that stimulate cell proliferation are expressed, which might produce uncontrolled tumor-like proliferation without regulation. The immunolocalization of ephrin receptors in differentiating epidermal, muscle, and cartilaginous tissues supports the hypothesis of tumor-suppressor activity by ephrin receptors (Pasquale, 2010).

The bioinformatics analysis of amino acid sequences between epitopes (Figure 3) suggests that the employed mouse antibody should recognize similar epitopes present in ephrin receptor-B4 (present in the database), and less so for -B3 and -B2 in *A. carolinensis*, and likely less also in *P. muralis* (although these genes are not sequenced in the latter

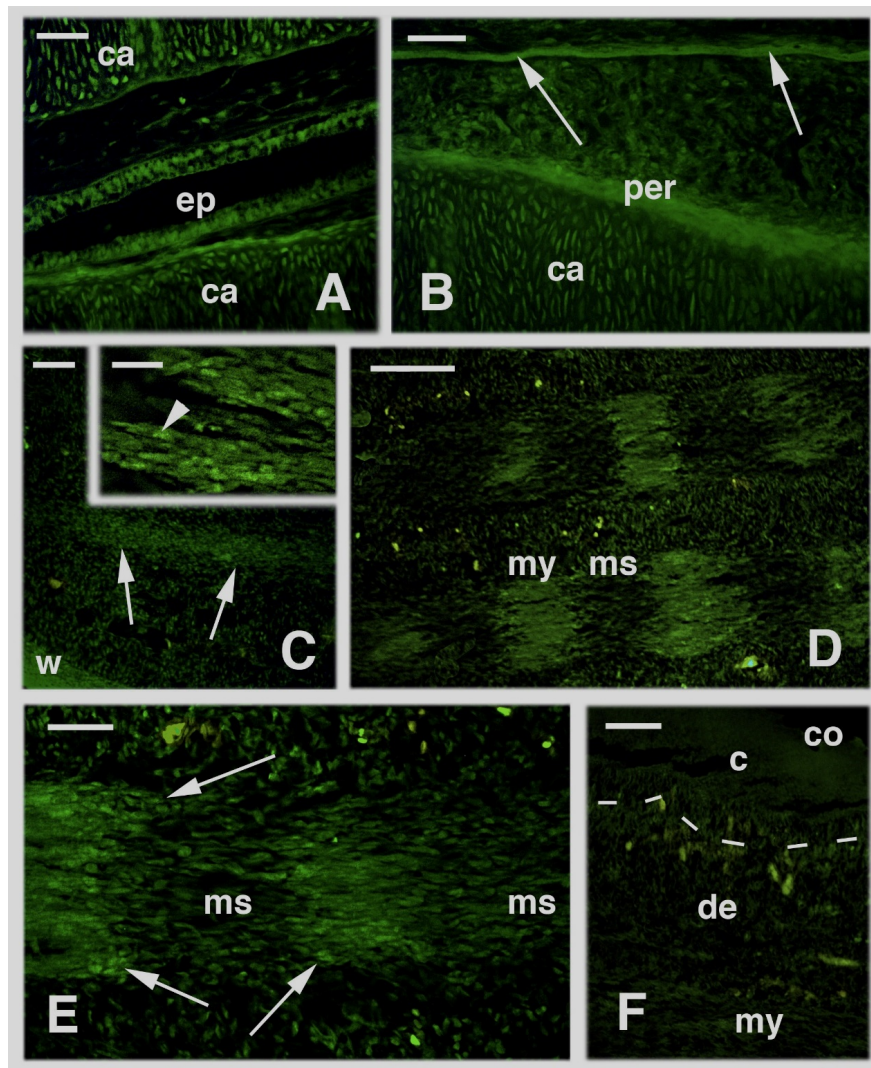


Figure 7 Immunofluorescence of differentiating tissues in proximal areas of regenerating cones

A: Ependymal canal surrounded by cartilaginous tube. Scale bar: 20 μ m. B: Immunofluorescent external perichondrium and endothelium of long blood vessel (arrows). Scale bar: 20 μ m. C: Immunolabelled pro-muscle aggregate not yet segmented at this stage of regeneration (arrows) by apical region of regenerating blastema. Scale bar: 20 μ m. Inset shows labelled myoblasts and their nuclei (arrowhead). Scale bar: 10 μ m. D: More intense immunolabelled proximal segmented muscles. Scale bar: 20 μ m. E: Shape of inter-muscle and muscle segments (myomeres) with labelled nuclei at extremities of myotubes (arrows). Scale bar: 20 μ m. F: Immuno-negative control sections showing area comprising proximal epidermis (underlined by dashes), dermis, and part of a myomere. Scale bar: 20 μ m. ca: regenerating cartilage; ep: ependymal; my: myotome; ms: myoseptum; w: wound epidermis.

species). The immunoblotting results showed that very low immunoreactive bands were detected within the expected molecular weight (MW) for the entire receptor, i.e., 120–140 kDa (Figure 4). Instead the main band at 60–65 kDa, partially specific as it was probably mixed with other abundant proteins of similar MW, was interpreted as a degraded form of the original protein. It remains undetermined whether this lower MW form was derived from a physiological or artifact process of degradation due to the extraction method.

The present results are partially supported by biochemical

studies on nervous tissues, fibroblasts in culture, and other mouse organs, where ephrin receptor-B1 and -B2 can produce degraded forms at 65 and 45 kDa under the proteolytic action of matrix metalloproteases (Lin et al., 2012; Tomita et al., 2006). These enzymes are present in the blastema (Gilbert et al., 2015), as also shown in previous transcriptome study on *P. muralis* (Vitulo et al., 2017a). The protein fragments could be further processed to give rise to 15–17 kDa products. The cleavage of the intra-membrane and cytoplasmic region of the ephrin receptor operated by a γ -

secretase (Bong et al., 2007; Tomita et al., 2006) suggests that a cytoplasmic fragment of the receptor moves into the nucleus, although its proliferative or anti-proliferative role is not known. The nuclear localization seems to activate the transcriptional activator protein STAT3, which induces various cellular responses, including cell growth and movement, but also apoptosis (Bong et al., 2007).

In the present observation on lizard blastemas, we did not determine whether the nuclear localization seen in basal epidermal cells and muscle cells also activated specific genes and relative function. Based on the known role of complex ephrin receptors on the cytoskeleton (Klein, 2012; Palmer & Klein, 2003; Park & Lee, 2015), we suggest that possible cleavage of ephrin receptors determines intracellular responses, producing cytoskeletal rearrangements and repulsion among cells. This process induces the formation of boundaries and compartments within tissues, in particular in regenerating muscles that become segmented. Whether the 60–65 and 15–17 kDa immunoreactive bands detected in the lizard blastemas indicate biochemical processing of the ephrin receptors remains to be demonstrated as the main purpose of the Western blotting analysis was to detect the presence of immunoreactive bands in support of the immunolocalization study.

Ephrin receptors in regenerating epidermis

Ephrin-A2, -A3, and -A4 are the more common ephrin receptors found in the human epidermis, where they exert inhibitory activity on basal cell proliferation (tumor suppressors), while stimulating keratinocyte differentiation (Lin et al., 2012; Perez-White & Getsios, 2014). These receptors likely promote cell communication and adhesion among keratinocytes, modulating the formation of cell junctions (Lin et al., 2012; Perez-White & Getsios, 2014). In the suprabasal keratinocytes of the lizard epidermis, the cytoplasmic labelling appears mainly along the perimeter of keratinocytes, reflecting the localization of this receptor. Ephrins and their receptors may be involved in the differentiation of cells that give rise to beta- and alpha-corneous layers of the scales (Alibardi, 1994, 1995, 2014).

During the early stages of skin wound healing in mice, between 12 h to 7 d post injury, ephrin-B1 and its receptor ephrin-B2 are detected along the cell perimeter of migrating keratinocytes that cover open wounds (Nunan et al., 2015). It is believed that this process occurs by loosening the tight and adherens junctions, but not desmosomes, facilitating the rolling movement of migrating keratinocytes along the wound border. A likely rolling movement has also been shown in the regenerating wound epidermis of lizards (Alibardi, 1994) in regions equivalent to the lateral and apical wound epidermis where ephrin-receptor immunoreactivity is present. Once the epidermis covers the tail stump, it starts to stratify and proliferate to keep pace with the expanding mesenchymal blastema that pushes elongation of the regenerating tail.

The immunolocalization of ephrin receptors, especially of ephrin receptor-B4, the subtype most likely recognized by the present antibody, in basal cell nuclei of the apical wound

epidermis suggests that the receptor may be involved in the control of epidermal proliferation activity. These cells also contain most p53/63 immunolabelling, another negative regulator of cell proliferation (Alibardi, 2016). Basal keratinocytes contain high levels of proliferative markers such as telomerase, FGFreceptors, EGFreceptors, and c-myc (Alibardi, 2014, 2017a). The immunolocalization of anti-proliferative (tumor-suppressors) and proliferative (oncogenes or tumor activators) proteins in the basal layer of the apical regenerative epidermis indicates that strong competition between proliferative and anti-proliferative activities is present in these cells. Colocalization of activators and suppressor proteins in the same cells has been noted in other cases, reinforcing the concept of balanced regulation (Yang et al., 2014). In the wound epidermis of the apical regions of a lizard blastema, 0.5–1.5 mm from the tip, active cell multiplication occurs along the entire epidermis, but in more proximal regions, where scales are forming, the rate of cell multiplication decreases and becomes limited to smaller regions of the forming scales (Alibardi, 1994; Wu et al., 2014). In conclusion, ephrin receptors in concert with other tumor suppressors appear essential for the control of epidermal regeneration and scale morphogenesis.

Ephrin receptors in regenerating spinal cord and nerves

Ephrins and their receptors participate in the segregation of neurons in different neuromeres of the brain and also stimulate axonogenesis in the spinal cord (Henkemeyer et al., 1994; Klein, 2012; Palmer & Klein, 2003; Park & Lee, 2015). The regenerating spinal cord in the tail of lizards includes the ependyma of the simplified spinal cord, whose cells fasciculate the descending axons derived from neurons localized in the original spinal cord and those directed toward the tip of the blastema (Alibardi & Miolo, 1995; Simpson & Duffy, 1994). Peripheral nerves are instead derived from the last three spinal sensory ganglia proximal to the regenerating blastema and from motor neurons present in the closest spinal cord segments to the blastema (Cristino et al., 2000a, 2000b). Both nerves and ependymal cells contain ephrin receptors, suggesting that these proteins are also involved in axonogenesis during lizard tail regeneration.

Ephrin receptors in regenerating mesodermal tissues

The near to total absence of ephrin receptors in mesenchymal cells of the blastema indicates that these proteins are little expressed in undifferentiated cells. Conversely, the labelling of ephrin receptors in differentiating cells of forming blood vessels, myotomes, and perichondria of cartilaginous tubes suggests that these proteins are involved in the differentiation of mesodermal cells. The strong expression of ephrin receptors in segmental muscles implicates these proteins and their receptors in the determination of segmentation during regeneration, as is the case during development (Durbin et al., 1998; Stark et al., 2011). Only cells that express these receptors (myogenic) and not other types initially mixed with myoblasts, especially the fibroblasts destined to form inter-muscle septa (Figure 1B, C), appear capable of merging into

myotubes and myomeres. Ephrin receptors may determine the repulsion of myoblasts from fibroblasts mixed in the apical blastema, determining the initial formation of pro-muscle aggregates and later of the myomeres (Alibardi, 1995; Cox, 1969; Hughes & New, 1959; Figure 1A–D). Ephrin receptors may promote the aggregation of myogenic cells that initiate to form myotubes, with the latter elongating by the incorporation of new myoblasts. The lack of expression of numerous ephrin genes in limb blastemas (Vitulo et al., 2017a) further explains the absence of regeneration and segmentation of muscle cells in this organ, which is destined to form a short scarring outgrowth.

In contrast to the muscles, no patterned distribution of ephrin receptors was observed along the differentiating cartilaginous tube and no segmentation into vertebrae occurred, although this discrepancy between muscle and cartilage morphogenesis remains unexplained. Ephrins and their receptors are involved in the formation of the initial cartilaginous condensations in developing mammalian and avian limbs (Compagni et al., 2003; Davy et al., 2004; Wada et al., 2003), and this also appeared in the lizard's growing blastema. Condensing cartilaginous cells express ephrin-B1, whereas the forming perichondrium more intensely expresses ephrin receptor-A4. We hypothesize that an altered developmental mechanism determines the localization of ephrin-B receptors along the entire perichondrium formed around the two peripheries of the cartilaginous tube (Alibardi, 2014; Lozito & Tuan, 2015, 2016; Figure 1E). This even expression of ephrin receptors is somehow correlated with the lack of segmentation of the cartilaginous tube. Future experimental studies that perturb the pattern of expression of ephrins and their receptors, especially ephrin receptors-B4 and -B6, may confirm or refute this hypothesis.

CONCLUSION

The high up-regulation of ephrin receptors detected by previous transcriptome research (Vitulo et al., 2017a) in combination with the results of the present study suggest that ephrin receptors are present in the regenerating tail. We hypothesize that these proteins act as possible tumor suppressors and differentiating factors that normalize the growth of the proximal tissues located at some distance (0.5–1.0 mm) from the tip of the tail blastema. It is likely that the ordered process leading to tail regeneration depends on cross-talk between positive genes that stimulate cell proliferation (oncogenes) and those limiting proliferation (tumor suppressors) that instead trigger differentiation. When the balance is shifted toward proliferation, as in the apical blastema, cell multiplication increases, whereas in more proximal regions anti-proliferative processes prevail and the rate of cell multiplication decreases or is limited to smaller regions of the forming scales, muscles, cartilage, nerves, and blood vessels. Ephrin receptors, in concert with other tumor suppressors (e.g., *Rb*, *p53/63*, *apc*), are likely essential to maintain the growth of the blastema without turning it into an

uncontrolled tumor outgrowth.

COMPETING INTERESTS

The author declare that he has no competing interests.

AUTHORS' CONTRIBUTIONS

L.A. designed the study, conducted the analyses, and wrote the manuscript.

ACKNOWLEDGEMENTS

We thank Dr. F. Borsetti (Proteome Service, Department of Biology, University of Bologna) for electrophoretic analyses. We also thank the referee for help in improving the manuscript.

REFERENCES

- Alibardi L. 1994. Fine autoradiographical study on scale morphogenesis in the regenerating tail of lizards. *Histology and Histopathology*, **9**: 119–134.
- Alibardi L. 1995. Muscle differentiation and morphogenesis in the regenerating tail of lizards. *Journal of Anatomy*, **186**: 143–151.
- Alibardi L. 2014. Histochemical, biochemical and cell biological aspects of tail regeneration in lizard, an amniote model for studies on tissue regeneration. *Progress in Histochemistry and Cytochemistry*, **48**(4): 143–244.
- Alibardi L. 2015. Immunolocalization of FGF7 (KGF) in the regenerating tail of lizard suggests it is involved in the differentiation of the epidermis. *Acta Histochemica*, **117**(8): 718–724.
- Alibardi L. 2016. Immunolocalization of a p53/p63-like protein in the regenerating tail of the wall lizard (*Podarcis muralis*) suggests it is involved in the differentiation of the epidermis. *Acta Zoologica*, **97**(4): 395–406.
- Alibardi L. 2017a. Review: Biological and molecular differences between tail regeneration and limb scarring in lizard: an inspiring model addressing limb regeneration in amniotes. *Journal of Experimental Zoology*, **328B**(6): 493–514.
- Alibardi L. 2017b. Hyaluronate likely contributes to the immunosuppression of the regenerating tail blastema in lizards: implications for organ regeneration in amniotes. *Acta Zoologica*, **99**(4): 321–330.
- Alibardi L. 2017c. Review: Hyaluronic acid in the tail and limb of amphibians and lizards recreates permissive embryonic conditions for regeneration due to its hygroscopic and immuno-suppressive properties. *Journal of Experimental Zoology*, **328B**(8): 760–771.
- Alibardi L. 2017d. Wnt-1 immunodetection in the regenerating tail of lizard suggests it is involved in the proliferation and distal growth of the blastema. *Acta Histochemica*, **119**(3): 211–219.
- Alibardi L. 2018. Tail regeneration reduction in lizards after repetitive amputation or cauterization reflects an increase of immune cells in blastemas. *Zoological Research*, **39**(6): 413–423.
- Alibardi L, Meyer-Rochow VB. 1989. Comparative fine structure of the axial skeleton inside the regenerated tail of some lizard species and the tuatara (*Sphenodon punctatus*). *Gegembaurs Morphologisches Jahrbuch (Leipzig)*, **135**(5): 705–716.
- Alibardi L, Miolo V. 1990. Fine observation on nerves colonizing the regenerating tail of the lizard *Podarcis sicula*. *Histology and Histopathology*, **5**: 387–396.

- Bellairs AA, Bryant SV. 1985. Autotomy and regeneration in reptiles. In: Gans C, Billet F, Maderson PFA. *Biology of the Reptilia*, vol 15B. NY, USA: John Wiley & Sons, 302–410.
- Bong YS, Lee HS, Carim-Todd L, Mood K, Nishanian TG, Tessarollo L, Daar IO. 2007. EphrinB1 signals from the cell surface to the nucleus by recruitment of STAT3. *Proceedings of the National Academy of Sciences of the United States of America*, **104**(44): 17305–17310.
- Compagni A, Logan M, Klein R, Adams RH. 2003. Control of skeletal patterning by ephrinB1-EphB interactions. *Developmental Cell*, **5**(2): 217–230.
- Cox PG. 1969. Some aspects of tail regeneration in the lizard, *Anolis carolinensis*. I. A description based on histology and autoradiography. *Journal of Experimental Zoology*, **171**(2): 127–150.
- Cristino L, Pica A, Della Corte F, Bentivoglio M. 2000a. Plastic changes and nitric oxide synthase induction in neurons that innervate the regenerated tail of the lizard *Gekko gecko*. I. Response of spinal motoneurons to tail amputation and regeneration. *Journal of Comparative Neurology*, **417**(1): 60–72.
- Cristino L, Pica A, Della Corte F, Bentivoglio M. 2000b. Plastic changes and nitric oxide synthase induction in neurons that innervate the regenerated tail of the lizard *Gekko gecko*. II. The response of dorsal root ganglion cells to tail amputation and regeneration. *Brain Research*, **871**(1): 83–93.
- Davy A, Aubin J, Soriano P. 2004. Ephrin-B1 forward and reverse signaling are required during mouse development. *Genes & Development*, **18**(5): 572–583.
- Durbin L, Brennan C, Shiomi K, Cooke J, Barriors A, Shanmugalingam S, Guthrie B, Lindberg R, Holder N. 1998. Eph signaling is required for segmentation and differentiation of the somites. *Genes & Development*, **12**(19): 3096–3109.
- Fisher RE, Geiger LA, Stroik LK, Hutchins ED, George RM, DeNardo DF, Kosumi K, Rawls JA, Wilson-Rawls J. 2012. A histological comparison of the original and regenerated tail in the green anole, *Anolis carolinensis*. *Anatomical Record*, **295**(10): 1609–1619.
- Gilbert EAB, Delorme SL, Vickaryous MK. 2015. The regeneration blastema of lizards: an amniote model for the study of appendage replacement. *Regeneration*, **2**(2): 45–53.
- Henkemeyer M, Mcglade J, Holmyard D, Marengere LEM, Olivier JP, Conlon RA, Letwin KC, Pawson T. 1994. Immunolocalization of the Nuk receptor tyrosine kinase suggests roles in segmental patterning of the brain and axonogenesis. *Oncogene*, **9**(4): 1001–1014.
- Hughes A, New D. 1959. Tail regeneration in the geckonid lizard, *Sphaerodactylus*. *Development*, **7**: 281–302.
- Hutchins ED, Markov GJ, Eckalbar WL, Gorge RM, King JM, Tokuyama MA, Geiger LA, Emmert N, Ammar MJ, Allen AP, Siniard AL, Corneveaux JJ, Fisher RE, Wade J, DeNardo DF, Rawls JA, Huentelman MJ, Wilson-Rawls J, Kosumi K. 2014. Transcriptomic analysis of tail regeneration in the lizard *Anolis carolinensis* reveals activation of conserved vertebrate developmental and repair mechanisms. *PLoS One*, **9**(8): e105004.
- Klein R. 2012. Eph/ephrin signalling during development. *Development*, **139**: 4105–4109.
- Lin KT, Wang B, Getsios S. 2012. Eph/ephrin signaling in epidermal differentiation and disease. *Seminars in Cell Developmental Biology*, **23**(1): 92–101.
- Liu Y, Zhou O, Wang Y, Luo L, Yang J, Yang L, Liu M, Li Y, Qian YT, Zheng Y, Li M, Li J, Gu Y, Han Z, Xu M, Wang Y, Zhu C, Yu B, Yang Y, Ding F, Jiand J, Yang H, Gu X. 2015. *Gekko japonicus* genome reveals evolution of adhesive toe pads and tail regeneration. *Nature Communications*, **6**: 10033..
- Lozito TP, Tuan RS. 2015. Lizard tail regeneration: regulation of two distinct cartilage regions by indian hedgehog. *Developmental Biology*, **399**(2): 249–262.
- Lozito TP, Tuan RS. 2016. Lizard tail skeletal regeneration combines aspects of fracture healing and blastema-based regeneration. *Development*, **143**: 2946–2957.
- Nunan R, Campbell J, Mori R, Pitulescu ME, Jiang WG, Harding KG, Adams RH, Nobes CD, Martin P. 2015. Ephrin-Bs drive junctional downregulation and actin stress fiber disassembly to enable wound re-epithelialization. *Cell Reports*, **13**(7): 1380–1395.
- Palmer A, Klein R. 2003. Multiple roles of ephrins in morphogenesis, neuronal networking, and brain function. *Genes Development*, **17**: 1429–1450.
- Park I, Lee HS. 2015. EphB/ephrinB signaling in cell adhesion and migration. *Molecular and Cell*, **38**(1): 14–19.
- Pasquale EB. 2010. Eph receptors and ephrins in cancer: bidirectional signalling and beyond. *Nature Review in Cancer*, **10**: 165–180.
- Perez-White BE, Getsios S. 2014. Eph receptor and ephrin function in breast, gut, and skin epithelia. *Cell Adhesion and Migration*, **8**(4): 327–338.
- Poliakov A, Cotrina M, Wilkinson DG. 2004. Diverse roles of eph receptors and ephrins in the regulation of cell migration and tissue assembly. *Developmental Cell*, **7**(4): 465–480.
- Simpson SB, Duffy MT. 1994. The lizard spinal cord: a model system for the study of spinal cord injury and repair. *Progress in Brain Research*, **103**: 229–241.
- Stark DA, Karvas RM, Siegel AL, Cornelison DDW. 2011. Eph/ephrin interactions modulate muscle satellite cell motility and patterning. *Development*, **138**(24): 5279–5289.
- Tomita T, Tanaka S, Morohashi Y, Iwatsubo T. 2006. Presenilin-dependent intramembrane cleavage of ephrin-B1. *Molecular Neurodegeneration*, **1**: 1.
- Vitulo N, Dalla Valle L, Skobo T, Valle G, Alibardi L. 2017a. Transcriptome analysis of the regenerating tail vs. the scarring limb in lizard reveals pathways leading to successful vs. unsuccessful organ regeneration in amniotes. *Developmental Dynamics*, **246**(2): 116–134.
- Vitulo N, Dalla Valle L, Skobo T, Valle G, Alibardi L. 2017b. Down-regulation of lizard immuno-genes in the regenerating tail and myogenes in the scarring limb suggests that tail regeneration occurs in an immuno-privileged organ. *Protoplasma*, **254**(6): 2127–2141.
- Wada N, Tanaks H, Ide H, Nohno T. 2003. Ephrin-A2 regulates position-specific cell affinity and is involved in cartilage morphogenesis in the chick limb bud. *Developmental Biology*, **264**(2): 550–563.
- Wu P, Alibardi L, Chuong CM. 2014. Lizard scale regeneration and development: a model system to analyze mechanisms of skin appendages morphogenesis in amniotes. *Regeneration*, **1**: 15–26.
- Yang HB, Song W, Chen LY, Li QF, Shi SL, Kong HY, Chen P. 2014. Differential expression and regulation of prohibitin during curcumin-induced apoptosis of immortalized human epidermal HaCaT cells. *International Journal of Molecular Medicine*, **33**(3): 507–514.

Genetic diversity and temporal changes of an endemic cyprinid fish species, *Ancherythroculter nigrocauda*, from the upper reaches of Yangtze River

Dong-Dong Zhai^{1,2}, Wen-Jing Li^{1,2}, Huan-Zhang Liu¹, Wen-Xuan Cao¹, Xin Gao^{1,*}

¹ Key Laboratory of Aquatic Biodiversity and Conservation of Chinese Academy of Sciences, Institute of Hydrobiology, Chinese Academy of Sciences, Wuhan Hubei 430072, China

² University of Chinese Academy of Sciences, Beijing 100049, China

ABSTRACT

Small populations with low genetic diversity are prone to extinction. Knowledge on the genetic diversity and structure of small populations and their genetic response to anthropogenic effects are of critical importance for conservation management. In this study, samples of *Ancherythroculter nigrocauda*, an endemic cyprinid fish from the upper reaches of Yangtze River, were collected from five sites to analyze their genetic diversity and population structure using mitochondrial cytochrome *b* gene and 14 microsatellite loci. Haplotype diversity, nucleotide diversity, and expected heterozygosity indicated that the *A. nigrocauda* populations had low genetic diversity, and decreased heavily from 2001 to 2016. Significant genetic differentiation was found among different populations in the *cyt b* gene and SSR markers based on the genetic differentiation index (F_{ST}), whereas no differentiation was found in 2001. Haplotype genealogy showed that eight out of 15 haplotypes were private to one population. The SSR STRUCTURE analysis showed that there were four genetic clusters in the *A. nigrocauda* samples, with each population forming a single cluster, except for the Chishui River (CSR) and Mudong River (MDR) populations, which formed a common cluster.

Open Access

This is an open-access article distributed under the terms of the Creative Commons Attribution Non-Commercial License (<http://creativecommons.org/licenses/by-nc/4.0/>), which permits unrestricted non-commercial use, distribution, and reproduction in any medium, provided the original work is properly cited.

Copyright ©2019 Editorial Office of Zoological Research, Kunming Institute of Zoology, Chinese Academy of Sciences

Therefore, loss of genetic diversity and increased genetic differentiation were found in the *A. nigrocauda* populations, which could be attributed to dam construction, overfishing, and water pollution in the upper Yangtze River. It is therefore recommended that the government should ban fishing, control water pollution, increase river connectivity, and establish artificial breeding and stocking.

Keywords: Genetic diversity; Population structure; Temporal change; Conservation

INTRODUCTION

Genetic diversity of a species determines its adaptive capacity and evolutionary potential (Altizer et al., 2003; Pinsky & Palumbi, 2014). Small populations of narrowly distributed species often have low genetic variation within populations but high genetic differentiation among populations due to genetic drift and restricted gene flow (Gibson et al., 2008; Hamrick & Godt, 1996; Young et al., 1996). Moreover, adverse anthropogenic influences can accelerate loss of genetic diversity within populations and differentiation among

Received: 01 December 2018; Accepted: 16 April 2019; Online: 16 May 2019

Foundation items: This work was supported by the Special Program for Basic Science and Technology Research (2014FY120200), Research Project of China Three Gorges Corporation (0799570), Research Project of Hubei Key Laboratory of Three Gorges Project for Conservation of Fishes (SXSX/4381), and Sino BON-Inland Water Fish Diversity Observation Network

*Corresponding author, E-mail: gaoxin@ihb.ac.cn

DOI: 10.24272/j.issn.2095-8137.2019.027

populations (Frankham, 2002). Genetic impoverishment can accelerate the process of local extinction of small populations (Hedrick & Kalinowski, 2000). An understanding of the genetic variability and structure of small populations and their genetic responses to anthropogenic effects is of critical importance for conservation management (Keyghobadi, 2007; Zhang et al., 2007) and for formulating the appropriate scales and subunits (Moritz, 1999) for sustainable long-term conservation.

The Yangtze River is the largest river in China and the third longest river in the world, with a total length of 6 300 km and a drainage area of 1 800 000 km². The Yangtze River supports 378 fish species, of which 162 are endemic (Yu et al., 2005), representing the highest fish diversity in the Palearctic region (Matthews, 1998). The upper Yangtze River refers to the reach above Yichang City and reportedly contains 124 endemic fish species (Cao, 2011). Therefore, the upper Yangtze River is a crucial area for the conservation of fish diversity and genetic resources. However, due to dam construction, overfishing, and water pollution, fish diversity in this region has decreased sharply and many species have become endangered (Fu et al., 2003; Park et al., 2003; Zhong & Power, 1996).

Ancherythroculter nigrocauda, belonging to Cyprinidae in Cypriniformes, is an important commercial and aquaculture species in China and an endemic fish from the upper Yangtze River, where it predominantly inhabits the main river and its tributaries (Ding, 1994). This species is sedentary and lays adhesive eggs from April to August during the rainy season (Cao et al., 2007; Liu et al., 2013). The minimum age of sexual maturity of *A. nigrocauda* is one year, and the body length at 50% sexual maturity estimated to be 106 and 125 mm for males and females, respectively (Liu et al., 2013). Its absolute fecundity varies from 11 300 to 504 630 eggs, with a mean of 162 377 eggs (Liu et al., 2013). In recent years, however, the natural populations and distribution areas of *A. nigrocauda* have declined significantly (Liu, 2013). While previous studies have reported on the age and growth (Xue & He, 2001), reproductive biology (Liu et al., 2013), and artificial propagation (Tan et al., 2004; Yin & Lv, 2010) of *A. nigrocauda*, very little is known about the genetic diversity and structure of populations in the upper Yangtze River. Liu et al. (2005) conducted a study on the genetic diversity and population structure of *A. nigrocauda* with samples collected from 2001 to 2002 in the upper Yangtze River, and found high genetic diversity and no genetic differentiations among different geographical populations. However, that study had a limited sample size (43 samples from three localities) and only recovered a 546 bp fragment of the cytochrome *b* (cyt *b*) gene. Moreover, due to a sharp decline in the natural populations of *A. nigrocauda* over the past few decades and substantial environmental changes in the upper Yangtze River after the impoundment of the Three Gorges Dam (TGD), it is likely that both the genetic diversity and population structure of *A. nigrocauda* in the upper Yangtze River have been impacted.

In the current study, samples of *A. nigrocauda* were collected from five sites in the upper Yangtze River. We

analyzed the genetic diversity and population structure of fish samples from the five different sites based on the cyt *b* gene and simple sequence repeat (SSR) markers and compared the results with those of Liu et al. (2005). The cyt *b* gene was used in the current study for better comparison with Liu et al. (2005). The cyt *b* gene is part of the mitochondrial genome, whereas SSR loci are distributed on genomes and have advantages of high polymorphism and codominance, therefore, the combination of cyt *b* gene and SSR markers is a powerful tool in studies on population genetics. This study aimed to determine the genetic diversity and population structure, as well as temporal changes, of *A. nigrocauda* in the upper Yangtze River, and provide important information for the conservation of this species.

MATERIALS AND METHODS

Samples collection and DNA extraction

From 2016 to 2017, a total of 239 *A. nigrocauda* samples were collected from five localities (Longxi River (LXR), Chishui River (CSR), Mudong River (MDR), Modao Stream (MDS), and Daning River (DNR)) in the upper Yangtze River (Figure 1, Table 1). Dorsal muscle used for DNA extraction was clipped from each of the fish, and then preserved in 95% alcohol in 5 mL cryogenic vials and stored at -20 °C. Total DNA was extracted from alcohol preserved muscle tissue using proteinase K digestion at 55 °C for 3–5 h, followed by phenol/chloroform extraction (Kocher et al., 1989).

Table 1 Sampling sites, sample site codes, GPS locations, and samples sizes of *A. nigrocauda* in the upper Yangtze River, China

Sample site	Code	GPS location (N E)	Sample size (n)
Longxi River	LXR	28°54'46" 105°30'51"	64
Chishui River	CSR	28°48'03" 105°50'22"	38
Mudong River	MDR	29°33'56" 106°50'16"	36
Modao Stream	MDS	30°49'04" 108°51'46"	39
Danang River	DNR	31°16'37" 109°49'00"	62

mtDNA amplification and sequencing

All 239 samples were used for mtDNA amplification. The mtDNA cyt *b* gene was amplified using polymerase chain reaction (PCR) in 30 µL reactions containing 3 µL of reaction buffer (200 mmol/L Tris-HCL pH 8.4, 500 mmol/L KCL, 50 mmol/L MgCL), 1.5 µL of dNTPs (1 mmol/L), 1 µL of each primer (10 µmol/L), 0.25 µL (2.5 U) of *Taq* DNA polymerase, 3 µL of template DNA, and 20.25 µL of H₂O. Primer sets were L14724 5'-GACCTGAAAAACCACCGTTG-3' and H15915 5'-CTCCGATCT CCGGATTACAAGAC-3' (Xiao et al., 2001). The PCR profile was initial denaturation at 94 °C for 4 min; followed by 35 cycles at 94 °C for 45 s, 54 °C for 45 s, and 72 °C for 1 min; then one cycle at 72 °C for 10 min. The PCR products were purified and sequenced by Shanghai DNA Biotechnologies Company.

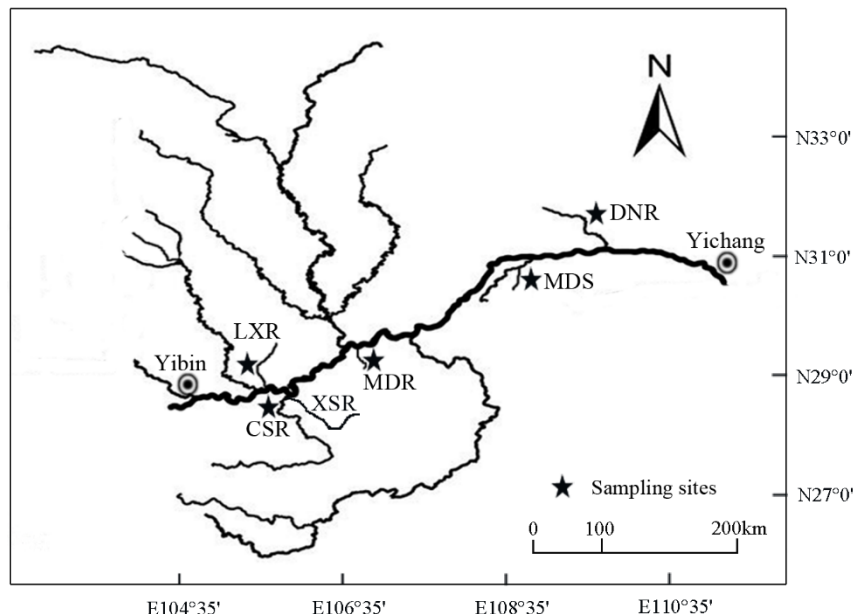


Figure 1 Sampling sites (stars) of *A. nigrocauda* in upper Yangtze River

LXR: Longxi River; CSR: Chishui River; MDR: Mudong River; MDS: Modao Stream; DNR: Daning River.

SSR amplification and electrophoresis

A total of 161 samples from the five localities (sample size of each locality is described in Table 7) and 14 polymorphic SSR loci were used in this study. Primers for the 14 microsatellite loci were developed using fast isolation with the amplified fragment length polymorphism (AFLP) of sequences containing repeats (FIASCO) protocol. The specific sequence, optimum annealing temperature, and GenBank accession No. for each microsatellite primer are listed in Supplementary Table S1. Amplification of DNA was performed in a 10 μ L reaction mixture. The PCR profile was initial denaturation at 94 °C for 3 min; followed by 28 cycles at 94 °C for 30 s, annealing temperature for 40 s, and 72 °C for 1 min; then one cycle at 72 °C for 10 min. The PCR products were electrophoresed in 8% non-denaturing polyacrylamide gels on a Sequi-Gen GT system (Bio-Rad, USA). The gels were then stained using Ultra GelRed before being photographed. Lastly, the allele sizes were obtained manually by referring to the pBR322 DNA/Msp I marker (Tiangen Biotechnologies, China).

mtDNA sequence analysis

MEGA7 was used to align and edit the nucleotide sequences (Kumar et al., 2016). The haplotype frequency, haplotype diversity, and nucleotide diversity were calculated with DnaSP v5.10 (Librado & Rozas, 2009). Arlequin v3.0 (Excoffier et al., 2005) was used to perform analysis of molecular variance (AMOVA) and compute pairwise F_{ST} values (Excoffier et al., 1992). A neighbor-joining (NJ) phylogenetic tree was constructed using MEGA7 (Kumar et al., 2016). The median joining algorithm from Network 4.6 was used to construct a haplotype network (Bandelt et al., 1999). Tajima's D and Fu's F_s tests were implemented in Arlequin v3.0 (Excoffier et al.,

2005) to test for departure from neutrality due to population expansion or selection. Mismatch distribution analysis was used to further detect demographic expansion using DnaSP v5.10 (Librado & Rozas, 2009).

In addition, we compared our results with that of Liu et al. (2005) to determine the temporal changes in genetic diversity and population structure of *A. nigrocauda* from 2001 to 2016. Sequences from this study were downloaded from GenBank (accession Nos. AY493869–AY493886) and reanalyzed using the above methods. Because the obtained length of the *cyt b* gene was only 546 bp in Liu et al. (2005), we also aligned and edited our sequences to 546 bp to ensure accurate comparison and analysis. Our specific sample sites in the Longxi and Mudong rivers were the same as those of Liu et al. (2005), and our sample site in Chishui River was next to the sample site of Liu et al. (2005) in Xishui River, a tributary of Chishui River. Thus, we compared the present genetic diversity and population structure of *A. nigrocauda* from these three localities with the results of Liu et al. (2005).

SSR data analysis

Micro-checker v2.2.1 (Van Oosterhout et al., 2004) was used to check possible large allele dropout, scoring errors due to stuttering, and null alleles. Deviations from the Hardy-Weinberg equilibrium (HWE) and linkage disequilibrium (LD) across all pairs of loci were assessed in GENEPOP v4.7.0 (Rousset, 2008) using the exact test with Markov chain algorithm (Guo & Thompson, 1992; P -values were estimated from 10 000 dememorizations, 100 batches, and 5 000 iterations per batch). Significance levels for multiple comparisons were adjusted using the sequential Bonferroni correction (Rice, 1989).

The number of alleles (A), observed (H_o) and expected (H_e) heterozygosity, and polymorphic information content (PIC) per locus were calculated using Cervus v3.0 (Kalinowski et al., 2007). Standardized allelic richness (A_r) was calculated using Fstat v2.9.3.2 (Goudet, 2001). Arlequin v3.0 (Excoffier et al., 2005) was used to perform analysis of molecular variance (AMOVA) and compute pairwise F_{ST} values (Excoffier et al., 1992).

The heterozygote excess test was performed to detect recent bottleneck effects using Bottleneck v1.2.02 with the Wilcoxon test under the Two-Phased Mutation Model (TPM) (Cornuet & Luikart, 1996). Piry et al. (1999) suggested that the TPM of mutation for microsatellite loci was appropriate with 95% single-step changes and a variance of 12.

Bayesian assignment analysis was applied to infer the number of genetically differentiated clusters (K) using STRUCTURE v2.3.4 (Pritchard et al., 2000). We performed 10 replications for each K starting from one to nine (400 000 iterations with 100 000 burn-in periods) under an admixture model and correlated allele frequencies within populations (Falush et al., 2003). The optimal K value was determined by comparing the mean log probability $\text{LnP}(K)$ and calculating the ΔK value for each K (Evanno et al., 2005) using Structure Harvester (Earl & vonHoldt, 2012; available at <http://taylor0.biology.ucla.edu/structureHarvester/>). Outputs from Structure Harvester were further analyzed using CLUMPP v1.1.2 (Jakobsson & Rosenberg, 2007), which estimates membership coefficients across replicate analyses. Outputs from CLUMPP were then used directly as inputs in DISTRUCT v1.1 (Rosenberg, 2003), which assists in the visual presentation of these estimated membership coefficients. According to previous studies, individuals were able to assign to one of the inferred clusters when the corresponding membership proportion was ≥ 0.80 (Mukesh et al., 2013; Oliveira et al., 2008).

RESULTS

Cyt *b* gene marker

Genetic diversity and demographic history

Following alignment, a 1 140 bp cyt *b* gene sequence was obtained for 239 individuals. No deletions or insertions were observed. The average base composition was A=29.19%, T=27.59%, G=14.45%, and C=28.76%. Within the 1 140 bp region, 13 sites were variable, including nine parsimony informative sites and four singleton variable sites. We identified 15 haplotypes (GenBank accession Nos.: MH665369–MH665383) from the 239 individuals, and the numbers of haplotypes ranged from four to nine for each sampled population. For the five populations, haplotype diversity ranged from 0.488 to 0.794, with a mean value of 0.786. Nucleotide diversity ranged from 0.084% to 0.163%, with a mean value of 0.141% (Table 2).

Some Tajima's D and Fu's F_s test values were negative in the five populations, though none were statistically significant, which suggests no expansion for the *A. nigrocauda*

populations (Table 2). Furthermore, all mismatch distributions for each population and the whole population exhibited a multimodal distribution (Figure 2), further indicating no population expansion.

Population structure

The AMOVA based on haplotype frequencies revealed that 76.19% of the genetic variation occurred within populations, whereas 23.81% occurred among populations, thus suggesting significant genetic variation among the populations (Table 3). Pairwise F_{ST} values between the populations are listed in Table 4. Results showed significant genetic differentiation between each population pair, except for that between the MDS and DNR populations.

The NJ phylogenetic tree indicated there were four clades of the 15 haplotypes (Figure 3), which was confirmed with the haplotype network (Figure 4). Each of the four clades was shared by three to five populations; thus, no obvious genealogical geographic pattern was formed. In regard to haplotype distribution, Hap 1, Hap 2, and Hap 3 were the main haplotypes, shared by more than three populations; however, eight of the 15 haplotypes were found in one population only.

Temporal changes

A total of 43 sequences from Liu et al. (2005) were obtained for the LXR, CSR, and MDR populations. The haplotype diversities of the three analysed populations were 0.812, 1.000, and 0.833 in Liu et al. (2005), but 0.469, 0.656, and 0.707 in the present study, respectively. The nucleotide diversities of the three analysed populations were 0.436%, 0.488%, and 0.400% in Liu et al. (2005), but 0.090%, 0.204%, and 0.177% in the present study, respectively. These results indicated that the genetic diversity of *A. nigrocauda* has declined sharply in the three sampling sites from 2001 to 2016 (Table 5). The pairwise F_{ST} values among the three populations were -0.018 62, 0.013 38, and -0.044 13 (all non-significant, $P > 0.05$) in Liu et al. (2005) and 0.095 23, 0.185 18, and 0.092 84 (all significant $P < 0.05$) in the present study. These results demonstrated significant genetic differentiation in 2016 but not in 2001 (Table 6).

SSR marker

Genetic diversity and bottleneck effects

No large allele dropout or scoring errors due to stuttering were detected by Micro-Checker; however, An63 and An114 in LXR, An72 in CSR, An65 in MDS, and An63 and An65 in DNR all showed the presence of null alleles. Eleven out of 70 tests differed significantly from the HWE after Bonferroni correction, whereas no significant deviation from the HWE was detected in any locus across all populations (Supplementary Table S2). No linkage disequilibrium was found among SSR locus pairs, except for An63 and An114 in the CSR population and An63 and An76 in the DNR population.

For the five populations, the average number of alleles per population ranged from 4.929 to 10.286 and the average allelic richness per population ranged from 4.817 to 9.876.

Table 2 Haplotype frequency distribution, haplotype diversity, nucleotide diversity, and neutrality tests for five *A. nigrocauda* populations based on mitochondrial cyt *b* analysis

Sample site	LXR (64)	CSR (38)	MDR (36)	MDS (39)	DNR (62)	Total (239)	GenBank accession Nos.
Haplotype frequency							
Hap1	0.296 9	0.052 6	0.222 2	0.512 8	0.548 4	0.347 3	MH665369
Hap2			0.027 8	0.384 6	0.290 3	0.142 3	MH665370
Hap3	0.656 3	0.342 1	0.111 1		0.032 3	0.255 2	MH665371
Hap4					0.016 1	0.004 2	MH665372
Hap5	0.015 6	0.026 3	0.083 3		0.096 8	0.046 0	MH665373
Hap6					0.016 1	0.004 2	MH665374
Hap7		0.078 9	0.388 9	0.025 6		0.075 3	MH665375
Hap8		0.184 2				0.029 3	MH665376
Hap9		0.263 2	0.027 8			0.046 0	MH665377
Hap10		0.026 3				0.004 2	MH665378
Hap11	0.015 6	0.026 3	0.055 6			0.016 7	MH665379
Hap12	0.015 6					0.004 2	MH665380
Hap13				0.076 9		0.012 6	MH665381
Hap14			0.055 6			0.008 4	MH665382
Hap15			0.027 8			0.004 2	MH665383
Haplotype diversity	0.488±0.050	0.789±0.038	0.794±0.049	0.598±0.046	0.614±0.048	0.786±0.016	
Nucleotide diversity	0.000 84±0.000 09	0.001 63±0.000 13	0.001 55±0.000 11	0.001 09±0.000 11	0.000 92±0.000 07	0.001 41±0.000 04	
Tajima's <i>D</i>	0.283 64	0.326 94	-0.238 51	0.139 25	-0.039 54	0.094 36	
<i>P</i> -value	0.650	0.679	0.426	0.612	0.518	0.577	
Fu's <i>F_s</i>	-0.014 25	-1.109 99	-2.255 98	1.259 59	-0.677 17	-0.559 56	
<i>P</i> -value	0.496	0.323	0.132	0.759	0.386	0.419	

Data are based on 239 samples of *A. nigrocauda* from upper Yangtze River, China. Numbers in brackets indicate number of individuals from each sample site.

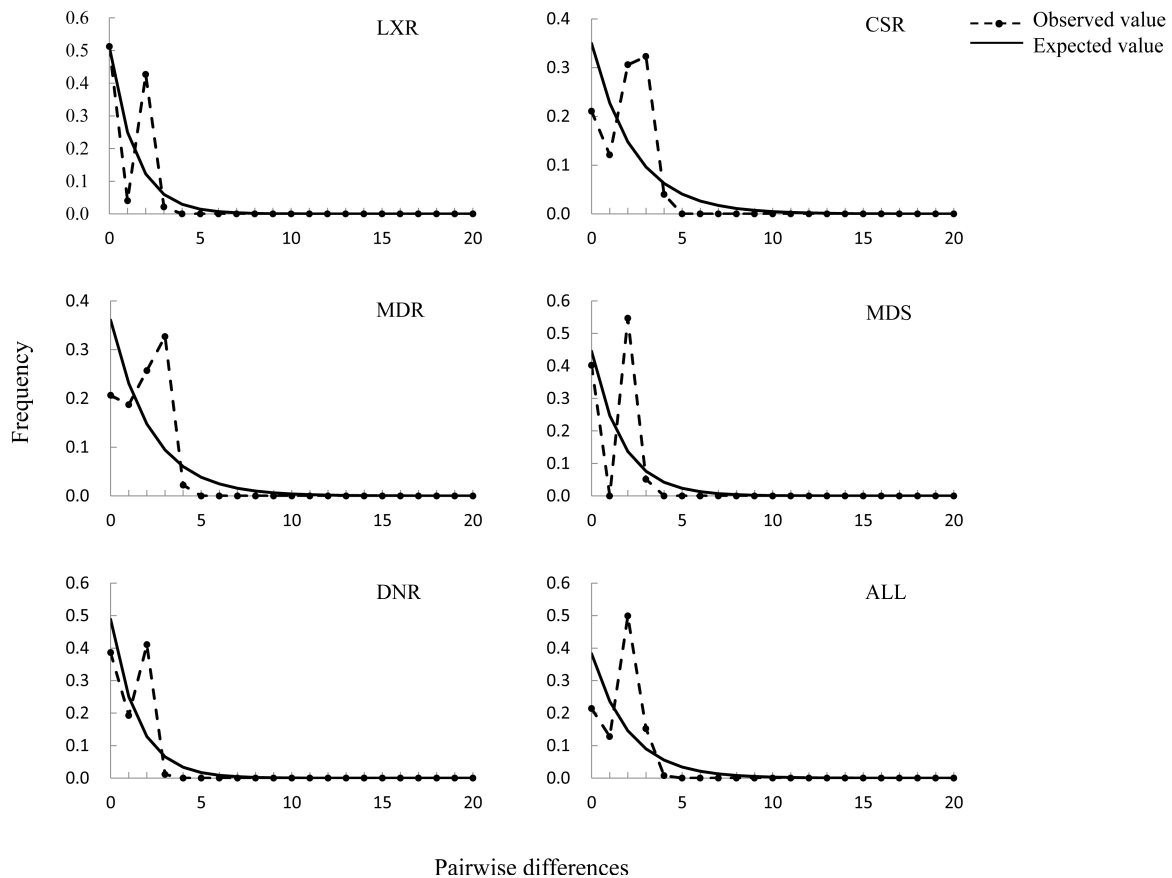


Figure 2 Mismatch distributions for each analyzed population and all 239 samples of *A. nigrocauda* sampled from upper Yangtze River

Table 3 Analysis of molecular variance (AMOVA) for five *A. nigrocauda* populations based on mtDNA and SSR analyses

Source of variation	df	Sum of squares	Variance component	Percentage variation	F_{ST}	P
mtDNA						
Among populations	4	40.543	0.201 96	23.81	0.238 14	0
Within populations	234	151.189	0.646 11	76.19		
Total	238	191.732	0.848 07			
SSR						
Among populations	4	309.614	1.127 46	18.98	0.189 83	0
Within populations	317	1 525.355	4.811 84	81.02		
Total	321	1 834.969	5.939 31			

Data are based on 239 and 161 samples of *A. nigrocauda* from upper Yangtze River, China, respectively.

The average observed heterozygosity per population ranged from 0.595 to 0.746, whereas the average expected heterozygosity per population ranged from 0.649 to 0.816. No significant heterozygote excess ($P > 0.05$) was detected for the five populations under the TPM, indicating no recent bottleneck effects (Table 7).

Population structure

Similarly, for SSR analysis, AMOVA revealed significant genetic differentiation among the five populations ($F_{ST} =$

0.18983, $P < 0.05$) (Table 3). The pairwise F_{ST} values varied from 0.088 86 to 0.246 93, which were all statistically significant ($P < 0.05$) after Bonferroni correction, suggesting significant genetic differentiation between each population pair (Table 4). When conducting STRUCTURE analysis, $\text{LnP}(K)$ showed no clear peak, but ΔK reached a maximum value when $K=4$, inferring there were four genetic clusters in the *A. nigrocauda* samples (Figure 5). The membership proportions of the four inferred genetic clusters in the five populations are listed in Table 8, which showed little gene flow among the five

Table 4 Pairwise F_{ST} values based on *cyt b* analysis of 239 samples (below diagonal) and SSR analysis of 161 samples (above diagonal) of *A. nigrocauda* from five different sites in upper Yangtze river, China

Population	LXR	CSR	MDR	MDS	DNR
LXR		0.226 56*	0.228 63*	0.246 93*	0.211 17*
CSR	0.152 51*		0.088 86*	0.187 23*	0.173 27*
MDR	0.113 45*	0.102 40*		0.163 89*	0.203 83*
MDS	0.348 66*	0.296 86*	0.260 19*		0.149 23*
DNR	0.342 81*	0.320 61*	0.282 98*	– 0.00 426	

*: $P < 0.05$ after Bonferroni correction.

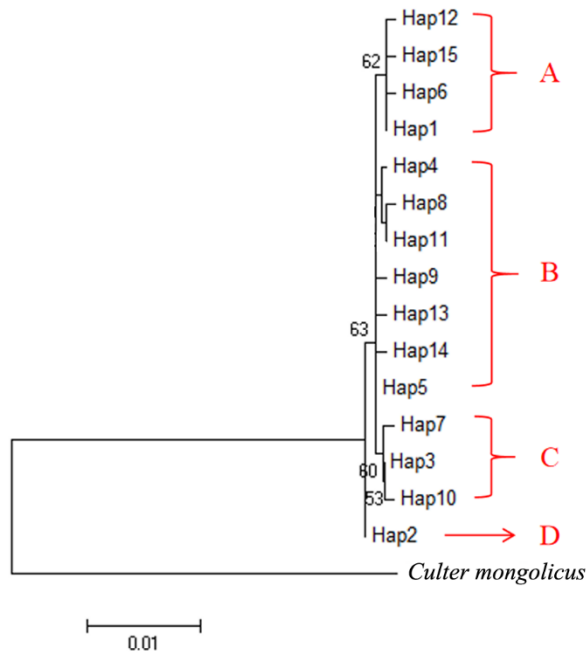


Figure 3 Neighbor-joining phylogenetic tree of 15 haplotypes of *A. nigrocauda* samples from five different sites in upper Yangtze River, China, inferred from *cyt b* sequences
A to D represent four clades.

populations, except for between CSR and MDR. The membership proportions of the four inferred clusters in each sample are listed in Supplementary Table S3. After removing the individuals that could not be assigned to one of the four clusters, the remaining samples from each population formed a single cluster, except for the CSR and MDR populations, which formed a common cluster. AMOVA revealed significant genetic differences among the four clusters ($F_{ST}=0.16596$, $P < 0.05$) (Table 9).

DISCUSSION

Genetic diversity

The present study indicated that *A. nigrocauda* had lower genetic diversity compared to other endemic fishes in the

upper Yangtze River. For instance, Li et al. (2018) reported haplotype and nucleotide diversities for the *Hemiculterella sauveigi* from the Chishui River of 0.895 and 0.487%, respectively. Zhang & Tan (2010) reported average observed and expected heterozygosities for the largemouth bronze gudgeon (*Coreius guichenoti* Sauvage et Dabry) from the upper Yangtze River of 0.838 and 0.841, respectively. The genetic diversity of *A. nigrocauda* from Longxi River was the lowest among the five sample sites, which could be attributed to population fragmentation due to the eight constructed dams along that river (Wang, 1994). Dams can decrease genetic diversity and increase genetic drift by reducing effective population size and limiting gene flow among populations (Jager et al., 2001). Hänfling & Weetman (2006) found that the genetic diversity of isolated upstream river sculpin (*Cottus gobio*) population was lower than that of downstream population, and Zhao et al. (2016) found the same result in fragmented *Sinibrama macrops* populations in Min River, China.

Comparison between our results and those of Liu et al. (2005) indicated that the genetic diversity of *A. nigrocauda* has declined sharply in the upper Yangtze River from 2001 to 2016. This loss of genetic diversity could be attributed to adverse anthropogenic factors, such as damming, overfishing, and water pollution. *Ancherythroculter nigrocauda* is a cyprinid fish endemic to the upper Yangtze River, and has developed a high degree of adaptability to the lotic environment of this region during its long evolution. However, the Three Gorges Project and Jinsha River Project in the upper Yangtze River have fragmented the river and transformed the free-flowing water into a lacustrine environment (Neraas & Spruell, 2001; Nilsson et al., 2005), which has reduced the natural habitats of *A. nigrocauda*. Thus, the populations of *A. nigrocauda* have decreased accordingly (Park et al., 2003). Moreover, overfishing, which is common in the Yangtze River (Gao, 2008; Liu, 2013; Wang et al., 2015; Xiong et al., 2016; Zhu & Chang, 2008), has probably reduced population size and genetic diversity of *A. nigrocauda* through fishing mortality. Similarly, water pollution (He et al., 2011; Liu et al., 2009; Xu, 2010; Yi et al., 2016) in the upper Yangtze River has also probably reduced population size by imperiling the feeding and reproductive biology of the fish.

Population structure

Both *cyt b* and SSR markers showed significant genetic differentiations among the populations in the present study. Based on the pairwise F_{ST} values, no significant genetic differentiation was observed between the MDS and DNR populations in the *cyt b* analysis. However, this differed from the SSR analysis results, suggesting that the SSR marker may be more sensitive than the *cyt b* marker in studying genetic variation, especially among closely related populations or populations sampled over a reduced geographical scale (Estoup et al., 1998; Harrison & Hastings, 1996).

According to our reanalysis, however, no genetic differentiation was found among the populations by *cyt b* analysis in Liu et al. (2005), which might be due to the small

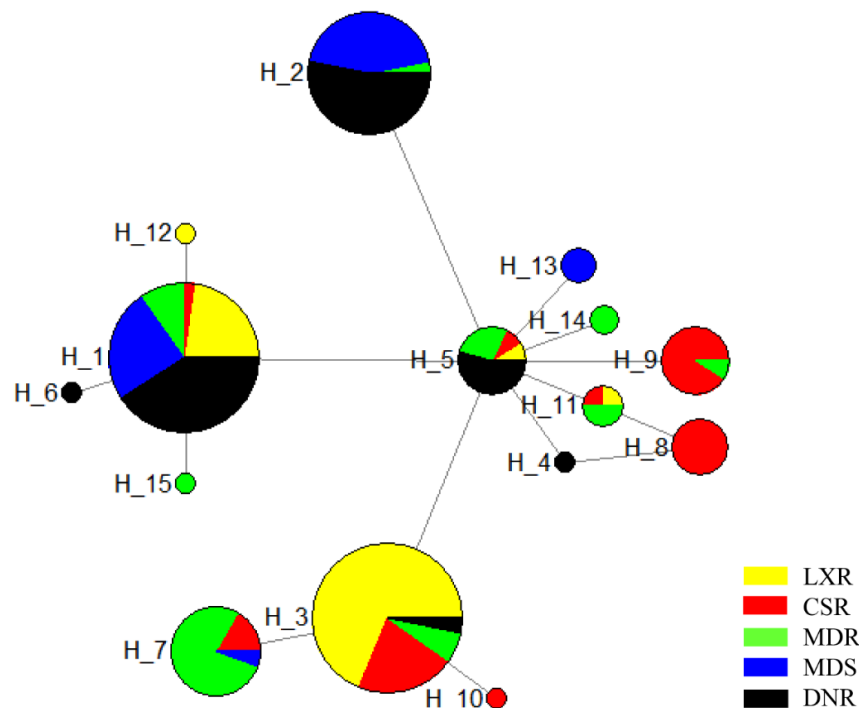


Figure 4 Median-joining network of 15 haplotypes of *A. nigrocauda* samples from five different sites in upper Yangtze River, China, inferred from *cyt b* gene sequences

Each circle represents a haplotype, and its size is proportional to its total frequency.

sample size. Studies have shown that modification of ecological environments by human activities can affect fish population genetic structure (Meldgaard et al., 2003; Zhang et al., 2011). *Ancherythroculter nigrocauda* is a sedentary fish with a relatively small scope of activity and adhesive egg reproduction (Cao et al., 2007); thus, gene flow between different populations mainly depends on the dispersal of larvae. Before the TGD impounding of water to 135 m in 2003, the upper Yangtze River was a free-flowing water environment, which allowed the *A. nigrocauda* larvae to disperse over longer distances, leading to gene flow between different populations. This likely explains the lack of genetic differentiation among the studied populations in Liu et al. (2005). After 2003, however, the TGD changed the hydrological regime in the upper Yangtze River from lotic to lentic. This reduced the dispersal range of *A. nigrocauda* larvae and decreased gene flow between the different populations, resulting in genetic differentiation due to isolation of the fish populations (Young et al., 2018). Similarly, damming and isolation of populations reduced the population sizes, leading to genetic differentiation via increased genetic drift (Jager et al., 2001). Low level gene flow among populations resulting from restricted dispersal of larvae has been well documented in many studies (Dong et al., 2012; Han et al., 2015; Yang & Li, 2018).

Demographic history

A unimodal pattern of mismatch distribution is indicative of

populations that have experienced recent expansions, whereas multimodal distributions are indicative of populations at demographic equilibrium (Rogers & Harpending, 1992; Slatkin & Hudson, 1991). Moreover, negative and statistically significant values of Tajima's D or Fu's F_s tests are suggestive of populations that have experienced expansion (Fu, 1997; Tajima, 1989). Therefore, in the present study, the neutrality test and mismatch distribution results suggested no expansion of the *A. nigrocauda* populations. Generally, bottleneck effects are always followed by population expansion. Here, thus, it was reasonable that no bottleneck effects were detected for any of the five populations.

Implications for conservation

Genetic diversity is influenced by many factors, including historical and anthropogenic factors. In the present study, no bottlenecks or population expansions were detected; thus, anthropogenic activity was likely responsible for the loss of genetic diversity of *A. nigrocauda*. Therefore, it is necessary to decrease the negative impacts of anthropogenic activity on the *A. nigrocauda* populations. As the dams in the Longxi River are producing little electric power or are deserted, it is suggested that these dams should be removed preferentially to restore river connectivity. In addition, further studies are needed to investigate and minimize the adverse impacts of the TGD on fish populations. A 10-year fishing ban in the Chishui River has been in place since January 2017 to help in the recovery of fish stocks. In the same vein, we suggest that

Table 5 Haplotype frequency distribution, haplotype diversity, and nucleotide diversity of three *A. nigrocauda* populations in 2001 and 2016 based on 546 bp *cyt b* sequence

Haplotype	LXR (2001)	LXR (2016)	MDR (2001)	MDR (2016)	CSR (2001)	CSR (2016)
Hap1			1	14		3
Hap2					1	7
Hap3	10	42	1	4	5	14
Hap4	1	21	1	16		14
Hap5		1				
Hap6				1		
Hap7				1		
Hap8	1					
Hap9	1					
Hap10	1					
Hap11	1					
Hap12	2		1		1	
Hap13	4				2	
Hap14	1					
Hap15	1					
Hap16	1					
Hap17			1			
Hap18			1			
Hap19			1		1	
Hap20					1	
Hap21					1	
Haplotype diversity	0.812	0.469	1	0.656	0.833	0.707
Nucleotide diversity	0.004 36	0.000 90	0.004 88	0.002 04	0.004 00	0.001 77

Data are based on a total of 43 and 138 samples of *A. nigrocauda* sampled from upper Yangtze River, China, in 2001 and 2016, respectively.

Table 6 Pairwise F_{ST} values between *A. nigrocauda* populations in 2016 (below diagonal) and 2001 (above diagonal) based on 546 bp *cyt b* sequences of 138 and 43 samples, respectively, from three different sites in upper Yangtze River, China

Population	LXR	CSR	MDR
LXR		– 0.018 62	0.013 38
CSR	0.095 23*		– 0.044 13
MDR	0.185 18*	0.092 84*	

*: $P < 0.05$ after Bonferroni correction.

fishing in the main stream of the Yangtze River and its tributaries should be eliminated. Moreover, as water pollution is another significant issue, the government should prevent factories from discharging wastewater into the Yangtze River and undertake centralized management of domestic wastewater.

Artificial breeding and stocking are feasible methods to increase fish abundance, although the sources and numbers of parental fish are important (Dudgeon, 2011; Fu et al., 2003). In the present study, there were significant genetic

Table 7 Parameters of genetic variation and P -values for heterozygote excess test of five *A. nigrocauda* populations, inferred from 14 pairs of SSR markers

Population	A	A_r	H_o	H_e	P
LXR(32)	4.929	4.817	0.595	0.649	0.428
CSR(31)	7.429	7.321	0.652	0.727	0.879
MDR(32)	7.000	6.817	0.594	0.665	0.998
MDS(32)	8.571	8.312	0.694	0.765	0.914
DNR(34)	10.286	9.876	0.746	0.816	0.923

Data are based on 161 samples of *A. nigrocauda* from upper Yangtze River, China. A : Observed allele; A_r : Allelic richness; H_o : Observed heterozygosity; H_e : Expected heterozygosity. Numbers in brackets indicate number of individuals from each sample site.

differentiations among the populations, and STRUCTURE analysis showed that there were four distinct genetic clusters. Therefore, it would be necessary to use a wide variety of parental fish in the artificial breeding of *A. nigrocauda* to increase the quality of seed stock from hatcheries, which

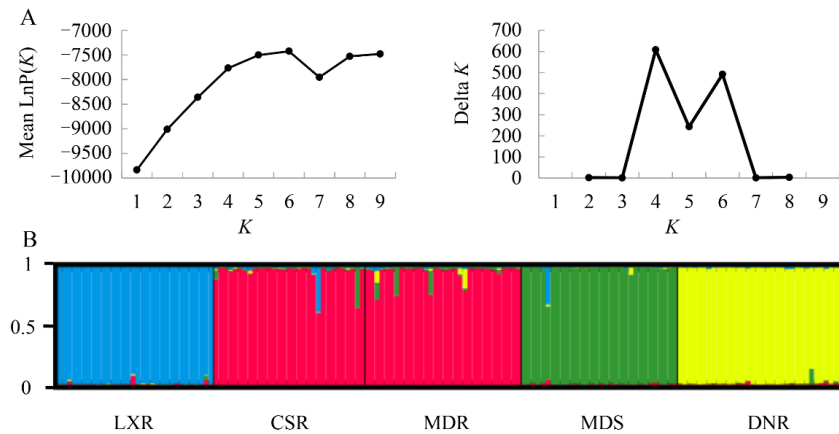


Figure 5 STRUCTURE analysis based on genotypes at 14 microsatellite loci from 161 unique *A. nigrocauda* individuals sampled from five different sites in upper Yangtze River, China

A: Estimations of mean log probability $\text{LnP}(K)$ and ΔK values for $K=1-9$ using Structure Harvester. $K=4$ is shown as the optimal value; B: Proportions of each individual assigned to each inferred cluster. Four colors indicate four inferred distinct genetic clusters. Sampling sites of individuals are shown at the bottom.

Table 8 Membership proportions of four inferred genetic clusters in five populations based on STRUCTURE analysis of SSR data

Population	Cluster 1	Cluster 2	Cluster 3	Cluster 4	Total sample size (<i>n</i>)
LXR	0.008	0.003	0.003	0.986	32
CSR	0.957	0.017	0.006	0.021	31
MDR	0.954	0.026	0.014	0.006	32
MDS	0.008	0.973	0.006	0.014	32
DNR	0.006	0.008	0.981	0.004	34

Table 9 Analysis of molecular variance (AMOVA) for four inferred genetic clusters based on STRUCTURE analysis of SSR data

Source of variation	<i>df</i>	Sum of squares	Variance component	Percentage variation	F_{ST}	<i>P</i>
Among clusters	3	243.265	1.008 81	16.60	0.165 96	0
Within clusters	306	1 551.342	5.069 74	83.40		
Total	309	1 794.606	6.078 55			

would ensure better survivability during river reintroduction. Moreover, the *A. nigrocauda* populations in the upper Yangtze River need to be managed as multiple genetic units.

SUPPLEMENTARY DATA

Supplementary data to this article can be found online.

COMPETING INTERESTS

The authors declare that they have no competing interests

AUTHORS' CONTRIBUTIONS

H.Z.L., W.X.C., and X.G. designed the study and revised the manuscript. D. D. Z. performed the laboratory work and wrote the manuscript. W. J. L. helped in data analysis. All authors read and approved the final version of the manuscript.

ACKNOWLEDGEMENTS

We are grateful to Zhi Zhang, Ming-Zheng Li, Zhong-Hua Duan, Ning Qiu, and many fisher folk for their help in *A. nigrocauda* sampling. We also thank Zheng Gong, Lin Chen, and other colleagues for their help in the use of software.

REFERENCES

- Altizer S, Harvell D, Friedle E. 2003. Rapid evolutionary dynamics and disease threats to biodiversity. *Trends in Ecology and Evolution*, **18**(11): 589–596.
- Bandelt HJ, Forster P, Röhl A. 1999. Median-joining networks for inferring intraspecific phylogenies. *Molecular Biology and Evolution*, **16**(1): 37–48.
- Cao W. 2011. The current situation and conservation measure of fish resource in the Yangtze River. *Jiangxi Fishery Sciences and Technology*, (2): 1–4. (in Chinese)
- Cao W, Chang J, Qiao Y, Duan Z. 2007. Fish Resources of Early Life

- History Stages in Yangtze River. Beijing, China: China Water Power Press. (in Chinese)
- Cornuet JM, Luikart G. 1996. Description and power analysis of two tests for detecting recent population bottlenecks from allele frequency data. *Genetics*, **144**(4): 2001–2014.
- Ding R. 1994. The Fishes of Sichuan, China. Chengdu, Sichuan, China: Sichuan Publishing House of Science and Technology. (in Chinese)
- Dong YW, Wang HS, Han GD, Ke CH, Zhan X, Nakano T, Williams GA. 2012. The impact of Yangtze River discharge, ocean currents and historical events on the biogeographic pattern of *Cellana toreuma* along the China Coast. *PLoS One*, **7**(4): e36178.
- Dudgeon D. 2011. Asian river fishes in the Anthropocene: threats and conservation challenges in an era of rapid environmental change. *Journal of Fish Biology*, **79**(6): 1487–1524.
- Earl DA, Vonholdt BM. 2012. STRUCTURE HARVESTER: a website and program for visualizing STRUCTURE output and implementing the Evanno method. *Conservation Genetics Resources*, **4**(2): 359–361.
- Estoup A, Rousset F, Michalakis Y, Cornuet J, Adriamanga M, Guyomard R. 1998. Comparative analysis of microsatellite and allozyme markers: a case study investigating microgeographic differentiation in brown trout (*Salmo trutta*). *Molecular Ecology*, **7**(3): 339–353.
- Evanno G, Regnaut S, Goudet J. 2005. Detecting the number of clusters of individuals using the software STRUCTURE: a simulation study. *Molecular Ecology*, **14**(8): 2611–2620.
- Excoffier L, Laval G, Schneider S. 2005. Arlequin (version 3.0) an integrated software package for population genetics data analysis. *Evolutionary Bioinformatics*, **1**(4A): 47–50.
- Excoffier L, Smouse PE, Quattro JM. 1992. Analysis of molecular variance inferred from metric distances among DNA haplotypes: application to human mitochondrial DNA restriction data. *Genetics*, **131**(2): 479–491.
- Falush D, Stephens M, Pritchard JK. 2003. Inference of population structure using multilocus genotype data: linked loci and correlated allele frequencies. *Genetics*, **164**(4): 1567–1587.
- Frankham R, Ballou JD, Briscoe DA. 2002. Introduction to Conservation Genetics. Cambridge: Cambridge University Press.
- Fu C, Wu J, Chen J, Wu Q, Lei G. 2003. Freshwater fish biodiversity in the Yangtze River basin of China: patterns, threats and conservation. *Biodiversity and Conservation*, **12**(8): 1649–1685.
- Fu YX. 1997. Statistical tests of neutrality of mutations against population growth, hitchhiking and background selection. *Genetics*, **147**(2): 915–925.
- Gao X. 2008. Conservation Biology of Rare and Endemic Fishes of the Yangtze River. Ph. D. dissertation, Institute of Hydrobiology, Chinese Academy of Sciences, Wuhan, 155. (in Chinese)
- Gibson JP, Rice SA, Stucke CM. 2008. Comparison of population genetic diversity between a rare narrowly distributed species and a common widespread species of *Alnus* (Betulaceae). *American Journal of Botany*, **95**(5): 588–596.
- Goudet J. 2001. FSTAT, a program to estimate and test gene diversities and fixation indices. <http://www.unil.ch/izea/software/fstat.html>.
- Guo SW, Thompson EA. 1992. Performing the exact test of Hardy-Weinberg proportion for multiple alleles. *Biometrics*, **48**(2): 361–372.
- Hamrick JL, Godt MJW. 1996. Conservation genetics of endemic plant species. In: Avise JC, Hamrick JL. Conservation Genetics. New York, USA: Chapman and Hall, 281–304.
- Han ZQ, Zhu WB, Zheng W, Li PF, Shui BN. 2015. Significant genetic differentiation between the Yellow Sea and East China Sea populations of cocktail shrimp *Trachypenaeus curvirostris* revealed by the mitochondrial DNA COI gene. *Biochemical Systematics and Ecology*, **59**: 78–84.
- Hänfling B, Weetman D. 2006. Concordant genetic estimators of migration reveal anthropogenically-enhanced source-sink population structure in the river sculpin, *Cottus gobio*. *Genetics*, **173**(3): 1487–1501.
- Harrison S, Hastings A. 1996. Genetic and evolutionary consequences of metapopulation structure. *Trends in Ecology and Evolution*, **11**(4): 180–183.
- He Q, Peng S, Zhai J, Xiao H. 2011. Development and application of a water pollution emergency response system for the Three Gorges Reservoir in the Yangtze River, China. *Journal of Environmental Sciences*, **23**(4): 595–600.
- Hedrick PW, Kalinowski ST. 2000. Inbreeding depression in conservation biology. *Annual Review of Ecology and Systematics*, **31**: 139–162.
- Jager HI, Chandler JA, Lepla KB, Winkle WV. 2001. A theoretical study of river fragmentation by dams and its effects on white sturgeon populations. *Environmental Biology of Fishes*, **60**(4): 347–361.
- Jakobsson M, Rosenberg NA. 2007. CLUMPP: a cluster matching and permutation program for dealing with label switching and multimodality in analysis of population structure. *Bioinformatics*, **23**(14): 1801–1806.
- Kalinowski ST, Taper ML, Marshall TC. 2007. Revising how the computer program CERVUS accommodates genotyping error increases success in paternity assignment. *Molecular Ecology*, **16**(5): 1099–1106.
- Keyghobadi N. 2007. The genetic implications of habitat fragmentation for animals. *Canadian Journal of Zoology*, **85**(10): 1049–1064.
- Kocher TD, Thomas WK, Meyer A, Edwards SV, Pääbo S, Villablanca FX, Wilson AC. 1989. Dynamics of mitochondrial DNA evolution in animals: amplification and sequencing with conserved primers. *Proceedings of the National Academy of Sciences of the United States of America*, **86**(16): 6196–6200.
- Kumar S, Stecher G, Tamura K. 2016. MEGA7: molecular evolutionary genetics analysis version 7.0 for bigger datasets. *Molecular Biology and Evolution*, **33**(7): 1870–1874.
- Li W, Wang H, Liu H, Cao W, Wang X, Yu J, Zhu X. 2018. Genetic diversity and population demographic history of *Hemiculterella sauagei* in the Chishui River. *Acta Hydrobiologica Sinica*, **42**(1): 106–113. (in Chinese)
- Librado P, Rozas J. 2009. DnaSP v5: a software for comprehensive analysis of DNA polymorphism data. *Bioinformatics*, **25**(11): 1451–1452.
- Liu C. 2013. Studies on the Biology, Population Dynamics and Genetic Diversity of *Ancherythroculter nigrocauda*. Ph.D. dissertation, Institute of Hydrobiology, Chinese Academy of Sciences, Wuhan, 139. (in Chinese)
- Liu C, Gao X, Wang H, Liu H, Cao W, Danley PD. 2013. Reproductive characteristics of *Ancherythroculter nigrocauda*, an endemic fish in the upper Yangtze River, China. *Fisheries Science*, **79**(5): 799–806.
- Liu H, Zhu Y, Wang J, Tan D. 2005. Population genetic structure of an endemic cyprinid fish, *Ancherythroculter nigrocauda*, in the upper reaches of the Yangtze River and its implication for conservation. *Korean Journal of Genetics*, **27**(4): 361–367.
- Liu RM, Yang ZF, Shen ZY, Yu SL, Ding XW, Xing W, Fang L. 2009. Estimating nonpoint source pollution in the upper Yangtze River using the export coefficient model, remote sensing, and geographical information system. *Journal of Hydraulic Engineering*, **135**(9): 698–704.
- Matthews WJ. 1998. Patterns in Freshwater Fish Ecology. New York, USA:

Chapman and Hall.

- Meldgaard T, Nielsen EE, Loeschcke V. 2003. Fragmentation by weirs in a riverine system: A study of genetic variation in time and space among populations of European grayling (*Thymallus thymallus*) in a Danish river system. *Conservation Genetics*, **4**(6): 735–747.
- Moritz C. 1999. Conservation units and translocations: strategies for conserving evolutionary processes. *Heredity*, **130**(3): 217–228.
- Mukesh, Fernandes M, Han J, Sathyakumar S. 2013. Genetics driven interventions for *ex situ* conservation of red junglefowl (*Gallus gallus murghi*) populations in India. *Zoo Biology*, **32**(5): 476–483.
- Neraas LP, Spruell P. 2001. Fragmentation of riverine systems: the genetic effects of dams on bull trout (*Salvelinus confluentus*) in the Clark Fork River system. *Molecular Ecology*, **10**(5): 1153–1164.
- Nilsson C, Reidy CA, Dynesius M, Revenga C. 2005. Fragmentation and flow regulation of the world's large river systems. *Science*, **308**(5720): 405–408.
- Oliveira R, Godinho R, Randi E, Ferrand N, Alves PC. 2008. Molecular analysis of hybridisation between wild and domestic cats (*Felis silvestris*) in Portugal: implications for conservation. *Conservation Genetics*, **9**(1): 1–11.
- Park YS, Chang J, Sovan L, Cao W, Brosse S. 2003. Conservation strategies for endemic fish species threatened by the Three Gorges Dam. *Conservation Biology*, **17**(6): 1748–1758.
- Pinsky ML, Palumbi SR. 2014. Meta-analysis reveals lower genetic diversity in overfished populations. *Molecular Ecology*, **23**(1): 29–39.
- Piry S, Luikart G, Cornuet JM. 1999. Computer note. BOTTLENECK: a computer program for detecting recent reductions in the effective size using allele frequency data. *Journal of Heredity*, **90**(4): 502–503.
- Pritchard JK, Stephens M, Donnelly P. 2000. Inference of population structure using multilocus genotype data. *Genetics*, **155**(2): 945–959.
- Rice WR. 1989. Analyzing tables of statistical tests. *Evolution*, **43**(1): 223–225.
- Rogers AR, Harpending H. 1992. Population growth makes waves in the distribution of pairwise genetic differences. *Molecular Biology and Evolution*, **9**(3): 552–569.
- Rosenberg NA. 2003. DISTRUCT: a program for the graphical display of population structure. *Molecular Ecology Notes*, **4**(1): 137–138.
- Rousset F. 2008. GENEPOP'007: a complete re-implementation of the genepop software for Windows and Linux. *Molecular Ecology Resources*, **8**(1): 103–106.
- Slatkin M, Hudson RR. 1991. Pairwise comparisons of mitochondrial DNA sequences in stable and exponentially growing populations. *Genetics*, **129**(2): 555–562.
- Tajima F. 1989. Statistical method for testing the neutral mutation hypothesis by DNA polymorphism. *Genetics*, **123**(3): 585–595.
- Tan DQ, Wang JW, Yan TM, Dan SG. 2004. Studies on the artificial propagation of *Ancherythroculter nigrocauda*. *Resources and Environment in the Yangtze Basin*, **13**(2): 193–196. (in Chinese)
- Van Oosterhout C, Hutchinson WF, Wills DPM, Shipley P. 2004. Micro-checker: software for identifying and correcting genotyping errors in microsatellite data. *Molecular Ecology Resources*, **4**(3): 535–538.
- Wang J. 1994. The cascade hydroelectric dams of Longxi River. *Sichuan Water Conservancy*, **15**(6): 52–54. (in Chinese)
- Wang T, Gao X, Wang J, Jakovlić I, Dan SG, Liu HZ. 2015. Life history traits and implications for conservation of rock carp *Procypris rabaudi* Tchang, an endemic fish in the upper Yangtze River, China. *Fisheries Science*, **81**(3): 515–523.
- Xiao W, Zhang Y, Liu H. 2001. Molecular systematics of Xenocyprinae (Teleostei: Cyprinidae): taxonomy, biogeography, and coevolution of a special group restricted in East Asia. *Molecular Phylogenetics and Evolution*, **18**(2): 163–173.
- Xiong F, Liu H, Duan X, Liu S, Chen D. 2016. Estimating population abundance and utilization of *Rhinogobio ventralis*, an endemic fish species in the upper Yangtze River. *Biodiversity Science*, **24**(3): 304–312.
- Xu Y. 2010. Study of Organic Pollution and Migration of Typical Organic Pollutants in the Upstream of the Yangtze River in Chongqing. *Master thesis, University of Xinan, Chongqing*, 46. (in Chinese)
- Xue Z, He X. 2001. Studies on the age and growth of *Ancherythroculter nigrocauda* Yih et Woo. *Journal of Southwest China Normal University*, **26**(6): 712–717. (in Chinese)
- Yang M, Li X. 2018. Population genetic structure of the mantis shrimp *Oratosquilla oratoria* (Crustacea: Squillidae) in the Yellow Sea and East China Sea. *Journal of Oceanology and Limnology*, **36**(3): 905–912.
- Yi YJ, Sun J, Tang CH, Zhang SH. 2016. Ecological risk assessment of heavy metals in sediment in the upper reach of the Yangtze River. *Environmental Science and Pollution Research*, **23**(11): 11002–11013.
- Yin H, Lv H. 2010. Studies on artificial propagation of *Ancherythroculter nigrocauda*. *Journal of Aquaculture*, **31**(5): 30–31. (in Chinese)
- Young A, Boyle T, Brown T. 1996. The population genetic consequences of habitat fragmentation for plants. *Trends in Ecology and Evolution*, **11**(10): 413–418.
- Young EF, Tysklind N, Meredith MP, de Bruyn M, Belchier M, Murphy EJ, Carvalho GR. 2018. Stepping stones to isolation: Impacts of a changing climate on the connectivity of fragmented fish populations. *Evolutionary Applications*, **11**(6): 978–994.
- Yu X, Luo T, Zhou H. 2005. Large-scale patterns in species diversity of fishes in the Yangtze River Basin. *Biodiversity Science*, **13**(6): 473–495. (in Chinese)
- Zhang B, Li M, Zhang Z, Goossens B, Zhu L, Zhang S, Hu J, Bruford MW, Wei F. 2007. Genetic viability and population history of the Giant Panda, putting an end to the “Evolutionary Dead End”? *Molecular Biology and Evolution*, **24**(8): 1801–1810.
- Zhang F, Duan Y, Cao S, Wang J, Tan D. 2011. High genetic diversity in population of *Lepturichthys fimbriata* from the Yangtze River revealed by microsatellite DNA analysis. *Chinese Science Bulletin*, **57**(5): 487–491.
- Zhang F, Tan D. 2010. Genetic diversity in population of largemouth bronze gudgeon (*Coreius guichenoti* Sauvage et Dabry) from Yangtze River determined by microsatellite DNA analysis. *Genes and Genetic Systems*, **85**(5): 351–357.
- Zhao L, Chenoweth EL, Liu J, Liu Q. 2016. Effects of dam structures on genetic diversity of freshwater fish *Sinibrama macrops* in Min River, China. *Biochemical Systematics and Ecology*, **68**: 216–222.
- Zhong Y, Power G. 1996. Environmental impacts of hydroelectric projects on fish resources in China. *River Research and Applications*, **12**(1): 81–98.
- Zhu D, Chang J. 2008. Annual variations of biotic integrity in the upper Yangtze River using an adapted index of biotic integrity (IBI). *Ecological Indicators*, **8**(5): 564–572.

Non-invasive genetic analysis indicates low population connectivity in vulnerable Chinese gorals: concerns for segregated population management

Jing Yang^{1,*}, Guo-Fen Zhu^{2,#}, Jian Jiang³, Chang-Lin Xiang⁴, Fu-Li Gao¹, Wei-Dong Bao^{1,*}

¹ College of Biological Sciences and Technology, Beijing Forestry University, Beijing 100083 China

² College of Biology and Food Science, Hebei Normal University for Nationalities, Chengde Hebei 067000, China

³ Beijing Songshan National Nature Reserve Administration, Beijing 102115, China

⁴ Inner Mongolia Saihanwula National Nature Reserve Administration, Daban Inner Mongolia 025000, China

ABSTRACT

Detailed information on the size and genetic structure of wildlife populations is critical for developing effective conservation strategies, especially for those species that have suffered population decline and fragmentation due to anthropogenic activities. In the present study, we used a non-invasive approach combining fecal pellet sampling with mitochondrial DNA and nuclear DNA microsatellite marker analysis to monitor and compare the population structure of the Chinese goral (*Naemorhedus griseus*) in Beijing and northeast Inner Mongolia in China. Of the 307 fecal samples confirmed to be from *N. griseus*, 15 individuals (nine females and six males) were found in the Beijing population and 61 individuals (37 females and 24 males) were found in the Inner Mongolian population. Among these 76 individuals, we identified eight haplotypes and 13 nucleotide polymorphic sites from mtDNA and 45 alleles from 10 microsatellite loci. Spatially structured genetic variation and a significant level of genetic differentiation were observed between the two populations. In both populations, the sex ratios were skewed toward females, indicating high reproductive

potential, which is crucial for population recovery and conservation of this patchily distributed vulnerable species. We suggest that managing the two populations as evolutionarily significant units with diverse genetic backgrounds could be an effective solution for present population recovery, with the possible relocation of individuals among different groups to help ensure future goral species prosperity.

Keywords: Genetic diversity; Mitochondrial DNA; Microsatellite marker; *Naemorhedus griseus*; Non-invasive sampling; Sex ratio

INTRODUCTION

Determining the size, genetic diversity, and connectivity among populations is important for understanding the ability of target species to adapt to different habitat conditions (Banks & Lindenmayer, 2014; Dharmarajan et al., 2013) and for monitoring and developing conservation strategies for endangered species (Lande, 1988). Among the many factors affecting wildlife population dynamics, such as life history traits, spatial behaviors, predation pressure, human disturbance, and food resource abundance, the sex ratio is a

Open Access

This is an open-access article distributed under the terms of the Creative Commons Attribution Non-Commercial License (<http://creativecommons.org/licenses/by-nc/4.0/>), which permits unrestricted non-commercial use, distribution, and reproduction in any medium, provided the original work is properly cited.

Copyright ©2019 Editorial Office of Zoological Research, Kunming Institute of Zoology, Chinese Academy of Sciences

Received: 12 March 2019; Accepted: 27 June 2019; Online: 23 July 2019

Foundation items: This project was supported by the Beijing Municipal Committee of Science and Technology (Z121100000312107, Z181100005318004)

[#]Authors contributed equally to this work

^{*}Corresponding author, E-mail: wdbao@bjfu.edu.cn

DOI: 10.24272/j.issn.2095-8137.2019.058

fundamental biological index that can indicate population growth (Székely et al., 2014) and status (Lindström et al., 2002). For example, a greater number of females than males can imply that a population is increasing rather than decreasing (Cameron, 2004). However, determining the sex of individuals is often difficult in the field because heterogeneous habitats may block an observer's line of sight and target animals may hide or lack obvious external sex-specific characteristics (Lewis et al., 2002). Advances in molecular biology have allowed the use of animal feces, hair, eggshells, and food residue as non-invasive sources of DNA, which can be used in conservation genetics research (DeSalle & Amato, 2004). For example, fecal samples have been used in studies on rare and endangered animals involving species identification, sex determination, individual identification, effective population size estimation, and population genetic structure analysis (Haag et al., 2009; Mondol et al., 2009).

The Chinese goral (*Naemorhedus griseus*), a goat-like wild ungulate of similar body size, is mainly distributed in central and northern China (Hrabina, 2015; Smith & Xie, 2008; Mead, 1989). Excessive medicinal exploitation and habitat fragmentation have both resulted in rapid declines and isolation of goral populations throughout most of its range (State Forestry Administration, 2009). Currently, the Chinese goral is listed as a Class II state key protected wildlife species in China and has also been listed as Vulnerable (VU) on the International Union for Conservation of Nature Red List (Duckworth et al., 2008) and under Appendix I protection by the Convention on International Trade in Endangered Species of Wild Fauna and Flora. However, no accurate estimates currently exist for Chinese goral populations aside from a previous field observation related to population size and habitat selection (Chen et al., 1999). A systematic national survey on this species indicated that habitat fragmentation has forced the remaining populations to retreat in small numbers to patchy areas in nature reserves, resulting in severe isolation and increased extinction risk of local populations (State Forestry Administration, 2009). Furthermore, little is known regarding the genetic structure or molecular biology of these small-group goral populations living under the threat of habitat fragmentation, despite the importance of such knowledge in planning effective conservation strategies.

We previously conducted field surveys on wild animal diversity in the mountain ranges around Beijing and at a national nature reserve in Inner Mongolia, which revealed that goral populations were experiencing slow recovery. This recovery highlighted the need to investigate the biological traits of the populations for efficient conservation of this endangered species. Furthermore, the Inner Mongolian population was separated from all other geographical groups and may exhibit a different genetic background. Thus, we studied the structure and genetic connectivity of the goral populations to detect whether biological differences exist between the two groups, which may have valuable implications for isolated population management. In this study,

mitochondrial DNA (mtDNA) gene fragments and nuclear DNA microsatellite markers combined with non-invasive fecal sampling were used to examine the minimum population size, sex ratio, and genetic connectivity of two geographically separated populations of Chinese goral in the Beijing Songshan National Nature Reserve (BS) and Inner Mongolian Saihanwula National Nature Reserve (IMS). The BS population, which inhabits the mountain ranges around Beijing and is connected with nearby populations in Hebei Province, experienced severe population decline as a consequence of historical hunting for food and medicine before the promulgation of the Wildlife Protection Law in 1989. The present population is slowly recovering due to effective local government management of illegal hunting and livestock grazing (Chen et al., 2002). Several recent camera trapping surveys confirmed its re-appearance (Lan & Jin, 2016; Liu et al., 2012) and daily activity patterns in the mountain ranges of Beijing (Zhang et al., 2017). The IMS goral population inhabits the southern segments of Daxing'anling (Greater Khingan Mountain) of Inner Mongolia and is isolated in a national nature reserve surrounded by human settlements. Several ecological studies have been conducted by our research team on this population, including on food selection, sexual hormone variation, and habitat suitability evaluation (Tang et al., 2018, 2019).

The aims of the current study were to: (1) assess monitoring protocols, especially regarding sex structure and individual identification, by non-invasive genetic sampling to predict future population dynamics and guide development of conservation strategies; (2) evaluate the baseline genetic status of the two geographically separated populations for efficient management; and (3) acquire in-depth information in terms of restricted distribution area and population isolation for the IMS population to understand its genetic development trends under limited habitat conditions.

MATERIALS AND METHODS

Study areas and goral populations

This study was undertaken in the Beijing Songshan (BS) National Nature Reserve and Inner Mongolian Saihanwula (IMS) National Nature Reserve in China (Figure 1). The BS reserve is located in the Yanqing district, northwest of Beijing City (E115°43'–115°50', N40°29'–40°33'), and covers an area of 6 212 ha, mainly to preserve natural pine (*Pinus tabulaeformis*) forest, secondary deciduous broad-leaved forest, and various types of wild animals and plants, including the Chinese goral. The goral populations in Beijing are very patchy, with individuals found almost everywhere in mountain areas (Chen et al., 2002), but in small-sized groups (Liu et al., 2012; Zhang et al., 2017). The regional population is connected with southern conspecific populations in Hebei and Shanxi provinces through the Taihang Mountains (State Forestry Administration, 2009). The IMS reserve is located north of Balinyouqi Banner in Chifeng City (E118°18'–118°55', N43°59'–44°27') and covers an area of 100 400 ha. As a

forest nature reserve, IMS protects a rich ecosystem and numerous endangered wild animals, including red deer (*Cervus elaphus*), Eurasian lynx (*Lynx lynx*), gray wolf (*Canis lupus*), great bustard (*Otis tarda*), and black stork (*Ciconia nigra*). The Chinese goral population is the only remaining group in the Greater Khingan Mountains, and is in a state of severe isolation, with no viable populations nearby. Historical

corridors likely included the southern Greater Khingan Mountains connected with the Yanshan Mountains in the south (including Beijing) (Hrabina, 2015; Mead, 1989). However, these dispersal pathways became disconnected by human settlements on the plains between the mountains over centuries of anthropogenic movement (State Forestry Administration, 2009).

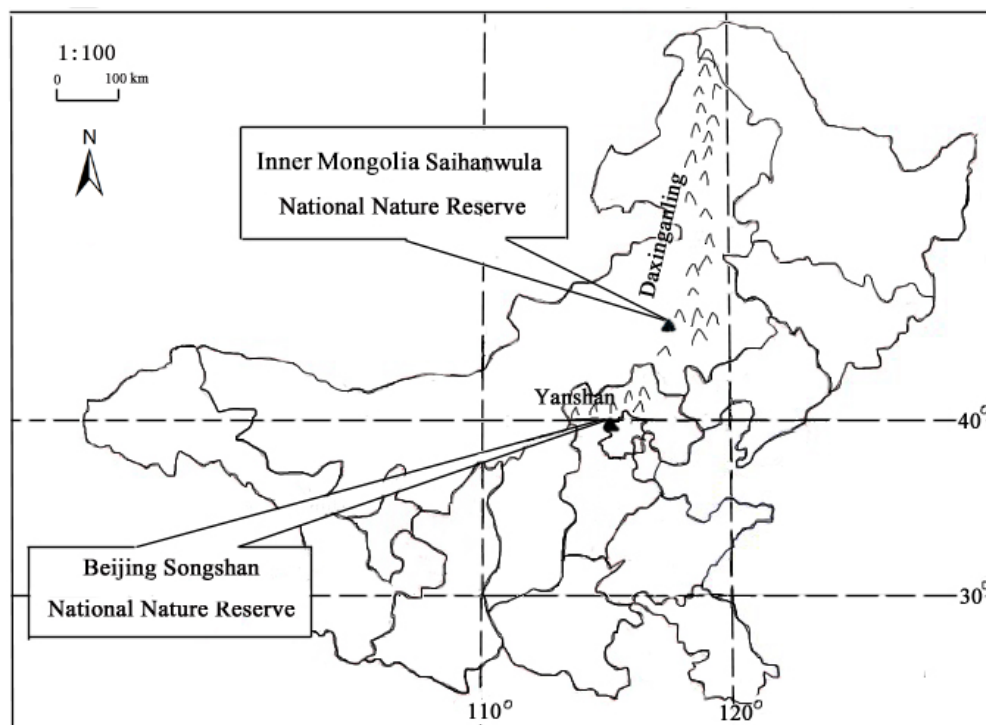


Figure 1 Locations of Beijing Songshan and Inner Mongolian Saihanwula National Nature Reserves in China

Sampling procedure

In November 2013, Chinese goral habitat survey and fecal sample collection were undertaken by reserve staff with the permission of the Departments of Natural Resources Management of the BS and IMS administrations. The sampling teams searched for goral pellets randomly in major habitats based on previous field observations. All fresh pellets were collected without considering outer shapes or distances between the pellet stacks to avoid sex bias. Only fresh (based upon color and moisture) fecal samples were taken. Newly purchased Ziploc bags and tools were used for sample collection to avoid possible DNA cross-contamination and all samples were stored in anhydrous ethanol at -20°C within 6 h of collection. The collection period lasted 10 d from 5 and 10 November in BS and IMS, respectively. GPS positions and collection times were recorded for each fecal sample. In addition, a muscle tissue sample from a dead adult female in IMS and a blood sample from a rescued male in Beijing were used as positive controls.

DNA extraction

We extracted DNA from the muscle and blood samples using

a TIANamp Genomic DNA Kit (Tiangen Biotech Co. Ltd., Beijing, China) and from fecal samples using an EZNA Stool DNA Kit (Omega, Dorivalle, GA, USA) following the manufacturer's protocols, with some modifications (Zhang et al., 2009) to improve the amount and quality of DNA extracted.

Species identification based on mtDNA

Two mtDNA fragments were used to identify species and analyze population genetic structure, respectively. Species were determined from the fecal samples via PCR using a partial mitochondrial cytochrome-b gene with goral species-specific primers, as per Kim et al. (2010) (i.e., BJGL-F1: 5'-CTGCCTAATTCTACAAATCCTA-3' and BJGL-R: 5'-TAGGAG GATTACCCCAATA-3'). Each experiment included a positive and negative control (DNase/Rnase-free deionized water template rather than DNA). Specific primers (i.e., DF249 5'-ACCCCATGCATATAAGCATG-3' and DR496 5'-GGATACGC ATGTTGACAAGG-3') were used to amplify a 227 bp segment of the mtDNA control region and were designed using Primer Premier 5 (Lalitha, 2000) in reference to the published mtDNA control region from the South Korean long-tailed goral (*Naemorhedus caudatus*) (GenBank accession Nos.:

EU259152, EU259154, EU259155, EU259165, EU259169, EU259171, and EU259176) (Kim et al., 2008, 2010). These segments were used to analyze the basic genetic structure of the two goral populations. The PCR conditions are shown in Supplementary Materials 1A. Both PCR products were isolated by electrophoresis in a 2% (w/v) agarose gel, and the control region PCR products were then further purified using a Wizard SV Gel and PCR Clean-Up System (Promega, Madison, WI, USA) before final sequencing by SinoGenoMax Co. Ltd. (Beijing, China).

Individual identification based on microsatellite loci

Ten microsatellite loci (SY12A, SY12B, SY48, SY58, SY71, SY76, SY84, SY84B, SY112, and SY129) were used for individual identification (An et al., 2005, 2010). Fluorescence labels (HEX or FAM) were added to the 5' terminus of the forward primers of all microsatellite loci. As fecal DNA in this analysis was very dilute, a two-step PCR procedure was used to increase the amplification rate and reduce the genotyping error rate (Piggott et al., 2004; Taberlet et al., 1999) (see Supplementary Materials 1B for PCR conditions). To guard against contamination, 75% alcohol was sprayed over the experimental table before and after setting up each PCR run. Each DNA sample underwent a minimum of five independent PCR runs for each microsatellite locus to reduce the effects of possible allelic dropout or false alleles (Broquet et al., 2007; Mondol et al., 2009; Taberlet et al., 1996).

The PCR products were assayed by electrophoresis on 2.5% agarose gels, and the amplified target fragments were delivered to SinoGenoMax Co., Ltd. (Beijing, China) for genotyping analysis using an ABI-PRISM 310 DNA Analyzer (Applied Biosystems, USA). Similarly, fluorescence of different DNA sizes of microsatellite alleles was determined using GeneMarker v2.4.0 (SoftGenetics LLC., State College, PA, USA) to confirm the genotyping results.

Sex discrimination

Nested PCR based on amplification of a Zn-finger gene on the X and Y chromosomes was used for sex identification, as successfully applied for Korean long-tailed goral (Kim et al., 2008, 2010). Detailed PCR procedures are provided in the Supplementary Materials 1C.

The PCR products were assayed by electrophoresis on 2.5% agarose gels to confirm sex. If the X and Y alleles were both detected or only the Y allele was detected in a sample, sex was determined to be male; if only the X allele was detected, sex was determined to be female. Samples without amplification products were considered failures. Each sample underwent a minimum of five independent PCR runs, and at least three consistent results were required for successful determination to reduce possible error from allelic loss (Scandura, 2005).

Genetic data analysis

The obtained mtDNA control region sequences were analyzed with Clustal W v2.0 for sequence alignment (Larkin et al., 2007) and were proofread by eye. DnaSP v5.0 (Librado &

Rozas, 2009) was used to identify haplotype frequency and number of polymorphic sites, haplotype diversity (h), nucleotide diversity (π), average number of nucleotide differences (k), coefficient of genetic differentiation between populations (F_{ST}), and significance level of differences. Gene flow (Nm) was calculated by MEGA5 software via F_{ST} and was used to analyze nucleotide composition and calculate genetic distances between haplotypes based on the Kimura double parametric method (Tamura et al., 2011). The haplotypes were compared with the Korean long-tailed goral homologous sequences (GenBank accession Nos.: EU259152–EU259176) to evaluate phylogenetic relationships. Arlequin v3.5 (Excoffier & Lischer, 2010) was used to determine F_u 's F_s (Fu, 1997) and Tajima's D (Tajima, 1989) to assess whether nucleotide polymorphisms deviated from expectations under neutral theory.

The neighbor-joining method in MEGA5 was employed to reconstruct phylogenetic relationships among partial mtDNA control region haplotypes. To acquire the phylogenetic tree root, homologous sequences of sheep (*Ovis aries*) KJ954145 were used as an outgroup. The confidence coefficient of the systematic tree was tested via bootstrap resampling with 1 000 simulated samples. In addition, the maximum parsimony median-joining network, which can effectively illustrate the relationships among sequences with low diversity, was used to further visualize genealogical relatedness among haplotypes with NETWORK v5.0.0.1 (Bandelt et al., 1999).

Micro-Checker software (Van Oosterhout et al., 2004) was applied to assess the null alleles of each microsatellite locus and to identify reliable genotyping for each sample. The frequencies of the null alleles were obtained using the Brookfield method (Van Oosterhout et al., 2004) employed in Micro-Checker, and the adjusted allele frequencies were then used to recompute heterozygosity (H_E null) and observed heterozygosity (H_O null) values in GenAlEx v6.5 (Peakall & Smous, 2010). Samples amplified with less than five loci were judged as failures and were excluded from subsequent analyses (Mondol et al., 2009). Arlequin v3.5 was used to examine the Hardy-Weinberg equilibrium and linkage disequilibrium (LD) and to calculate LD for all microsatellite loci, intra-population genetic differentiation coefficients (F_{ST}), and levels of significance. If a significant presence of null alleles was detected, we recalculated the F_{ST} with corrected genotype frequencies in GenAlEx v6.5. GenAlEx v6.5 and Cervus v3.0 (Kalinowski et al., 2007) were used to calculate allele number (N_a), number of effective alleles (N_e), observed heterozygosity (H_o), expected heterozygosity (H_e), and polymorphism information content (PIC) of each microsatellite locus.

RESULTS

Species identification, individual identification, and sex determination

In total, 40 and 332 fresh fecal samples were collected from BS and IMS, respectively. Among these, the partial

mitochondrial cytochrome *b* gene was successfully amplified in 33 samples from BS and 274 samples from IMS, which were thus identified as Chinese goral based on adequate DNA, with a species identification rate of 82.50% and 82.53%, respectively.

Genotyping results derived from the 10 pairs of microsatellite primers recognized 76 individuals from the 307 tested samples after removal of failed amplifications and duplicates, with 15 and 61 individuals recognized from the BS and IMS populations, respectively. The cumulative probabilities of two unrelated individuals sharing the same multi-locus (PID) for all loci estimated in Gimlet software were 0.000 04 and 0.000 01 for the BS and IMS populations, respectively. The corresponding probabilities of two full siblings (PIDsib) were 0.000 6 and 0.000 3, proving that the 10 loci used here were sufficient for accurately identifying individuals.

In total, 15 and 151 samples were identified as female and 14 and 92 were identified as male in BS and IMS, respectively. The sex identification success rates were 87.88% and 88.69% for the two groups of identified goral samples. After correcting for repeated individuals, we identified nine females and six males in the BS population, with a female to male ratio of 1.50: 1, which did not significantly deviate from 1: 1 ($\chi^2=2.77$, $P>0.05$), and 37

females and 24 males in the IMS population, with a female to male ratio of 1.54: 1, which also did not significantly deviate from 1:1 ($\chi^2=0.6$, $P>0.4$).

Genetic diversity of mtDNA control region

After individual identification, we obtained 76 partial mitochondrial control region sequences from the two populations. Thirteen polymorphic sites were detected from the 227 bp gene fragments by sequence alignment, with a rate of 5.73% for the mtDNA sequences. Within the 13 polymorphic sites, 13 transitions, three transversions, and no insertion/deletions were detected. All mutation sites were analyzed with Tajima's neutrality test, with an obtained Tajima's *D* value of 1.48 ($P>0.10$).

Eight control region haplotypes were identified, including three (BJ-A to BJ-C) from BS and five (NM-A to NM-E) from IMS. We found no shared haplotypes between the two geographic populations. The nucleotide sequences of BJ-A to BJ-C and NM-A to NM-E for the eight haplotypes were submitted to GenBank under accession Nos. KP330565 – KP330572.

Genetic parameters such as haplotype diversity (*h*), nucleotide diversity (π), and average number of nucleotide differences (*k*) indicated moderate genetic diversity for the two goral populations (Table 1).

Table 1 Genetic diversity parameters and demographic analyses of partial mtDNA control region from two goral populations in China

Population	<i>s</i>	<i>n</i>	<i>h</i>	π	<i>k</i>	Fu's <i>F_s</i>	Tajima's <i>D</i>
IMS	8	5	0.787±0.022	0.0107±0.0006	2.428	-2.059	1.002
BS	5	3	0.705±0.053	0.0097±0.0014	2.21	-0.077	0
Total	13	8	0.852±0.018	0.0217±0.0019	4.928	-3.009	1.97

s: Number of nucleotide polymorphism loci; *n*: Number of haplotypes; *h*: Haplotype diversity; π : Nucleotide diversity; *k*: Average number of nucleotide differences. There were no significant differences in parameters ($P>0.05$), except for Fu's *F_s* ($P<0.05$).

Genetic structure of microsatellite loci

We screened 10 pairs of polymorphic microsatellite primers to determine the genotypes of the populations. Among the identified Chinese goral feces, 26 samples from BS and 212 from IMS provided reliable and complete genotypes at the 10 loci, with genotyping success rates for BS and IMS of 77.79% and 77.37%, respectively. Forty-five alleles were detected in 10 polymorphic microsatellite loci, 25 were shared between the two populations, eight were exclusive to BS, and 12 were exclusive to IMS. The distribution frequencies of the 45 alleles in the two populations were not identical. The genetic diversities calculated by the microsatellite dataset are shown in Table 2. In the IMS population, the Micro-Checker results, with a 95% confidence interval, indicated that null alleles existed at three of the 10 loci (i. e., SY12B, SY71, and SY84B). The frequency of null alleles differed for the three microsatellite loci (i.e., 7.68% for SY12B, 7.44% for SY71, and 10.16% for SY84B). Thus, the values of observed heterozygosity for the IMS population slightly increased when the dataset was adjusted based on the null allele frequencies, but there was no change in the expected heterozygosity (Supplementary Materials 2). No evidence for genotyping

misjudgment caused by null alleles, strip discontinuity, or missing alleles was found within the 10 microsatellite loci in the BS population.

Table 2 Genetic diversity among 10 microsatellite loci observed in the two goral populations

Population	<i>N_a</i>	<i>N_e</i>	<i>H_O</i>	<i>H_E</i>	PIC
BS	3.300	2.944	0.607	0.650	0.578
IMS	3.700	3.400	0.630	0.691	0.629

BS: Beijing Songshan National Nature Reserve; IMS: Inner Mongolian Saihanwula National Nature Reserve. *N_a*: Average number of alleles; *N_e*: Number of effective alleles; *H_O*: Observed heterogeneity; *H_E*: Expected heterogeneity; PIC: Polymorphism information content.

Results further indicated that the SY12B ($P=0.004$) and SY84B ($P=0.024$) loci from the IMS goral population deviated clearly from the Hardy-Weinberg equilibrium, suggesting independent evolution of this population, whereas the other loci showed no deviation from the two populations. After 45 linkage disequilibrium tests with the 10 loci, SY84B and

SY112 from the BS population ($\chi^2=8.42$, $P<0.05$) and SY58 and SY84 from the IMS population showed linkage disequilibrium ($\chi^2=7.118$, $P<0.05$), with no linkage disequilibrium found in other loci. After sequential Bonferroni correction for pairwise comparisons, the differences in linkage disequilibrium loci were not significant, indicating that all loci were inherited independently and could be an accurate reflection of the genetic diversity status in the studied goral populations.

Genetic differentiation of haplotypes for two populations

The genetic distances between the eight mtDNA control region haplotypes ranged from 0.004 4 to 0.060 3, with an average of 0.031 8. The average genetic distances between haplotypes within the BS and IMS populations were 0.014 9 and 0.012 5, respectively. Maximum and minimum genetic distances were 0.022 4 and 0.008 9 for the BS population and 0.022 5 and 0.004 4 for the IMS population, respectively.

The inter-population genetic differentiation coefficient was estimated at $F_{ST}=0.774$ ($P<0.001$), suggesting a significant level of genetic differentiation between the two populations. The gene flow value for the two populations was $Nm=0.07$, showing that the inter-population genetic distance was large and that the number of migrating individuals was only 0.07 for each generation. These results thus revealed a lack of genetic exchange between the two populations. The neighbor-joining phylogenetic tree showed that the haplotypes were clustered into two large clades, the BS and IMS goral populations were clustered into one clade and the South Korea populations were clustered into the other clade (Figure 2A). The Chinese goral populations were further separated into two small independent branches, showing distinct genetic differentiation and a lack of gene flow. The median-joining network also grouped the haplotypes into a same topology, with several mutation steps existing between the two Chinese populations (Figure 2B).

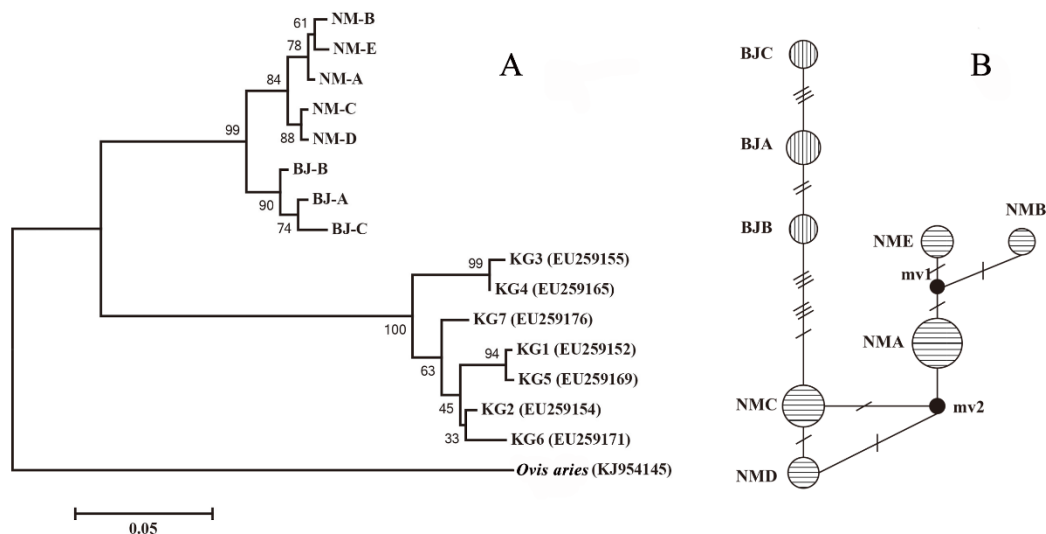


Figure 2 Integrative genetic analyses of mtDNA control region haplotypes in Chinese goral

A: Phylogenetic tree constructed by neighbor-joining method, NM-A to E, BJ-A to C, and KG1 to KG7 represent different haplotypes of IMS, BS, and Korean goral populations, respectively. B: Median-joining network constructed among eight haplotypes, each number indicates one mutation step between haplotypes, and un-sampled haplotypes are represented by small solid circles. Size of circles is related to frequency of haplotypes.

Phylogenetic discrepancy between populations

The F_{ST} genetic differentiation coefficient and Nei's genetic distance for the BS and IMS populations were 0.104 and 0.336, respectively. Considering the existence of null alleles, the recomputed F_{ST} and Nei's genetic distances were 0.065 and 0.334, respectively, with adjusted genotypes. These results indicated that the two populations had a moderate level of genetic differentiation. Cluster analysis based on STRUCTURE software showed that the BS and IMS populations were two separate clades with no interaction, indicating that genetic differentiation was significant, and the phylogenetic relationship was distant for the two populations (Figure 3).

DISCUSSION

Estimating the size of a wild animal population is central for managing game species and conserving rare and endangered animals. The Chinese goral is typically very alert and sensitive to disturbance. Furthermore, its fur is often indistinguishable from the surrounding rocks on the mountaintops it inhabits, which has caused great difficulties in traditional transect surveys. However, appropriate techniques to extract and analyze DNA from feces can help identify individuals in the field and avoid bias from repeated counting of a single individual (Haag et al., 2009). In the current study, we

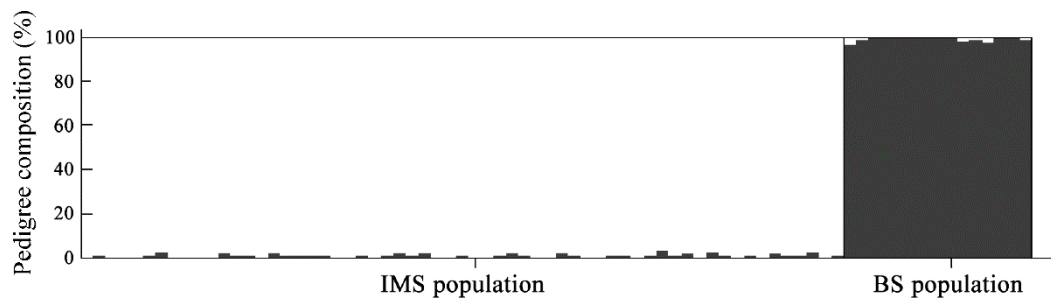


Figure 3 STRUCTURE clustering based on microsatellite genotypes of Chinese goral populations

BS: Beijing Songshan National Nature Reserve; IMS: Inner Mongolian Saihanwula National Nature Reserve.

identified at least 61 animals in the 100 km² sampling area in IMS and 15 animals in a 30 km² area in BS. These results, combined with the female-biased sex ratios, suggest a high recovery potential for these separate goral populations; however, further research into the genetic variations of their populations is needed to reveal the underlying mechanism.

Sex ratio analysis can be used to evaluate the structure and future development of an animal population (Kruuk et al., 1999); it can also provide basic data for planning and implementing effective management strategies to conserve rare and endangered wildlife (Bradshaw et al., 2003; Majumder et al., 2017). In this study, a sex-linked Zn-finger gene was used for sex structure analysis. Results showed a similar female-biased sex ratio in both populations, i.e., 1.54:1 (female to male) in IMS and 1.50:1 in BS. Although there was no statistical difference from the theoretical 1:1 ratio, the high female bias in the sex structure of the wild goral populations is expected to promote population recovery. A number of hypotheses have been proposed to explain adaptive sex-ratio variation in mammals (Cockburn et al., 2002). One commonly applied model for ungulates is the local resource competition (LRC) hypothesis, which states that competition for environmental resources may shape the primary sex ratio, and predicts that mothers with poor body condition should reproduce the sex that is more likely to disperse and consequently reduce local competition for resources between mothers and their offspring within the natal area (Clark, 1978). In our study areas, food resources are abundant (Li, 2005; Liu et al., 2012) and the females are in good condition (as confirmed by field camera trapping photos). However, the bare rock microhabitats to which gorals retreat when facing mammalian predators are limited. Thus, the high proportion of females within the populations may indicate a demographic variation due to the limited microhabitat resource pressure. Our ongoing GPS tracking captured six gorals at the IMS reserve, which were all females, thus confirming their high proportion. Furthermore, the preliminary home range results showed that sub-adult females ($n=3$) shared their small home ranges with adult females. Thus, the high female to male ratios in our study fit the LRC model prediction, in which healthy mothers reproduce more philopatric daughters than dispersal sons in environments with abundant food resources and limited bare rock microhabitats. Although our results

found a greater number of females in the two Chinese goral populations, thus indicating high reproductive potential and population growth, further in-depth field monitoring on the social structures and breeding behaviors is needed to reveal actual population growth trends, especially for the isolated population at IMS.

Average genetic distance and nucleotide diversity between haplotypes serve as important indicators of mtDNA genetic diversity. In mammals, a population is considered genetically diverse if the mean genetic distance between haplotypes is greater than 0.01, with higher values indicating greater genetic diversity (Nei, 1987). The overall genetic distances among haplotypes in the BS and IMS populations were 0.014 9 and 0.012 5, respectively, indicating rich genetic diversity in the two goral ranges. Compared to the average genetic distance among haplotypes, nucleotide diversity π can better reflect mtDNA diversity in a population (Nei, 1987). Nucleotide diversity in mammals can range from 0.003 to 0.04 with a maximum value of 0.1, with a higher π value indicating greater genetic diversity (Neigel & Avise, 1993). In this study, nucleotide diversities were 0.009 7 and 0.010 7 for the BS and IMS populations, respectively, indicating moderate genetic diversity. Compared to other Caprinae subfamily members, such as the Helan Mountain bharal (*Pseudois nayaur*) with $\pi=0.003$ 92 (Wang et al., 2006), red goral (*Naemorhedus baileyi*) with $\pi=0.000$ 88 (Xiong et al., 2013), and serow (*Capricornis sumatraensis*) with $\pi=0.024$ 9 (Liu et al., 2013), the goral populations in our study showed an intermediate level of nucleotide diversity.

Haplotype diversity can reflect recent changes in a population. In this study, the mtDNA control region showed a high level of haplotype diversity and moderate level of nucleotide diversity in the two geographically separated populations. Thus, it is reasonable to speculate that the two populations may have arisen from rapid growth of groups with small effective population sizes, similar to the reported population dynamics of the takin (*Budorcas taxicolor*) with high haplotype diversity and low nucleotide diversity (Li et al., 2003). Fossils of *Naemorhedus* species have been found in the middle and lower Pleistocene in China, upper Paleolithic deposits in Far East Russia, and the third and fourth interglacial periods in Korea (Mead, 1989), areas which are partially covered by the present-day distribution ranges,

indicating that *Naemorhedus* experienced a historical distribution range recovery after the quaternary glacial.

The existence of null alleles is one of the biggest drawbacks for microsatellite markers as they can generally increase F_{ST} and genetic distance values with decreasing within-population genetic diversity (Paetkau et al., 1997; Slatkin, 1995). Herein, among the 10 microsatellite markers in the two studied populations, three loci (i.e., SY12B, SY71, and SY84B) (see Supplementary Table S1) from the IMS population showed the possible existence of null alleles, which could be attributed to the low quality and quantity of fecal DNA (Waits et al., 2001). After adjustment of allele frequencies in these loci, the observed heterozygosity (H_O) for the three single markers increased remarkably, and the F_{ST} decreased from 0.104 to 0.065 between the two populations. This reduction may be slightly overestimated due to the evaluation method based on prior probabilities; however, the correction results still need to be carefully considered.

The estimated genetic differentiation between the two studied goral populations was $F_{ST}=0.774$ (in mitochondrial genes), which may reflect different demographic histories. The IMS population is the only remaining reproductively viable population in the Greater Khingan Mountains (State Forestry Administration, 2009), with severe isolation and habitat fragmentation from anthropogenic activities accelerating its independent evolution. Therefore, strengthening future monitoring would be an effective way to surveil the dynamics of genetic diversity on this isolated goral population for the purpose of maintaining long-term population viability.

The population size and sex ratio results provide baseline data for implementing effective population conservation strategies. The techniques used in this study, which include non-invasive fecal sampling followed by DNA extraction and analysis of population structure, are simple and accurate, with a relatively high success rate compared to other studies on herbivores (Broquet et al., 2007). Our research was performed after the first winter snowfall with an average air temperature below 0 °C and the fecal samples were fixed in anhydrous alcohol within several hours of collection to delay DNA degradation. Moreover, a two-step PCR procedure was used to increase the PCR amplification products and reduce the genotyping error rate. The relatively high identification rate confirmed the validity and reliability of the genotyping procedure, which should provide important guidance for future non-invasive genetic monitoring on goral population structures.

The mtDNA and microsatellite diversity analyses both showed significant levels of genetic differentiation between the BS and IMS goral populations. This implies that the distribution range of historically intact goral populations was segregated by expansion of human settlements and disappearance of connecting groups, leading to population isolation (State Forestry Administration, 2009). Habitat fragmentation and population segregation are severe factors threatening the effective conservation of many endangered wild animals throughout the world (Keil et al., 2015) and increasing the risk of extinction of isolated populations. Although it is difficult to assess whether the independent

evolution observed in the current study will have positive or negative effects on the long-term existence of populations, we would recommend that the two Chinese goral populations be preserved and monitored separately as evolutionarily significant units to maintain species genetic diversity within different management areas. If needed, based on further genetic monitoring, the translocation of individuals among geographically separated populations may improve the genetic diversity of the small segregated groups.

SUPPLEMENTARY DATA

Supplementary data to this article can be found online.

COMPETING INTERESTS

The authors declare that they have no competing interests.

AUTHORS' CONTRIBUTIONS

J.J., C.L.X., and W.D.B. drafted the experiments; J.Y. and G.F.Z. performed the experiments and wrote the paper; F.L.G. analyzed the data. All authors read and approved the final version of the manuscript.

ACKNOWLEDGEMENTS

We thank Ji-Gui Wu, Baart, and the staff of the two nature reserves for collecting the goral fecal samples. Grateful thanks are given to Alice Laguardia from BJFU for valuable comments and editing of the original manuscript. We thank NPG Language Editing for proof-reading the manuscript.

REFERENCES

- An J, Min MS, Sommer J, Louis E Jr, Brenneman R, Kwon SW, Shin NS, Lee H. 2005. Isolation and characterization of 15 microsatellite loci in the Korean goral (*Nemorhaedus caudatus*). *Molecular Ecology Resources*, **5**(2): 421–423.
- An J, Choi SK, Sommer J, Louis E Jr, Brenneman R, Zemanova B, Hájková P, Park G, Min MS, Kim KS, Lee H. 2010. A core set of microsatellite markers for conservation genetics studies of Korean goral (*Naemorhedus caudatus*) and its cross-species amplification in Caprinae species. *Journal of Veterinary Science*, **11**(4): 351–353.
- Bandelt HJ, Forster P, Röhl A. 1999. Median-joining networks for inferring intraspecific phylogenies. *Molecular Biology and Evolution*, **16**(1): 37–48.
- Banks SC, Lindenmayer DB. 2014. Inbreeding avoidance, patch isolation and matrix permeability influence dispersal and settlement choices by male *Agile antechinus* in a fragmented landscape. *Journal of Animal Ecology*, **83**(2): 515–524.
- Bradshaw CJA, Harcourt RG, Davis LS. 2003. Male-biased sex ratios in New Zealand fur seal pups relative to environmental variation. *Behavioral Ecology and Sociobiology*, **53**(5): 297–307.
- Broquet T, Ménard N, Petit E. 2007. Noninvasive population genetics: a review of sample source, diet, fragment length and microsatellite motif effects on amplification success and genotyping error rates. *Conservation*

Genetics, **8**(1): 249–260.

Cameron EZ. 2004. Facultative adjustment of mammalian sex ratios in support of the Trivers-Willard hypothesis: evidence for a mechanism. *Proceedings of the Royal Society of London B*, **271**(1549): 1723–1728.

Chen W, Gao W, Fu BQ. 2002. Mammals of Beijing. Beijing: Beijing Publishing House. (in Chinese)

Chen RB, Liu FY, Tian L, Zhang ZG. 1999. Quantitative distribution of *Naemorhedus goral* in Daqingshan Mountains. *Acta Scientiarum Naturalium Universitatis Neimongol*. **30**(2): 227–229. (in Chinese)

Clark AB. 1978. Sex ratio and local resource competition in a prosimian primate. *Science*, **201**(4351): 163–165.

Cockburn A, Legge S, Double MC. 2002. Sex ratios in birds and mammals: can the hypotheses be disentangled?. In: Hardy ICW (ed). *Sex Ratios: Concepts and Research Methods*. Cambridge: Cambridge University Press, 266–286.

DeSalle R, Amato G. 2004. The expansion of conservation genetics. *Nature Reviews Genetics*, **5**: 702–712.

Dharmarajan G, Beasley JC, Fike JA, Rhodes OE Jr. 2013. Effects of landscape, demographic and behavioral factors on kin structure: testing ecological predictions in a mesopredator with high dispersal capability. *Animal Conservation*, **17**(3): 225–234.

Duckworth JW, MacKinnon J, Tsytsulina K. 2008. *Naemorhedus caudatus*. The IUCN red list of threatened species 2008: e. T14295A4429742. Retrieved 10 December 2015.

Excoffier L, Lischer HEL. 2010. Arlequin suite ver 3.5: a new series of programs to perform population genetics analyses under Linux and Windows. *Molecular Ecology Resources*, **10**(3): 564–567.

Fu YX. 1997. Statistical tests of neutrality of mutations against population growth, hitchhiking and background selection. *Genetics*, **147**(2): 915–925.

Haag T, Santos AS, De Angelo C, Srbek-Araujo AC, Sana DA, Morato RG, Salzona FM, Eizirik E. 2009. Development and testing of an optimized method for DNA-based identification of jaguar (*Panthera onca*) and puma (*Puma concolor*) faecal samples for use in ecological and genetic studies. *Genetica*, **136**(3): 505–512.

Hrabina P. 2015. A new insight into the taxonomy and zoogeography of recent species of goral (*Nemorhaedus*, Bovidae, Ruminantia). *Gazella*, **42**: 33–91.

Kalinowski ST, Taper ML, Marshall TC. 2007. Revising how the computer program CERVUS accommodates genotyping error increases success in paternity assignment. *Molecular Ecology*, **16**(5): 1099–1106.

Keil P, Storch D, Jetz W. 2015. On the decline of biodiversity due to area loss. *Nature Communications*, **6**: 8837.

Kim BJ, Lee H, Lee SD. 2010. Species- and sex-specific multiple PCR amplifications of partial cytochrome b gene and Zfx/Zfy introns from invasive and non-invasive samples of Korean ungulates. *Genes & Genomics*, **31**(5): 369–375.

Kim BJ, Lee YS, An J, Park PKC, Okumura H, Lee H, Min MS. 2008. Species and sex identification of the Korean goral (*Nemorhaedus caudatus*) by molecular analysis of non-invasive samples. *Molecules & Cells*, **26**(3): 314–318.

Kruuk LEB, Clutton-Brock TH, Albon SD, Pemberton JM, Guinness FE. 1999. Population density affects sex ratio variation in red deer. *Nature*, **399**: 459–461.

Lalitha S. 2000. Primer premier 5. *Biotech Software & Internet Report*,

1: 270–272.

Lan H, Jin K. 2016. Infrared-triggered camera technology application in the investigation of mammals in Beijing Wulingshan national nature reserve. *Acta Theriologica Sinica*, **36**(3): 322–329. (in Chinese)

Lande R. 1988. Genetics and demography in biological conservation. *Science*, **241**(4872): 1455–1460.

Larkin MA, Blackshields G, Brown NP, Chenna R, McGettigan PA, McWilliam H, Valentin F, Wallace IM, Wilm A, Lopez R, Thompson JD, Gibson TJ, Higgins DG. 2007. Clustal W and Clustal X Version 2.0. *Bioinformatics*, **23**(21): 2947–2948.

Lewis S, Benvenuti S, Dall'Antonia L, Griffiths R, Money L, Sherratt TN, Wanless S, Hamer KC. 2002. Sex-specific foraging behaviour in a monomorphic seabird. *Proceedings of the Royal Society of London B: Biological Sciences*, **269**(1501): 1687–1693.

Li GL. 2005. Annals of Saihanwula Nature Reserve. Chifeng: Inner Mongolia Science and Technology Press. (in Chinese)

Li M, Meng S, Wei F, Wang J, Yong Y. 2003. Genetic diversity and population genetic structure of takin (*Budorcas taxicolor*). *Acta Theriologica Sinica*, **23**(1): 10–16. (in Chinese)

Librado P, Rozas J. 2009. DnaSP v5: a software for comprehensive analysis of DNA polymorphism data. *Bioinformatics*, **25**(11): 1451–1452.

Lindström J, Coulson T, Kruuk L, Forchhammer MC, Coltman DW, Clutton-Brock T. 2002. Sex-ratio variation in Soay sheep. *Behavioral Ecology and Sociobiology*, **53**(1): 25–30.

Liu F, Li DQ, Wu JG. 2012. Using infra-red cameras to survey wildlife in Beijing Songshan National Nature Reserve. *Acta Ecologica Sinica*, **32**(3): 730–739. (in Chinese)

Liu W, Yao YF, Yu Q, Ni QY, Zhang MW, Yang JD, Mai MM, Xu HL. 2013. Genetic variation and phylogenetic relationship between three serow species of the genus *Capricornis* based on the complete mitochondrial DNA control region sequences. *Molecular Biology Reports*, **40**(12): 6793–6802.

Majumder A, Qureshi Q, Sankar K, Kumar A. 2017. Long-term monitoring of a Bengal tiger (*Panthera tigris tigris*) population in a human-dominated landscape of Central India. *European Journal of Wildlife Research*, **63**: 17.

Mead JI. 1989. *Nemorhaedus goral*. *Mammalian Species*, **335**: 1–5.

Mondol S, Karanth KU, Kumar NS, Gopalaswamy AM, Andheria A, Ramakrishnan U. 2009. Evaluation of non-invasive genetic sampling methods for estimating tiger population size. *Biological Conservation*, **142**(10): 2350–2360.

Nei M. 1987. *Molecular Evolutionary Genetics*. New York: Columbia University Press.

Neigel JE, Avise JC. 1993. Application of a random walk model to geographic distributions of animal mitochondrial DNA variation. *Genetics*, **135**(4): 1209–1220.

Paetkau D, Waits LP, Clarkson PL, Craighead L, Strobeck C. 1997. An empirical evaluation of genetic distance statistics using microsatellite data from bear (*Ursidae*) populations. *Genetics*, **147**(4): 1943–1957.

Peakall R, Smouse PE. 2010. GenAlEx 6.5: genetic analysis in Excel. Population genetic software for teaching and research-an update. *Bioinformatics*, **28**(19): 2537–2539.

Piggott MP, Bellemain E, Taberlet P, Taylor AC. 2004. A multiplex pre-amplification method that significantly improves microsatellite amplification and error rates for faecal DNA in limiting conditions. *Conservation Genetics*, **5**(3): 417–420.

- Scandura M. 2005. Individual sexing and genotyping from blood spots on the snow: a reliable source of DNA for non-invasive genetic surveys. *Conservation Genetics*, **6**(5): 871–874.
- Slatkin M. 1995. A measure of population subdivision based on microsatellite allele frequencies. *Genetics*, **139**(1): 457–462.
- Smith AT, Xie Y. 2008. A guide to the mammals of China. New Jersey: Princeton University Press.
- State Forestry Administration. 2009. Resources survey on national key terrestrial wild animals in China. Beijing: China Forestry Publishing House. (in Chinese)
- Székely T, Weissing FJ, Komdeur J. 2014. Adult sex ratio variation: implications for breeding system evolution. *Journal of Evolutionary Biology*, **27**(8): 1500–1512.
- Taberlet P, Griffin S, Goossens B, Questiau S, Manceau V, Escaravage N, Waits LP, Bouvet J. 1996. Reliable genotyping of samples with very low DNA quantities using PCR. *Nucleic Acids Research*, **24**(16): 3189–3194.
- Taberlet P, Waits LP, Luikart G. 1999. Noninvasive genetic sampling: look before you leap. *Trends in Ecology & Evolution*, **14**(8): 323–327.
- Tajima F. 1989. Statistical method for testing the neutral mutation hypothesis by DNA polymorphism. *Genetics*, **123**(3): 585–595.
- Tamura K, Peterson D, Peterson N, Stecher G, Nei M, Kumar S. 2011. MEGA5: molecular evolutionary genetics analysis using maximum likelihood, evolutionary distance, and maximum parsimony methods. *Molecular Biology & Evolution*, **28**(10): 2731–2739.
- Tang SP, Mu LG, Wang XL, Zhang J, Liu B, Menghedalai, Bao WD. 2019. Habitat suitability assessment based on MaxEnt modeling of Chinese goral in Saihanwula national nature reserve, Inner Mongolia of northern China. *Journal of Beijing Forestry University*, **41**(1): 102–108. (in Chinese)
- Van Oosterhout C, Hutchinson WF, Wills DP, Shipley P. 2004. MICRO-CHECKER: software for identifying and correcting genotyping errors in microsatellite data. *Molecular Ecology Notes*, **4**: 535–538.
- Waits LP, Luikart G, Taberlet P. 2001. Estimating the probability of identity among genotypes in natural populations: cautions and guidelines. *Molecular Ecology*, **10**(1): 249–256.
- Wang XM, Cao LR, Liu ZS, Fang SG. 2006. Mitochondrial DNA variation and matrilineal structure in blue sheep populations of Helan Mountain, China. *Canadian Journal of Zoology*, **84**(10): 1431–1439.
- Xiong Z, Chen M, Zhang E, Huang MJ. 2013. Molecular phylogeny and taxonomic status of the red goral by cyt b gene analyses. *Folia Zoologica*, **62**(2): 125–129.
- Zhang YS, Jiang WJ, Jiang J, Wang D, Wu JG, Liu FM, Bao WD. 2017. Biodiversity monitoring of undergrowth birds and mammals in Beijing Songshan National Nature Reserve. *Chinese Journal of Wildlife*, **38**(3): 367–375. (in Chinese)
- Zhang W, Zhang Z, Xu X, Wei K, Wang X, Liang X, Zhang L, Shen FJ, Hou R, Yue BS. 2009. A new method for DNA extraction from feces and hair shafts of the South China tiger (*Panthera tigris amoyensis*). *Zoo Biology*, **28**(1): 49–58.

Postural effect on manual laterality during grooming in northern white-cheeked gibbons (*Nomascus leucogenys*)

Da-Peng Zhao^{1,*}, Bo-Song Li¹, Bao-Guo Li^{2,3}

¹ Tianjin Key Laboratory of Animal and Plant Resistance, College of Life Sciences, Tianjin Normal University, Tianjin 300387, China

² Shaanxi Key Laboratory for Animal Conservation, College of Life Sciences, Northwest University, Xi'an Shaanxi 710069, China

³ Center for Excellence in Animal Evolution and Genetics, Chinese Academy of Sciences, Kunming Yunnan 650223, China

ABSTRACT

Investigations on manual laterality in non-human primates can help clarify human evolutionary origins of hand preference and cerebral cognition. Although body posture can influence primate hand preference, investigations on how posture affects hylobatid manual laterality are still in their infancy. This study focused on how spontaneous bipedal behavioral tasks affect hand preference in Hylobatidae. Ten captive northern white-cheeked gibbons (*Nomascus leucogenys*) were chosen as focal subjects. Unimanual grooming during sitting posture and supported bipedal posture were applied as behavioral tasks. The gibbons displayed a modest tendency on left-hand preference during sitting posture and right-hand preference during supported bipedal posture, although no group-level hand preference was detected for either posture. From the sitting to supported bipedal posture, 70% of individuals displayed different degrees of right-side deviation trends. The strength of manual laterality in the supported bipedal posture was higher than that in the sitting posture. We found significant sex differences in manual laterality during supported bipedal posture but not during sitting posture. Thus,

to a certain degree, bipedal posture in *N. leucogenys* facilitates stronger hand preference, elicits a rightward trend in manual laterality, and produces sex-specific hand preference.

Keywords: Grooming; Hand preference; Hylobatidae; Posture

INTRODUCTION

Traditionally, hand preference was viewed as unique to humans (Corballis, 2002; Marchant & McGrew, 1998; Porac & Coren, 1981). However, increasing evidence shows that hand preference is common across vertebrates, including the primate order (Fagot & Vauclair, 1991; Vallortigara & Rogers, 2005; Ward & Hopkins, 1993; Zhao et al., 2016a, 2016b). Considering that behavioral lateralization is an observable measure of hemispheric functional asymmetry (Levy, 1977; Rogers, 2014), intensive studies on hand preference in non-human primates based on phylogenetic relationships can help reveal the evolutionary origins of human hand preference and cerebral cognition (Hopkins, 2007; Rogers et al., 2013; Salva et al., 2012; Wiper, 2017). Many factors (e.g., body posture, task complexity, tool use, emotion, division of labor in hand usage) can influence primate manual laterality, with various evolutionary theories proposed for primate evolution of hand preference (Hopkins, 2007; Leliveld et al., 2013; Mangalam et

Open Access

This is an open-access article distributed under the terms of the Creative Commons Attribution Non-Commercial License (<http://creativecommons.org/licenses/by-nc/4.0/>), which permits unrestricted non-commercial use, distribution, and reproduction in any medium, provided the original work is properly cited.

Copyright ©2019 Editorial Office of Zoological Research, Kunming Institute of Zoology, Chinese Academy of Sciences

Received: 21 January 2019; Accepted: 10 July 2019; Online: 23 July 2019

Foundation items: This study was supported by the National Natural Science Foundation of China (31200293, 31730104, 31772468)

*Corresponding author, E-mail: zdp_0609@163.com; skyzdp@tjnu.edu.cn

DOI: 10.24272/j.issn.2095-8137.2019.059

al., 2015; Rogers & Andrew, 2002; Versace & Vallortigara, 2015; Zhao et al., 2015, 2016a, 2016b).

Regarding body posture, the postural origin hypothesis states that (1) arboreal primates prefer using the right hand to support the body in trees and the left hand for manual tasks, whereas (2) more terrestrial primates prefer using the right hand during manual tasks (MacNeillage et al., 1987; MacNeillage, 1991). Increasing primate research lends support to the postural origin hypothesis (MacNeillage, 2007; MacNeillage et al., 2009). For example, with regard to spontaneous bimanual grooming and experimental tube tasks, chimpanzees (*Pan troglodytes*) show group-level right-hand preference (Hopkins, 2007; Hopkins et al., 2007), whereas Sichuan snub-nosed monkeys (*Rhinopithecus roxellana*) display group-level left-hand preference (Zhao et al., 2010, 2012). Furthermore, upright or bipedal posture can facilitate greater expression of primate hand preference toward the right or left side (e.g., prosimians: Sanford et al., 1984; Shaw et al., 2004; New World monkeys: Hashimoto et al., 2013; Roney & King, 1993; Old World monkeys: Blois-Heulin et al., 2007; Zhao et al., 2008a; apes: Braccini et al., 2010; Hopkins et al., 1993).

The small apes (family Hylobatidae) consist of the highly arboreal siamangs and gibbons, and are a crucial link connecting monkeys and great apes on the primate evolutionary branch (Guan et al., 2018). Among the increasing number of studies on primate hand preference, the Hylobatidae remain poorly researched (e.g., Heestand, 1987; Olson et al., 1990; Redmond & Lamperez, 2004; Stafford et al., 1990), with fewer than 10 hylobatid laterality studies conducted to date (Table 1). For the small apes, previous findings show that the direction and strength of manual laterality is both species- and task-specific (Table 1), with hylobatids showing stronger hand preference in complex tasks compared with simple tasks (e.g., *Symphalangus syndactylus*: Morino et al., 2017). To date, however, research on how posture affects hylobatid hand preference is still in its infancy, with only one relevant study addressing this topic using experimental bipedal reaching tasks (Olson et al., 1990) (Table 1).

The present study focused on how spontaneous bipedal behavioral tasks influence hand preference in northern white-cheeked gibbons (*Nomascus leucogenys*). We chose unimanual grooming during sitting posture and supported bipedal posture as the measured tasks because these behaviors are common in primates, especially arboreal species, thus facilitating interspecies comparison. As northern white-cheeked gibbons are a highly arboreal species, and based on the posture origin theory, we predicted that these gibbons will show a left-hand bias under any posture. As bipedal posture is reported to induce a right-side shift in hand preference in great apes (Braccini et al., 2010; Hopkins, 1993), we also predicted that the direction of hand preference would generally present a rightward trend from the sitting to supported bipedal posture.

MATERIALS AND METHODS

Study subjects

The focal subjects were 10 captive northern white-cheeked gibbons, which included five males (age range: 4–27; mean age \pm SE: 15.40 \pm 4.20 years) and five females (age range: 4–26; mean age \pm SE: 16.00 \pm 4.39 years). These gibbons lived in different enclosures at Tianjin Zoo and Beijing Zoo in China (Table 2). Zookeepers provided food (e.g., vegetables, fruits) once a day and water *ad libitum*.

We followed all applicable international and Chinese guidelines for the care and use of animals in this study. The academic committee at the College of Life Sciences, Tianjin Normal University of China approved all study procedures.

Behavioral observations

Unimanual grooming in the sitting posture was defined as grooming with one hand, with the other hand placed on the hindlimbs or grasping a branch/rope for support while sitting on the ground or a branch. Unimanual grooming in the supported bipedal posture was defined as grooming with one hand, with the other hand grasping a branch/rope for support while standing bipedally on the ground or a branch.

We collected data from March to June 2016 based on the methods described by Hopkins et al. (2007) and Zhao et al. (2010). The observation time for each study day was from 1000 h to 1500 h. We chose one gibbon subject randomly at a time when it was performing unimanual grooming. Once we identified the focal individual, we recorded data in 5 min observation periods with 10 s sampling intervals. We recorded both hand use (left or right) and mouth use (involved or not involved) in grooming at each sampling point. We excluded unimanual grooming involving the mouth from statistical analyses to avoid the potential effect of mouth use on manual laterality.

If the gibbon stopped unimanual grooming within the 5 min observation period and did not perform unimanual grooming within the following 30 s, observation on that individual was ended and we chose another gibbon based on the method mentioned above. If the gibbon continued unimanual grooming after the 5 min observation period, and no other subjects were observed performing unimanual grooming within visible distance, we continued a new 5 min observation period for the same gibbon. When multiple subjects performed unimanual grooming simultaneously, we chose the closest visible subject. If two subjects were at a similar distance from the observer, we chose the gibbon with less sampling data.

Data analysis

Statistical analyses were conducted on both individual-level and group-level hand preference. We assessed manual laterality at the individual level by the handedness index (HI) and z scores (Hopkins, 1999, 2013). We calculated HI scores based on the following formula: (right-hand use–left-hand use)/(right-hand use+left-hand use) (Hopkins, 1999). The HI scores ranged from –1.0 to 1.0. Positive and negative HI scores represented right- and left-hand preference, respectively. The

Table 1 Previous research on Hylobatidae manual laterality

Species	Condition	Number	Task	Main finding	Reference
<i>Symphalangus syndactylus</i>	Captive	13	Food reaching	(1) No individual was left- or right-handed; (2) No group-level handedness	Heestand, 1987
<i>Hylobates lar</i>	Captive	8	Floor retrieval	(1) Six individuals were left-handed, two individuals were right-handed based on chi-square analyses; (2) No group-level handedness	Olson et al., 1990
<i>H. lar</i>	Captive	6	Mesh retrieval	(1) All individuals were left-handed based on chi-square analyses; (2) Group-level right handedness was found	Olson et al., 1990
<i>H. concolor</i> , <i>H. lar</i> , <i>S. syndactylus</i>	Captive	19	Food reaching	(1) <i>H. concolor</i> , one individual was left-handed, three individuals were right-handed, three individuals were ambipreferent based on z scores; (2) <i>H. lar</i> , one individual was left-handed, three individuals were right-handed based on z scores; (3) <i>S. syndactylus</i> , two individuals were left-handed, three individuals were right-handed, three individuals were ambipreferent based on z scores; (4) No group-level hand preference was conducted for any species, and there was no group-level handedness for the mixed sample; (5) Adults showed stronger hand preference than immature individuals.	Stafford et al., 1990
<i>S. syndactylus</i>	Captive and semi-natural	25	Leading limb during brachiation	(1) For vocal condition, one individual was left-handed, two individuals were right-handed based on z scores; (2) For non-vocal condition, two individuals were left-handed, three individuals were right-handed based on z scores; (3) No group-level handedness was found for vocal and non-vocal conditions.	Redmond & Lamperez, 2004
<i>Nomascus leucogenys</i> , <i>N. gabriellae</i>	Captive	16	Leading limb during brachiation	(1) Two individuals were left-handed, five individuals were right-handed, and nine individuals were ambipreferent based on ABS-HI >0.20 scores; (2) No group-level handedness was found.	Barker, 2008
<i>S. syndactylus</i>	Wild	49	Water collecting	(1) When testing individuals with >6 data points, 22 individuals were left-handed, 10 individuals were right-handed, and four individuals were ambipreferent based on z scores, (2) Group-level left handedness was found.	Morino, 2011
<i>H. agillis</i> , <i>H. albibarbis</i> , <i>H. agillis</i> × <i>H. albibarbis</i> , <i>H. lar</i> , <i>H. muelleri</i> , <i>H. pileatus</i> , <i>N. leucogenys</i> , <i>S. syndactylus</i>	Captive	42	Tube task	(1) When testing individuals with >6 data points, for siamangs, 10 individuals were left-handed, two individuals were right-handed, and eight individuals were ambipreferent based on z scores; for mixed gibbon species, 10 individuals were left-handed, seven individuals were right-handed based on z scores; (2) Group-level left handedness was found in siamangs whereas no group-level handedness was found in mixed gibbon samples.	Morino et al., 2017
<i>N. leucogenys</i>	Captive	9	Ground reaching; Box task; Tube task	(1) For ground-reaching task, three individuals were left-handed, one individual was right-handed, and five individuals were ambipreferent based on chi-square analyses; (2) For box task, three individuals were left-handed, three individuals were right-handed, and three individuals were ambipreferent based on chi-square analyses; (3) For box task, three individuals were left-handed, four individuals were right-handed, and two individuals were ambipreferent based on chi-square analyses; (4) No group-level handedness was found for any task	Fan et al., 2017

absolute value of HI scores (ABS-HI) represented hand preference strength. We calculated z scores using frequency of left- and right-hand use. We considered individuals as left-handed ($z \leq -1.96$), right-handed ($z \geq 1.96$), or ambipreferent ($-1.96 < z < 1.96$) based on z scores. Furthermore, we used binomial tests for each subject for both postures and combined the probabilities from separate significance tests (Gibbs et al., 2007; Jones & Fiske, 1953; Zhao et al., 2016b). We assessed manual laterality at the group level by one-sample tests based on individual HI scores (Hopkins, 1999;

Zhao et al., 2012).

We applied Mann-Whitney U tests to examine sex differences in hand preference under different postures. We adopted repeated measures analysis of variance (ANOVA) (independent variable: postural conditions; dependent variable: HI/ABS-HI values) and non-parametric Wilcoxon signed ranks test to explore the postural effect on the direction and strength of manual laterality (Braccini et al., 2010). All statistical analyses were performed using SPSS v21.0, with significance at $P \leq 0.05$.

RESULTS

In the present study, there were no significant correlations between the number of observations per individual and HI values (sitting: $r=0.185$, $P=0.608$; standing: $r=0.260$, $P=0.467$) and ABS-HI values (sitting: $r=-0.172$, $P=0.635$; standing: $r=-0.473$, $P=0.167$). This suggests that individual differences in the total number of responses did not skew the distribution of handedness values.

Individual-level manual laterality

For the sitting posture, the HI and ABS-HI scores (mean \pm SE) were -0.009 ± 0.057 and 0.123 ± 0.039 , respectively. From the HI scores, we identified six gibbons as left-handed, three gibbons as right-handed, and one gibbon as ambipreferent (Table 2). From the binomial tests and z scores, we identified one gibbon as left-handed, two gibbons as right-handed, and seven gibbons as ambipreferent (Table 2).

For the supported bipedal posture, the HI and ABS-HI

scores (mean \pm SE) were 0.035 ± 0.093 and 0.187 ± 0.070 , respectively. From the HI scores, three gibbons were left-handed and seven gibbons were right-handed (Table 2). From the binomial tests and z scores, one gibbon was left-handed, one gibbon was right-handed, and eight gibbons were ambipreferent (Table 2).

For sitting to supported bipedal posture, based on HI scores, 60% of gibbons showed identical manual laterality (right-handed: one male and two females, left-handed: three females) and 40% showed varying degrees of right-side deviation from sitting to standing posture (four males). Based on the direction (i.e., HI values) and strength (i.e., ABS-HI values) of hand preference, 70% of gibbons showed varying degrees of right-side deviation (from negative and zero HI values to positive HI values: four males; increase in positive HI values: one female; decrease in negative HI values: two females) and 30% of gibbons showed varying degrees of left-side deviation (decrease in positive HI values: one male and one female; increase in negative HI scores: one female).

Table 2 Basic information on hand preference for unimanual grooming for each posture

Subject	Source	Gender	Age	Sitting posture					Supported bipedal posture				
				Left	Right	HI	z score	P score	Left	Right	HI	z score	P score
Beib	Beijing Zoo	Male	23	48	72	0.20	2.19	0.035	50	64	0.12	1.31	0.769
Caic	Beijing Zoo	Female	4	49	64	0.13	1.41	0.188	43	60	0.17	1.68	0.114
Hengh	Beijing Zoo	Female	26	50	81	0.24	2.71	0.009	84	88	0.02	0.30	0.819
Jingj	Beijing Zoo	Female	21	54	46	-0.08	-0.80	0.484	52	49	-0.03	-0.30	0.842
Qingq	Tianjin Zoo	Male	12	8	8	0.00	0.00	1.000	44	99	0.38	4.60	<0.001
Xiaoh	Beijing Zoo	Male	27	67	63	-0.03	-0.35	0.793	57	60	0.03	0.28	0.835
Xiaoz	Beijing Zoo	Male	4	99	88	-0.06	-0.80	0.465	66	81	0.10	1.24	0.248
Yuany	Tianjin Zoo	Male	11	106	100	-0.03	-0.42	0.728	11	20	0.29	1.62	0.150
Yuey	Tianjin Zoo	Female	22	51	22	-0.40	-3.39	0.001	54	9	-0.71	-5.67	<0.001
Ziye	Beijing Zoo	Female	7	55	49	-0.06	-0.59	0.624	52	50	-0.02	-0.20	0.921

Left: Frequency of left-hand use; Right: Frequency of right-hand use.

Group-level manual laterality

No group-level hand preference was detected during unimanual grooming for either posture (sitting posture: $t_9=-0.159$, $P=0.877$; supported bipedal posture: $t_9=0.377$, $P=0.715$). For hand use, however, the deviation from random distribution was significant for both postures (sitting posture: summed $\chi^2=38.309$, $df=20$, $P<0.01$; supported bipedal posture: summed $\chi^2=49.562$, $df=20$, $P<0.01$). Considering the mean HI scores for each posture, we found that the gibbons displayed a modest trend towards left-hand use bias during sitting posture and right-hand use bias during supported bipedal posture.

Sex differences

For the sitting posture, we found no significant sex differences in manual laterality (direction: $N_1=5$, $N_2=5$, $U=9.50$, $z=-0.631$, $P=0.528$; strength: $N_1=5$, $N_2=5$, $U=3.50$, $z=-1.892$, $P=0.059$). For the supported bipedal posture, however, significant sex differences were found for direction of hand preference ($N_1=5$,

$N_2=5$, $U=3.00$, $z=-1.984$, $P=0.047$) rather than strength of hand preference ($N_1=5$, $N_2=5$, $U=8.50$, $z=-0.841$, $P=0.401$).

Postural effect

Repeated measures ANOVA indicated no postural effect on manual laterality (direction: $F_{1,9}=0.422$, $P=0.532$; strength: $F_{1,9}=1.120$, $P=0.318$). Non-parametric Wilcoxon signed rank test showed the same result (direction: $z=-0.765$, $P=0.444$; strength: $z=-0.654$, $P=0.513$).

DISCUSSION

We investigated postural influence on manual laterality during spontaneous bipedal tasks in *N. leucogenys*, with the following important results: (1) there was a modest left-hand preference tendency in the sitting posture and a modest right-hand preference tendency in the supported bipedal posture, although group-level hand preference was not found for either posture; (2) from sitting to supported bipedal posture, based

on HI/ABS-HI values, 70% of individuals showed varying degrees of right-side deviation and 30% of individuals showed varying degrees of left-side deviation; (3) strength of hand preference during the supported bipedal posture was higher than that during the sitting posture; (4) significant sex differences in the direction of hand preference were found during supported bipedal posture but not during sitting posture.

Because of our limited sample size, general conclusions based on the present study should be treated with some caution due to potential statistical effects from the obtained data. For both postures, however, no significant correlation was detected between the number of observations per individual and HI/ABS-HI values. This suggests that individual differences in the amount of data collected did not affect the distribution of handedness values, and our findings on *N. leucogenys* can be considered valid.

For the unimanual grooming task, group-level hand preference was not found for either posture. Together with previous findings in the same species, which also showed no group-level hand preference for ground-reaching, tube, and box tasks (Fan et al., 2017), it suggest that neither simple nor complex tasks elicit group-level hand preference, regardless of posture and task spontaneity. This may be the result of selective pressures acting on this arboreal species; however, further research with a larger sample size is required to explore this question.

Hand preference during grooming has been investigated among various primate species (*P. paniscus*: Brand et al., 2017; *P. troglodytes*: Boesch, 1991; Marchant & McGrew, 1996; McGrew & Marchant, 2001; Hopkins et al., 2007; *R. roxellana*: Zhao et al., 2010). Unimanual grooming is a simple behavioral task performed in primates. Consistently, however, no group-level hand preference has been found during unimanual grooming among any tested species (e.g., Zhao et al., 2010). Compared with unimanual grooming, bimanual grooming is considered a complex behavioral task, with previous studies showing both group-level hand preference and stronger hand preference compared with unimanual grooming (Hopkins et al., 2007; Zhao et al., 2010). However, interspecific and intraspecific differences have been reported. For instance, group-level hand preference during bimanual grooming has been found in Sichuan snub-nosed monkeys (Zhao et al., 2010) but not in bonobos (*P. paniscus*) (Brand et al., 2017). For chimpanzees, group-level hand preference during bimanual grooming was found by Hopkins et al. (2007) but not by McGrew & Marchant (2001). For *N. leucogenys*, we found no group-level hand preference during unimanual grooming for either posture, consistent with previous findings in other primate species and, to some extent, supporting the task complexity hypothesis that strong preferences and group-level biases in manual laterality are more likely to appear in complex rather than simple tasks (Fagot & Vaucelai, 1991).

For the sitting posture, we found a modest tendency towards left-hand use for unimanual grooming in *N. leucogenys*. Given that *N. leucogenys* is an arboreal species, this finding agrees, to a certain extent, with the postural origin theory that arboreal species are apt to use the left hand for

manual behaviors when maintaining a quadrupedal or sitting posture in trees (MacNeillage et al., 1987; MacNeillage, 1991, 2007).

With regard to the postural effect on the direction of manual laterality, from sitting to supported bipedal posture, the general laterality tendency for hand preference in *N. leucogenys* shifted from left-hand use to right-hand use, with 70% of individuals displaying varying degrees of right-side deviation based on HI/ABS-HI values. This rightward effect on bipedal posture for *N. leucogenys* agrees with previous findings in great ape species (*Gorilla gorilla*: Olson et al., 1990; *P. paniscus*: Hopkins et al., 1993; except Vleeschouwer et al., 1995; *P. troglodytes*: Braccini et al., 2010; Hopkins, 1993; *Pongo pygmaeus*: Hopkins, 1993) and some monkey species (e.g., *Cebus apella*: Westergaard et al., 1998a; *Lophocebus albigena*: Blois-Heulin et al., 2007; *Macaca mulatta*: Westergaard et al., 1998b), but contrasts to several findings on leftward laterality trends (e.g., *Galago senegalensis*: Sanford et al., 1984; *H. lar*: Olson et al., 1990; *Saimiri sciureus*: King & Landau, 1993). These consistencies and inconsistencies on the postural effect on primate hand preference may be associated with species-specific foraging types (arboreal/terrestrial), bipedal posture habit (frequent/less), and task-specific demands (simple/complex, unimanual/bimanual) (Hanson et al., 2017; Hashimoto et al., 2013; Hopkins, 1993). For instance, the uniformity of the rightward laterality trend in bipedal posture for *N. leucogenys* and all great apes (Braccini et al., 2010; Hopkins, 1993; Hopkins et al., 1993; Olson et al., 1990) suggests that bipedalism may play a crucial role in driving the evolution of primate right handedness (Hopkins, 2007). In addition, while *N. leucogenys* showed a modest tendency towards right-hand use in unimanual grooming during bipedal posture, the lar gibbon (*H. lar*) has been reported to display group-level left handedness in a mesh retrieval task during bipedal posture (Olson et al., 1990). This disparity in manual laterality trends between two gibbon species could be a consequence of task-specific demands, which may require special manual operation of the lateralized brain (Hashimoto et al., 2013; Rogers et al., 2013).

In regard to the postural effect on strength of manual laterality, based on mean ABS-HI scores, *N. leucogenys* displayed a stronger hand preference during supported bipedal posture than during sitting posture, although there was no significant difference between the two postures. This finding to some extent supports current research suggesting that upright or bipedal postures may facilitate greater expression of primate hand preference (Hook-Costigan & Rogers, 1996; Hopkins, 1993; Roney & King, 1993; Westergaard et al., 1998a). For example, hand preference during both unsupported and supported bipedal posture is significantly greater than that during seated posture in chimpanzees (Braccini et al., 2010).

The northern white-cheeked gibbon is a monogamous species, with females bearing more breeding tasks than males (Bleisch et al., 2008; Fan, 2017). This suggests that, compared with males, females should spend more time in trees taking care of the next generation, which would partly

restrict the frequency of bipedal posture during foraging and movement. Sex differences in bipedal posture may drive sex-specific hand preference in response to the postural effect (i. e., from quadrupedal or sitting posture to bipedal posture). The present study preliminarily confirmed this viewpoint: (1) a significant sex difference in hand preference was found in bipedal posture but not in sitting posture; and, (2) in unimanual grooming during bipedal posture, all males showed right-handedness whereas three of the five females showed left-handedness. These results indicate that bipedal posture produces sex-specific manual laterality in this gibbon species.

In the current study, we focused on how posture affects hand preference in spontaneous behavioral tasks in northern white-cheeked gibbons. Results indicated that, to a certain degree, bipedal posture facilitated stronger hand preference, elicited a rightward trend in manual laterality, and exhibited sex-specific hand preference. Further comprehensive study exploring the effect of body posture on different behavioral tasks (e. g., foraging, grooming) under varying postures is required to further test the postural origin hypothesis in this species. In addition, future research should introduce more Hylobatidae species with larger sample size to clarify the postural effect on primate handedness evolution. The postural effect on both hand preference and foot preference in this species as well other non-human primates under natural conditions should also be studied (e.g., Zhao et al., 2008b).

COMPETING INTERESTS

The authors declare that they have no competing interests.

AUTHORS' CONTRIBUTIONS

D.P.Z. and B.G.L. conceived and designed the study. B.S.L. collected the data. D.P.Z. and B.S.L. analyzed the data. D.P.Z. wrote the manuscript. All authors read and approved the final version of the manuscript.

ACKNOWLEDGEMENTS

We thank Prof. Joanna M. Setchell for her valuable comments on the earlier manuscript. We are grateful to the staff of Tianjin Zoo and Beijing Zoo as well as Dr. Peng-Lai Fan for their friendly support.

REFERENCES

Barker MK. 2008. Gibbon hand preference studies at the endangered primate rescue center, Vietnam. *Vietnamese Journal of Primatology*, **2**(1): 41–45.

Bleisch B, Geissmann T, Manh Ha N, Rawson B, Timmins RJ. 2008. *Nomascus leucogenys*. The IUCN Red List of Species 2008, e. T39895A10272040. [http://dx. doi. org/10.2305/IUCN. UK. 2008. RLTS. T39895A10272040.en](http://dx.doi.org/10.2305/IUCN.UK.2008.RLTS.T39895A10272040.en). Downloaded on 18 May 2018.

Blois-Heulin C, Bernard V, Bec P. 2007. Postural effect on manual laterality in different tasks in captive grey-cheeked mangabey (*Lophocebus albigena*). *Journal of Comparative Psychology*, **121**(2): 205–213.

Boesch C. 1991. Handedness in wild chimpanzees. *International Journal of*

Primatology, **12**(6): 541–558.

Braccini S, Lambeth S, Schapiro S, Fitch WT. 2010. Bipedal tool use strengthens chimpanzee hand preference. *Journal of Human Evolution*, **58**(3): 234–241.

Brand CM, Marchant LF, Boose KJ, White FJ, Rood TM, Meinelt A. 2017. Laterality of grooming and tool use in a group of captive bonobos (*Pan paniscus*). *Folia Primatologica*, **88**(2):210–222.

Corballis MC. 2002. From Hand to Mouth: The Origins of Language. Princeton: Princeton University Press.

Fagot J, Vauclair J. 1991. Manual laterality in nonhuman primates: a distinction between handedness and manual specialization. *Psychological Bulletin*, **109**(1): 76–89.

Fan PF. 2017. The past, present, and future of gibbons in China. *Biological Conservation*, **210**(S1): 29–39.

Fan PL, Liu CY, Chen HY, Liu XF, Zhao DP, Zhang JG, Liu DZ. 2017. Preliminary study on hand preference in captive northern white-cheeked gibbons (*Nomascus leucogenys*). *Primates*, **58**(1): 75–82.

Gibbs SEB, Lea SEG, Jacobs LF. 2007. Flexible use of spatial cues in the southern flying squirrel (*Glaucomys volans*). *Animal Cognition*, **10**(2): 203–209.

Guan ZH, Ma CY, Fei HL, Huang B, Ning WH, Ni QY, Jiang XL, Fan PF. 2018. Ecology and social system of northern gibbons living in cold seasonal forests. *Zoological Research*, **39**(4): 255–265.

Hanson NKI, Thorpe SKS, Chappell J. 2017. Arboreal postures elicit hand preference when accessing a hard-to-reach foraging device in captive bonobos (*Pan paniscus*). *International Journal of Primatology*, **38**(4): 717–731.

Hashimoto T, Yamazaki Y, Iriki A. 2013. Hand preference depends on posture in common marmosets. *Behavioural Brain Research*, **248**: 144–150.

Heestand JE. 1987. Behavioral Lateralization in Four Species of Apes?. Ph. D. dissertation, Seattle: University of Washington.

Hook-Costigan MA, Rogers LJ. 1996. Hand preference in New World primates. *International Journal of Comparative Psychology*, **9**(4): 173–207.

Hopkins WD. 1993. Posture and reaching in chimpanzees (*Pan troglodytes*) and orangutans (*Pongo pygmaeus*). *Journal of Comparative Psychology*, **107**(2): 162–168.

Hopkins WD. 1999. On the other hand: statistical issues in the assessment and interpretation of hand preference data in nonhuman primates. *International Journal of Primatology*, **20**(6): 851–866.

Hopkins WD. 2007. The Evolution of Hemispheric Specialization in Primates. San Diego: Academic Press.

Hopkins WD. 2013. Comparing human and nonhuman primate handedness: challenges and a modest proposal for consensus. *Developmental Psychobiology*, **55**(6): 621–636.

Hopkins WD, Bennett A, Bales SL, Lee J, Ward JP. 1993. Behavioral laterality in captive bonobos (*Pan paniscus*). *Journal of Comparative Psychology*, **107**(4):403–410.

Hopkins WD, Russell JL, Remkus M, Freeman H, Schapiro SJ. 2007. Handedness and grooming in *Pan troglodytes*: comparative analysis between findings in captive and wild individual. *International Journal of Primatology*, **28**(6): 1315–1326.

Jones LV, Fiske DW. 1953. Models for testing the significance of combined results. *Psychological Bulletin*, **50**(5): 375–382.

King JE, Landau VI. 1993. Manual preference in varieties of reaching in squirrel monkeys. In: Ward JP, Hopkins WD. Primate Laterality: Current

- Behavioral Evidence of Primate Asymmetries. New York: Springer, 107–124.
- Leliveld LMC, Langbein J, Puppe B. 2013. The emergence of emotional lateralization: evidence in non-human vertebrates and implications for farm animals. *Applied Animal Behaviour Science*, **145**(1–2): 1–14.
- Levy J. 1977. The mammalian brain and the adaptive advantage of cerebral asymmetry. *Annals of the New York Academy of Sciences*, **299**(1): 264–272.
- MacNeilage PF. 1991. The “postural origins” theory of primate neurobiological asymmetries. In: Krasnegor NA, Rumbaugh DM, Schiefbusch RL. Biological and Behavioral Determinants of Language Development. New Jersey: Lawrence Erlbaum Associates, 165–188.
- MacNeilage PF. 2007. Present status of the postural origins theory. In: Hopkins WD. The Evolution of Hemispheric Specialization in Primates. San Diego: Academic Press, 59–91.
- MacNeilage PF, Studdert-Kennedy MG, Lindblom B. 1987. Primate handedness reconsidered. *Behavior and Brain Sciences*, **10**(2): 247–263.
- MacNeilage PF, Rogers LJ, Vallortigara G. 2009. Origins of the left & right brain. *Scientific American*, **301**(1): 60–67.
- Mangalam M, Desai N, Singh M. 2015. Division of labor in hand usage is associated with higher hand performance in free-ranging bonnet macaques, *Macaca radiata*. *PLoS One*, **10**(3): e0119337.
- Marchant LF, McGrew WC. 1996. Laterality of limb function in wild chimpanzees of Gombe National Park: comprehensive study of spontaneous activities. *Journal of Human Evolution*, **30**(5): 427–443.
- Marchant LF, McGrew WC. 1998. Human handedness: an ethological perspective. *Human Evolution*, **13**(3–4): 221–228.
- McGrew WC, Marchant LF. 2001. Ethological study of manual laterality in the chimpanzees of the Mahale Mountains, Tanzania. *Behaviour*, **138**(3): 329–358.
- Morino L. 2011. Left-hand preference for a complex manual task in a population of wild siamangs (*Symphalangus syndactylus*). *International Journal of Primatology*, **32**(3): 793–800.
- Morino L, Uchikoshi M, Bercovitch F, Hopkins WD, Matsuzawa T. 2017. Tube task hand preference in captive hylobatids. *Primates*, **58**(3): 403–412.
- Olson DA, Ellis JE, Nadler RD. 1990. Hand preferences in captive gorillas, orang-utans and gibbons. *American Journal of Primatology*, **20**(2): 83–94.
- Porac C, Coren S. 1981. Lateral Preferences and Human Behavior. New York: Springer.
- Redmond J, Lamperez A. 2004. Leading limb preference during brachiation in the gibbon family member, *Hylobates syndactylus* (siamangs): a study of the effects of singing on lateralisation. *Laterality*, **9**(4): 381–396.
- Rogers L, Vallortigara G, Andrew RJ. 2013. Divided Brains: The Biology and Behaviour of Brain Asymmetries. New York: Cambridge University Press.
- Rogers LJ. 2014. Asymmetry of brain and behavior in animals: its development, function, and human relevance. *Genesis*, **52**(6): 555–571.
- Rogers LJ, Andrew RJ. 2002. Comparative Vertebrate Lateralization. Cambridge: Cambridge University Press.
- Roney LS, King JE. 1993. Postural effects on manual reaching laterality in squirrel monkeys (*Saimiri sciureus*) and cotton-top tamarins (*Saguinus oedipus*). *Journal of Comparative Psychology*, **107**(4): 380–385.
- Salva OR, Regolin L, Mascalon E, Vallortigara G. 2012. Cerebral and behavioural asymmetries in animal social recognition. *Comparative Cognition & Behavior Reviews*, **7**: 110–138.
- Sanford C, Guin K, Ward JP. 1984. Posture and laterality in the bushbaby (*Galago senegalensis*). *Brain Behavior and Evolution*, **25**(4): 217–224.
- Shaw MC, Wolfe LD, Panger MA. 2004. The potential effects of sex, posture and living condition on lateralized behaviors in ring-tailed lemurs (*Lemur catta*). *Human Evolution*, **19**(2): 113–129.
- Stafford DK, Milliken GW, Ward JP. 1990. Lateral bias in feeding and brachiation in hylobates. *Primates*, **31**(3): 407–414.
- Vallortigara G, Rogers LJ. 2005. Survival with an asymmetrical brain: advantages and disadvantages of cerebral lateralization. *Behavioral and Brain Sciences*, **28**(4): 575–589.
- Versace E, Vallortigara G. 2015. Forelimb preferences in human beings and other species: multiple models for testing hypotheses on lateralization. *Frontiers in Psychology*, **6**: 233.
- Vleeschouwer KD, van Elsacker L, Verheyen RF. 1995. Effect of posture on hand preferences during experimental food reaching in bonobos (*Pan paniscus*). *Journal of Comparative Psychology*, **109**(2): 203–207.
- Ward JP, Hopkins WD. 1993. Primate Laterality: Current Behavioral Evidence of Primate Asymmetries. New York: Springer.
- Westergaard GC, Kuhn HE, Suomi SJ. 1998a. Effects of upright posture on hand preference for reaching vs. the use of probing tools by tufted capuchins (*Cebus apella*). *American Journal of Primatology*, **44**(2): 147–153.
- Westergaard GC, Kuhn HE, Suomi SJ. 1998b. Bipedal posture and hand preference in humans and other primates. *Journal of Comparative Psychology*, **112**(1): 55–64.
- Wiper ML. 2017. Evolutionary and mechanistic drivers of laterality: A review and new synthesis. *Laterality*, **22**(6): 740–770.
- Zhao DP, Ji WH, Watanabe K, Li BG. 2008a. Hand preference during unimanual and bimanual reaching actions in Sichuan snub-nosed monkeys (*Rhinopithecus roxellana*). *American Journal of Primatology*, **70**(5): 500–504.
- Zhao DP, Li BG, Watanabe K. 2008b. First evidence on foot preference during locomotion in Old World monkeys: a study of quadrupedal and bipedal actions in Sichuan snub-nosed monkeys (*Rhinopithecus roxellana*). *Primates*, **49**(4): 260–264.
- Zhao DP, Gao X, Li BG. 2010. Hand preference for spontaneously unimanual and bimanual coordinated tasks in wild Sichuan snub-nosed monkeys: implication for hemispheric specialization. *Behavioural Brain Research*, **208**(1): 85–89.
- Zhao DP, Hopkins WD, Li BG. 2012. Handedness in nature: first evidence on manual laterality on bimanual coordinated tube task in wild primates. *American Journal of Physical Anthropology*, **148**(1): 36–44.
- Zhao DP, Wang Y, Han KJ, Zhang HB, Li BG. 2015. Does target animacy influence manual laterality of monkeys? first answer from northern pig-tailed macaques (*Macaca leonina*). *Animal Cognition*, **18**(4): 931–936.
- Zhao DP, Wang Y, Wei XY. 2016a. Hand preference during bimanual coordinated task in northern pig-tailed macaques *Macaca leonina*. *Current Zoology*, **62**(4): 385–391.
- Zhao DP, Tian XL, Liu XC, Chen ZY, Li BG. 2016b. Effect of target animacy on hand preference in Sichuan snub-nosed monkeys (*Rhinopithecus roxellana*). *Animal Cognition*, **19**(5): 977–985.

A new species of Mountain Dragon (Reptilia: Agamidae: *Diploderma*) from the *D. dymondi* complex in southern Sichuan Province, China

DEAR EDITOR,

Despite continuous studies on the cryptic diversity of the *Diploderma flaviceps* complex in Southwest China for the past decade, little attention has been given to other widespread congeners in China. Combining both morphological and phylogenetic data, we describe a new species of *Diploderma* from populations identified previously as *D. dymondi* in the lower Yalong River Basin in southern Sichuan Province. The new species is morphologically most similar to *D. dymondi* and *D. varcoae*, but it can be differentiated by a considerable genetic divergence and a suite of morphological characters, including having taller nuchal crest scales, smaller tympana, and a distinct oral coloration. Additionally, we discuss other putative species complexes within the genus *Diploderma* in China.

Mountain Dragons of the genus *Diploderma* Hallowell, 1861 were recently resurrected from the paraphyletic genus *Japalura* sensu lato (Wang et al., 2019a). Despite the recent split, *Diploderma* still represents one of the most diverse groups of agamid lizard from Asia, including 25 species recognized currently, with most species found in China (Wang et al., 2019a, 2019b). Although increasing attention has been paid to cryptic diversity within the genus in Southwest China during the past decade, most studies have focused on a single species complex, *D. flaviceps*, only (Manthey et al., 2012; Wang et al., 2015, 2016, 2017, 2019a), with few studies on other congeners that also have widespread distributions. One such example is *D. dymondi* (Boulenger, 1906).

First described from the Jinsha River Valley at Yunnan Fu (= Dongchuan) in northeastern Yunnan Province, *D. dymondi* was first diagnosed by a small set of morphological characters, particularly the presence of exposed tympana

(Boulenger, 1906). Based on this diagnosis, all populations of *Diploderma* in Southwest China with exposed tympana were identified historically as *D. dymondi*, and the species was recorded to have a wide distribution in Southwest China, including along the Nu River (=Salween) Basin in northwestern Yunnan Province (Wu, 1992; Yang & Rao, 2008; Zhao et al., 1999), the lower Jinsha River Basin in northern Yunnan Province and southern Sichuan Province (Boulenger, 1906; Deng & Jiang, 1998; Zhao et al., 1999; Zhao, 2003), the central parts of the Yunnan-Guizhou Plateau (Boulenger, 1906), and the Yalong River Basin in Sichuan Province (Deng & Jiang, 1998; Zhao et al., 1999; Zhao, 2003; Figure 1). However, later taxonomic works revealed distinct species among the populations identified previously as *D. dymondi*, including *D. varcoae* (Boulenger, 1918) from the central Yunnan-Guizhou Plateau and *D. slowinskii* (Rao, Vindum, Ma, Fu, Wilkinson, 2017) from the Nu River Basin in western Yunnan Province. Such discoveries suggest that *D. dymondi*, as currently recognized, represents a complex of unique evolutionary lineages that warrant further investigation. Interestingly, few studies have examined the taxonomic status of several populations of *D. dymondi* across its range (Rao et al., 2017). As different species of *Diploderma* occupy distinct river courses in Southwest China (Manthey et al., 2012; Wang et al., 2019a), it is highly possible that the unexamined populations of *D. dymondi* in different river courses along the Jinsha River represent additional diversity.

Received: 21 August 2019; Accepted: 26 August 2019; Online: 02 September 2019

Foundation items: This research was supported by the Strategic Priority Research Program of Chinese Academy of Sciences (XDA 20050201), National Key Research and Development Program of China (2017YFC0505202), the Second Tibetan Plateau Scientific Expedition and Research (STEP) program (2019QZKK0501), and the Animal Branch of the Germplasm Bank of Wild Species CAS (Large Research Infrastructure Funding) to J. Che; NSF GRFP (2017216966) to K. Wang; and the cooperative program of the State Key Laboratory of Genetic Resources and Evolution, KIZ (GREKF16-12) to C. Siler and J. Che

DOI: 10.24272/j.issn.2095-8137.2019.034

Open Access

This is an open-access article distributed under the terms of the Creative Commons Attribution Non-Commercial License (<http://creativecommons.org/licenses/by-nc/4.0/>), which permits unrestricted non-commercial use, distribution, and reproduction in any medium, provided the original work is properly cited.

Copyright ©2019 Editorial Office of Zoological Research, Kunming Institute of Zoology, Chinese Academy of Sciences

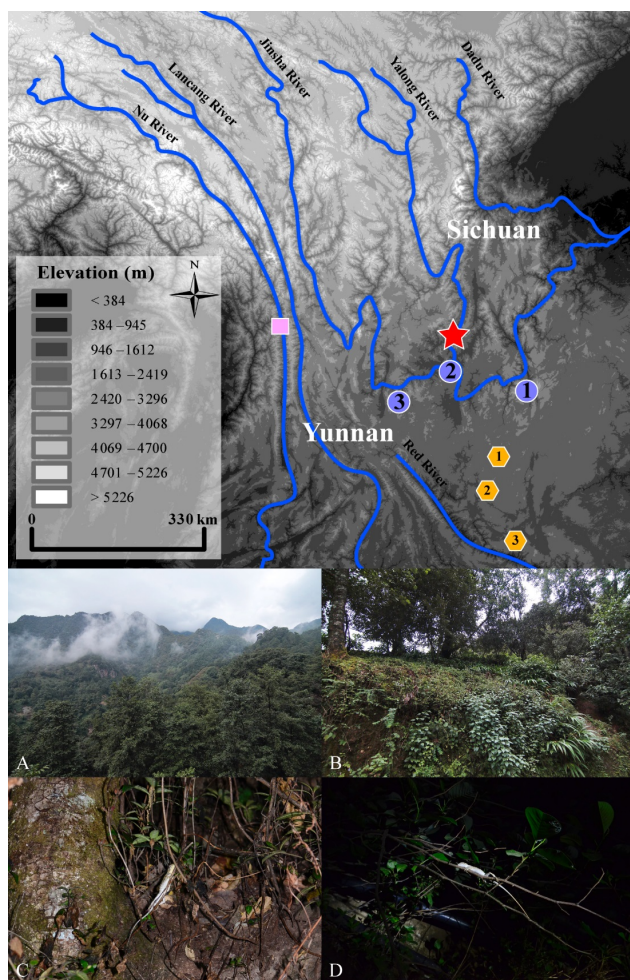


Figure 1 Distribution of *Diploderma dymondi* species complex in Southwest China (top) and macro- (A and B) and micro- (C and D) habitats of *D. swild* sp. nov. (bottom)

Different shapes represent type localities of different species (Star: *Diploderma swild* sp. nov.; Circle: *D. dymondi*; Rectangle: *D. slowinskii*; and Hexagon: *D. varcoae*), where numbered shapes represent additional known localities of each species (circle 1: Panzhihua City, Sichuan Province; circle 2: Dayao, Yunnan; hexagon 1: Yuxi, Yunnan; hexagon 2: Mengzi, Yunnan). Photos of habitats were taken at the type locality. Photos by Kai Wang and Ben-Fu Miao.

During herpetological surveys in southern Sichuan Province from 2017 to 2019, specimens of previously identified *D. dymondi* were collected from the lower Yalong River Basin, a main tributary of the Jinsha River, and a historical specimen of previously identified *D. dymondi* from southern Sichuan Province was examined in the museum collection. As the examined population of *D. cf. dymondi* forms a monophyletic group and possesses considerable genetic distances from closely related congeners based on mitochondrial marker, and given it is also morphologically distinct from all recognized congeners, we here describe this lineage as a new species.

A total of nine specimens of the new species were collected

from Yanbian County, Panzhihua District, southern Sichuan Province, China (Figure 1). In addition to the newly collected specimens, a single specimen of the new species from Xichang, Sichuan Province, and 20 recognized species of congeners from the following natural history museum collections were also examined (Supplementary material (Appendix I)).

Total genomic DNA for the new species was extracted from liver tissues, and the mitochondrial gene NADH dehydrogenase subunit 2 (*ND2*, 1 035 bp (coding region), 182 bp (tRNAs)) was amplified and sequenced by using published primers (Wang et al., 2019a). In addition to the newly generated sequences, genetic data for 18 species of *Diploderma* and representatives of two outgroup genera (*Pseudocalotes* and *Acanthosaura*) were obtained from GenBank (Supplementary Table S1).

To infer the mitochondrial gene tree among sampled congeners, both Bayesian inference (BI) and maximum likelihood (ML) analyses were conducted on the final alignment (Supplementary material (Methods)). To root the resulting mitochondrial gene trees, *Acanthosaura lepidogaster* and *Pseudocalotes* species were chosen as the outgroup, following recent higher-level agamid work (Wang et al., 2019b). Uncorrected genetic pairwise distances (*P*-distances) were also obtained for the coding region of *ND2* (1 035 bp) for closely related congeners using PAUP v. 4.0b10 (Swofford, 2003).

All specimens were measured by using a digital caliper to the nearest 0.1 mm, except for tail length, which was measured to the nearest 1 mm using a ruler. The morphometric characters were measured following Wang et al. (2018), with some additional morphological characteristics added (Supplementary material (Methods)). Color names and codes follow Köhler (2012).

To examine whether the putative new species occupy distinct morphological spaces with respect to morphologically similar congeners, and whether the morphological clustering coincide with the phylogenetic clades recovered from our molecular data set, Principle Component Analysis (PCA) and Discriminant Analysis of Principle Components (DAPC) were performed. Because all known species of *Diploderma* are sexually dimorphic (Wang et al., 2019a, 2019b), morphometric data were analyzed separately for males and females.

The resulting topologies from BI and ML analyses are highly consistent, with a few exceptions only where support values are strong in Maximum Likelihood analyses (bootstrap support [BS]>70) but not in Bayesian analyses (posterior probability [PP]<0.95; Figure 2). The genus *Diploderma* is shown to be a monophyletic group with strong support (Clade A, BS 98, PP 1.00; support values are given in this order hereafter). All recognized species of *Diploderma* (except *D. laevis*, *D. micangshanense*, and *D. varcoae*, which each only has a single individual) are shown as monophyletic with strong support (100/1.00), with two major clades, Clade B (92/1.00) and Clade C (100/1.00), observed within the genus (Figure 2). Within Clade C, all sampled individuals from Yanbian County form a clade (100/1.00). *Diploderma dymondi* is shown as

sister to *D. varcoae* with strong support (Clade E, 100/1.00; Figure 2), and this whole clade forms a monophyletic group with individuals from the Yanbian population (Clade D, 65/0.94; Figure 2).

We observe low intraspecific genetic divergence within the Yanbian population (*P*-distances of 0.1%–0.3% ; Supplementary Table S2). However, compared to closely related congeners, individuals from the Yanbian population are observed to be 10.9%–13.1% divergent from topotypic *D. dymondi*, 12.1%–12.4% from *D. varcoae*, 16.5%–18.0% from *D. slowinskii*, and 15.6%–16.1% from *D. flaviceps* (Supplementary Table S2).

For morphometric characters PCA analyses reveal three major components with eigen values greater than one for both

males and females, which together captures 81.2% and 81.5% of the total variance, respectively (Supplementary Tables S3, S4). For males, the first major principal component (PC) loads most heavily on the relative tail length (TAL/SVL) and relative head depth (HD/HL); the second major PC loads most heavily on the relative nuchal crest length (TNC/HL) and relative forelimb length (FLL/SVL); and the third major PC loads most heavily on the relative head width (HW/HL) (Supplementary Table S3). For females, the first major PC loads most heavily on relative head depth (HD/HW and HD/HL); the second major PC loads most heavily on relative forelimb length (FLL/SVL) and relative head width (HW/HL); and the third major PC loads most heavily on relative tail length (TAL/SVL) (Supplementary Table S4). For DPAC

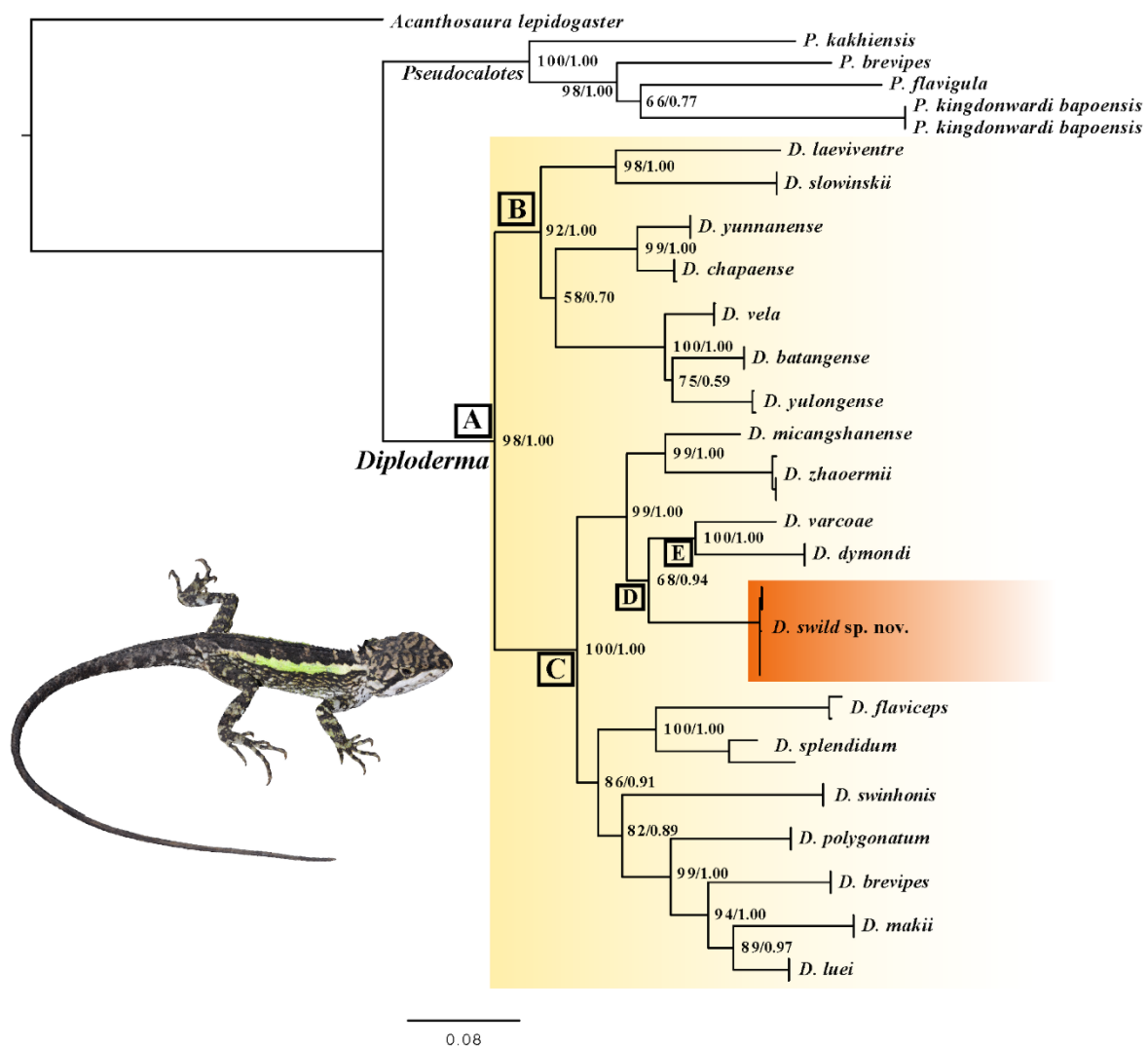


Figure 2 Phylogenetic relationships among species of the genus *Diploderma* based on both Maximum Likelihood and Bayesian analyses of mitochondrial DNA (ND2)

Maximum Likelihood topology shown with both Maximum Likelihood bootstrap and Bayesian posterior probability values mapped on each node (in this order), except for terminal nodes that unify multiple individuals of the same species, which are all well supported across analyses (100/1.00). Photo by Kai Wang.

results, both males and females of the putative new species occupy distinct morphospace with respect to recognized, similar congeners, with no overlap with recognized congeners for the 95% confident intervals (Figure 3).

For pholidosis and ornamentation characters, individuals from Yanbian and Xichang are phenotypically most similar to *D. dymondi* and *D. slowinskii*, with all species possessing exposed tympana, transverse gular folds, and smooth

dorsolateral stripes in males. However, the Yanbian and Xichang populations possess a suite of unique morphological characters that differentiate them from both species and all other congeners, including the presence of taller nuchal crests, exposed and relatively smaller tympana, and distinct Light Chrome Orange (Color 76) coloration of the oral cavity and tongue (for details, see comparison section below; Figures 4; Tables 1, 2).

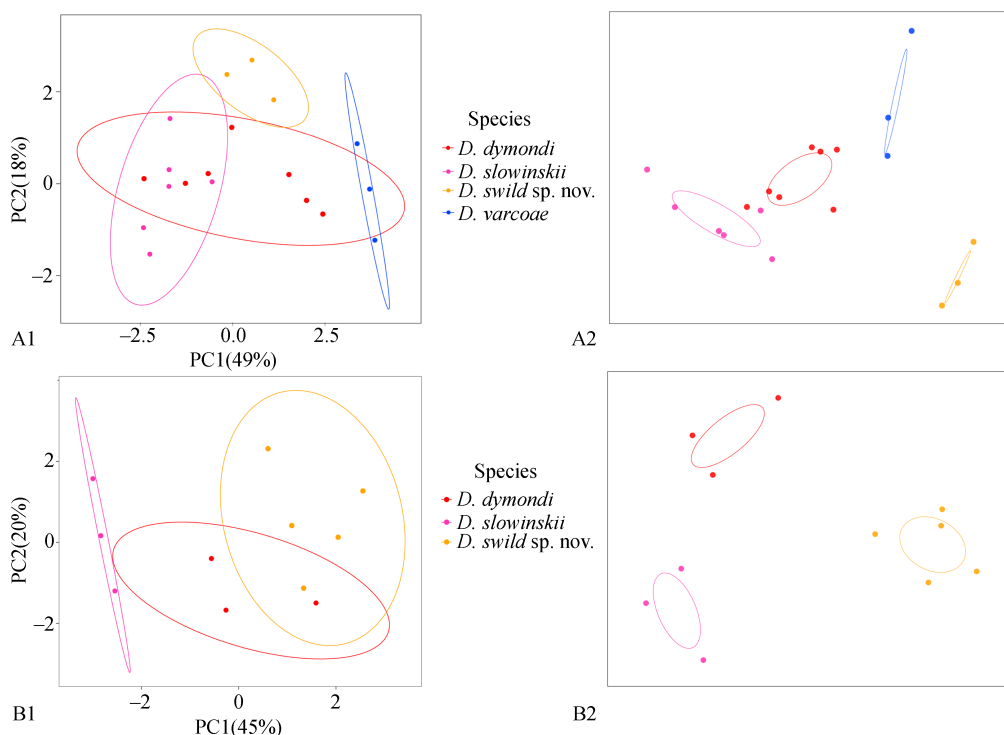


Figure 3 PCA (1) and DAPC (2) analyses of relative morphometric measurements for males (A) and females (B) of *D. swild* sp. nov. and closely related congeners

For males, *D. dymondi*, *D. slowinskii*, and *D. varcoae* are included; while for females, *D. varcoae* is excluded due to limited samples size.



Figure 4 Comparisons in life of males (1 and 3) and females (2 and 4) of *Diploderma dymondi* (A) and *D. swild* sp. nov. (B), showing the different colorations of dorsal and lateral body and oral cavity and tongue

A1, A3: KIZ 040148, from Panzhihua, Sichuan, China; A2, A4: KIZ 040149, from Panzhihua, Sichuan, China; B1, B3: Holotype KIZ 034912; B2, B4: Paratopotype KIZ 040125. Photos by Kai Wang and Ke Jiang.

Table 1 Morphological comparisons among species of the *Diploderma dymondi* complex, including *D. dymondi*, *D. slowinskii*, *D. varcoae*, and *D. swild* sp. nov. (All measurements are in mm)

	<i>D. swild</i> sp. nov.		<i>D. dymondi</i>		<i>D. varcoae</i>		<i>D. slowinskii</i>	
Sex	M	F	M	F	M	F	M	F
Sample size (<i>n</i>)	3	7	8	4	4	2 (*)	7	4
SVL	59.8–71.7 (66.6)	59.7–76.8 (68.8)	64.9–82.3 (72.8)	65.0–79.2 (71.1)	54.5–60.3 (56.8)	63.9–66.1 (65.0)	88.6–99.5 (95.0)	66.8–89.7 (80.0)
TAL/SVL (%)	224.4–239.0 (233.3)	200.4–221.0 (209.7)	220.3–255.8 (235.1)	200.0–227.2 (214.3)	184.2–198.8 (193.7)	187.7 (–)	227.4–246.7 (235.8)	231.3–245.1 (237.8)
HW/HL (%)	65.84–71.5 (67.9)	64.9–71.9 (68.1)	59.7–68.6 (63.6)	63.1–69.1 (66.1)	70.0–76.1 (72.0)	71.8–74.6 (73.2)	59.2–68.0 (63.6)	57.3–66.6 (62.4)
HD/HL (%)	52.0–55.4 (53.3)	50.0–59.6 (54.1)	47.9–57.1 (51.2)	50.6–53.8 (52.4)	55.6–56.0 (55.8)	57.2 (–)	43.3–49.1 (46.2)	43.6–47.2 (45.8)
HD/HW (%)	73.4–83.4 (78.6)	76.99–83.0 (79.4)	78.4–84.1 (80.6)	77.8–82.3 (79.4)	78.2–80.1 (79.2)	79.6 (–)	70.1–76.7 (72.7)	73.0–76.1 (73.4)
FLL/SVL (%)	46.3–48.7 (47.2)	41.9–49.2 (45.0)	44.8–48.5 (47.3)	42.6–47.1 (44.6)	40.5–45.4 (43.4)	41.7–46.9 (44.3)	43.2–49.9 (45.7)	44.7–47.6 (46.2)
HLL/SVL (%)	72.0–78.1 (75.1)	66.9–78.1 (70.5)	74.8–82.9 (78.3)	69.0–77.4 (73.4)	60.9–67.6 (64.4)	63.1–69.0 (66.05)	70.5–83.6 (76.9)	72.9–81.9 (79.0)
TRL/SVL (%)	44.4–53.1 (49.1)	44.0–51.0 (48.1)	40.8–49.8 (45.7)	46.6–52.6 (49.2)	45.4–49.0 (47.0)	47.9–50.7 (49.3)	41.4–46.4 (43.0)	40.8–51.4 (46.8)
TNC/HL (%)	12.0–12.4 (12.1)	8.1–11.8 (10.2)	4.6–6.6 (5.3)	4.4–6.0 (5.0)	4.0–7.1 (6.1)	3.8–6.1 (5.0)	3.2–5.7 (4.6)	3.8–5.3 (4.3)
TD/OD (%)	26.7–42.9 (37.3)	41.9–49.2 (44.9)	49.4–59.0 (54.8)	50.3–61.2 (54.4)	58.4–67.3 (62.9)	55.11 (–)	27.3–40.9 (33.5)	31.0–41.8 (35.3)

For character abbreviations see Supplementary Methods. Average values are given in parentheses; for scale count, such average is rounded to the nearest whole number. *: Indicates differential sample size for female *Diploderma varcoae*, where for tail length, head depth, and tympanic diameter, only a single specimen (KIZ 034294) was measured. F: Female; M: Male. –: Not available.

Taxonomic account

Diploderma swild sp. nov. Wang, Wu, Jiang, Chen, Miao, Siler, Che (Figures 1, 4 and 5; Tables 1, 2; Supplementary Table S5)

Synonyms: *Japalura dymondi* Deng et al., 1991: 27. Zhao et al., 1999: 110–111. Zhao, 2003: 82–83. *Japalura flaviceps* Deng et al., 1991: 27. Zhao et al., 1999: 111–115. Zhao, 2003: 84.

Holotype: KIZ 034912, adult male from Hongbao Village, Yanbian County, Panzhihua District, Sichuan Province, China (WGS 84, E101.558°, N27.104°, 2 318 m a.s.l.), collected by Ben-Fu Miao on October 15, 2017.

Paratype: CIB 1871/105074, adult male from Xichang, Liangshan Prefecture, Sichuan Province, China, collector and collecting time unknown. KIZ 034913, adult female; KIZ 034914, 034894, sub-adult males, collected by Ben-Fu Miao on August 2017. KIZ 040935, adult male, collected by Ben-Fu Miao and Kai Wang on April 10, 2019; KIZ 040124, sub-adult female; KIZ 040125–27, adult females, collected by Kai Wang, Jia-Wei Wu, Gedeng Nima, and Ben-Fu Miao on April 23, 2018.

Diagnosis: The new species can be diagnosed from

congeners by a combination of the following morphological characteristics: (1) body length moderate, SVL 59.8–71.7mm in adult males, 57.2–76.8 mm in adult females; (2) tail long, TAL 224.4%–239.0% SVL in adult males, 200.4%–221.0% in adult females; (3) hind limbs moderate, HLL 66.9%–78.1% SVL; (4) head length, width, and depth moderate, HL 30.8%–32.5% SVL, HW 64.9%–71.9% HL, HD 50.0%–54.1% HL, HD 73.4%–80.6% HW; (4) MD 35–44; (5) F4S 18–22; (6) T4S 23–27; (7) tympana exposed; (8) tympana moderate in size, TD 26.7%–49.2% OD; (9) nuchal crest tall, clearly differentiated from dorsal crests, TNC 12.0%–12.4% HL in adult males, 8.1%–11.8% in adult females; (10) transverse gular fold present, relatively shallow; (11) ventral scales of head and body distinctively keeled; (12) ventral head and ventrolateral body scales largely homogeneous in size with few enlarged scales scattered randomly; (13) gular spots absent in both sexes; (14) dorsolateral stripes distinct in males, smooth edged, Chartreuse (Color 89) in color; faint or indistinct in females, White, Cream Color (Color 12), or Spectrum Yellow (Color 79) in color; (15) ventral body white with Jet Black (Color 300) speckles or with two wide, parallel, Light Yellow Ocher (Color 13) lateral patches distributed from chest to region anterior to vent; and (16) anterior oral cavity and tongue Light Chrome Orange (Color 76), posterior parts of palate marbled Dark Neutral Gray (Color 299).

Table 2 Pholidosis and coloration comparisons among species of the *Diploderma dymondi* complex, including *D. dymondi*, *D. slowinskii*, *D. varcoae*, and *D. swild* sp. nov.

	<i>D. swild</i> sp. nov.	<i>D. dymondi</i>	<i>D. varcoae</i>	<i>D. slowinskii</i>
Sample size (<i>n</i>)	9 (*)	12	3	4
SL	6–10 (7)	7–9 (8)	7 or 8 (8)	6–8 (7)
IL	7–9 (8)	8–11 (9)	8 or 9 (8)	7–9 (8)
NSL	0 or 1 (1)	0 or 1 (1)	1 (1)	0 or 1 (1)
MD	35–44 (42)	41–51 (45)	38–41 (38)	47–53 (50)
F4S	18–22 (20)	16–21 (19)	15–20 (17)	20–23 (21)
T4S	23–27 (25)	22–27 (24)	19–24 (21)	24–28 (27)
SOR	3 or 4 (3)	3 or 4 (3)	3 or 4 (4)	2 or 3 (3)
PTS	1–4 (2)	2–4 (3)	3 or 4 (4)	3–5 (5)
PTY	3–7 (5)	4–9 (6)	3–6 (4)	4–6 (5)
PRS	5–10 (8)	6–10 (9)	6–11 (8)	4–8 (6)
CO	Light chrome orange	Spectrum violet	Light chrome orange	Pale pinkish buff
CT	Marbled drak neutral gray	Spectrum violet	Light chrome orange	Pale pinkish buff
CTG	Light chrome orange	Pale pinkish buff	Light chrome orange	Pale pinkish buff
CDS	Chartreuse	Chartreuse	Light buff	Chartreuse
SDS	Smooth	Smooth	Jagged	Smooth

For character abbreviations see Supplementary Methods. Average value of each scale count is given in parentheses, which are rounded to the nearest whole number. *: Indicate differential sample sizes for *Diploderma swild* sp. nov., where for F4S, T4S, and PTS, the sample sizes are eight, seven, and seven, respectively.

Comparisons: The new species is morphologically most similar to, and confused historically with, *D. dymondi*, in which both species have exposed tympana and green, smooth-edged dorsolateral stripes in males. However, *D. swild* sp. nov. can be differentiated from *D. dymondi* by having relatively taller nuchal crest scales (TNC 12.0%–12.4% HL in males, 8.1%–11.8% in females vs. 4.6%–6.6% in males, 4.4%–6.0% in females), smaller tympana (TD 26.7%–49.2% OD vs. 49.4%–61.2%), a distinct coloration of oral cavity (Light Chrome Orange (Color 76) vs. Spectrum Violet (Color 186) or Jet Black (Color 300)), and tongue (Light Chrome Orange (Color 76) vs. Light Flesh Color (Color 250)) (Tables 1, 2), as well as by presence of enlarged scales on the ventral surface of head scales (vs. absent).

Diploderma swild sp. nov. is also similar to *D. slowinskii* and *D. varcoae* morphologically, where all three species have exposed tympana. However, the new species can be differentiated from *D. slowinskii* by having a smaller maximum body size (maximum SVL reaching 76.8 mm vs. reaching 99.5 mm), fewer middorsal scales count (MD 35–44 vs. 47–53), distinct oral coloration in life (Light Chrome Orange (Color 76) vs. Light Flesh Color (Color 250)), and by the presence of distinct, white lip stripes (vs. absent); and from *D. varcoae* by having much larger nuchal crest scales (TNC 12.0%–12.4% HL in males, 8.1%–11.8% in females vs. 4.0%–7.1% in males, 3.8%–6.1% in females), smaller tympana (TD 26.7%–49.2% OD vs. 55.1%–67.3%), different shape and color of dorsolateral stripes in males (Smooth edged, Chartreuse

(Color 89) or Yellow Green (Color 103) vs. strongly jagged, Light Buff (Color 2)), different ecology (arboreal vs. terrestrial), and by the presence of a transverse gular fold (vs. absent) (Tables 1, 2).

Compared to other members of the same clade (Clade C, Figure 2), the new species differ from *D. flaviceps* by having a longer tail (TAL>200.4% SVL vs. <193.9%), taller nuchal crests (TNC 12.0%–12.4% HL in males, ≥8.1% in females vs. ≤6.1% in males, ≤5.6% in females), different shape and coloration of dorsolateral stripes in males (smooth edged, Chartreuse (Color 89) or Yellow Green (Color 103) vs. strongly jagged, Cream Color (Color 12)), as well as by the presence of dark distinct radial stripes around eyes (vs. absent), and by the absence of hollow, rhomboid shaped patterns along dorsal midline of the body (vs. present); from *D. micangshanense* by having exposed tympana (vs. concealed), different shape and coloration of dorsolateral stripes in males (smooth edged, Chartreuse (Color 89) or Yellow Green (Color 103) vs. strongly jagged, Cream Color (Color 12)), a distinct coloration of oral cavity and tongue (Light Chrome Orange (Color 76) vs. Light Flesh Color (Color 250)), and by the presence of a transverse gular fold (vs. absent); from *D. splendidum* by having exposed tympana (vs. concealed) and a distinct coloration of oral cavity and tongue (Light Chrome Orange (Color 76) vs. Light Flesh Color (Color 250)); from *D. zhaoermii* by having exposed tympana (vs. concealed), a distinct shape of dorsolateral stripes in males (smooth edged vs. strongly jagged), a distinct oral coloration in life (Light Chrome Orange (Color 76) vs.

Light Flesh Color (Color 250)), and by the absence of distinct gular spots in males (vs. present); and from all island congeners (*D. brevipes*, *D. luei*, *D. makii*, *D. polygonatum*, and *D. swinhonis*) by having exposed tympana (vs. concealed) and by the presence of a transverse gular fold (vs. absent).

For congeners in the different Clade (Clade B, Figure 2), the new species differs by having exposed tympana (vs. concealed) and a shallow transverse gular fold (vs. prominent and deep). Additionally, *D. swild* **sp. nov.** differs from all members of Clade B except for *D. laeviventre* (including *D. chapaense*, *D. batangense*, *D. vela*, *D. yulongense*, and *D. yunnanense*) by having smooth edged, dorsolateral stripes in males (vs. strongly jagged), and from all but *D. chapaense* and *D. yunnanense* by having a distinct coloration of oral cavity and tongue (Light Chrome Orange (Color 76) vs. Light Flesh Color (Color 250)), heterogeneous ventral head scales and ventrolateral body scales (vs. homogeneous), and taller nuchal crests (TNC 12.0%–12.4% HL in males, $\geq 8.1\%$ in females vs. $\leq 6.1\%$). Furthermore, *D. swild* **sp. nov.** differs from *D. laeviventre* by having fewer middorsal scale count (35–44 vs. 57–59), different scale texture of ventral scales (strongly keeled vs. smooth), and by the absence of distinct gular spots in both sexes (vs. present); and from *D. chapaense* and *D. yunnanense* by having a transverse gular fold (vs. absent), and by the absence of distinct W-shaped ridges on occipital head (vs. present) and the absence of gular spots (vs. present).

For congeners that do not have genetic data, the new species differs from all by having exposed tympana (vs. concealed). Additionally, *D. swild* differs from *D. brevicaudum* by having a much longer tail (TAL $\geq 200.4\%$ SVL vs. $\leq 150.0\%$); from *D. drukdaypo* by having a longer tail (TAL $\geq 200.4\%$ SVL vs. $\leq 175.1\%$), distinctively keeled ventral scales (vs. smooth or feebly keeled), and strongly developed nuchal crests (vs. feebly developed); from *D. grahami* by having strongly developed nuchal crests (vs. feebly developed) and by the absence of granular scales on the head and body (vs. present); from *D. hamptoni* by having parallel dorsolateral stripes (vs. diagonally away from dorsal midline toward posterior direction); from *D. iadinum* by having a longer tail (TAL $\geq 200.4\%$ SVL vs. $\leq 196.4\%$), a distinct dorsal coloration (Clay Color (Color 18) to Warm Sepia (Color 40) vs. Yellowish Spectrum Green (Color 128) to Emerald Green (Color 143)), a distinct coloration of oral cavity and tongue (Light Chrome Orange (Color 76) vs. Light Flesh Color (Color 250)), and by the absence of gular spots in both sexes (vs. present); and from *D. fasciatum* by having a longer tail (TAL $\geq 200.4\%$ SVL vs. $\leq 180.5\%$), a distinct coloration of oral cavity and tongue (Light Chrome Orange (Color 76) vs. Light Flesh Color (Color 250)), and different ornamentation patterns on the dorsal bodies in males and females (two smooth edged dorsolateral stripes vs. single hourglass-shaped transverse marking on mid dorsum).

Description of holotype: Medium sized agamid species, SVL 58.84 mm, body not compressed dorsally; tail long, slender,

TAL 239% SVL; limbs moderate, forelimb 48.8% SVL, hind limb 78.1% SVL. Head moderate, head width 65.8% head length, head depth 52.0% head length, head depth 78.9% head width; snout relatively long, snout–eye distance 39.2% head length. Rostral rectangular, three times longer than height, separated from nasal by single scale; nasal polygonal in shape, separated from first supralabial by single small scale; supralabials 7/7, each with single, strong, lateral keel, last one longest; supralabials and orbit separated by three scale rows, medial row much larger, all distinctively keeled with lateral keels; supraciliaries 7/7, first anterior three each overlapping one-third of its total length with succeeding one, remaining ones overlapping between one-third to one-fourth of their length; two distinctively enlarged, sub-pyramidal shaped scales posterior-superior to orbit, with anterior one more laterally elongated; enlarged, convex, keeled scales between posterior orbit and anterior tympanum, 7/8, forming lateral ridge between orbit and tympanum on each side; tympana exposed, somewhat oval in shape, relatively small, TD 42.2% OD; enlarged, conical scales posterior-superior to tympana, well developed, 4/5.

Dorsal head scales mostly homogeneous in size and shape, with few ones distinctively enlarged and randomly distributed, all scales distinctively keeled; four enlarged, keeled scales forming Y-shaped arrangement on dorsal snout anterior to orbit, with tip of such Y-shaped arrangement three small scales posterior to rostral; interparietal spear-tip in shape, with tip pointing posteriorly, parietal eye indistinct; 5/6 enlarged, convex scales in C-shaped arrangement on each side of temporal head, with opening of C-shaped arrangements facing each other and symmetrical along dorsal midline; single, distinctively raised, conical scale on lateral temporal region on each side, superior to lateral ridge between orbit and tympanum; enlarged, raised, conical scales post-occipital on each side of head, well developed, 2/3.

Dorsal body scales distinctively keeled, heterogeneous in size and shape; nuchal crest 11, in tall triangular shape, clearly differentiated from dorsal crest; dorsal crest highly serrated, well developed, differentiated from remaining dorsal scales; middorsal scale count 38; distinctively enlarged dorsal body scales somewhat conical in shape, tips raised at posterior ends; some enlarged dorsal body scales arranged in two paravertebral rows on each side of body, with first row about single scale-row away from dorsal crest, second row along superior border of dorsolateral stripe, further away from dorsal crest; remaining enlarged dorsal scales scattered randomly. Dorsal forelimb scales homogeneous on upper arm, heterogeneous on lower arm, with few enlarged, subpyramidal scales on posterolateral side; dorsal hind limb scales heterogeneous, with enlarged conical scales on posterolateral thigh.

Mental pentagonal in shape, in contact with first pair of supralabials and chin shields; chin shields 7/8, two or three scale rows separated from infralabials; infralabials 8/9, each bearing single, strong, lateral keel; remaining ventral scales distinctively keeled, largely homogeneous in size and shape; small number of enlarged scales scattered randomly on

posterior half of ventral head, largest of these roughly three times size of nearby background scales; post-rectal conical scales 10/7, distinctly enlarged and raised, resulting in spiky appearance. Gular pouch present, distinct in life, indistinct after preservation; lateral gular fold present in life, absent after preservation; transverse gular fold present, shallow. Ventral body scales distinctively keeled, largely homogeneous in size and shape, with small number of enlarged scales scattered on ventrolateral body only. Ventral limb scales largely homogeneous in size and shape, all distinctively keeled; Finger IV and Toe IV longest; subdigital lamellae well modified, 20/21 beneath Finger IV, 25/24 beneath Toe IV. Tail scales distinctively keeled, carinate in lateral rows.

Coloration of holotype in life: The background color of the dorsal surface of the head is Straw Yellow (Color 53). Four distinct, Jet Black (Color 300) transverse patterns are scattered evenly between the snout and the posterior margins of the orbits on the dorsal surface of the head. The anterior most pattern is U-shaped, compared with the remaining patterns which are X-shaped. Irregular, Jet Black (Color 300) pigmentation patterns are present on the occipital and temporal regions of the head. Distinct, Jet Black (Color 300) radial stripes are present around the eyes, 10/10, with two inferior stripes below the eyes intercepting with the white lip stripe on each side of the head. Within the oral cavity, the anterior parts of the roof, sides of the mouth, and the tongue are Light Chrome Orange (Color 76), and the posterior parts of the palate and visible parts of the deep throat are marbled Dark Neutral Gray (Color 299).

Two smooth-edged, dorsolateral stripes run from the occipital region of head to the pelvis, one on each side. The most anterior parts of the dorsolateral stripes from the neck to the pectoral region are white, which then sharply transition to Chartreuse (Color 89) posteriorly. The dorsal region of the body between dorsolateral stripes is nearly uniform Sepia (Color 286), with some fade, Jet Black (Color 300), triangular patterns. The background coloration of dorsal limbs and lateral surfaces of the body inferior to the dorsolateral stripes is Olive Brown (Color 278). Straw Yellow (Color 53), Medium Lime Green (Color 115), or White scales are scattered randomly on lateral surfaces of body inferior to dorsolateral stripes. Straw Yellow (Color 53) or Buff (Color 5) colored scales are arranged in transverse bands on dorsal surfaces of forelimbs and hind limbs. A distinct white stripe is present on the ventrolateral surface of thigh on each side, extending from pelvis to two third of the thigh. The background coloration of dorsal and lateral surfaces of the tail is uniform Sepia (Color 286). Four Light Buff (Color 2) bands are evenly distributed on the anterior half of the tail and gradually become indistinct posteriorly. The ventral surfaces of head, limbs, and body are uniform white with no distinct ornamentations. The ventral surface of the tail is uniform Light Buff (Color 5) (Figure 4).

Coloration of holotype in preservation: Although ornamentation structure remains largely the same following preservation, most coloration fades in intensity and shade.

Specifically, the Jet Black (Color 300) transverse patterns on the dorsal surface of head fade and become Raw Umber (Color 22), the Chartreuse (Color 89) dorsolateral stripes become Pale Cyan (Color 157), the Medium Lime Green (Color 115) scales of lateral body become Cyan White (Color 156), and the Sepia (Color 286) color of the dorsal body and limbs becomes Olive Color (Color 16) (Figure 5).

Variations: Detailed morphometric and pholidosis variation are summarized in Supplementary Table S5. Like other congeners, sexual dimorphism is evident in *D. swild* sp. nov., where males (KIZ 034912, 040935, CIB1871/105074) differ from females by having a longer tail (TAL 224.4%–239.0% SVL in males vs. ≤221.0% in females), taller nuchal crest (TNC 12.0%–12.4% HL in males vs. 8.1%–11.8% in females), and distinct coloration and ornamentation, including differences in lateral body ornamentation (almost uniform Olive Brown (Color 278) or Clay Color (Color 20) in males vs. white, Chamois (Color 84), or Light Greenish Yellow (Color 87) with Sepia (Color 279) or Jet Black (Color 300) reticulated patterns in females), dorsolateral stripes (distinct, smooth-edged, Chartreuse (Color 89) in male vs. indistinct, jagged, white, Cream Color (Color 12), or Spectrum Yellow (Color 79) in females), gular coloration (uniform white in males vs. uniform white, Cream Yellow (Color 82), or Dark Spectrum Yellow (Color 78) with few black speckles in females), and coloration of ventral body (white in males vs. speckled white or speckled white with two parallel, Light Yellow Ocher (Color 13) lateral patches in females).

Etymology: The specific name "*swild*", which is a noun, is derived from the name of the Chinese Conservation Organization, Swild Studio (西南山地工作室). We name the species after the organization in honoring its continuous contributions on promoting citizen science, nature photography, and public outreach on the wildlife conservation in Southwest China, particularly in the Hengduan Mountain Regions where the new species is native. Suggested English Common Name: Swild Mountain Dragon; Suggested Chinese Common Name: 山地龙蜥 (Pinyin: Shan Di Long Xi).

Natural history: The new species is arboreal, inhabiting broad-leaf forest at elevation between 1 800–2 200 m a.s.l. (Figure 1). To date, the new species has been collected from the type locality in Yanbian County and Xichang of Liangshan Prefecture, Sichuan Province only, but individuals were also recorded from Huili County, further east from the type locality (personal communication). Although the type locality of the species is protected by the Ertan National Natural Reserve, much of the protected area is at high elevation where the species is far less abundant. As little is known about the distribution range other than few isolated localities, we propose to list the species as Data Deficient (DD) for IUCN assessment, and we call for future ecological study to determine its conservation status.

Individuals were observed foraging both on trees and on the ground during the day, but only resting on twigs or thin stems

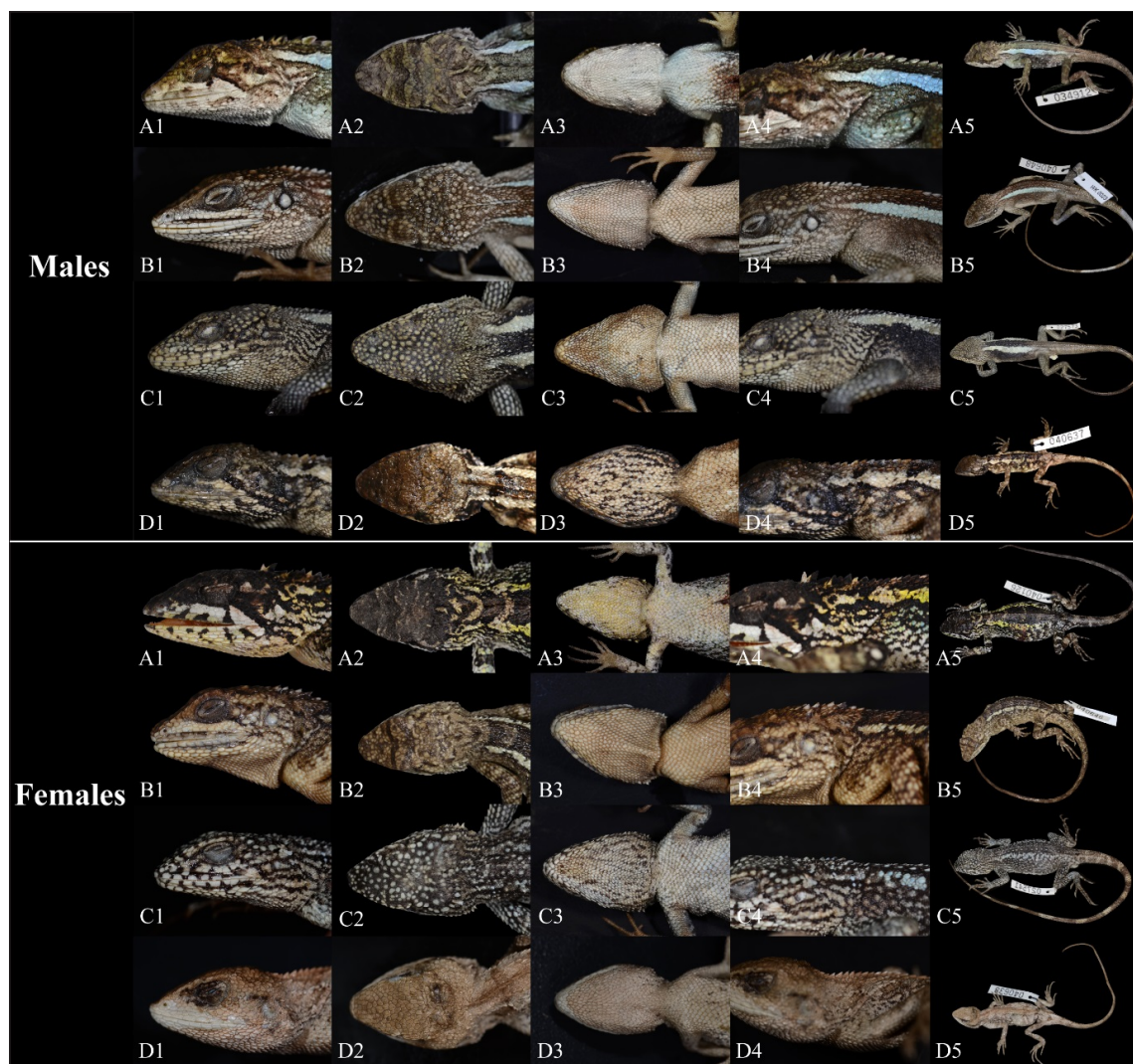


Figure 5 Comparisons between males and females of *Diploderma swild* sp. nov. (A), *D. dymondi* (B), *D. slowinskii* (C), and *D. varcoae* (D) in preservative, depicting differences in the lateral (1), dorsal (2), and ventral (3) head regions, the nuchal crest (4), and in overall body ornamentation (5) (Photos by Kai Wang)

of bushes at night from about 1 m to 2–3 m above ground (Figure 1). Road-killed individuals are common at the type locality, especially at low-elevation site (about 1 200 m a.s.l.). Possible predators may be lizard-eating snakes such as *Ptyas nigromarginatus*, *Lycodon liuchengchaoi*, and *Elaphe carinata*, which are all common at the type localities. No sympatric distribution between the *D. swild* sp. nov. and *D. dymondi* were observed in the field. Based on our field surveys, the new species inhabits the moister, montane area that is further away from the much dryer main course of the Jinsha River, where *D. dymondi* inhabits (Figure 1). Such differences in abiotic habitat may indicate ecological divergence between the two otherwise similar species. Further ecological studies are needed to gain a better understanding on the ecology of these mountain dragons in this region.

NOMENCLATURAL ACTS REGISTRATION

The electronic version of this article in portable document format represents a published work according to the International Commission on Zoological Nomenclature (ICZN), and hence the new names contained in the electronic version are effectively published under that Code from the electronic edition alone (see Articles 8.5–8.6 of the Code). This published work and the nomenclatural acts it contains have been registered in ZooBank, the online registration system for the ICZN. The ZooBank LSIDs (Life Science Identifiers) can be resolved and the associated information can be viewed through any standard web browser by appending the LSID to the prefix <http://zoobank.org/>.

Publication LSID:

urn: lsid: zoobank. org: pub: 31EEFAD0-0452-44DD-B60E-

66360C922836

Diploderma swild LSID:

urn: lsid: zoobank. org: act: 2CB71FB0-D2C7-4215-9BA0-7C954BE49CBA

SCIENTIFIC FIELD SURVEY PERMISSION INFORMATION

Permission for field surveys in Sichuan Province was granted by the Forestry Department and National Reserves of China. Project approval (BBCJ-2014-001) was issued by the Kunming Institute of Zoology, Chinese Academy of Sciences.

SUPPLEMENTARY DATA

Supplementary data to this article can be found online.

COMPETING INTERESTS

The authors declare that they have no competing interests.

AUTHORS' CONTRIBUTIONS

K.W., J.W.W., and B.F.M. collected specimens in the field. K.J. supervised the morphological data collection. K.W. and J.M.C. collected morphological data. K.W. conducted genetic analyses and submitted to GenBank, which was supervised by C.D.S. and J.C.. K.W. wrote the manuscript with inputs from other authors. C.D.S. and J.C. revised the manuscript. All authors read and approved the final version of the manuscript.

ACKNOWLEDGEMENTS

We thank D. Hollis (ROM) for editing the English language of the manuscript; Mr. J. Ren for taking photographs at CIB; Mr. G. Nima and Mr. L. He for their great assistances in the field; Dr. V. Deepak for his helps in examining specimens and taking photographs; Drs. Y. Wang and J. Li (CIB), Drs. R. Brown and L. Welton (KU), Mr. W. Addison (NMNH), Mr. J. Vindum and Ms. L. Scheinberg (CAS), and Drs. J. Hanken and J. Losos (MCZ) for their great supports in allowing us examine specimens or facilitate specimen loans.

Kai Wang^{1,2,*}, Jia-Wei Wu³, Ke Jiang¹, Jin-Min Chen¹,
Ben-Fu Miao¹, Cameron D. Siler², Jing Che^{1,*}

¹ State Key Laboratory of Genetic Resources and Evolution,
Kunming Institute of Zoology, Chinese Academy of Sciences,
Kunming Yunnan 650223, China

² Sam Noble Oklahoma Museum of Natural History and
Department of Biology, University of Oklahoma, Norman,
Oklahoma 73072, USA

³ Chengdu Museum of Nature Exploration, Chengdu Sichuan
610017, China

*Corresponding authors, E-mail: chej@mail.kiz.ac.cn;
kai.wang-2@ou.edu

REFERENCES

- Boulenger GA. 1906. Descriptions of new reptiles from Yunnan. *Annals and Magazine of Natural History*, **17**(102): 567–568.
- Boulenger GA. 1918. Description of a new lizard of the genus *Acanthosaura* from Yunnan. *Annals and Magazine of Natural History*, **2**(8): 162.
- Deng Q, Yu Z, Zeng F. 1991. Herpetological Survey in Panzhihua City, Sichuan. *Sichuan Journal of Zoology*, **10**(2): 27–29.
- Deng Q, Jiang Y. 1988. Notes on *Japalura dymondi* (Boulenger) from China. *Acta Herpetologica Sinica*, **7**: 149–150.
- Köhler G. 2012. Color Catalogue for Field Biologists. *Herpeton, Offnbach*.
- Manthey U, Denzer W, Hou M, Wang XH. 2012. Discovered in historical collections: two new *Japalura* species (Squamata: Sauria: Agamidae) from Yulong Snow Mountains, Lijiang Prefecture, Yunnan, PR China. *Zootaxa*, **3200**(1): 27–48.
- Rao DQ, Vindum JV, Ma XH, Fu MX, Wilkinson JA. 2017. A new species of *Japalura* (Squamata, Agamidae) from the Nu River Valley in Southern Hengduan Mountains, Yunnan, China. *Asian Herpetological Research*, **8**(2): 86–95.
- Swofford DL. 2003. PAUP: Phylogenetic Analysis Using Parsimony (*and other methods). Version 4. Sinauer Associates, Sunderland.
- Wang K, Jiang K, Deepak V, Abhijit D, Hou M, Che J, Siler CD. 2018. On the occurrences of *Japalura kumaonensis* and *Japalura tricarinata* (Reptilia: Sauria: Draconinae) in China. *Herpetologica*, **74**(2): 181–190.
- Wang K, Jiang K, Pan G, Hou M, Siler CD, Che J. 2015. A new species of *Japalura* (Squamata: Sauria: Agamidae) from Upper Lancang (Mekong) valley of Eastern Tibet, PR China. *Asian Herpetological Research*, **6**(3): 159–168.
- Wang K, Jiang K, Ren JL, Zou DH, Wu JW, Che J, Siler CD. 2019a. A new species of dwarf *Japalura* sensu lato (Reptilia: Squamata: Agamidae) from the upper Mekong River in Eastern Tibet, China, with notes on morphological variation, distribution, and conservation of two congeners along the same river. *Zootaxa*, **4544**(4): 505–522.
- Wang K, Jiang K, Zou DH, Yan F, Siler CD, Che J. 2016. Two new species of *Japalura* (Squamata: Agamidae) from the Hengduan Mountain Range, China. *Zoological Research*, **37**(1): 41–56.
- Wang K, Che J, Lin SM, Deepak V, Aniruddha DR, Jiang K, Jin JQ, Chen HM, Siler CD. 2019b. Multilocus phylogeny and revised classification for Mountain Dragons of the genus *Japalura* s. l. (Reptilia: Agamidae: Draconinae) from Asia. *The Zoological Journal of the Linnean Society*, **185**(1): 246–267.
- Wang K, Ren JL, Jiang K, Yuan ZY, Che J, Siler CD. 2017. Rediscovery of the enigmatic Mountain Dragon, *Japalura yulongensis* (Reptilia: Sauria: Agamidae), with notes on its natural history and conservation. *Zootaxa*, **4318**(2): 351–363.
- Wu J. 1992. The analysis of amphibious reptile fauna in Gaoligongshan Reserve of Yunnan. *Acta Herpetologica Sinica*, **1**: 88–95.
- Yang DT, Rao DQ. 2008. Amphibia and Reptilia of Yunnan. Yunnan Science and Technology Press, China.
- Zhao EM. 2003. Colored Atlas of Reptiles of Sichuan. China Forestry Publishing House, China.
- Zhao EM, Zhao KT, Zhou KY. 1999. Fauna Sinica, Reptilia, Vol. 2: Squamata, Lacertilia. Science Press, China.

Nest sanitation facilitates egg recognition in the common tailorbird, a plaintive cuckoo host

DEAR EDITOR,

Nest sanitation is a ubiquitous behavior in birds and functions to remove foreign objects that accidentally have fallen into their nests. In avian brood parasitism, the host's ability to recognize and reject parasitic eggs is a specific anti-parasitic behavior. Previous studies have shown that egg recognition may have evolved from nest sanitation behavior; however, few studies have offered evidence in support of this hypothesis. In the current study, we added one real white egg and one model egg to the nests of common tailorbirds (*Orthotomus sutorius*), the main host of plaintive cuckoos (*Cacomantis merulinus*), to explore the relationship between egg recognition ability in hosts and nest sanitation behavior. Results showed that common tailorbirds rejected both non-mimetic blue model eggs and mimetic white model eggs at a similar rate of 100%, but only rejected 16.1% of mimetic real white eggs. The egg rejection behavior of common tailorbirds towards both real and model eggs was consistent. However, when both blue model eggs and real white eggs were simultaneously added to their nests, the probability of rejecting the mimetic real white egg increased to 50%. The addition of blue model eggs not only increased the occurrence of nest sanitation behavior but also increased the ability to recognize and reject parasitic eggs. This suggests that nest sanitation may facilitate egg rejection in common tailorbird hosts.

Nest sanitation is an important and ubiquitous behavior in birds that results in the removal of foreign objects and waste materials from their nests. Birds swallow, transport, or bury nest objects to ensure cleanliness and thus reduce the risk of shell damage and chick infection by pathogens and parasitic worms (Guigueno & Sealy, 2012, 2017; Ibáñez-Álamo et al., 2017). Birds not only remove chick feces, eggshells, unhatched eggs, and dead chicks but also foreign objects (Guigueno & Sealy, 2009; Moskát et al., 2003). In avian brood

parasitism, many hosts rely on differences in egg color, size, markings, and shape to differentiate between their own eggs and those that are parasitic (Davies & Brooke, 1988; Poláčiková & Grim, 2010; Rothstein, 1975b, 1982), and thus identify such eggs as foreign objects to be discarded from the nest. For example, the American robin (*Turdus migratorius*) rejects and removes model eggs that deviate from their own in dominant color, size, and markings (Luro et al., 2018). This form of egg rejection could be considered as a type of nest sanitation behavior. Therefore, we propose the following question: Does egg rejection behavior in birds evolve from nest sanitation behavior? Nest sanitation may be an important stage in the evolution of egg recognition in hosts because nest sanitation, egg recognition, and parasitic egg rejection reduce the reproductive costs incurred from raising another bird's progeny (Davies & Brooke, 1989; Payne, 1977). Egg rejection in birds is usually achieved by grasping or puncturing the eggs with their beaks and removing the eggs from the nest (Moksnes et al., 1991; Rohwer & Spaw, 1988). Both egg rejection and nest sanitation behavior involve the removal of foreign or unwanted matter from the nest.

Rothstein (1975a) first proposed that nest sanitation behavior may be a pre-adaptation of egg rejection. Moskát et al. (2003) further proposed a hierarchical concept to explain the relationship between nest sanitation and egg rejection behavior: i.e., (1) host rejection of all non-egg-like objects is a general cleaning mechanism; and, (2) hosts that recognize their own eggs can differentiate between objects similar to their eggs and parasitic eggs. In other words, the greater the differences, e.g., in appearance, between the foreign object and the egg, the stronger the bird's ability to differentiate between them, and the more likely that the foreign objects will be rejected. An initial study of red-winged blackbirds (*Agelaius phoeniceus*) showed removal of model eggs that mimicked broken eggs but not rejection of parasitic cowbird eggs (Kemal & Rothstein, 1988; McMaster & Sealy, 1997). Yang et al. (2015a) added a peanut shell alongside a model egg in the

Open Access

This is an open-access article distributed under the terms of the Creative Commons Attribution Non-Commercial License (<http://creativecommons.org/licenses/by-nc/4.0/>), which permits unrestricted non-commercial use, distribution, and reproduction in any medium, provided the original work is properly cited.

Copyright ©2019 Editorial Office of Zoological Research, Kunming Institute of Zoology, Chinese Academy of Sciences

Received: 28 April 2019; Accepted: 26 July 2019; Online: 22 August 2019

Foundation items: This study was supported by the National Natural Science Foundation of China (31672303 to C.C.Y., and 31472013, 31772453 and 31970427 to W.L.)

DOI: 10.24272/j.issn.2095-8137.2019.054

nests of barn swallows (*Hirundo rustica*), a host of common cuckoos (*Cuculus canorus*), and found that the probability of rejecting model eggs increased significantly in the presence of a half peanut shell. Furthermore, Yang et al. (2015b) showed that the rate of rejection of foreign eggs increased with the rate of rejection of non-egg-shaped objects in barn swallows. These results suggest a possible association between nest sanitation behavior and egg recognition in cuckoo hosts.

The study of Mermoz et al. (2016) on brown-and-yellow marshbirds (*Pseudoleistes virescens*) did not directly discuss the role of nest sanitation behavior in egg rejection by hosts but suggested that adding one spotted-blue artificial egg increased the rejection rate of cowbird eggs. However, when Peer (2017) followed the method of Yang et al. (2015a) and added a piece of flagging tape or a pinecone bract scale to the nest of red-winged blackbirds, they found that the addition of foreign material did not affect the host's rejection rate of cowbird eggs. Su et al. (2018) added peanut shells and model eggs to the open nests of brown-breasted bulbuls (*Pycnonotus xanthorrhous*) and found that nest sanitation behavior did not affect egg recognition ability in this species. Evidently, the effects of nest sanitation behavior on egg recognition differ among species, and thus the connection between these behaviors in birds remains unclear (Luro & Hauber, 2017). As such, further studies on more species are required to validate the role of nest sanitation behavior on the evolution of egg recognition and egg rejection behavior.

Most previous studies on the relationship between egg rejection ability and nest sanitation behavior have used non-egg-shaped objects to stimulate birds (Luro & Hauber, 2017; Peer, 2017; Su et al., 2018; Yang et al., 2015a). According to Moskát et al. (2003), the more dissimilar the shape of a foreign object compared to the host egg, the more likely that nest sanitation behavior will be elicited. However, although egg-shaped objects better simulate cuckoo eggs, few studies have used egg-shaped objects to stimulate nest sanitation behavior in hosts (Mermoz et al., 2016).

Common tailorbirds are one of the main hosts of plaintive cuckoos (*Cacomantis merulinus*) (Nahid et al., 2016; Payne, 2005; Tunheim et al., 2019; Yang et al., 2012). They are extremely sensitive to the appearance of foreign eggs and frequently reject eggs that exhibit a different color or pattern to their own (Yang et al., 2016). In the current study, using egg-shaped objects (i.e., mimetic real white eggs and non-mimetic blue and white model eggs), we tested whether egg recognition ability in common tailorbirds could be stimulated to examine the relationship between nest sanitation and egg rejection behavior. As egg-shaped objects can better simulate cuckoo eggs (Mermoz et al., 2016), we predicted that the addition of a real white egg together with a blue model egg would significantly increase the rejection rate of real white eggs compared to the group in which only real white eggs were added.

The study site is located at the Nonggang National Nature Reserve in Guangxi, southwest China (N22°13', E106°42') at an altitude of 150–650 m a. s. l.. The site has a typical subtropical monsoon climate with an annual mean

temperature of 20.8–22.4 °C and annual mean rainfall of 1 150–1 550 mm (Zhou & Jiang, 2008).

The study was conducted during the breeding season (March–September) in 2018. Common tailorbirds are one of the most abundant bird species in the study area and the main host for plaintive cuckoos, with a general parasitism rate of 17.0% (Yang et al., 2016). Common tailorbirds usually lay 4–5 brown-spotted blue or white eggs, with the plaintive cuckoos also laying eggs of similar (but not identical) color and pattern (Tunheim et al., 2019; Yang et al., 2016). Tailorbird hosts with blue clutches eject 100% of conspecific white eggs but accept 100% of conspecific blue eggs; similarly, tailorbird hosts with white clutches eject 100% of conspecific blue eggs and accept nearly all conspecific white eggs (Yang et al., 2016). The common tailorbird is a local resident species with a relatively long breeding season from mid-March until the end of September (Yang et al., 2016). These birds build nests in broad-leaf forests or shrubs at the edges of mountains by stitching together 1–3 leaves (Tunheim et al., 2019).

In this study, we carried out experiments on nests containing spotted-white eggs (Figure 1A). The mean weight, length, and width of the common tailorbird eggs were 0.92 ± 0.01 g, 15.50 ± 0.07 mm, and 11.09 ± 0.06 mm (mean \pm SD, same below; $n=38$), respectively. Real white eggs (Figure 1B) were purchased from munia (*Lonchura* spp.) suppliers with mean weight, length, and width of 1.03 ± 0.02 g, 16.60 ± 0.32 mm, and 12.36 ± 0.29 mm ($n=20$), respectively. Blue and white soft clays were manually molded into model eggs before they were baked for setting and were similar in size and shape to the common tailorbird eggs (Figure 1C, D). The mean weight, length, and width of the model eggs were 1.56 ± 0.01 g, 15.79 ± 0.16 mm, and 11.46 ± 0.08 mm ($n=15$) respectively.

We followed the methods of Yang et al. (2015a) to carry out egg rejection tests during the early stage of incubation. All experimental nests were independent and not parasitized. The experiments were carried out during the breeding season and were randomly performed. Four experimental groups were used: (1) real white eggs were added to 31 common tailorbird nests to test recognition ability. These eggs differed from common tailorbird eggs in that they were immaculate; (2) blue model eggs that differed greatly in color were added to 12 nests and (3) white model eggs that were similar in background color but without spots were added to 12 nests to test if the birds were able to recognize these as foreign eggs; (4) one blue model egg and one real white egg (Figure 1E) were added to 16 nests to examine the effects of nest sanitation on egg rejection behavior. Videos were then used to record the egg rejection behavior of the common tailorbirds. The experimental period was 6 d, and the study either ended when rejection occurred or after 6 d. Nests were monitored every 1–2 d for evidence of egg ejection and removal of model eggs (Yang et al., 2015a, 2019).

Data analysis was performed using IBM SPSS 25.0 software (IBM Corp., Armonk, NY, USA). Fisher's exact test was used to compare the probability of rejecting real white

eggs in different experimental groups. All tests were two-tailed, and the significance level was $P < 0.05$. All data are presented as mean \pm SD.

The experiments reported here comply with the current laws of China. All animal procedures performed in this research were in accordance with the ethical standards of the Animal Research Ethics Committee of Hainan Provincial Education Centre for Ecology and Environment, Hainan Normal University (permit no. HNECEE-2012-002).

The common tailorbirds generally used their bills to remove the model and real eggs. Of the 31 nests in the first group, real white eggs were rejected from only five nests (16.1%). In the second and third groups, the blue and white model eggs were rejected from all 12 nests (100%), respectively (Table 1). In the fourth group, however, although the blue model eggs were rejected from all 16 nests (100%), the real white eggs

were rejected from only eight nests (50.0%) (Table 1). Differences were observed in the time taken to reject real eggs (from 1–4 d) and model eggs (within 5 h after parasitism). When both real eggs and blue model eggs were added, the bird rejected the blue model egg before the real egg. No differences were observed between nests with the addition of white model eggs and blue model eggs (100% ejection in both cases). However, there was a highly significant difference in the rejection rates between nests with only real white eggs and nests with white or blue model eggs added ($\chi^2 = 38.176$, $df = 2$, $P < 0.001$). There was also a significant difference in the rejection rates between nests with only real white eggs and nests with both real eggs and blue model eggs ($\chi^2 = 6.051$, $df = 1$, $P = 0.02$), i.e., the addition of blue model eggs increased the rejection rate of real white eggs from 16.1% to 50%.

Table 1 Number of nests in which a model egg was rejected (% total nests) and number of nests in which a real white egg was rejected (% total nests)

Experimental group	Model egg rejection (%)	Egg rejection (%)	Number of nests tested
One real white egg	–	5 (16.1)	31
One blue model egg	12 (100)	–	12
One white model egg	12 (100)	–	12
One blue model egg and one real white egg	16 (100)	8 (50.0)	16

–: Not available.

Egg rejection by hosts remains one of the most striking examples in nature of how discrimination in social behavior evolves (Gloag & Beekman, 2019). Our results showed that common tailorbirds possessed strong nest sanitation ability, and that nest sanitation behavior directly affected egg recognition of real white eggs. Therefore, nest sanitation behavior increased the probability of foreign egg rejection. The rate at which common tailorbirds reject real mimetic white eggs was previously reported to be low (Yang et al., 2016). However, Yang et al. (2016) used conspecific white eggs with spots, whereas we used white eggs without spots. In our study, the recognition and rejection of 100% of the white and blue model eggs by the common tailorbirds demonstrated strong nest sanitation and egg recognition abilities. Interestingly, when both blue model eggs and real white eggs were added to a nest, the proportion of real white eggs rejected increased significantly, suggesting that rejection of blue model eggs elicited egg rejection behavior in these cuckoo hosts. We also found that the tailorbirds rejected the blue model eggs before they rejected the real white eggs.

Previous studies on nest sanitation and egg rejection behavior have suggested that a host's egg recognition ability is an extension of its nest sanitation behavior (Guigueno & Sealy, 2009, 2017; Moskát et al., 2003; Yang et al., 2015a, 2015b). Yang et al. (2015a) studied the relationship between nest sanitation and egg rejection in barn swallows, a host of common cuckoos, and found that the addition of peanut shells alongside model eggs significantly increased the probability of the model eggs being rejected compared to nests in which only model eggs were added. This suggests that nest

sanitation behavior in hosts can significantly affect egg recognition. In our study, common tailorbirds rapidly rejected 100% of the egg-shaped blue model and white model eggs added to their nests. These model eggs had the same effect as peanut shells in Yang et al. (2015a).

The rejection of all model eggs suggests a ubiquitous cleaning method and further implies that common tailorbirds have a strong ability to recognize and exclude egg-shaped objects similar in size to their own, which is consistent with the second stage of recognition of egg-shaped objects mentioned by Moskát et al. (2003). When the blue model egg was added alongside the real white egg, rejection ability increased because the sudden appearance of an obvious foreign object stimulated nest sanitation behavior. This resulted in the tailorbirds paying greater attention to other objects in the nest, i.e., their egg recognition ability was also activated, thereby increasing the egg rejection rate.

Common tailorbird nests are leaf-shaped and similar to cavity nests. During the hatching stage, foreign objects can fall into such nests. In addition, common tailorbirds are hosts to plaintive cuckoos and experience high cuckoo parasitism pressure (Nahid et al., 2016; Tunheim et al., 2019). Undoubtedly, parasitic eggs are major foreign objects in their nests. At the same time, plaintive cuckoos and common tailorbirds both produce spotted-white or spotted-blue eggs. However, when plaintive cuckoos parasitize the nests of common tailorbirds, the color of their eggs does not exactly match that of the host's (Yang et al., 2016). This difference in color between the parasitic and host eggs significantly increases the probability of egg rejection. In this sense, egg

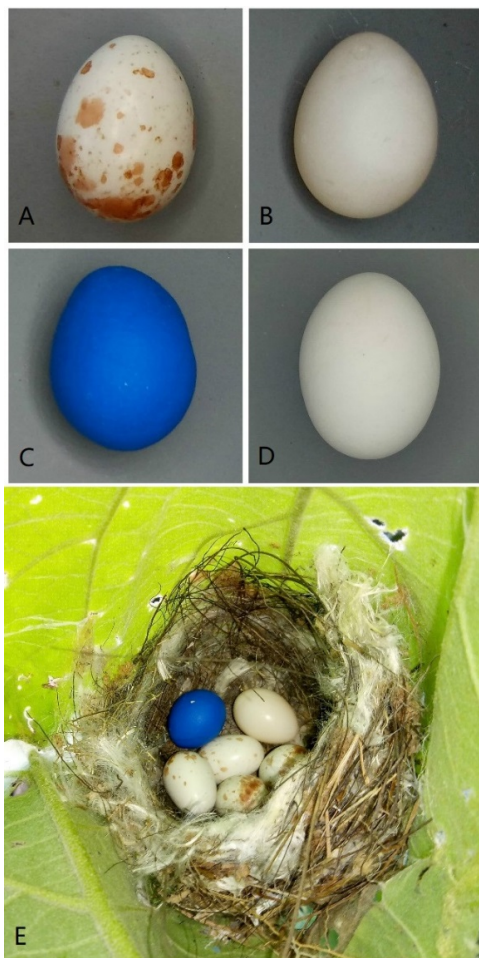


Figure 1 Photographs of common tailorbird egg (A), real white egg (B), blue model egg (C), white model egg (D), and example of experimental group with addition of one real white egg and one blue model egg (E) (Photos by Chang-Zhang Feng)

recognition is promoted in common tailorbirds through the presence of parasitic eggs that are recognizably different in color (Yang et al., 2016). This is similar to the removal of egg-shaped objects that differ from host eggs during nest sanitation behavior. However, the difference lies in egg color (Moskát et al., 2003). Common tailorbirds reject blue model eggs before rejecting real white eggs. This suggests that nest sanitation behavior evolved before egg recognition. In addition, egg rejection behavior in common tailorbirds toward model eggs and real white eggs is similar. This shows that egg rejection behavior is an extension of nest sanitation behavior. After blue model eggs were added, nest sanitation behavior was strengthened while the ability to reject real white eggs also increased.

Differences in egg recognition abilities are found among different bird species and populations, which explains why some previous studies found no relationship between nest sanitation and egg rejection. For example, the addition of

foreign objects had no effect on the rejection rate of foreign eggs in red-winged blackbirds, an egg acceptor of cowbirds (Kemal & Rothstein, 1988; McMaster & Sealy, 1997; Peer, 2017). Furthermore, the addition of peanut shells to brown-breasted bulbul nests (an egg rejecter) had no effect on the rejection of model eggs (Su et al., 2018). However, Yang et al. (2015a) found that the addition of peanut shells to barn swallow nests improved the rejection rate of model eggs. Common tailorbirds can recognize foreign eggs without stimulation of nest sanitation behavior, but the addition of obvious foreign objects may increase its motivation to recognize eggs in the nest and time spent checking. Evidently, more studies on the relationship between host nest sanitation behavior and egg rejection abilities are required to explain the origin of egg rejection ability.

The experiments carried out in the present study showed no significant differences between artificial model eggs and real eggs. This agrees with the results of Peer et al. (2002), who placed model eggs and brown-headed cowbird (*Molothrus ater*) eggs into northern mockingbird (*Mimus polyglottos*) nests and found no differences in the rates at which real eggs and model eggs were rejected. Guigueno & Sealy (2012) also determined that the shape and size of model eggs are important factors in host rejection of non-egg-shaped objects. Here, common tailorbirds rejected 100% of non-mimetic white model eggs added to their nest, but accepted some mimetic real white eggs, indicating that these birds can distinguish between white model and real eggs. This also suggests that more attention should be paid to bias in birds with strong egg recognition abilities (e.g., Yang et al., 2019) when model eggs are used to test host egg recognition in brood parasitism studies. In addition, understanding the phylogenetic distribution and transitions of nest sanitation and egg rejection behavior should facilitate future research (Liang et al., 2013).

In conclusion, our study showed that common tailorbirds possessed strong nest sanitation and recognition abilities and used their bills to remove model eggs similar in shape and size to their own. In addition, we demonstrated that the removal of egg-shaped foreign objects (e.g., model eggs) directly improved the birds' egg recognition ability. The association between egg ejection and nest sanitation in common tailorbirds provides valuable information on the cognitive decision-making processes of this plaintive cuckoo host. Furthermore, our study suggests that egg recognition ability in birds likely evolved from nest sanitation behavior and that egg recognition is a more advanced form of nest sanitation behavior.

COMPETING INTERESTS

The authors declare that they have no competing interests.

AUTHORS' CONTRIBUTIONS

W.L. designed the study; C.F. carried out field experiments; C.Y. performed laboratory and statistical analyses. C.F. wrote the draft manuscript; W.L. helped improve the manuscript. All authors read and approved the final

ACKNOWLEDGEMENTS

We are grateful to two anonymous referees for their constructive comments. We would like to thank Nonggang National Nature Reserve for their help and cooperation, and Bo Zhou and Jian-Chou Nong for their assistance in field work.

Chang-Zhang Feng¹, Can-Chao Yang¹, Wei Liang^{1,*}

¹ Ministry of Education Key Laboratory for Ecology of Tropical Islands, College of Life Sciences, Hainan Normal University, Haikou Hainan 571158, China

*Corresponding author, E-mail: liangwei@hainnu.edu.cn

REFERENCES

- Davies NB, Brooke MdeL. 1988. Cuckoos versus reed warblers: Adaptations and counteradaptations. *Animal Behaviour*, **36**(1): 262–284.
- Davies NB, Brooke MdeL. 1989. An experimental study of co-evolution between the cuckoo, *Cuculus canorus*, and its hosts. I. Host egg discrimination. *Journal of Animal Ecology*, **58**(1): 207–224.
- Gloag R, Beekman M. 2019. The brood parasite's guide to inclusive fitness theory. *Philosophical Transactions of the Royal Society B*, **374**(1769): 20180198.
- Guigueno MF, Sealy SG. 2009. Nest sanitation plays a role in egg burial by yellow warblers. *Ethology*, **115**(3): 247–256.
- Guigueno MF, Sealy SG. 2012. Nest sanitation in passerine birds: Implications for egg rejection in hosts of brood parasites. *Journal of Ornithology*, **153**(1): 35–52.
- Guigueno MF, Sealy SG. 2017. Implications of nest sanitation in the evolution of egg rejection. In: Soler M. Avian Brood Parasitism: Behaviour, Ecology, Evolution and Coevolution. Cham, Switzerland: Springer International Publishing AG, 385–399.
- Ibáñez-Álamo JD, Rubio E, Soler JJ. 2017. Evolution of nestling faeces removal in avian phylogeny. *Animal Behaviour*, **124**(1): 1–5.
- Kemal RE, Rothstein SI. 1988. Mechanisms of avian egg recognition: Adaptive responses to eggs with broken shells. *Animal Behaviour*, **36**(1): 175–183.
- Liang W, Yang C, Wang L, Møller AP. 2013. Avoiding parasitism by breeding indoors: cuckoo parasitism of hirundines and rejection of eggs. *Behavioral Ecology and Sociobiology*, **67**(6): 913–918.
- Luro AB, Hauber ME. 2017. A test of the nest sanitation hypothesis for the evolution of foreign egg rejection in an avian brood parasite rejecter host species. *The Science of Nature*, **104**(3–4): 14.
- Luro AB, Igic B, Croston R, López AV, Shawkey MD, Hauber ME. 2018. Which egg features predict egg rejection responses in American robins? Replicating Rothstein's (1982) study. *Ecology and Evolution*, **8**(3): 1673–1679.
- McMaster DG, Sealy SG. 1997. Red-winged blackbirds (*Agelaius phoeniceus*) accept prematurely hatching brown-headed cowbirds (*Molothrus ater*). *Bird Behavior*, **12**(3–4): 67–70.
- Mermoz ME, Haupt C, Fernández GJ. 2016. Brown-and-yellow marshbirds reduce their acceptance threshold of mimetic brood parasite eggs in the presence of non-mimetic eggs. *Journal of Ethology*, **34**(1): 65–71.
- Moskát C, Székely T, Kisbenedek T, Karcza Z, Bártl I. 2003. The importance of nest cleaning in egg rejection behaviour of great reed warblers *Acrocephalus arundinaceus*. *Journal of Avian Biology*, **34**(1): 16–19.
- Nahid MI, Fossøy F, Begum S, Røskoft E, Stokke BG. 2016. First record of common tailorbird (*Orthotomus sutorius*) parasitism by plaintive cuckoo (*Cacomantis merulinus*) in Bangladesh. *Avian Research*, **7**: 14.
- Payne RB. 1977. The ecology of brood parasitism in birds. *Annual Review of Ecology and Systematics*, **8**(1): 1–28.
- Payne RB. 2005. The Cuckoos. Oxford, UK: Oxford University Press.
- Peer BD. 2017. Nest sanitation does not elicit egg ejection in a brown-headed cowbird host. *Animal Cognition*, **20**(2): 371–374.
- Peer BD, Ellison KS, Sealy SG. 2002. Intermediate frequencies of egg ejection by northern mockingbirds (*Mimus polyglottos*) sympatric with two cowbird species. *The Auk*, **119**(3): 855–858.
- Polačiková L, Grim T. 2010. Blunt egg pole holds cues for alien egg discrimination: Experimental evidence. *Journal of Avian Biology*, **41**(2): 111–116.
- Rohwer S, Spaw CD. 1988. Evolutionary lag versus bill-size constraints: A comparative study of the acceptance of cowbird eggs by old hosts. *Evolutionary Ecology*, **2**(1): 27–36.
- Røskoft E, Korsnes L, Pedersen HC, Moksnes A, Braa AT, Lampe HM. 1991. Behavioural responses of potential hosts towards artificial cuckoo eggs and dummies. *Behaviour*, **116**(1–2): 64–89.
- Rothstein SI. 1975a. An experimental and teleonomic investigation of avian brood parasitism. *Condor*, **77**(3): 250–271.
- Rothstein SI. 1975b. Mechanisms of avian egg-recognition: Do birds know their own eggs?. *Animal Behaviour*, **23**(5): 269–278.
- Rothstein SI. 1982. Mechanisms of avian egg recognition: Which egg parameters elicit responses by rejecter species?. *Behavioral Ecology and Sociobiology*, **11**(4): 229–239.
- Su T, Yang C, Chen S, Liang W. 2018. Does nest sanitation elicit egg rejection in an open-cup nesting cuckoo host rejecter?. *Avian Research*, **9**: 27.
- Tunheim OH, Stokke BG, Wang L, Yang C, Jiang A, Liang W, Røskoft E, Fossøy F. 2019. Development and behavior of plaintive cuckoo (*Cacomantis merulinus*) nestlings and their common tailorbird (*Orthotomus sutorius*) hosts. *Avian Research*, **10**: 5.
- Yang C, Chen M, Wang L, Liang W, Møller AP. 2015a. Nest sanitation elicits egg discrimination in cuckoo hosts. *Animal Cognition*, **18**(6): 1373–1377.
- Yang C, Huang Q, Wang L, Jiang A, Stokke BG, Fossøy F, Tunheim OH, Røskoft E, Liang W, Møller AP. 2016. Plaintive cuckoos do not select tailorbird hosts that match the phenotypes of their own eggs. *Behavioral Ecology*, **27**(3): 835–841.
- Yang C, Liang W, Antonov A, Cai Y, Stokke BG, Fossøy F, Moksnes A, Røskoft E. 2012. Diversity of parasitic cuckoos and their hosts in China. *Chinese Birds*, **3**(1): 9–32.
- Yang C, Wang L, Liang W, Møller AP. 2015b. Nest sanitation behavior in hirundines as a pre-adaptation to egg rejection to counter brood parasitism. *Animal Cognition*, **18**(1): 355–360.
- Yang CC, Wang LW, Liang W, Anders Møller. 2019. High egg rejection rate in a Chinese population of grey-backed thrush (*Turdus hortulorum*). *Zoological Research*, **40**(3): 226–230.
- Zhou F, Jiang A. 2008. A new species of babbler (Timaliidae: *Stachyris*) from the Sino-Vietnamese border region of China. *The Auk*, **125**(2): 420–424.

Zoological Research Editorial Board

EDITOR-IN-CHIEF

Yong-Gang Yao

Kunming Institute of Zoology, CAS, China

ASSOCIATE EDITORS-IN-CHIEF

Wai-Yee Chan

The Chinese University of Hong Kong, China

Xue-Long Jiang

Kunming Institute of Zoology, CAS, China

Yun Zhang

Kunming Institute of Zoology, CAS, China

Yong-Tang Zheng

Kunming Institute of Zoology, CAS, China

MEMBERS

Amir Ardeshir

University of California, Davis, USA

Yu-Hai Bi

Institute of Microbiology, CAS, China

Le Ann Blomberg

Beltsville Agricultural Research Center, USA

Kevin L. Campbell

University of Manitoba, Canada

Jing Che

Kunming Institute of Zoology, CAS, China

Ce-Shi Chen

Kunming Institute of Zoology, CAS, China

Jiong Chen

Ningbo University, China

Peng-Fei Fan

Sun Yat-Sen University, China

Michael H. Ferkin

University of Memphis, USA

Nigel W. Fraser

University of Pennsylvania, USA

Patrick Giraudoux

University of Franche-Comté, France

Cyril C. Grueter

The University of Western Australia, Australia

David Hillis

University of Texas at Austin, USA

David Irwin

University of Toronto, Canada

Nina G. Jablonski

Pennsylvania State University, USA

Wei-Zhi Ji

Kunming Institute of Zoology, CAS, China

Xiang Ji

Nanjing Normal University, China

Jian-Ping Jiang

Chengdu Institute of Biology, CAS, China

Le Kang

Institute of Zoology, CAS, China

Julian Kerbis Peterhans

Roosevelt University, USA

Esther N. Kioko

National Museums of Kenya, Kenya

Randall C. Kyes

University of Washington, USA

Ren Lai

Kunming Institute of Zoology, CAS, China

David C. Lee

University of South Wales, UK

Shu-Qiang Li

Institute of Zoology, CAS, China

Wei Liang

Hainan Normal University, China

Hua-Xin (Larry) Liao

Duke University, USA

Si-Min Lin

Taiwan Normal University, China

Huan-Zhang Liu

Institute of Hydrobiology, CAS, China

Jian-Hua Liu

South China Agricultural University, China

Wen-Jun Liu

Institute of Microbiology, CAS, China

Meng-Ji Lu

University Hospital Essen, University DuisburgEssen, Germany

Masaharu Motokawa

Kyoto University Museum, Japan

Victor Benno Meyer-Rochow

University of Oulu, Finland

Nikolay A. Poyarkov, jr.

Lomonosov Moscow State University, Russia

Xiang-Guo Qiu

University of Manitoba, Canada

Rui-Chang Quan

Xishuangbanna Tropical Botanical Garden, CAS, China

Michael K. Richardson

Leiden University, The Netherlands

Christian Roos

Leibniz-Institute for Primate Research, Germany

Bing Su

Kunming Institute of Zoology, CAS, China

Kunjbihari Sulakhiya

Indira Gandhi National Tribal University, Amarkantak, India

John Taylor

University of Victoria, Canada

Christoph W. Turck

Max Planck Institute of Psychiatry, Germany

Wen Wang

Northwestern Polytechnical University, China

Fu-Wen Wei

Institute of Zoology, CAS, China

Jun-Hong Xia

Sun Yat-sen University, China

Guo-Jie Zhang

University of Copenhagen, Denmark

Ya-Ping Zhang

Chinese Academy of Sciences, China

Wu Zhou

The University of Mississippi, USA

ZOOLOGICAL RESEARCH
动物学研究
Bimonthly, Since 1980



Editor-in-Chief: Yong-Gang Yao

Executive Editor-in-Chief: Yun Zhang

Editors: Su-Qing Liu Long Nie

Edited by Editorial Office of Zoological Research

(Kunming Institute of Zoology, Chinese Academy of Sciences, 32 Jiaochang Donglu, Kunming,

Yunnan, Post Code: 650223 Tel: +86 871 65199026 E-mail: zoores@mail.kiz.ac.cn)

Sponsored by Kunming Institute of Zoology, Chinese Academy of Sciences; China Zoological Society©

Supervised by Chinese Academy of Sciences

Published by Science Press (16 Donghuangchenggen Beijie, Beijing 100717, China)

Printed by Kunming Xiaosong Plate Making & Printing Co, Ltd

Domestic distribution by Yunnan Post and all local post offices in China

International distribution by China International Book Trading Corporation (Guoji Shudian) P.O.BOX 399,
Beijing 100044, China

Advertising Business License 广告经营许可证: 滇工商广字66号



Domestic Postal Issue No.: 64-20

Price: 15.0 USD/80.0 CNY



ISSN 2095-8137

